UNIVERSIDADE FEDERAL DE SANTA CATARINA
CENTRO DE TECNOLOGIA
PROGRAMA DE PÓS-GRADUAÇÃO EM ENGENHARIA MECÂNICA

Rafael Becker Meier

Numerical study of combustion instabilities and low-temperature chemistry effects in premixed flames under internal combustion engine conditions

Florianópolis
2022

Rafael Becker Meier

Numerical study of combustion instabilities and low-temperature chemistry effects in premixed flames under internal combustion engine conditions

Thesis submitted to the Graduate Program in Mechanical Engineering at the Federal University of Santa Catarina to obtain the title of Doctor in Thermal Sciences.

Advisor: Prof. Amir A. M. de Oliveira Júnior, Ph.D.

2022

Florianópolis

Rafael Becker Meier

Numerical study of combustion instabilities and low-temperature chemistry effects in premixed flames under internal combustion engine conditions

This work at doctoral level was evaluated and approved by an examining board composed of the following members:

Prof. Guenther Carlos Krieger Filho, Dr. Eng.
University of São Paulo, USP

Prof. Fernando Marcelo Pereira, Dr. Eng.
Federal University of Rio Grande do Sul, UFRGS

Prof. Leonel Rincón Cancino, Dr. Eng.
Federal University of Santa Catarina, UFSC

This doctoral thesis was judged adequate as partial requisite to the degree of Doctor in Mechanical Engineering and approved on its final version by the Graduate Program in Mechanical Engineering.

Documento assinado digitalmente
Henrique Simas
Data: 05/06/2023 14:13:14-0300
CPF: ***.194.639-**
Verifique as assinaturas em https://v.ufsc.br

Prof. Henrique Simas, Dr. Eng.
Coordinator of the Graduate Program

Documento assinado digitalmente
AMIR ANTONIO MARTINS DE OLI...JUNIOR
Data: 02/06/2023 10:52:35-0300
CPF: ***.526.889-**
Verifique as assinaturas em https://v.ufsc.br

Prof. Amir A. M. de Oliveira Júnior, Ph.D.
Advisor

Florianópolis, 2022

To my parents

RESUMO EXPANDIDO

Introdução

O crescimento econômico mundial é uma soma positiva de benefícios onde mais pessoas têm acesso a mais bens e serviços. Ao mesmo tempo, a espinha dorsal do crescimento encontra-se, invariavelmente, no aumento da disponibilidade e consumo de energia. Uma das estratégias para mitigar os efeitos antropogênicos sobre o clima do planeta é reduzir as emissões dos modais de transporte. Embora a mudança a longo prazo aponte para um uso maior de eletrificação, e de combustíveis alternativos, como o hidrogênio verde e biocombustíveis, a ação imediata concentra-se na redução de peso e no aumento da eficiência de motores veiculares. O avanço na tecnologia da combustão é um dos componentes e, portanto, a eficiência termodinâmica dos motores deve ser aumentada para diminuir a emissão de gases de efeito estufa e poluentes.

Metodologia

Este estudo concentra-se na investigação das propriedades químicas, físicas e de transporte de chamas pré-misturadas pobres, amplamente utilizadas em motores de ignição por centelha para automóveis e em sistemas avançados de turbinas a gás para geração de energia. Além disso, são estudados combustíveis tradicionais, como simulacros da gasolina, e combustíveis renováveis promissores, como metano, dimetil éter e hidrogênio. A tese utiliza abordagens numéricas para investigar o comportamento da ignição e propagação de chamas em condições relevantes de motor. O trabalho está dividido em duas partes principais. A primeira parte volta-se para o estudo dos efeitos hidrodinâmicos e termo-difusivos de chamas de metano, dimetil éter e hidrogênio. Na segunda parte, o trabalho enfoca o processo de combustão onde a química de baixa temperatura desempenha um papel essencial e está relacionada ao limite de detonação de motores.

Resultados e discussões

Os efeitos das instabilidades, curvatura, deformações normais e tangenciais na taxa de estiramento da chama e velocidade de deslocamento da chama foram estudados usando simulações numéricas diretas para chamas canônicas, planares e de Bunsen, para três diferentes misturas pobres de combustível/ar, metano, DME e hidrogênio. A correlação entre a velocidade da chama e o número de Karlovitz mostrou-se semelhante para metano e DME. A fração de massa de hidrogênio ao longo da superfície da chama apresenta uma forte deficiência na região de curvatura positiva e excesso na região de curvatura negativa em comparação com a chama plana adiabática. Esta tendência é observada não apenas ao longo da superfície da chama, mas também em toda a distribuição de hidrogênio na direção normal. Para o hidrogênio, a chama de Bunsen mostra que a interação entre cinética química e taxa de estiramento modifica substancialmente a taxa de queima local para misturas pobres. Regiões com curvatura positiva podem queimar mais que o dobro da velocidade da chama plana, enquanto a curvatura negativa pode causar a extinção

desta. Na configuração de chama plana, os resultados mostram que a velocidade local da chama depende da taxa de crescimento das instabilidades. Estas crescem mais rapidamente em um valor específico de curvatura da chama relacionado ao comprimento de onda de perturbações iniciais. A chama plana em um domínio amplo mostra que as perturbações iniciais levam a um comportamento de propagação caótico onde a frente de chama é continuamente enrugada e composta por um espectro de pequenas cristas integradas em grandes comprimentos ondas semelhantes a dedos enrugados. Uma regressão linear feita com a correlação entre a curvatura local da frente de chama e a velocidade de consumo de combustível mostrou que o desvio da teoria de estiramento linear é menor para os pontos com curvaturas menores, enquanto para altos valores negativos, o desvio aumenta. A detonação do motor limita o desempenho e a eficiência de motores de ignição por centelha altamente comprimidos. O efeito do primeiro estágio de ignição na detonação do motor foi analisado usando um modelo quasi-dimensional. O modelo de chama CFM foi usado para modelar a combustão turbulenta e cinco modelos de cinética química reduzida foram aplicados ao processo de terminação da chama. Um motor CFR modificado, operando com duas misturas PRF, foi usado para testar a capacidade preditiva dos modelos e identificar as condições iniciais que levam à detonação. Embora os modelos de cinética química usados prevejam curvas de atraso de ignição semelhantes, eles não resultam nas mesmas previsões de detonação. Os resultados evidenciam a importância dos modelos químicos captarem corretamente o início da chama de baixa temperatura na região de NTC nos diagramas de atraso de ignição. Um mecanismo químico foi selecionado e então usado para identificar os tempos de atraso de ignição do primeiro e segundo estágio e sua dependência com a velocidade de rotação do motor e da taxa de compressão. Os resultados indicaram que a ignição de primeiro e segundo estágio se correlacionam de forma relativamente simples com a velocidade do motor e a taxa de compressão. Uma análise de sensibilidade evidenciou que apenas uma fração da química de baixa temperatura contribui para a ignição do primeiro estágio, e sua ocorrência determina o início da detonação do motor, sugerindo que a escolha de um aditivo inibidor do primeiro estágio pode atrasar a detonação nos motores de ignição por centelha. Além disso, foi investigada a formação e propagação de chama fria pré-misturada em condições relevantes de motores de combustão usando simulações numéricas diretas. O estudo forneceu informações físicas e químicas sobre as transições estruturais da chama e seus efeitos na velocidade da chama e no processo de autoignição. O efeito termo-físico foi avaliado parametricamente e os resultados mostram que, em condições transitórias, a temperatura tem um efeito menos significativo do que a pressão na velocidade da chama laminar. Para os casos simulados, a estrutura de chama dupla é substancialmente afetada pela pressão na qual o termo reativo se torna dominante à medida que a pressão aumenta. Ao contrário da chama quente, a frente fria mostrou que com o aumento da pressão, sua taxa de queima também aumenta, pois é estruturalmente mais dependente do termo reativo do que do termo difusivo. Uma investigação foi realizada para determinar o efeito das dimensões de um ponto quente sobre

a inicialização e propagação de uma chama fria. O estudo mostrou que a inicialização da chama fria depende de um tamanho crítico para dar origem a uma frente fria. No entanto, uma vez que uma chama fria é iniciada, não é uma condição obrigatória que a química de baixa temperatura promova um processo de autoignição.

Palavras-chave: *Chamas pré-misturadas pobres, instabilidades de chama, detonação em motores, autoignição, velocidade de chama laminar, química de baixa temperatura.*

ABSTRACT

Worldwide economic growth turns out to be a positive-sum of benefits where more people can access more goods and services. At the same time, the growth backbone relies on the increase in energy availability and consumption. One of the strategies to mitigate the anthropogenic effects of global climate change is reducing transportation emissions. While long-term change points to a larger use of electrification, green hydrogen, and biofuels, immediate action has focused on weight reduction and increasing vehicular efficiency. The advances in combustion technology are one of the components, and therefore, the thermodynamic efficiency of engines should be increased in order to decrease the emission of greenhouse gases and pollutants. This study focuses on the investigation of chemical, physical and transport properties of lean premixed flames, which are widely utilized in spark-ignition engines for automotive and in advanced gas turbine systems for power generation. In addition, traditional fuels such as gasoline surrogates and promising renewable fuels such as methane, dimethyl ether, and hydrogen are analyzed. The thesis uses numerical approaches to investigate flame ignition and propagation behavior at relevant engine conditions. The work is divided into two main parts. The first framework turns to study flame hydrodynamic and thermo-diffusivity effects of methane, dimethyl ether, and hydrogen flames. In the second part, the work focuses on the combustion process where low-temperature chemistry plays an essential role and is related to the engine knocking limit. The effects of flame instabilities, curvature, normal and tangential strains in the flame stretch rate and flame displacement speed were studied using DNS for canonical flames; slot burners, Bunsen and planar flames, for three different lean fuels/air mixtures, methane, DME and hydrogen. The correlation between flame speed and the Karlovitz's number is similar for methane and DME. The mass fraction of hydrogen along the flame surface presents a strong deficiency in the positive curvature region and strong excess in the negative curvature region compared to the planar, adiabatic flame. The trend is observed not only in the position of the flame surface but also in the entire distribution along the normal direction. For hydrogen, the Bunsen flame shows that stretch-chemistry and diffusion interaction substantially modify the local burning rate for sufficient lean mixtures. Positively curved regions may burn more than twice the flat flame speed, while negative curvature may cause flame front extinction. In the planar flame configuration, the outcomes show that the local flame speed depends on the growth rate. The instabilities grow faster at a specific value of flame curvature related to the front wavelength. The planar flame in a broad domain shows that the initial perturbations lead to a chaotic flame behavior where the wrinkled front is composed of a range of small crests and trough-shapes geometries, formed transversally by great wavelengths made up of smaller ones. A linear regression, made with the correlation of curvature and consumption speed, showed that the deviation from the linear theory is lower for the smaller curved points, while for higher negative values, the deviation increases. Engine knocking limits the performance

and efficiency of highly compressed, downsized, spark ignition engines. The effect of the first-stage ignition on the engine knocking was analyzed using a quasi-dimensional model. The standard coherent flame model is used for the turbulent combustion and five available reduced chemical kinetics models are applied to the end-gas process. A modified CFR engine, operating with two PRF mixtures, is used to test the predictive capacity of the models and to identify the onset conditions leading to knocking. Although the chemical kinetics models used predict similar ignition delay curves, they do not result in the same knocking predictions. The results evidence the importance that the chemistry correctly captures the start, from high to low-temperature, of the negative temperature coefficient region. The selected model is then used to identify the first and second-stage ignition delay times and their dependence on engine speed and compression ratio. The results indicate that the first and second-stage ignition correlate in a relatively simple form with engine speed and compression ratio. A sensitivity analysis evidences that only a fraction of the low-temperature chemistry contribute to the first-stage ignition, and its occurrence determines the onset of the engine knocking, suggesting that a choice of a first-stage inhibiting additive could delay knocking in SI engines. In addition, it was investigated the premixed cool flame formation and propagation at relevant combustion engines' conditions using DNS. The study provides physical and chemical insights into flame structural transitions and their effects on flame speed and the autoignition process. The results are focused on the impact of thermophysical properties under the flame speed and the structure of flames during the low-temperature chemistry. The thermophysical effect was parametrically evaluated and the results show that, at transient condition, the temperature has a less significant effect than the pressure on laminar flame speed. For cases simulated, the double flame structure is substantially affected by the pressure in which the reactive term becomes dominant as pressure is raised. Unlike the hot flame, the cool front showed that with the pressure raises, its burning rate also increases since it is structurally more dependent on the reactive term than the diffusive term. The hot spot size investigation shows that the cool flame initialization depends on a critical size to give rise to a cool front. However, once a cool flame is initiated is not a madatory condition that the low-temperature chemistry will promote an autoignition process since the active chemistry behind the front also showed a dependence on the hot spot size.

Keywords: *Lean premixed flames, flame instabilities, engine knocking, autoignition, laminar flame speed, low-temperature chemistry.*

List of Figures

List of Tables

Nomenclature

Roman symbols

A	area
$\mathcal{A}$	amplitude of perturbation
A_l	flame laminar area
c_p	isobaric heat capacity
$D_{m,i}$	diffusion coefficient of the i component into the mixture
Da	Damköhler number
f_{wall}	flame-wall interaction effect
H	height
h	total sensible enthalpy
h_i^o	enthalpy of formation of species i
$\tilde{h}$	molar enthalpy
$j_i^{''}$	diffusive mass flux
K	flame stretch rate
k	transverse wavenumber
$\dot{k}_j$	rate constant for either the forward or reverse reaction j
Ka	Karlovitz number
$\mathscr{L}$	Markstein length
L_f	induction length
L_p	hot spot size
l	characteristic length
l_0	integral scales of the turbulent flow
Le	Lewis number
m	mass
Ma	Markstein number
MW	molecular weight
$\vec{n}$	normal vector
p	pressure
Pr	Prandtl number
$\dot{Q}$	heat release rate
$\dot{Q}^{'''}$	volumetric heat release rate

$\dot{Q}'''_{max}$	maximum heat release rate of flat flame
R_f	flame front radius
R_u	universal gas constant
$\dot{r}$	reaction rate
$S_{i,j}^{Rel}$	relative sensitivity
S_a	absolute flame speed
S_c	flame consumption speed
S_d	flame displacement speed
$\tilde{S}_d$	density-weighted flame displacement speed
S_l^0	flat flame speed
s	flame arc-length
Sc	Schmidt number
t	time
$\vec{t}$	tangential vector
T	temperature
$\vec{V}$	flow velocity
$\vec{V}_f$	flame velocity
V	volume
v'_{rms}	root mean square of the velocity fluctuation
Y_i	mass fraction of component i
X_i	molar fraction of component i

Greek symbols

α	thermal diffusivity
β	Zel'dovich number
Γ	efficiency function of the turbulent flow
δ_l^0	flat flame thickness
δ_r	reacting zone thickness
θ	crank angle
ϑ	crank angle degrees related to ignition delay
κ	curvature
λ	heat conductivity
λ	wavelengths
μ	viscosity
ν	stoichiometric coefficient
Ξ	wrinkling factor
ρ	density
σ	density ratio
τ	characteristic time
τ_{1st}	first autoignition stage

τ_{2nd}	second autoignition stage
υ	specific volume
Φ	flame iso-surface
ϕ	equivalence ratio
Ω	engine speed
ω	growth rate
$\dot{\omega}_i'''$	reaction rate

Abbreviations

BDC	Bottom Dead Center
CAD	Crank Angle Degree
CFD	Computional Fluid Dynamics
CFF	Cool Flame Front
CFR	Cooperative Fuel Research Engine
CI	Compression Ignition
CR	Compression Ratio
DNS	Direct Numerical Simulation
EBI-DNS	Engler-Bunte-Institute Direct Numerical Simulation tool
EGR	Exghaust Gas Recirculation
EVO	Exhaust Valve Opening
FSD	Flame Surface Density
HCCI	Homogenous Charge Compression Ignition
HFF	Hot Flame Front
HRR	Heat Release Rate
IC	Internal Combustion
IDT	Ignition Delay Time
IEA	International Energy Agency
IVC	Inlet Valve Closing
LTC	Low-Temperature Chemistry
LTI	Low-Temperature Ignition
NTC	Negative Temperature Coefficient
ON	Fuel Octane Number
OpenFOAM	Open source Field Operation And Manipulation
PRF	Primary Reference Fuel
RCCI	Reactivity Controlled Compression Igntion
RCM	Rapid Compression Machine
RON	Research Octane Number
RPM	Rotation Per Minute
SCh	Start of Chemistry
SI	Spark Ignition

ST	Shock-Tube
TDC	Top Dead Center
TRF	Toluene Primary Reference Fuel

Subscripts

$1st$	first stage
$2nd$	second stage
b	burned gas
ch	chemical
DL	Darrieus-Landau instabilities
F	fuel
f	flame
g	gas
$h \rightarrow b$	from the homogeneous region to the equilibrium condition
h	homogeneous region
i	species i
ig	ignition
j	reaction j
k	species different than i
m	mixture-averaged
$mech$	mechanical work
n	normal direction
o	flame iso-surface
p	spot
r	reactions
res	residence
SI	spark ignition
sc	start chemstry
TD	thermo-diffusive instabilities
t	tangential direction
u	unburned gas
$u \rightarrow h$	from the unburned to the homogeneous region
$wall$	related to wall effects

Contents

Chapter 1

Introduction

1.1 ENERGY SCENARIO

Worldwide economic growth turns out to be a positive-sum of benefits where more people can access more goods and services. At the same time, the growth backbone relies on the increase in energy availability and consumption, Fig. 1.1. From the '70s to 2019, the energy demand was supplied mainly by coal, oil and natural gas. In 50 years, the dependence on combustion dropped from 87 to 80% in which the nuclear and renewable sources (e.g. geothermal, solar and wind) increased their contribution in the energy chain. In the transport sector, the global emissions in 2018 accounted for 8,285 $MtCO_2$, which is equivalent to 24% of the total CO_2 emissions from energy [1]. From this total, 45.1% was produced by passenger vehicles, including cars, motorcycles, buses and trains. The average carbon footprint of a medium-sized petrol car is estimated as 192 gCO_2 per passenger-kilometer [2].

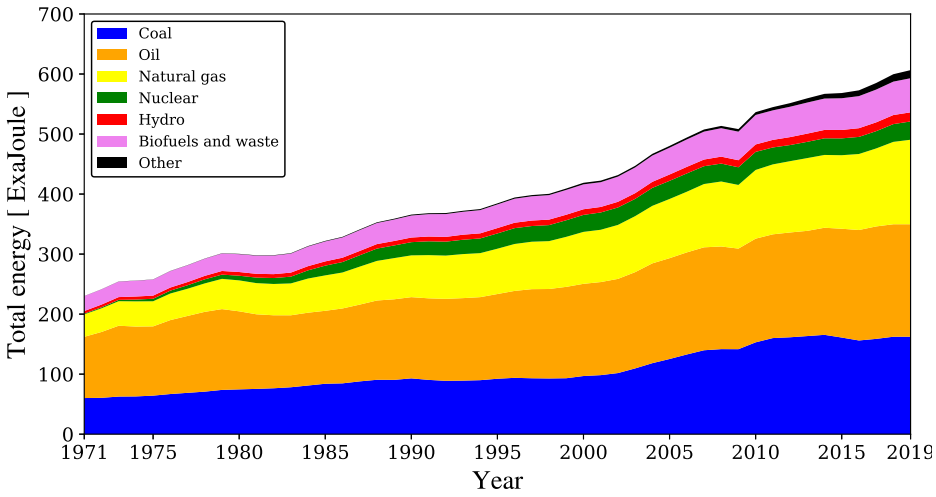

Figure 1.1: World total energy supply by source from 1971 to 2019. Source: IEA [3].

Currently, there are an estimated 1.2 billion passenger cars globally, and the numbers are still growing [4]. In addition to greenhouse gas emissions, other pollutants such as nitrogen

oxides, carbon monoxide, particulate matter, and soot are formed and released during the combustion process. Biofuels beneficially impact on CO_2 emissions; however, they carry the drawback to producing high toxicity aldehydes like formaldehyde, acetaldehyde and acrolein [5].

Figure 1.2 compares some examples of energy sources and device's specific power. Nowadays, pure electric or battery vehicles have a significant market share in passenger cars sales [6]. Nevertheless, if it is withdrew the nuclear fission and fusion process in Fig. 1.2a, the hydrocarbons/Li-ion (cobalt) ratio is at least an order of magnitude while H_2/Li-ion (cobalt) reaches two orders of magnitude. In the absence of a breakthrough in electrochemical technology for energy storage, batteries will remain lacking in their gravimetric and volumetric energy densities compared to combustion devices, Fig. 1.2b. The corollary of this is that even if light-duty vehicles convert to batteries, those required for heavy-duty vehicles will be massive. Moreover, stationary central storage of renewable electricity will also require massive and expensive resources and this will necessitate the continued use of combustion to provide electrical capacity for the grid [7].

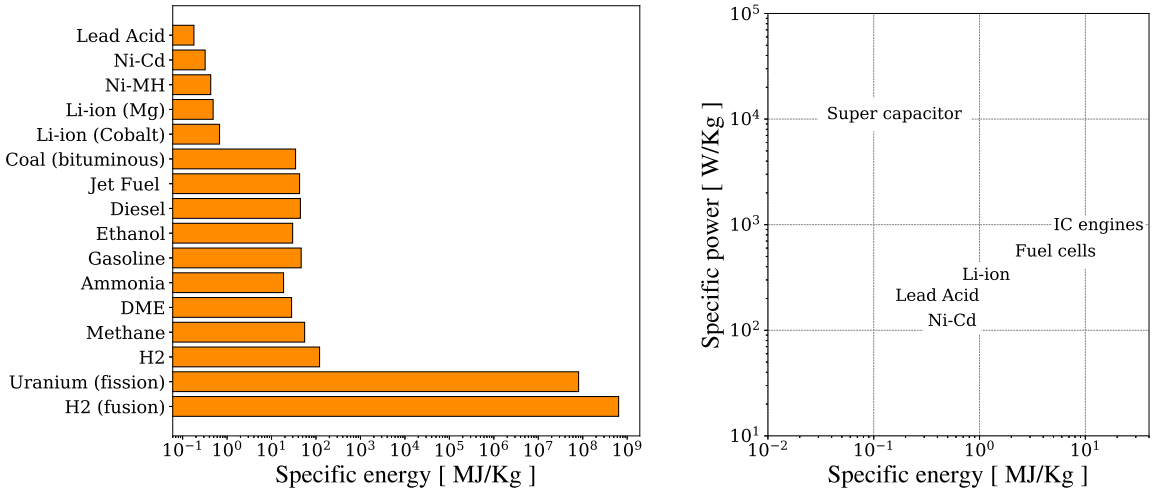

Figure 1.2: Comparison of specific energy, (a) for energy sources and batteries and (b) for some devices and its specfic power.

One of the strategies to mitigate the anthropogenic effects on global climate change is to reduce the emissions from transportation. While long-term change points to a larger use of electrification, green hydrogen, and biofuels, immediate action has focused on weight reduction and increasing vehicular efficiency. The advances in combustion technology is one of the components and, therefore, the thermodynamic efficiency of engines should be increased in order to decrease the emission of greenhouse gases and pollutants.

1.2 COMBUSTION IN ENGINES

In engines, the combustion process is a complex phenomenon that couples turbulent reacting flows with heat transfer. For IC engines and even in gas turbines, for certain regimes, the process occurs transiently, adding more complexity and difficulties for understanding all physical and chemical aspects involved.

In a combustion chamber, a flame originates at places with the most favorable conditions of temperature and concentrations gradients, where the reactions can stabilize, forming an interface that propagates towards the unburned gas [8]. Based on the temperature gradients, the reacting front can propagates as a deflagrative wave, or it can become a shock wave and even a detonation wave [9]. Phenomenologically, a flame initialization can be classified into two modes: forced-ignition or autoignition [10]. The force-ignition results from electrical discharge (spark), heated surface, shock wave, or pilot flame, with the locally initiated flame front subsequently reaching a self-propagating state where the ignition source can be removed without extinguishing the combustion process. Unlike forced-ignition, the autoignition (self-ignition) is caused by chain branching of thermal feedback in a homogeneous mixture without the input of either an external source of thermal energy or active radicals into the system [11]. In the last 30 years, the autoignition process received substantial attention from scientific and company researchers since it plays a key role in modern spark ignition (SI), compression ignition (CI), and ultra-lean combustion engines such as HCCI (homogeneous charge compression ignition) and RCCI (reactivity controlled compression igntion) [12–16]. It is related to the fundamentals of flame initialization and stabilization as well fuel efficiency and exhaust emissions. The mainly parameter that characterize the autoignition is called ignition delay time and it quantifies the elapsed period that a reactive mixture takes to reach a thermal explosion. According to the classical theory, as the temperature and pressure increase, the ignition delay time (IDT) decreases monotonically as a linear logarithm function of temperature. Unlike simple hydrocarbons (less than three carbon atoms), the complex molecules present a non-monotonic behavior with temperature called negative temperature coefficient (NTC) [10,17]. It refers a certain low- to intermediate-temperature range where the IDT increases with increasing initial temperature. This range is typically between 600 and 800 K at 1 atm [18]. The additional delay is caused by the low-tempertarure chemistry that slows down the chain branching given rise to the so called cool flame [19]. Underneath the difficulty of controlling and enhancing the combustion systems is found the low-temperature chemistry and cool flames. For SI engines, cool flames have long been considered a key process reponsible for engine knock [14, 20]. The developing of HCCI and RCCI engines faces several technical challenges due to the system operates in the NTC region and the increasined igntion sensitivity to fuel chemistry at LTC. As the result, the combustion-phase is maintained between the knocking and stability/misfire limits [16,21,22]. In a diesel engine, the cool flame significantly affects the hot temperature

chemistry. The in-cylinder condition is highly stratified which combined with the complex ignition chemistry of the fuel, create a fast-moving cool flame that controls the overall ignition behavior [13].

Hydrogen has the potential to be the sustainable fuel of the future, decrease the global dependence on fossil fuel resources, and lower the pollutant emissions from the transportation industry [23]. In the transition to a hydrogen based energy system, fuel flexible gas turbines are needed to utilise blends of hydrogen and other gaseous fuels, such as natural gas. Combustors need to cope with a wide range of natural gas/H_2-mixtures as well as with fast changes in the fuel composition. In the medium-term, fuel-flexible gas turbines capable of burning hydrogen/natural gas blends containing higher amounts of H_2 than nowadays need to be developed. In the long-term, gas turbines offering the full fuel flexibility (any blend of hydrogen and natural gas as well as pure hydrogen) are seen as foreseen technologies. Further development effort is required to derive technical solutions with respect to the following challenges associated with high hydrogen contents in the fuel; (1) Autoignition, higher autoignition risk due to lower ignition delay time, (2) Flashback, higher flashback risk due to higher flame speed or lower ignition delay time, (3) Modified thermo-acoustic amplitude level and frequencies, (4) Increased NO_x emissions, (5) Reduced lifetime need for more cooling of hot gas path components due to increased heat transfer [24]. The third item is still an instigating research area since it orignates from hydrogen's specific burning properties. Compared to natural gas flames, hydrogen flames exhibit significantly different thermoacoustic behaviour. This is due to higher flame speed, shorter ignition delay time and distinct flame stabilisation mechanisms resulting in different flame shapes, positions and different reactivity. Therefore, the risk of combustion dynamics (self-sustained combustion oscillations at or near the acoustic frequency of the combustion chamber) in modern gas turbines operated on hydrogen-rich fuels is expected to increase compared to natural gas operation. This implies that undesired and dangerous phenomena, such as combustion instabilities, flashback lean blow out, are likely to occur not only at steady conditions, but also more dangerously during transient operation, e.g. when rapid power changes are required and/or fuel composition changes.

1.3 MOTIVATION AND OBJECTIVES

This study focuses on the chemical, physical and transport properties of lean premixed flames, which are widely utilized in spark-ignition engines for automotive and in advanced gas turbine systems for power generation. In addition, tradicional fuels as gasoline surrogates and promising renewable fuels such as methane, dimethyl ether and hydrogen are analysed. Through numerical approaches, this thesis aims to investigate the flames ignition and propagation behavior at relevant engines conditions.

The study was divided into three frameworks. The first framework 1.3.1 turns to study of flame hydrodynamic and thermo-diffusivity effects of methane, dimethyl ether

and hydrogen flames. The second and third frameworks focus on combustion process where the low-temperature chemistry plays an essential role. Due to the different orders of magnitude in which the physical and chemical events occur in an IC engines, the two last approaches are divided as illustrated in Fig. 1.3. In the second approach 1.3.2, a thermodynamic spark-ignition engine model was developed to understand the behavior of the cool flame initialization and the role of chemical kinetics mechanisms in the onset knocking defintion. The third framework 1.3.3 investigates the low-temperature chemistry's effect on the one-dimension free flame propagation. Furthermore, a study on the cool flame front ignition and propagation from hot spots is performed. The specific motivation and objectives of the present study are described below.

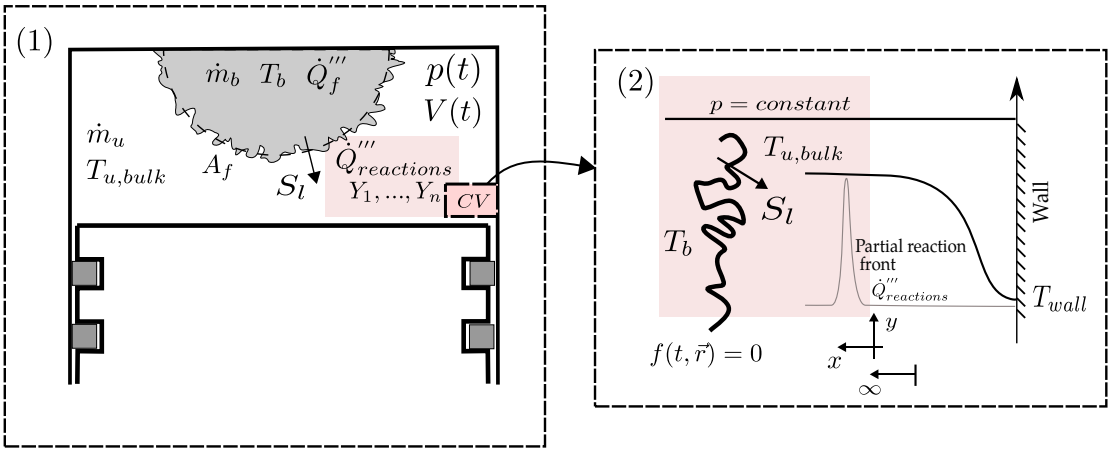

Figure 1.3: Schematic of the frameworks scales used in this work.

1.3.1 Flame instabilities

The increase in energy efficiency and fuel flexibility requirements for internal combustion engines and gas turbines have pushed the development of premixed and partially premixed mixture combustion systems to work under higher pressure, higher temperature and leaner mixtures. In addition, fit the current power generation and transportation devices to renewable sources is one of the upcoming challenges in combustion technology. Even with petroleum dominance as the energy carrier in the last century, hydrogen based resources has always attracted the interest of the scientific community since these resources are capable of generating power without contributing to emissions of carbon dioxide. Recent efforts in the use of hydrogen fuels focus in the concept of electrofuels (e-fuels) [7], however if one considers the application of e-fuels in internal combustion engines and in gas turbines, for instance, then several issues regarding the stability of the combustion process involving hydrogen fuels must be considered [24–27].

Premixed flames are characterized by their apparent and consumption flame speed [28]. The consumption flame speed results from the temperature and species distribution within the flame, while the apparent flame speed is a consequence of the interaction with the unburned flow field. Under a flame sheet approximation, the preheating and reaction

zones are collapsed into an infinitesimally thin region. In respect to this flame surface, the unburned flow field may have normal and tangential components. The normal component advects the flame sheet, developing flame curvature that interacts with thermal-diffusive and flow instabilities. The tangent component causes flame stretch, which is also present in a transient flame.

When subjected to a higher magnification, the laminar flame presents outer and inner structures: a preheating zone, with thickness δ_l, characterized by temperature and species mass fraction gradients, and a reaction zone, with thickness $\delta_r \ll \delta_l$, characterized by a distributed reaction region. The flame curvature changes the gradients of temperature and chemical species concentration in the preheating zone, changing the direction of the heat and mass transport vectors. These in turn affect the flame structure by changing the temperature and species concentrations in the reaction zone. The flame then seeks a new equilibrium structure and position in respect to the flow field. This interplay has important effects in many combustion phenomena such as flame stabilization, flashback, blowout, local extinction and re-ignition [29].

When flame sheet theories are compared to flame structure simulations, several aspects are undefined a priori, e.g., which isotherm or isoconcentration surface defines the position of the flame front, on which the flame curvature and stretch are calculated. Therefore, describing a complete laminar flame structure in terms of flame kinematics parameters is not a direct exercise.

In particular, lean hydrogen/air flames are prone to combustion instabilities. These instabilities substantially change the dynamics of the flame front and the associated heat release rate. The present-day combustion models cannot give an accurate quantitative description of the interaction of such instabilities with the background of turbulent flow. For instance, recent investigations suggest that the thermo-diffusive mechanism could be a source of additional flame wrinkling in turbulent flames [28, 30], however, these effects are not properly captured by combustion models, which often neglect the effect of these instabilities in turbulent flames. In practical systems, the presence of flame instabilities can act as a double-edged sword since they can create conditions that may cause damage and mechanical failures in the combustion device, while at the same time, these instabilities may be favorable for mixing enhancement and the subsequent increasing of the combustion burning rate rate [31].

Flame instabilities are caused due to two different mechanisms; the hydrodynamic instability and thermo-diffusive instability. The former arises from the density jump across the flame front, and it is largely responsible for the wrinkled aspect of the reactive front. Fluid dynamic considerations show that the deceleration of the flow ahead of flame, as illustrate by the flow streamlines at the flame front, has always a destabilizing effect which in turns yields to the exponential growth of the amplitude of the perturbations developing along the front, $\mathcal{A} \sim \mathrm{e}^{(iky+\omega t)}$. This physical process is always present in any flame and it is an inherent combustion phenomenon. The thermo-diffusive instabilities can act in both

directions, in the sense that they contribute to the increasing destabilization of the flame front while at the same time, due to preferential diffusion, this instability can lead to the decay of the formation of cellular structures at the front. The dynamics of this mechanics depends strongly on the balance between heat and mass diffusion transport.

Experiments carried out in spherical bombs, shown in Fig. 1.4, are able to show the development of instabilities [32,33]. For rich hydrocarbon-air or lean-hydrogen air mixtures, characterized by a Lewis number sufficiently less than one, the cellular appearance takes place shortly after the ignition. Contrarily, lean hydrocarbon-air and rich-hydrogen air mixtures, the formation of cellular structures only occurs if the hot radius is larger than a critical value. Before, the flame front curvature is large, and due to the high Lewis number, the molecular diffusion exerts a stabilizing influence on the small disturbances damping the expansion effect. After the flame reaches the critical size, the thermal expansion dominates the process giving rise to the cellular appearance.

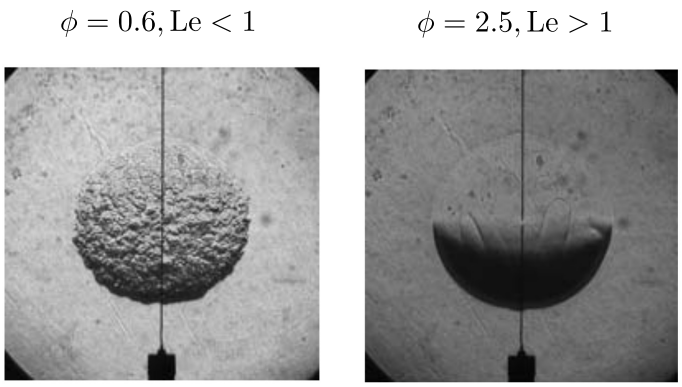

Figure 1.4: Schlieren images of outwardly propagating spherical flames of hydrogen-air for $\phi = 0.6$ and $\phi = 2.5$ at $p = 5$ atm. Source: Jomaas *et al.* [33].

Here, the interplay between flow and flame position and structure is analyzed as well the hydrodynamic and thermo-diffusive effects in two canonical flames, Bunsen flames, and planar flames, using direct numerical simulations. For this purpose, the chapter is divided into two main parts. First, a study was carried out in a slot-burner configuration where flames with $\mathrm{Le} \geq 1$ were analyzed. The focus here is: (1) developing and testing algorithms for premixed flame simulation and tracking, (2) analyzing the flame kinematics under different definitions of the location of the flame sheet, and (3) analyzing the effect of flame strain and curvature in local stretch rate, displacement speed, transport and reaction within the flame. In the second part, the simulations turn to hydrogen flames where the Bunsen and planar flames are assessed regarding the stretch-chemistry interaction and its consequence in generating instabilities. The analysis starts from a Bunsen flame in which the thermo-diffusive instabilities can be isolated from the hydrodynamic influence. For the planar flames, the instabilities linear growth are evaluated, taking into account a range of perturbations wavelengths in order to map the dynamics of cellular structure formation. Further, a broad domain and full-time simulation will be performed with the

aim to observe the spectrum of curvature wavelengths developing at the flame front, such that, based on these results, it will be possible to quantify the effects of the wrinkled flame front in the combustion burning rate.

1.3.2 Autoignition in SI engines

The thermodynamic efficiency of SI engines is mostly limited by knocking which is associated with the unburned "end-gas" autoignition [14, 34]. For the last decade, advancements in downsized, highly compressed engines have pushed the limits of knocking resistance [35]. However, further advancement has been hampered by the inherit difficulty in directly observing the chemical and physical phenomena leading to knocking, as well as, understanding the detailed effects of the fuel chemistry in the onset of engine knocking [36]. The use of modeling to understand knocking and also as a tool to design and optimize fuels and engines has increased in importance in the last years [14]. The usability of the models increase when they are comprehensive and run sufficiently fast to be incorporated in numerical simulation codes.

From the chemical point of view, many current methodologies to predict the conditions that lead to knocking and the severity of the wave propagation that follows rely on detailed or reduced chemical kinetics mechanisms to predict the chemistry of flame propagation and auto ignition [37]. Commercial fuels are complex mixtures of hydrocarbons and other oxygenated species and their complete chemical kinetics description requires hundreds of chemical species and thousands of chemical reactions [38]. The predictions of these mechanisms are tested against measurements in canonical experiments, such as shock-tube (ST) and rapid compression machine (RCM) ignition delay times and species concentrations in laminar flames, counter flow, uniform flow, and perfectly-stirred reactors. However, even when comparison to measurements predict general behavior, there is no certainty that the mechanisms will be able to provide good prediction of device specific measurements [39], specially when low-temperature chemistry is involved. When considerations of cost, computational time, and predictability of measurements are taken into consideration, the decision to model real devices fall back to either using simple, mostly incomplete, classical knocking models, or to a complete dismissal of the modeling effort and a complete reliance in global engine measurements.

The objectives of this part are two-fold. First, an analysis is performed of the prediction of the onset of knocking at a relatively simple engine simulation using 5 detailed and reduced mechanisms for a PRF mixture. It is shown that even when the mechanisms provide similar predictions of ignition delay time, they fail to produce consistent predictions of the onset of knocking under transient engine conditions. One of the mechanisms in then selected and used to analyze the effects that the timing and intensity of the first-stage ignition result in the main ignition event. A regime diagram for the onset of knocking is draw that summarizes the characteristics of the first-stage ignition that lead to the main ignition.

1.3.3 Low-temperature chemistry

Many combustion devices for transport and stationary applications such as gas turbines, after-burners and internal combustion engines use fossil fuels and biomass which are composed of complex organic molecules. Such fuels show a similar dynamic property during the autoignition process called low-temperature chemistry (LTC). It is an intrinsic, short-lived transient effect that manifests in combustion process when specific conditions of temperature, pressure and concentration are met. In the laminar free-flame propagation, the LTC can arise when the ignition timescale of the unburnt mixture ahead of the flame front is close to the flow residence time, modifying the temperature and mixture, consequently it affects the burning rate of the subsequent hot flame. In the presence of stratified conditions, the LTC gives rise to a flame structure defined as cool flame front (CFF). This phenomenon is recognized as autoignition assisted flame propagation [19,40,41].

Near the wall of combustion engines, the burning process is closely linked to low temperature oxidation. Due to the existence of large temperature and fuel concentration gradients the end-gas process affects the boundary layer combustion [42]. In spark ignition engines, the presence of such conditions can lead to knocking phenomena which are the limiting factor to engine efficiency [14]. In diesel engines, combustion is initiated by a two-staged autoignition that includes both low- and high-temperature chemistry. The location and timing of both stages of autoignition are important parameters that influence the development and stabilisation of the flame. For conventional diesel combustion, LTC is present during both the ignition and quasi-stable phases. For low-temperature diesel combustion, a quasi-stable flame does not exist and the LTC occupies a large portion of the cylinder and persists long after the high-temperature ignition develops [12, 13]. For aircrafts, a reheat concept is used in gas turbines which consists of two combustor stages that operate at lean premixed conditions. In the reheat combustor, the second stage can be stabilized primarily by an autoignition process [43]. Table 1.1 compares the typical low-temperature ignition (LTI or 1st autoignition stage) timescales of hydrocarbons fuels with the characteristic timescale of engines and turbulent flames.

Table 1.1: Comparison of LTI timescales of n-alkanes with the timescales in engines, turbulent flow, and flames. Note that the engine timescales depend on the engine design, operating conditions, and fuel. Source: Ju *et al.* [19].

Physical process	Timescales, ms
Low-temperature ignition	0.1-1000
Gasoline engine (20 CAD)	2
Diesel engine (10 CAD)	1
Gas turbine engine	1-5
Turbulence eddy, $l/u^{'}$	0.1 - 100
Flame time scale, δ_l/S_l	0.1-10

It is seen that at engine pressures (20-100 bar), the LTI delay time can be comparable to or even shorter than the timescale of engine combustion process, turbulent flows eddies, and the flame time scale [19].

Accordingly, controlling the autoignition and LTC shows great potential to enhance the combustion efficiency and thereby tackles the twofold concern of increasing burning rate through the flame speed as well as limiting the occurrence of undesirable combustion modes. Thus, advances in the understanding and controlling strategies of transient cool flame can be the key to reaching a combustion process with better energy efficiency [44].

The overall goal of this framework is to investigate the premixed cool flame formation and propagation at relevant combustion engine's like conditions through direct numerical simulation (DNS). The study provides physical and chemical insights into flame structural transitions and their effects on flame speed and the autoignition process. It branches on two main fronts. First, an analysis is performed of the impact on LTC in the main flame front (or hot flame front - HFF) at steady and transient conditions. Second, a transient study is carried out isolating the cool flame front as a hot pocket kernel investigating its ignition and propagation properties.

1.4 OUTLINE

Chapter 2 presents a brief theoretical background regarding the local flame speed and cool flames, which are general subjects of this work. Different definitions of flame speed are discussed, the concept of low-temperature chemistry, cool and warm flames are introduced. The following chapters present their background about the specific themes approached.

In Chapter 3, an analysis of classical flame propagating theory and direct numerical simulations results was performed in order to observe the interplay between flow aerodynamics and local flame speed when premixed flames undergo hydrodynamic, thermo-diffusive effects and self-sustainable instabilities in two canonical configurations, Bunsen flames, and planar flames.

Chapter 4 is concerned about the onset knocking. The initialization of cool flames in spark-ignition engines is studied by analyzing different kinetics mechanisms. The emphasis is on investigating the effect of engine speed, compression ratio, and chemical kinetics on low-temperature chemistry.

Chapter 5 is focused on flame structural and propagating behavior when the residence time of unburned mixture ahead the main front is sufficient to give rise a cool flame front. Analyses are carried out over the flow-chemistry interaction and the effects of inlet temperature and pressure. Also, it is investigated the thermophysical and transport properties of the cool flame front in order to understand how its interface interacts with the flow, heat loss, and the burning process.

Chapter 6 summarizes the present findings in theses analyses and provides recommendations for future works.

Chapter 2

Fundamentals and numerical models

This chapter introduces an overview of the main topics discussed in this work; the concept of low-temperature chemistry, cool and warm flames, and the local flame speed. In addition, it is presented the numerical solvers and governing equations used to tackle the reacting problems.

2.1 AUTOIGNTION IN HYDROCARBONS

The autoignition process occurs when the thermodynamic state of a reacting mixture can give rise to a spontaneous ignition without any external heat source. The hydrocarbon's autoignition properties depend on the structure of the fuel molecule. Normal alkanes, such as n-heptane, ignite at lower temperatures than other alkanes with the same carbon number. This property results from its linear chain structure containing only saturated bonds, which implies that there are no preferred collision directions for the degradation of the fuel molecule. Thus, n-alkanes have a relatively short ignition delay time over the entire temperature range. On the other hand, branched alkanes, such as iso-octane, present preferential collision directions, and longer ignition delay. The current way of understanding autoignition is based on discussing the main reaction paths related to the ignition delay measured in a shock-tube or in a RCM. The use of RCM and ST allows a more direct and accurate relationship between temperature, pressure, stoichiometry and time required for the thermal explosion. The analysis of the associated chemical mechanisms allows for elucidation the essential intermediate reactions in the initiation, propagation and branching of the chain reactions, providing a detailed description of the behavior of the various hydrocarbons. This subject is discussed in detail in the works of Curran [45], Tanaka [46], Davidson *et al.* [47], He *et al.* [48], Walton *et al.* [49], Cancino *et al.* [50], Cancino *et al.* [51], Mehl *et al.* [52] and AlAbbad *et al.* [53].

Hydrocarbons as n-alkanes with more than two carbon atoms exhibit specific experimental characteristics that can be generalized [17]. They form aldehyde groups that shorten the ignition delay. Hydrocarbons exhibit the cool flame phenomenon, except for methane and ethane. This phenomenon results in the formation of two stages of heat

release, which means that the dependence on the global reaction rate of a fuel does not show a monotonic behavior with increasing temperature. It is defined as the negative temperature coefficient characterized by a range of relatively low temperatures that raise the IDT as the temperature increases.

2.1.1 Cool flames and knocking

During flame propagation in the engine cylinder, the pressure and local temperature ahead of the flame front increase exponentially. Roughly speaking, when the elapsed time to completely burn the unburned fraction ahead of the flame exceeds the autoignition delay time, the end-gas will experience autoignition..

In the last two decades, several studies, e.g. [37, 40, 54–58], have shown that the onset of knocking is affected by the existence of a region of negative temperature coefficient in the ignition delay time curve for the fuel-air mixture. Works in rapid-compression machines (RCM) concluded that the knocking originates from the localized development of hot spots in an inhomogeneous temperature field. However, in temperatures in the NTC range, colder spots may experience ignition before hotter spots.

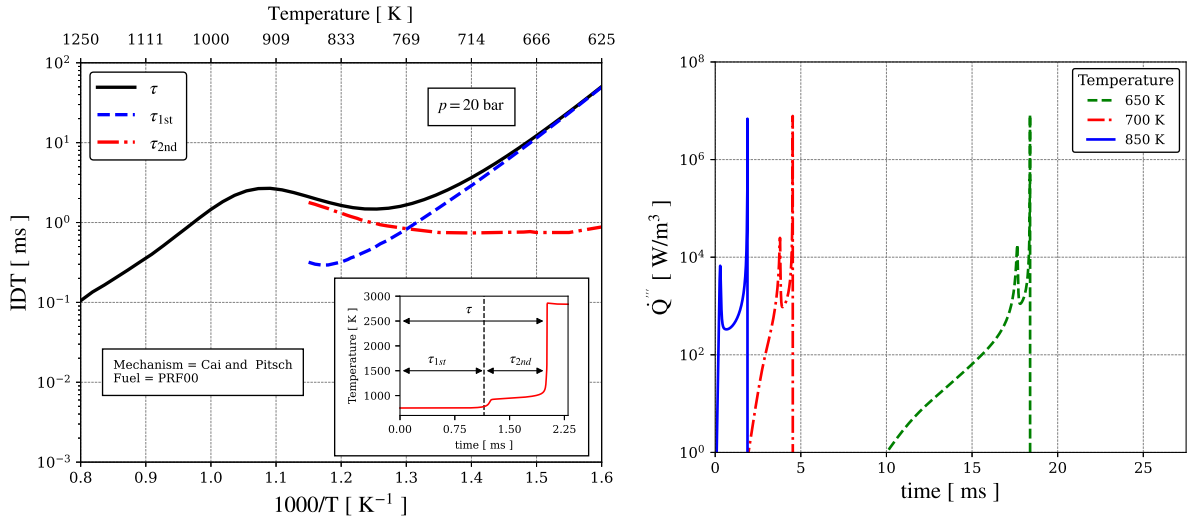

Figure 2.1: Ignition delay time for an adiabatic and isobaric reactor of homogeneous stoichiometric PRF00/air mixture: (a) Ignition delay time and (b) Volumetric heat release rate history for ignition processes at 650 K, 700 K and 850 K.

Figure 2.1a presents the IDT behaviour of an n-heptane/air mixture (PRF00) at 20 bar, calculated using the Cai and Pitsch chemical kinetics mechanism [59]. The NTC region exists from about 800 K to 900 K. The inset in the lower right corner shows the temperature evolution of the thermal ignition starting at 900 K. We notice the existence of the first-stage ignition at $\Delta t = \tau_{1st}$, followed by the second-stage ignition $\Delta t = \tau_{2nd}$ milliseconds later. The overall ignition delay time is $\tau = \tau_{1st} + \tau_{2nd}$. The first-stage and second-stage ignition delay times are represented by the blue dashed and the red dash-dot

lines, respectively. At temperatures below 700 K, the first-stage ignition delay, τ_{1st}, is much larger than τ_{2nd}. When the temperature exceeds 800 K, the second-stage ignition delay, τ_{2nd}, becomes larger than the first-stage. Above 850 K, the second-stage ignition delay prevails . Figure 2.1b shows the heat release rate at these three temperatures. In each curve, the first peak is the first-stage ignition and the second peak is the second-stage ignition. The elapsed time in which they occur change depending on the initial temperature. At 650 K, the overall ignition delay time is about three times that at 700 K, and the first-stage delay ignition has the largest contribution to the overall ignition delay (τ_{2nd} is about 3.5 % of τ). At 850 K, at the end of the NTC region, the ignition delay is only about half that at 700 K. However, τ_{1st} is only about 14 % of τ. The trend continues and the first-stage ignition vanishes when $T > 900$ K.

2.1.2 Thermal ignition chemistry

The basic chemistry leading to thermal ignition is well known. Basically, the reactions that promote thermal ignition are those that lead to the rapid build up of a radical pool sufficient to initiate and sustain radical chain propagation and heat release. The reactions that inhibit thermal ignition are those that lead to radical termination. Differently from what occurs in flames, during thermal ignition the higher alcanes respond along different reaction paths, depending on the temperature and pressure.

Ju *et al.* [19] presented a flame classification based on the main reaction pathways that determine the chemistry at low, intermediate, and high temperatures. The reaction pathways that define the cool, warm, and hot flames for an alkane are schematically depicted in Fig. 2.2.

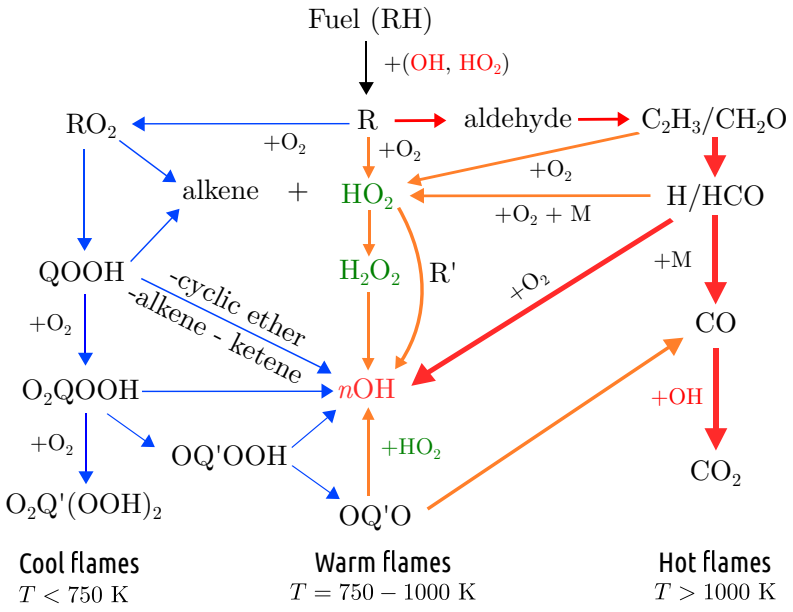

Figure 2.2: A schematic of key reaction pathways at high, intermediate, and low temperatures (blue arrows: $T < 750$ K; yellow arrows: $750 < T < 1000$ K; red arrows: $T > 1000$ K) for hot, warm, and cool flames, adapted from Ju *et al.* [19].

The first low temperature reaction channels for the oxidation of alkanes were proposed by Knox [60], Fish [61], Pollard [62], Cox and Cole [63], and Walker and Morley [64].

At low temperatures ($T < 750$ K), the reaction pathway R $\rightharpoonup$ RO_2 $\rightharpoonup$ QOOH $\rightharpoonup$ O_2QOOH $\rightharpoonup$ $OQ^{'}O + 2\,OH$ produces multiple radicals and is the low-temperature chain branching pathway governing fuel oxidation in cool flames (see also [38]). As the temperature increases, the chain propagation pathway R $\rightharpoonup$ RO_2 $\rightharpoonup$ QOOH $\rightharpoonup$ OH + cyclic ether becomes so fast that the low temperature R $\rightharpoonup$ RO_2 $\rightharpoonup$ QOOH $\rightharpoonup$ O_2QOOH $\rightharpoonup$ $OQ^{'}O + 2\,OH$ chain-branching pathway is suppressed. Moreover, the reverse reactions $R + O_2 \rightleftharpoons RO_2$ and $QOOH + O_2 \rightleftharpoons O_2QOOH$ as well as the decomposition of RO_2 to olefin, $RO_2 \rightharpoonup$ alkene + HO_2 further reduce the formation of RO_2. As such, the slowdown of radical production results in the NTC effect in which the O_2QOOH, QOOH, and RO_2 decomposition reactions are the main contributors.

At intermediate temperatures (750 - 1000 K), fuel oxidation is governed by a branching process involving HO_2. At these temperatures, HO_2 can be directly produced via RO_2 and QOOH trough $RO_2 + HO_2$ and QOOH $\rightharpoonup$ OH + cyclic ether $\rightharpoonup$ alkene + HO_2. A small alkyl radical ($R^{'}$) formed via RO_2 or QOOH decomposition can also react with HO_2 in $R^{'} + HO_2 \rightharpoonup R^{'}O + OH$ to form an active OH radical and an alkoxy radical $R^{'}O$. In addition, the reaction between aldehyde (aldehyde + $HO_2 \rightharpoonup H_2O_2 + R^{'}CO$, e.g., CH_2CHO) and O_2 via $R^{'}CO + O_2 \rightharpoonup$ aldehyde + CO + OH also produces an active OH radical and smaller aldehydes (e.g., CH_2O). Furthermore, the reaction between $R^{'}O$ with O_2 via $R^{'}O + O_2 \rightharpoonup$ aldehyde + HO_2 leads to an (excited) aldehyde moldecule and HO_2. The excited state of formaldehyde ($CH_2O \cdot$) formed via reactions $R^{'}CO + O_2 \rightharpoonup$ aldehyde + CO + OH and $R^{'}O + O_2 \rightharpoonup$ aldehyde + HO_2 produces the faint blue, luminescence of cool flames. The subsequent $CH_2O \rightharpoonup HCO \rightharpoonup HO_2 \rightharpoonup H_2O_2 \rightharpoonup {}_2OH$ reaction pathway converts CH_2O into a second OH radical. It should also be noted that this chain-branching process is relatively slow and is sensitive to oxygen concentration. Because of the existence of this intermediate-temperature chain-branching reaction pathway, a dual-stage warm flame can exist between the cool flame and the hot flame.

At high temperatures ($T > 1000$ K), the induction period is most sensitive to the chain branching reactions $CH_3 + O_2 \rightharpoonup CH_3O + O$ and $H + O_2 \rightharpoonup OH + O$, being the later the reaction with the largest sensitivity. The reactions $CH_3 + CH_3 + M \rightleftharpoons C_2H_6 + M$ and $H + CH_4 \rightharpoonup CH_3 + H_2$ play important roles in inhibiting the thermal ignition. The concentration of HO_2 increases through primary initiation and, more significantly, through H-atom abstraction reactions with molecular oxygen. At temperatures below 1500 K, $RH + HO_2 \rightharpoonup CH_3 + H_2O_2$ followed to $H_2O_2 + M \rightleftharpoons {}_2OH + M$ leads to the additional radical formation. This buildup of H_2O_2 and its subsequent decomposition into OH is an important characteristic of the thermal ignition. Simultaneously, the formation of formaldehyde CH_2O from alkyl radicals and its subsequent decomposition further increases the radical pool.

As a result, formaldehyde CH_2O emerges as a good tracer for intermediate and high

temperature ignition, since it is formed in the first-stage ignition and consumed at later stages of the autoignition. Its abundance in the end-gas region is used for detecting and studying the occurrence of exothermic kernels using two-dimensional laser induced fluorescence (2D-LIF) [65]. Hydroperoxides (QOOH) are also important during gas phase fuel chemistry in internal combustion engines as they trigger the first-stage autoignition of gasoline and diesel fuel components [66]. The second-stage autoignition is related to the fast H_2O_2 consumption.

Under certain conditions, a cool flame may propagate as a wave. Stable premixed cool flames have been experimentally observed and numerical simulations have investigated the complex transitions and flame structures that originate from the interactions between the cool and the high-temperature flames. These interactions may be important for internal combustion engines, since the location of the cool flame can influence the ignition delay time and engine knocking in spark ignition engines [40, 56–58].

2.2 FLAME SPEEDS

The speed of a laminar planar unstretched freely propagating one-dimensional flame, S_l^0, is the reference speed for all combustion studies, Fig. 2.3. It is defined as the propagation speed of a deflagration wave relative to the unburned mixture velocity. It has a precise meaning when the flame is planar and propagates steadily because the mass flow rate through the flame is constant and uniform. In this reference flame, the entire structure travels consuming the unburned mixture at a constant speed S_l^0. In practice, the flame speed in simulations have to be computed from two methods: trough the consumption of a chemical specie or relative to the energy equation, yielding the consumption speed S_c, or from the movement of the flame surface resulting in the displacement speed S_d [28,29,67–69]. For unstretched flame, the results for both models are equivalent, although S_c comes from a global property and S_d is computed locally. The following subsections describe how the S_l^0 is computed in terms of S_c and S_d.

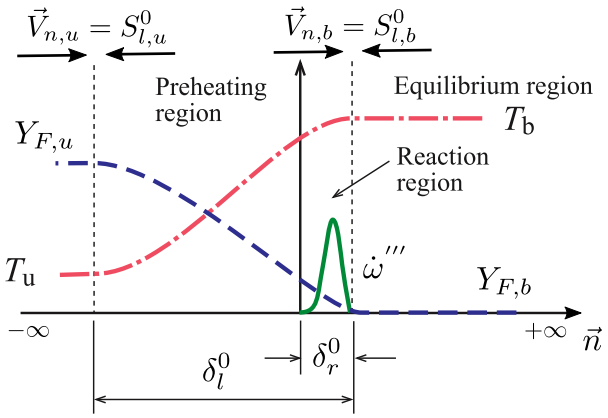

Figure 2.3: Laminar unstretched freely propagating flame structure.

2.2.1 Consumption speed

The consumption speed is a quantity resulting from an integral over all flame structure, Fig. 2.3. The conservation equation for the fuel in a reacting mixture yields

$$\rho\frac{\partial Y_F}{\partial t} + \rho\vec{V}\cdot\nabla Y_F = \nabla\cdot(\rho D_{m,F}\nabla Y_F) + \dot{\omega}_F^{'''}, \tag{2.1}$$

where ρ is the fluid density, $\vec{V}$ is the flow velocity, Y_F is the fuel mass fraction and $D_{m,F}$ and $\dot{\omega}_F^{'''}$ are the diffusion coefficient of the fuel into the mixture and the fuel reaction rate, respectively. The flame structure is steady-state, so the time derivative is zero. For the integration of the entire domain from the unburnt to the burnt gas, in a coordinate system normal to the flame propagation, $\vec{n}$, it results in

$$\int_{-\infty}^{+\infty}\rho\vec{V}_n\frac{dY_F}{d\vec{n}}d\vec{n} = \int_{-\infty}^{+\infty}\frac{d}{d\vec{n}}\left(\rho D_{m,F}\frac{dY_F}{d\vec{n}}\right)d\vec{n} + \int_{-\infty}^{+\infty}\dot{\omega}_F^{'''}d\vec{n}. \tag{2.2}$$

The diffusion term vanishes on the right-hand side since there is no gradient at the domain inlet or outlet. The equation for the flame consumption speed is given by

$$S_c = \frac{1}{\rho_u(Y_{F,u} - Y_{F,b})}\int_{-\infty}^{+\infty}\dot{\omega}_F^{'''}d\vec{n}. \tag{2.3}$$

2.2.2 Displacement speed

Since the flame structure remains as a continuous group of scalar properties propagating according to the flame speed, any local variable can be used as a reference in terms of the relative motion of the flame regarding the velocity field. The displacement speed can be expressed as the difference between the flow speed $\vec{V}\cdot\vec{n}$ and the absolute front speed $\vec{V}_f\cdot\vec{n}$, which gives

$$S_d = (\vec{V}_f - \vec{V})\cdot\vec{n} = S_a - \vec{V}\cdot\vec{n}. \tag{2.4}$$

The local variable chosen as the reference gives rise to the scalar iso-surface representing the entire flame. So, the local iso-surface, Φ, defines the normal vector to the flame front

$$\vec{n} = \frac{\nabla\Phi}{|\nabla\Phi|}, \tag{2.5}$$

replacing Eq. (2.5) into (2.4), it results in

$$S_d = \vec{V}_f\cdot\vec{n} - \vec{V}\cdot\vec{n} = \frac{1}{|\nabla\Phi|}\frac{\partial\Phi}{\partial t} + \vec{V}\frac{\nabla\Phi}{|\nabla\Phi|} = \frac{1}{|\nabla\Phi|}\frac{D\Phi}{Dt}. \tag{2.6}$$

Equation (2.6) shows that the displacement speed represents the material derivative for the flame propagation in which the absolute speed is the transient therm and the advection term is related to the flow field. Using Eq. (2.1)'s right hand-side in the Eq. (2.6) yields

$$S_d = \frac{1}{\rho_u |\nabla Y_F|}(\nabla \cdot \rho D_{m,F} \nabla Y_F) + \dot{\omega}_F'''), \tag{2.7}$$

which gives a physical interpretation of displacement speed. The equation above can be split into two terms, the reaction contribution and diffusive contribution,

$$S_{diff} = \frac{1}{\rho |\nabla Y_F|}(\nabla \cdot \rho D_{m,F} \nabla Y_F), \;\; S_{reac} = \frac{1}{\rho |\nabla Y_F|}(\dot{\omega}_F'''). \tag{2.8}$$

This means that for an unstretched flame

$$S_d = S_{reac} + S_{diff}. \tag{2.9}$$

For the stretched flame, however, the curvature, gradient of mass fraction and reaction affect the flame displacement speed.

The iso-surface representing the flame surface used for calculating S_d is typically selected within the flame, where variations in density from its unburned value have taken place, affecting the mass flux through this surface. For a meaningful comparison between values of the displacement speed defined at different locations, S_d is often normalized by the ratio of local density ρ to the density if the fresh mixture ρ_u yielding,

$$\tilde{S}_d = \frac{\rho S_d}{\rho_u} \tag{2.10}$$

The density-weighted flame displacement speed, $\tilde{S}_d$, can be directly compared to the laminar flame speed S_l for the same reactant mixture [69].

2.3 GOVERNING EQUATIONS AND MODELING

Numerical simulation tools were used to investigate the effects of hydrodynamic and preferential diffusion instabilities on premixed flames with Lewis numbers above and below unity and, evaluate the role of low-temperature chemistry during end-gas conditions like those found in IC engines. In this work, two general approaches were applied. A thermodynamic analysis was performed using an in-house code coupled to the Cantera library [70] in order to investigate the autoignition process in SI engines. The second one turns to the study of the flame front propagating and unsteady LTC effects over flame propagation using the CFD code EBI-DNS (Engler-Bunte-Institute Direct Numerical Simulation) [71].

Cantera is an open-source suite of tools used to compute transport properties derived from rigorous kinetic gas theory and chemical kinetics source terms [72]. The EBI-DNS implementation uses OpenFOAM's [73] standard capabilities coupled to the Cantera library, which address detailed transport coefficients to momentum, species, and energy equations, Fig. 2.4. The CFD solver uses Cantera's routines employing a splitting operator technique with the highly optimized library Sundials CVODE [74]. It is used to perform a

time integration of each cell as a batch reactor over the CFD time step using methods designed for stiff systems of differential equations. The following subsections present a brief description of the chemical, thermodynamic, transport and flow models used in this work [75].

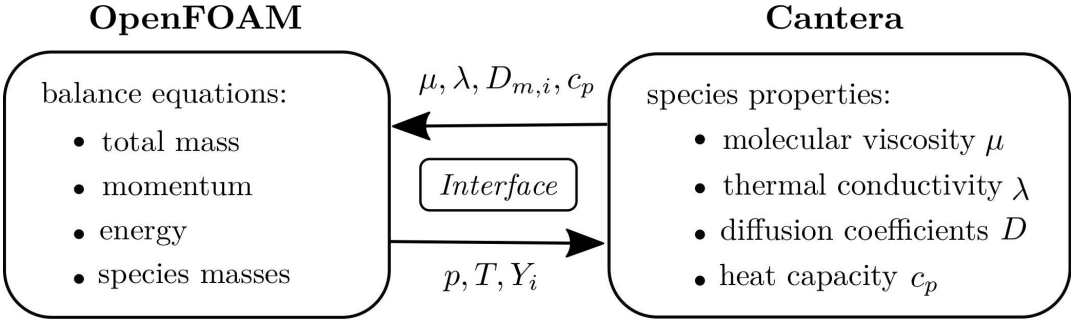

Figure 2.4: Working principle of the EBI-DNS solver. OpenFOAM's capabilities for solving the balance equations with the finite volume method coupled with Cantera's abilities to compute detailed thermophysical properties and transport coefficients, adapted from Zirwes [75].

2.3.1 Chemical model

The overall rate of changes of species i, $\dot{\omega}_i^{'''}$, is split into a forward molar reaction rate $\dot{r}_j^{'}$ of reaction j and a reverse rate, $\dot{r}_j^{''}$ [72]. They are defined as

$$\dot{r}_j^{'} = k_j^{'} \prod_i \left(\frac{\rho Y_i}{\mathrm{MW}_i} \right)^{e_{i,j}^{'}}, \qquad \dot{r}_j^{''} = k_j^{''} \prod_i \left(\frac{\rho Y_i}{\mathrm{MW}_i} \right)^{\nu_{i,j}^{''}}, \tag{2.11}$$

where $k_j^{'}$ ($k_j^{''}$) is the forward (reverse) rate constant of reaction j. MW_i is the molecular weight of species i and $e_{i,j}^{'}$ the species reaction order, which elementary reactions is the same as the stoichiometric coefficient $\nu_{i,j}^{'}$ ($\nu_{i,j}^{''}$) of the reactant (product) species i and reaction j. The rate constants $\dot{k}_j$ for either the forward or reverse reaction can be computed as standard three-parameter Arrhenius reactions

$$\dot{k}_j = A_j T^{\beta_r} exp\left(-\frac{E_{a,r}}{R_u T} \right), \tag{2.12}$$

where R_u is the universal gas constant. For pressure reactions dependence, the special treatments are used as Lindemann falloff reactions, Troe falloff reactions and SRI. Another supported reaction type are plog reactions, where the rate constants are interpolated logarithmically from pressure.

The global reaction rate of species i is obtained with

$$\dot{\omega}_i^{'''} = \dot{r} \mathrm{MW}_i \sum_j \left(\nu_{i,j}^{''} - \nu_{i,j}^{'} \right) \left(\dot{r}_j^{'} - \dot{r}_j^{''} \right). \tag{2.13}$$

2.3.2 Thermodynamic properties

JANAF polynomials (also known as NASA polynomials) [76] are used to compute the specific molar enthalpy $\tilde{h}_i$, specific molar entropy $\tilde{s}_i$ and specific molar isobaric heat capacity $\tilde{c}_{p,i}$, where

$$\frac{\tilde{c}_{p,i}}{R_u} = a_{i,0} + a_{i,1}T + a_{i,2}T^2 + a_{i,3}T^3 + a_{i,4}T^4, \tag{2.14}$$

$$\frac{\tilde{h}_i}{R_u T} = a_{i,0} + \frac{a_{i,1}}{2}T + \frac{a_{i,2}}{3}T^2 + \frac{a_{i,3}}{4}T^3 + \frac{a_{i,4}}{5}T^4 + \frac{a_{i,5}}{T}, \tag{2.15}$$

$$\frac{\tilde{s}_i}{R_u} = a_{i,0}\ln T + a_{i,1}T + \frac{a_{i,2}}{2}T^2 + \frac{a_{i,3}}{3}T^3 + \frac{a_{i,4}}{4}T^4 + a_{i,6}. \tag{2.16}$$

Two sets of coefficients $a_{i,0}$ - $a_{i,6}$ for a low and a high temperature range are read from the reaction mechanism file for each species. The corresponding mass specific quantities are

$$c_{p,i} = \frac{\tilde{c}_{p,i}}{\mathrm{MW}_i}, \quad h_i = \frac{\tilde{h}_i}{\mathrm{MW}_i}, \quad s_i = \frac{\tilde{s}_i}{\mathrm{MW}_i}. \tag{2.17}$$

The mixture properties are computed from the mixing rules for ideal mixtures, in which

$$\mathrm{MW}_g = \sum_i X_i \mathrm{MW}_i = \left(\sum_i \frac{Y_i}{\mathrm{MW}_i} \right)^{-1}, \tag{2.18}$$

$$h = \sum_i Y_i h_i = \frac{1}{\mathrm{MW}_g} \sum_i X_i \tilde{h}_i, \tag{2.19}$$

$$c_p = \sum_i Y_i c_{p,i} = \frac{1}{\mathrm{MW}_g} \sum_i X_i \tilde{c}_{p,i}, \tag{2.20}$$

and $X_i = Y_i \mathrm{MW}_g / \mathrm{MW}_i$ is the mole fraction of species i.

2.3.3 Mass diffusion

All simulations presented in this work apply the mixture-averaged diffusion model, also known as Hirschfelder-Curtiss approximation. This approximation allows to simplify the Maxwell-Stefan equations to yield a closed expression for the species diffusion fluxes [77]

$$\begin{aligned} j_i'' = &- \rho D_{m,i} \nabla Y_i \\ &- \rho Y_i D_{m,i}^{mole} \left(1 - \frac{\mathrm{MW}_i}{\mathrm{MW}_g} \right) \frac{1}{p} \nabla p - D_i^T \frac{1}{T} \nabla T + \rho D_{m,i}^{mole} \frac{\mathrm{MW}_i}{\mathrm{MW}_g} \frac{\rho}{p} Y_i \left(\sum_k Y_k \vec{f}_k - \vec{f}_i \right). \end{aligned} \tag{2.21}$$

$D_{m,i}$ is the ordinary diffusion coefficient of species i through species k for the current mixture relative to the mass fraction gradient, D_i^T is the thermal diffusion coefficient of

species i and $D_{m,i}^{mole}$ is the diffusion coefficient relative to the mole fraction gradient. The terms in the second line of Eq. (2.21) are the pressure diffusion, thermal diffusion and species movement due to external forces, which are neglected in the numerical solver. Pressure diffusion is typically relevant only for high Mach number flames where considerable pressure gradients occur, external forces can be omitted because no charged particles are included in the simulation and thermal diffusion plays a subordinate role for the methane and very lean hydrogen flames.

2.3.4 Transport properties

The transport properties (dynamic viscosity μ_i , heat conductivity λ_i and binary diffusion coefficients $\mathcal{D}_{i,k}$) for each species are calculated from the Chapman-Enskog solution of kinetic gas theory [72, 78]

$$\mu_i = \frac{5}{16}\frac{\sqrt{\pi \mathrm{MW}_i k_B T}}{\pi \sigma_i^2 \Omega_{ii}^{(2,2)*}\sqrt{N_A}}, \tag{2.22}$$

$$\mathcal{D}_{i,k} = \frac{1}{p}\frac{3}{16\pi\sigma_{k,i}^2\Omega_{k,i}^{(1,1)*}}\sqrt{\frac{2\pi k_B^3 T^3}{m_{k,i}}}, \tag{2.23}$$

$$\lambda_i = \frac{\mu_i}{\mathrm{MW}_i}\left(f_{trans,i}\tilde{c}_{v,trans} + f_{rot,i}\tilde{c}_{v,rot,i} + f_{vib,i}\tilde{c}_{v,vib,i}\right), \tag{2.24}$$

where k_B is the Boltzmann constant, N_A Avogadro's constant and σ_i the Lennard–Jones collision diameter of species i. The reduced mass $m_{k,i}$, reduced Lennard–Jones collision diameter $\sigma_{k,i}$ and reduced Lennard–Jones well-depth $\epsilon_{k,i}$ of species k and i are calculated from

$$m_{k,i} = \frac{\mathrm{MW}_k \mathrm{MW}_i}{N_A(\mathrm{MW}_i + \mathrm{MW}_k)}, \quad \epsilon_{k,i} = \sqrt{\epsilon_k \epsilon_i}\xi^2, \quad \sigma_{k,i} = \frac{1}{2}(\sigma_k + \sigma_i)\xi^{-\frac{1}{6}}, \tag{2.25}$$

where ϵ_i is the Lennard-Jones well-depth of species i. ξ is a correction for the interaction of non-polar and polar species. If both species k and i are polar (polarizability $\alpha_k > 0$ and $\alpha_i > 0$), or both species are non-polar ($\alpha_k = 0$ and $\alpha_i = 0$), ξ is unity. If one species is polar (species p) and the other is non-polar (species n), ξ is obtained from [77, 79]

$$\xi = 1 + \frac{1}{4}\alpha_n^* \bar{\mu}_p^{*2}\sqrt{\frac{\epsilon_p}{\epsilon_n}}, \quad \alpha_n^* = \frac{\alpha_n}{\sigma_n^3}, \quad \bar{\mu}_p^* = \frac{\bar{\mu}_p}{\sqrt{\sigma_p^3 \epsilon_p}}, \tag{2.26}$$

where $\bar{\mu}_p$ is the dipole moment of species p and α_n the polarizability of species n. The collision integrals ${\Omega_{k,i}}^{(1,1)*}$ are computed from collision integrals ${\Omega_{k,i}}^{(2,2)*}$ [80, 81]

$${\Omega_{k,i}}^{(1,1)*} = \frac{{\Omega_{k,i}}^{(2,2)*}}{A_{k,i}^*}, \tag{2.27}$$

in which $A_{k,i}^*$ and $\Omega_{k,i}^{(2,2)*}$ are tabulated [29, 82] as functions of the reduced temperature $T_{k,i}^*$ and the reduced dipole moment $\delta_{k,i}^*$,

$$\delta^*_{k,i} = \frac{1}{2}\frac{\bar{\mu}^2_{k,i}}{\epsilon_{k,i}\sigma^3_{k,i}}, \quad \bar{\mu}_{k,i} = \sqrt{\bar{\mu}_k \bar{\mu}_i}, \quad T^*_{k,i} = \frac{k_B T}{\epsilon_{k,i}}. \tag{2.28}$$

The heat conductivity, λ_i, is calculated based on the following parameters

$$f_{vib,i} = \frac{p\mathcal{D}_{i,i}}{\mu_i}\frac{\mathrm{MW}_i}{R_u T}, \tag{2.29}$$

$$f_{trans,i} = \frac{5}{2}\left(1 - \frac{2}{\pi}\frac{\tilde{c}_{v,rot,i}A_i}{\tilde{c}_{v,trans}B_i}\right), \tag{2.30}$$

$$f_{rot,i} = f_{vib,i}\left(1 + \frac{2}{\pi}\frac{A_i}{B_i}\right), \tag{2.31}$$

$$A_i = \frac{5}{2} - f_{vib,i}, \tag{2.32}$$

$$B_i = Z_{rot,i}\frac{F_i(298\ \mathrm{K})}{F_i(T)} + \frac{2}{\pi}\left(\frac{5}{3}\frac{\tilde{c}_{v,rot,i}}{R_u} + f_{vib,i}\right), \tag{2.33}$$

$$\tilde{c}_{v,trans} = \frac{3}{2}R_u, \tag{2.34}$$

$$F_i(T) = 1 + \frac{\pi^{1.5}}{\sqrt{T^*_i}}\left(\frac{1}{2} + \frac{1}{T^*_i}\right) + \left(\frac{\pi^2}{4} + 2\right)\frac{1}{T^*_i}, \tag{2.35}$$

$$T^*_i = \frac{k_B T}{\epsilon_i}, \tag{2.36}$$

$$\tilde{c}_{v,rot,i} = \begin{cases} 0, & \text{if monoatomic} \\ R_u, & \text{if linear} \\ \frac{3}{2}R_u, & \text{otherwise} \end{cases}, \tag{2.37}$$

$$\tilde{c}_{v,vib,i} = -\tilde{c}_{v,rot,i} + \tilde{c}_{p,i} - \frac{5}{2}R_u. \tag{2.38}$$

The last result is obtained from $\tilde{c}_v = \tilde{c}_{v,rot} + \tilde{c}_{v,vib} + \tilde{c}_{v,trans}$ and $\tilde{c}_v = \tilde{c}_p - R_u$ (for ideal gases).

Because the calculation of the transport properties is computationally expensive, λ_i, $\mathcal{D}_{i,k}$, and $\sqrt{\mu_i}$ are calculated once at the start of the solver for 50 equidistant temperatures. The results are used to fit the coefficients of the following polynomials of the logarithmic temperature

$$\lambda_i = \sqrt{T}\left(d_{i,0} + d_{i,1}\ln T + d_{i,2}\ln^2 T + d_{i,3}\ln^3 T + a_{i,4}\ln^4 T\right), \tag{2.39}$$

$$\mathcal{D}_{i,k} = \frac{1}{p}T^{1.5}\left(c_{ik,0} + c_{ik,1}\ln T + c_{ik,2}\ln^2 T + c_{ik,3}\ln^3 T + c_{ik,4}\ln^4 T\right), \tag{2.40}$$

$$\sqrt{\mu_i} = T^{0.25}\left(b_{i,0} + b_{i,1}\ln T + b_{i,2}\ln^2 T + b_{i,3}\ln^3 T + b_{i,4}\ln^4 T\right). \tag{2.41}$$

The mixing rules for obtaining the properties of the gas mixture are [78]

$$\lambda = \frac{1}{2}\left(\sum_k X_k\lambda_k + \frac{1}{\sum_k \frac{X_k}{\lambda_k}}\right), \tag{2.42}$$

$$\mu = \sum_k \frac{\mu_k X_k}{\sum_i \tilde{\Phi}_{k,i} X_i}, \tag{2.43}$$

$$\tilde{\Phi}_{k,i} = \frac{\left(1 + \sqrt{\frac{\mu_k}{\mu_i}\sqrt{\frac{\mathrm{MW}_i}{\mathrm{MW}_k}}}\right)^2}{\sqrt{8\left(1 + \frac{\mathrm{MW}_k}{\mathrm{MW}_i}\right)}}, \tag{2.44}$$

where $\tilde{\Phi}_{k,i}$ is a coefficient for the Wilke mixing rule to obtain accurate viscosity values for the reacting gas mixture. The mixture averaged diffusion coefficients are computed from [72], in which

$$D_{m,i}^{mole} = \frac{1 - Y_i}{\sum_{k\neq i}\frac{X_k}{\mathcal{D}_{k,i}}}, \tag{2.45}$$

$$D_{m,i} = \left(\sum_{k\neq i}\frac{X_k}{\mathcal{D}_{i,k}} + \frac{X_i}{1 - Y_i}\sum_{k\neq i}\frac{Y_i}{\mathcal{D}_{i,k}}\right)^{-1}. \tag{2.46}$$

In summary, the following molecular data have to be provided for each species i:

- Lennard-Jones well-depth as ϵ_i/k_B
- Lennard-Jones collision diameter as $10^{10}\sigma_i$
- polarizability as $10^{30}\alpha_i$
- dipole moment as $10^{25}\bar{\mu}_i/\sqrt{10}$
- reference rotational relaxation collision number $Z_{rot,i}$ at $T = 298$ K
- molecule geometry (monoatomic, linear, non-linear)

2.3.5 Reacting flow model

The governing equations (assuming ideal gases and perfect mixtures) that make up the system of balance equations are as follows [28, 71].

Conservation of total mass:

$$\frac{\partial\rho}{\partial t} + \nabla\cdot\rho\vec{V} = 0, \tag{2.47}$$

where ρ is the density, t is time and $\vec{V}$ the fluid velocity vector.

Conservation of momentum:

$$\frac{\partial \rho \vec{V}}{\partial t} + \nabla \cdot \rho \vec{V}\vec{V} = -\nabla p + \nabla \cdot \overline{\overline{\tau}} + \rho \vec{g}, \tag{2.48}$$

in which p is the pressure, $\vec{g}$ is the gravitational acceleration. The viscous stress tensor $\overline{\overline{\tau}}$ is computed for a Newtonian fluid using the Stokes assumption

$$\overline{\overline{\tau}} = \mu \left(\nabla \vec{V} + (\nabla \vec{V})^T - \frac{2}{3} \overline{\overline{I}} \nabla \cdot \vec{V} \right). \tag{2.49}$$

$\overline{\overline{I}}$ is the identity tensor and μ the dynamic viscosity.

Conservation of mass for species:

$$\frac{\partial \rho Y_i}{\partial t} + \nabla \cdot \rho(\vec{V} + \vec{V}_c) Y_i = \dot{\omega}_i''' - \nabla \cdot j_i'', \;\; i = 1, .., N-1 \tag{2.50}$$

where Y_i is the mass fraction species i and $\dot{\omega}_i'''$ its reaction rate. N is the number if species. The correction velocity $\vec{V}_c$ force the sum of all diffusive fluxes j_i'' to be zero

$$\vec{V}_c = -\frac{1}{\rho} \sum_{i=1}^{N} j_i''. \tag{2.51}$$

The diffusive mass flux is computed using a mixture-averaged model derived from the Stefan-Maxwell equations [72], neglecting pressure and temperature diffusion (Soret effect), it results in

$$j_i'' = -\rho D_{m,i} \nabla Y_i. \tag{2.52}$$

$D_{m,i}$ is the diffusion coefficient of species i in the mixture.

Conservation of energy:

$$\frac{\partial \rho h}{\partial t} + \nabla \cdot \rho \vec{V} h = -\nabla \cdot \dot{Q}'' + \frac{\partial p}{\partial t} - \sum_{i=1}^{N} h_i^o \dot{\omega}_i'''. \tag{2.53}$$

The transport of energy is formulated in terms of the total sensible enthalpy $h = h_s + \frac{1}{2}\vec{V} \cdot \vec{V}$ and

$$-\nabla \cdot \dot{Q}'' = \underbrace{\nabla \cdot \left(\frac{\lambda}{c_p} \nabla h_s \right) - \sum_{i=1}^{N} \nabla \cdot \left(\frac{\lambda}{c_p} h_{s,i} \nabla Y_i \right)}_{\nabla \cdot (\lambda \nabla T)} - \sum_{i=1}^{N} \nabla \cdot \left(h_{s,i} \hat{j}_i'' \right). \tag{2.54}$$

λ is the heat conductivity of the mixture, c_p the isobaric heat capacity and T the temperature. Viscous work, potential energy, radiation and Dufour effect are neglected. The sensible enthalpy $h_{s,i}$ of species i and the sensible enthapy of the mixture h_s for ideal gases is

$$h_{s,i} = h_i - h_i^o, \;\; h_s = \sum_{i=1}^{N} Y_i h_{s,i}, \tag{2.55}$$

and $h_i^o = h_i(298\ \mathrm{K})$ is the enthalpy of formation of species i. The corrected diffusive mass flux $\hat{j}_i''$ is given by

$$\hat{j}_i'' = j_i'' - Y_i \sum_{i=1}^{N} j_i'', \tag{2.56}$$

and Fouries's second law $\nabla \cdot (\lambda \nabla T)$ is rewritten (assuming ideal gases and that all species have the same temperature) in order to obtain the first term on the r.h.s. of Eq. (2.54), which can is discretized implicitly.

The equation for the ideal gases closes the system of partial differential equations

$$\rho = \frac{p \mathrm{MW}_g}{R_u T}. \tag{2.57}$$

Chapter 3

Flames dynamic

The flame speed is defined as the propagation speed of a deflagration wave relative to the unburned mixture velocity. It has a precise meaning when the flame is planar and propagates steadily because the mass flow rate through the flame is constant and uniform. In this reference flame, the entire structure travels consuming the unburned mixture at a constant speed S_l^0. For multidimensional flows, the flame speed is a local property because the mass flow rate through the flame is neither constant, nor uniform. In multidimensional flow, the flame undergoes a continuous stretching, which affects the transport rates and results in a change of the flame speed. Figure 3.1 presents the flame surface separating the burned and unburned mixture, a flame sheet approximation, and the laminar flame structure, which is the basis for a thin flame approximation [28, 29, 67]. The following sections discuss the approaches to estimating the flame speed of stretched flames.

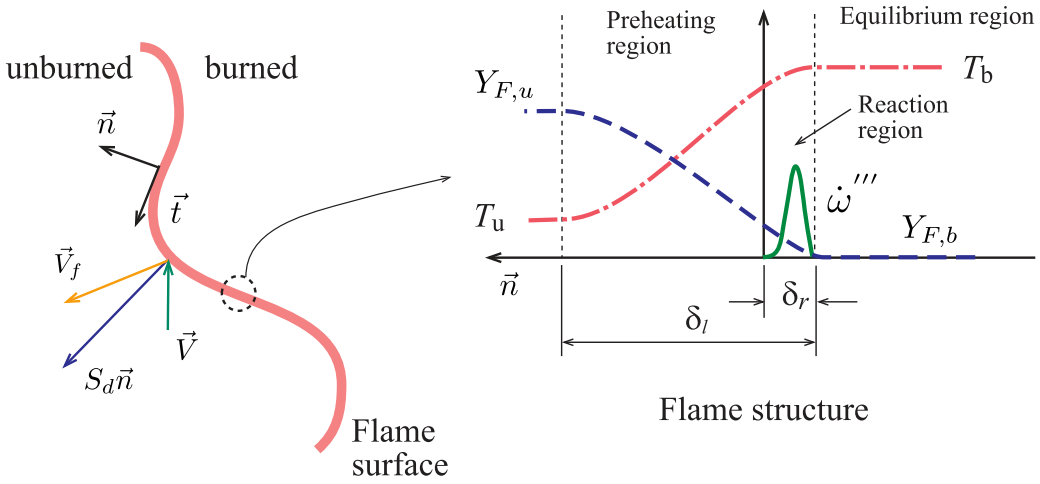

Figure 3.1: Flame sheet approximation and laminar flame structure.

3.1 THEORETICAL BACKGROUND

3.1.1 Flame sheet approximation

A phenomenological relation between flame speed and flame stretch can be obtained in the framework of a hydrodynamic model based on a flame sheet approximation [83]. Assuming that the flame is a surface of discontinuity separating the unburned from the burned mixtures, the flame stretch rate, K, is defined as the fractional rate of change of a Lagrangian flame surface element A,

$$\mathrm{K} = \frac{1}{A}\frac{dA}{dt}. \tag{3.1}$$

The stretch rate is positive when the flame surface expands and negative otherwise. Assuming that the local flame speed S_l is affected by the stretch rate, a perturbation of the laminar (planar) flame speed $S_l(0) = S_l^0$ by the local stretch rate $(\mathrm{K} - 0)$ can be represented as

$$S_l(\mathrm{K}) = S_l(0) + \frac{\partial S_l(0)}{\partial \mathrm{K}}(\mathrm{K}-0) + \frac{1}{2!}\frac{\partial^2 S_l(0)}{\partial \mathrm{K}^2}(\mathrm{K}-0)^2 + ... + \frac{1}{n!}\frac{\partial^n S_l(0)}{\partial \mathrm{K}^n}(\mathrm{K}-0)^n. \tag{3.2}$$

The first-order sensitivity coefficient of the flame speed to stretch rate is referred to as the Markstein length [84],

$$\mathscr{L} = -\frac{\partial S_l(0)}{\partial \mathrm{K}}. \tag{3.3}$$

For weakly-stretched flames, the linear regime for the stretched flame may be represented as

$$S_l = S_l^0 - \mathscr{L}\mathrm{K}. \tag{3.4}$$

In this linear regime, the Markstein length becomes a phenomenological parameter that depends on the properties of the unburned mixture.

The flame stretch rate is simply associated to the flame curvature and flow velocity as

$$\mathrm{K} = S_l^0 \ (\nabla \cdot \vec{n}) - \vec{n} \cdot \nabla \vec{V} \cdot \vec{n}. \tag{3.5}$$

In this model, the displacement velocity of the flame surface is associated to S_l^0. The first term in the r.h.s. is the effect of flame curvature $\kappa = \nabla \cdot \vec{n}$. The second term is the strain rate imposed on the flame by flow velocity gradients.

Using δ_l^0 and S_l^0 as characteristic length and velocity scales, the nondimensional form of Eq. (3.4) becomes

$$\frac{S_l}{S_l^0} = 1 - \mathrm{Ma}\ \mathrm{Ka}, \tag{3.6}$$

where $\mathrm{Ka} = \mathrm{K}(\delta_l^0/S_l^0)$ is the nondimensional stretch rate, or Karlovitz number, and $\mathrm{Ma} = \mathscr{L}/\delta_l^0$ is the Markstein number. The Karlovitz number is a ratio of the flame characteristic time scale $\tau_f \sim \delta_l^0/S_l^0$ and the stretch characteristic time scale $\tau_\mathrm{K} \sim 1/\mathrm{K}$, i.e.,

the time required to double the flame surface area. From the laminar flame characteristic length and speed scales,

$$\delta_l^0 \sim \frac{\alpha}{S_l^0}, \qquad \left(S_l^0\right)^2 \sim \frac{\alpha}{\rho_u}\dot{\omega}_F^{'''}, \tag{3.7}$$

where α is the thermal diffusivity and $\dot{\omega}_F^{'''}$ is an overall fuel reaction rate, the Karlovitz number becomes

$$\mathrm{Ka} = \mathrm{K}\frac{\delta_l^0}{S_l^0} \sim \frac{\rho_u \mathrm{K}}{\dot{\omega}_F^{'''}}. \tag{3.8}$$

This relation expresses that the effects of curvature are more pronounced for weakly burning flames, such as in lean and near extinction conditions.

Equations (3.4) and (3.5) are used in the G-equation flamelet model for the flame surface approximation [67]. This is the essence of the hydrodynamic model. This model lacks in the approximation for the displacement velocity and a more precise definition of flame stretch rate. These are addressed next.

3.1.2 Flame stretch rate

The flame stretch rate can be directly related to the kinematics of the flame surface. The flame displacement velocity is defined as the normal component of the relative velocity of the flame surface in respect to the flow. It differs from the laminar (planar) flame speed because of flame curvature and unsteadiness. Naming S_d the displacement speed and $\vec{u}_o$ the flow velocity of the unburned mixture in the vicinity of the flame surface, the local propagation velocity of the flame surface $\vec{V}_f$ is

$$\vec{V}_f = \vec{V} + \ S_d\vec{n}, \tag{3.9}$$

where $S_d\ \vec{n}$ is the displacement velocity and $\vec{n}$ is the normal unit vector at the flame surface, pointed to the unburned mixture side, Fig. 3.1.

Starting from Eq. (3.1), the flame stretch rate may be expressed in different equivalent forms [29]:

$$\begin{aligned} \mathrm{K} &= \nabla_t \cdot \vec{V}_{f,t} + \left(\vec{V}_f \cdot \vec{n}\right)(\nabla \cdot \vec{n}) , \\ &= \nabla_t \cdot \vec{V}_t + S_a\,(\nabla \cdot \vec{n}) , \\ &= \nabla \cdot \vec{n} \times \left(\vec{V} \times \vec{n}\right) + \left(\vec{V} \cdot \vec{n}\right)(\nabla \cdot \vec{n}) + S_d\,(\nabla \cdot \vec{n})\,. \end{aligned} \tag{3.10}$$

In these equations, ∇_t is the nabla operator along a plane tangent to the flame surface. The first term in the right-hand side, $\nabla_t \cdot \vec{V}_f = \nabla_t \cdot \vec{V}_{f,t} = \nabla_t \cdot \vec{V}_t = \nabla \cdot \vec{n} \times (\vec{V} \times \vec{n}) = -\vec{n} \cdot \nabla \times (\vec{V} \times \vec{n})$, is the tangential strain rate related to the flow-nonuniformity (the extensional contribution). It exists only when the flow is oblique to the surface, $\vec{V} \times \vec{n} \neq 0$. The contraction or expansion of the flame surface depends on the sign of the surface divergent of the tangent component of the flame velocity. In the second term, $\vec{V}_f \cdot \vec{n} = S_a = \vec{V} \cdot \vec{n} + S_d$ is the normal velocity of the flame surface. The second term,

$(\vec{v}_F \cdot \vec{n})(\nabla \cdot \vec{n}) = S_a\ (\nabla \cdot \vec{n})$, is the stretch rate caused by flame unsteadiness and curvature of the flame surface (the dilatational contribution). This term can be divided in the normal strain rate, $\left(\vec{V} \cdot \vec{n}\right)(\nabla \cdot \vec{n})$, and the displacement speed, $S_d\,(\nabla \cdot \vec{n})$, effects. The curvature, $\kappa = \nabla \cdot \vec{n}$, is positive when the flame is convex towards the unburned gas. The tip of a bunsen burner is concave towards the unburned mixture, therefore presenting negative curvature.

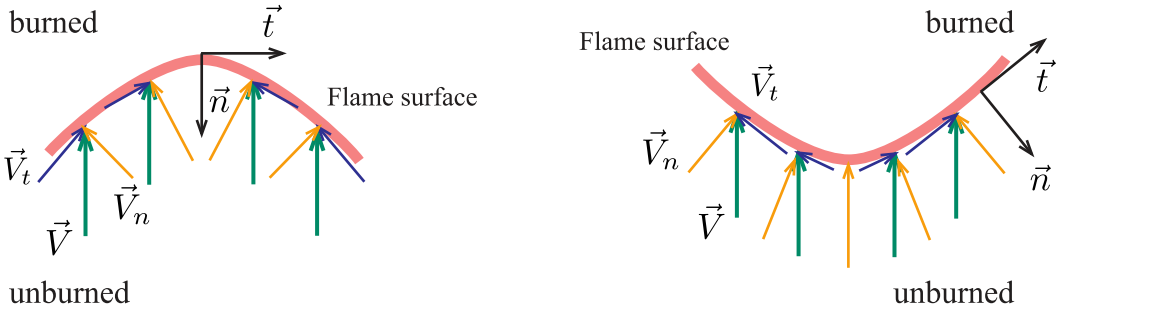

(a) Concave towards the unburned mixture:

$$\kappa = \nabla \cdot \vec{n} < 0$$
$$\nabla_t \cdot \vec{V}_t < 0$$
$$(\vec{V} \cdot \vec{n})\ \kappa > 0$$
$$S_d(\nabla \cdot \vec{n}) < 0$$

(b) Convex towards the unburned mixture:

$$\kappa = \nabla \cdot \vec{n} > 0$$
$$\nabla_t \cdot \vec{V}_t > 0$$
$$(\vec{V} \cdot \vec{n})\ \kappa < 0$$
$$S_d(\nabla \cdot \vec{n}) > 0$$

Figure 3.2: Effect of flame curvature on stretch rate. The green arrows are the flow field at the flame surface $\vec{V}$, assumed uniform, the yellow vectors are the normal component $\vec{V}_n$ and the blue vectors are the tangent component $\vec{V}_t$.

Figure 3.2 illustrates the effect of flame curvature on stretch rate. A uniform flow velocity field $\vec{V}$ is used for simplicity. Figure 3.2a presents a flame surface that is concave towards the unburned mixture. The tangent component of the flow velocity $\vec{V}_t$ points towards the vertex, thus resulting in flame compression. This effect is expressed by the tangential strain rate component. The tangent component of the flow velocity at the surface $\vec{V}_t$ decreases towards the vertex. Therefore, the tangential strain rate is negative, $\nabla_t \cdot \vec{V}_t < 0$, indicating flame compression. The normal strain rate depends on the normal component of the flow velocity and flame curvature. The normal component of the flow velocity at the surface $\vec{V}_n$ is negative and the curvature is also negative, $\kappa = \nabla \cdot \vec{n} < 0$. Then, the normal strain rate becomes positive, $(\vec{V} \cdot \vec{n})\ \kappa > 0$. For the convex surface, Fig. 3.2b, the tangential component of the flow velocity results in flame extension, which is confirmed by $\nabla_t \cdot \vec{V}_t > 0$. For the normal strain rate, the curvature is positive, $\kappa = \nabla \cdot \vec{n} > 0$, and $(\vec{V} \cdot \vec{n})\ \kappa < 0$.

For a stationary flame, $\vec{V}_f = 0$ and the second term of Eq. (3.10) is identically equal to zero. The tangential component of the flame surface velocity, in the flame sheet approximation, is equal to the tangential component of the flow velocity at the flame

surface, $\vec{V}_{f,t} = \vec{V}_t$, while $\vec{V}_{f,n} = \vec{V}_n + S_d\ \vec{n} = 0$. Therefore,

$$\mathrm{K} = \nabla_t \cdot \vec{V}_{f,t} = \nabla_t \cdot \vec{V}_t = \nabla_t \cdot \left(\vec{V} - \vec{V}_n\right) = \nabla_t \cdot \vec{V} + S_d\ \nabla \cdot \vec{n}. \tag{3.11}$$

As a result, for the stationary flame, the concave surface of Figure 3.2a experiences compression and the stretch rate is negative, $\mathrm{K} < 0$, while that for Figure 3.2b experiences extension and the stretch rate is positive, $\mathrm{K} > 0$. Using the definition of Karlovitz number, $\mathrm{Ka} = \mathrm{K}(\delta_l^0/S_l^0)$, Eq. (3.11) may be nondimensionalized as

$$\mathrm{Ka} = \mathrm{Ka_s} + \mathrm{Ka_c}, \tag{3.12}$$

where the tangential strain and curvature effects are

$$\mathrm{Ka_s} = \frac{\delta_l^0}{S_l^0}\nabla_t \cdot \vec{V}, \qquad \mathrm{Ka_c} = \frac{\delta_l^0}{S_l^0} S_d\ \nabla \cdot \vec{n}. \tag{3.13}$$

This definition of stretch rate may be used in the G-equation formulation and a better approximation for the displacement velocity S_d can be obtained with the thin flame model, as follows.

3.1.3 Thin flame approximation

The next level of amplification, reveals the flame preheating zone, with characteristic length scale δ_l, and a thin reaction zone, with characteristic length scale $\delta_r \ll \delta_l$. They are identified in Fig. 3.1.

The flame surface can be associated to the iso-surface of a flame scalar property. One possibility is to take an iso-concentration line of a reactant i as the locus of the flame surface. Then, the flame surface is the iso-surface $Y_i(\vec{x}, t) = Y_{i,0}$, where $Y_{i,0}$ is a constant that will be defined later. Considering that Y_i is consumed in the flame, the surface unit normal vector becomes

$$\vec{n} = \frac{\nabla Y_i}{|\nabla Y_i|}. \tag{3.14}$$

The flame is a surface of constant mass fraction that is Lagrangian advected by $\vec{V}_f$. Therefore, on the flame surface,

$$\frac{DY_i}{Dt} = \frac{\partial Y_i}{\partial t} + \vec{V}_f \cdot \nabla Y_i = 0. \tag{3.15}$$

The conservation equation for the species i, may be written as

$$\rho\frac{\partial Y_i}{\partial t} + \rho\vec{V} \cdot \nabla Y_i = \nabla \cdot (\rho D_{m,i} \nabla Y_i) + \dot{\omega}_i'''. \tag{3.16}$$

Applying this equation on the flame surface, using Eq. (3.15) for the transient term, and recalling that $\vec{V}_f = \vec{V} + S_d\ \vec{n}$,

$$S_d = -\frac{\nabla \cdot (\rho D_{m,i} \nabla Y_i) + \dot{\omega}_i'''}{\rho|\nabla Y_i|}, \tag{3.17}$$

in which all operations are taken on the flame surface. From Eq. (3.14), the divergent term in the right-hand side may be expanded as,

$$\nabla \cdot (\rho D_{m,i} \nabla Y_i) = \rho D_{m,i} |\nabla Y_i| \, (\nabla \cdot \vec{n}) + \vec{n} \cdot \nabla \left(\rho D_{m,i} \, \vec{n} \cdot \nabla Y_i \right). \tag{3.18}$$

The first term in the right-hand side accounts for the flame curvature, $\kappa = \nabla \cdot \vec{n}$, differently than the unstretched flame, Eq. (2.9). The displacement speed from Eq. (3.17) becomes [85]

$$S_d = S_{diff} + S_{reac} - D_{m,i}\kappa, \tag{3.19}$$

where,

$$S_{diff} = \frac{\vec{n} \cdot \nabla \left(\rho D_{m,i} \, \vec{n} \cdot \nabla Y_i \right)}{\rho |\nabla Y_i|}, \qquad S_{reac} = \frac{\dot{\omega}_i'''}{\rho |\nabla Y_i|}. \tag{3.20}$$

S_{diff} is the diffusion term in the normal direction, as seen in Eq. (2.8). The an unstretched, planar, steady flame, is defined as

$$\rho_u S_l^0 = \rho (S_{diff} + S_{reac}) \tag{3.21}$$

For the thin flame as seen in Fig. 3.1, however, gradient of mass fraction, reaction and the curvature, or also called tangential diffusion [86], affect the flame displacement speed.

An order of magnitude estimate can be derived by applying Eq. (3.19) to the flame structure represented in Fig. 3.1. The diffusion coefficient, $D_{m,i}$, can be generalized as $\mathcal{D} \sim S_d \mathscr{L}$. Replacing Eq. (3.21), the previous relation and using Eq. (2.10) in Eq. (3.19), we have

$$\tilde{S}_d = S_l^0 - S_l^0 \mathscr{L} \kappa. \tag{3.22}$$

Equation (3.22) can be normalized regarding S_l^0, yielding

$$\frac{\tilde{S}_d}{S_l^0} = 1 - \mathscr{L} \kappa. \tag{3.23}$$

Various expressions may be found for the Markstein length in the literature [83, 84, 87–92]. For constant viscosity, lean, single-step flames with variable density, Clavin and Joulin [88] proposed

$$\mathscr{L} = \delta_l \left(\frac{T_b}{T_b - T_u} \ln \left(\frac{T_b}{T_u} \right) + \frac{1}{2} \beta (\mathrm{Le}_{eff} - 1) \frac{T_u}{T_b - T_u} \int_0^{\frac{T_b - T_u}{T_u}} \frac{\ln(1+x)}{x} dx \right). \tag{3.24}$$

β is the Zel'dovich number or activation energy parameter, Le_{eff} is the effective Lewis number of the mixture, and T_u and T_b are the temperatures of the unburned and burned gases, respectively.

Equations (3.23) and (3.24) evidence the effect of flame curvature and Lewis number in the displacement speed. The flame displacement becomes greater than the laminar flame speed, $\tilde{S}_d > S_l^0$, when the curvature is negative, $\kappa < 0$. Also, the density-weighted flame displacement speed increases as the Lewis number becomes larger than one, Le > 1, since the $\mathscr{L} > 0$. For lean mixtures of hydrocarbons/air, at the tip of a Bunsen flame, the curvature is negative and $\tilde{S}_d > S_l^0$. For hydrogen flames, Le < 1, the Markstein length becomes negative and for a negative curvature, the burning rate results in $\tilde{S}_d < S_l^0$. These variations on flame speed are directly related to thermo-diffusive instabilities discussed in Section 3.1.5.

The description above forms the classical understanding of the effects of flame stretch rate in the displacement flame speed. From the measurement point of view, several authors have invested a considerable effort in devising ways to reduce heat loss and in correctly accounting for the effect of flame stretch rate in laboratory flames, such that the local consumption speed approximates adequately the laminar flame speed, i.e., the speed of a planar, adiabatic flame [93]. Two aspects are not taken into account in the thin flame approach reviewed above: (1) The transport of heat and mass is restricted to the normal direction. Tangential transport is not accounted for. The temperature and mass fraction gradients are smaller in the tangential direction, however, as flames become weaker, their thermal thickness increase and flame stability becomes affected by transport along the flame, (2) variable transport properties and detailed chemistry are not taken into account. Therefore, the effects of phenomena, such as cool flame, cannot be analyzed. Cool flames occur for fuels exhibiting negative temperature coefficient ignition delay time curves at unburned temperatures from 600 K to 900 K at normal and high pressures [38, 94]. To account for these effects, full DNS models are needed. Here, the results of DNS models are used to calculate the displacement speed using the classical formulation of the thin flame model given by Eq. (3.19).

3.1.4 Hydrodynamic instability

The linear theory (for small disturbances) of flame instabilities was proposed, independly, in the works of Darrieus [95] and Landau [96]. Restricting to the case of slow combustion (deflagration) and to situations involving only relatively small disturbances at the front, these investigations have shown that in the "thin" flame approximation, i.e., the flame front is treated as a surface of discontinuity, the dynamics of the planar front is unconditionally unstable. The so-called Darrieus-Landau (DL) theory assumes that any spatially periodic perturbation, e.g. in the flame front area as illustrated in Fig. 3.3, can be modeled as

$$f^{'} = \mathcal{A}(x)\mathrm{e}^{(iky+\omega t)}, \tag{3.25}$$

where $f^{'}$ is the spatial fluctuation of the flame surface area. This results from the decomposition of the instantaneous front, f, in two terms: $f = \bar{f} + f^{'}$, where the average

term is $\bar{f} = 0$. The amplitude of the developing perturbation is $\mathcal{A}$, while $k = 2\pi/\lambda$ is the transverse wavenumber, with λ and ω, respectively, the wavelength of the perturbation and its growth rate.

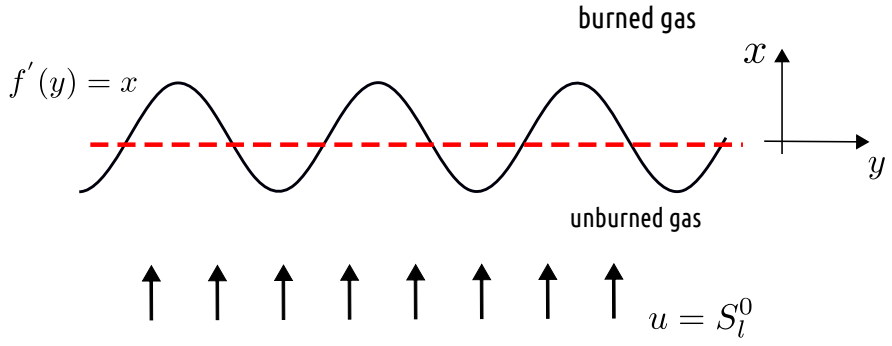

Figure 3.3: The perturbed surface of a planar flame.

The physical variables are also affected by the initial perturbation and can be written as $u = \overline{u} + u'$, $v = \overline{v} + v'$ and $p = \overline{p} + p'$ where,

$$u' = U(x)\mathrm{e}^{(iky+\omega t)}, \qquad v' = V(x)\mathrm{e}^{(iky+\omega t)}, \qquad p' = P(x)\mathrm{e}^{(iky+\omega t)}. \tag{3.26}$$

The capital letters identify the nominal values. The growth rate of the perturbation, ω, as obtained using linear stability theory, is given by

$$\omega = \omega_{DL} S_l k, \qquad \omega_{DL} = \frac{1}{\sigma+1}(\sqrt{\sigma^3 + \sigma^2 - \sigma} - \sigma), \tag{3.27}$$

which $\omega_{DL}(\sigma)$ is a constant that depends on the density ratio between unburnt and burnt gases, $\sigma = \rho_u/\rho_b$. Since in combustion process, $\sigma > 1$, then $\omega_{DL} > 0$ and the initial disturbances will always grow in amplitude for all wavelengths. Moreover, the growth rate increases as k becomes larger, implying that the short waves grow faster than the long waves.

3.1.5 Thermo-diffusive instability

As can be seen in experiments such as of Fig. 1.4, flames do not always evolve to wrinkled fronts. In order to take into account the thermo-diffusive effect to Darrieus-Landau theory, Eq. (3.27) was implemented by works performed by Pelce and Clavin [97], Matalon and Matkowsky [98] and Frankel and Sivashinsky [99] yielding

$$\omega = \omega_{\mathrm{DL}} S_l k - S_l \delta_l^0 [B_1 + \beta(\mathrm{Le}_{eff} - 1)B_2 + \mathrm{Pr}B_3]k^2. \tag{3.28}$$

Here, B_1, B_2 and B_3 are positive constants that depends solely on σ. These three terms correspond to thermal, molecular and viscous diffusion, respectively, and Pr is the Prandtl number. The thermal and viscous coefficients tend to stabilize the perturbations. The

molecular term can act towards destabilizing or stabilizing the front. It is controlled by the transport balance between species and heat diffusion represented by Lewis number depicted in Fig. 3.4. If the Le < 1 and the flame front is convex towards the fresh gases, reactants diffuse towards burnt gases faster than heat diffuses toward the unburn gas. These reactants are heated and burn more quickly, increasing the local flame speed S_l, which is higher than flame speed S_l^0. On the other hand, for fronts convex towards the burnt gases, reactants diffuse in a large zone and the flame speed is decreased compared to S_l^0. This event increases the surface area. When the Le > 1, the local flame speed tends to stabilize the front (decreasing the surface area). In the Eq. (3.28), the Lewis number is present as the effective Lewis number. This represents the average value of the fuel and oxidizer Lewis numbers weighted more heavily with respect to the deficient component in the mixture [83].

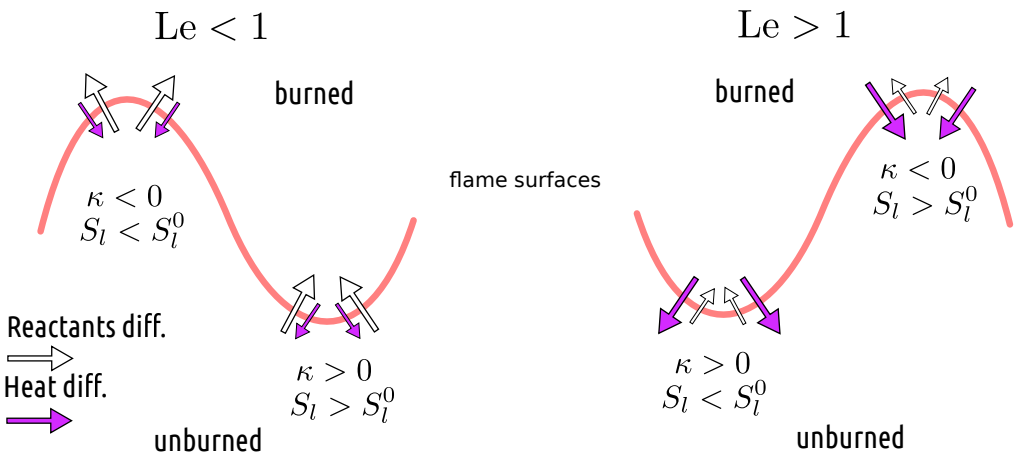

Figure 3.4: Effect of Lewis number and flame curvature, κ, on local flame speed, S_l. Adapted from Poinsot and Veynante [28].

3.2 MATERIALS AND METHODS

3.2.1 Computational methods

In this chapter, direct numerical simulations are used to evaluate the role of stretch-chemistry interaction and its impact on flames dynamics. The study approaches three canonicals flames configurations, slot burner, a Bunsen flame, and a planar flame. They are important sources of information to assess the role of each instability mechanism in the definition of local flame speed.

The flows are modeled employing the finite volume method for Navier-Stokes equations at low-Mach limit. The computations were performed using OpenFOAM's [73] standard capabilities coupled to EBI-DNS implementation [71] which address detailed transport coefficients to momentum, species and energy equations. The simulations employed

three different fuels-air mixtures with specific chemical mechanisms. For the methane/air simulations, the reduced mechanism of Kee *et al.* [100] with 17 species and 58 elementary reactions was used. The simulations for dimethyl-ether/air mixtures used a reduced chemical mechanism consisting of 30 species and 175 reactions, with 9 species assumed to exist under quasi-steady state, Bhagatwala *et al.* [101]. For the hydrogen/air simulations, it was used the Li *et al.* [102] reaction mechanism containing 9 species and 38 elementary reactions.

The computational configurations are two-dimensional slabs subject to a prescribed inlet velocity. In order to increase the time and spatial discretization accuracy, the second-order backward difference method for time in combination with a third-order for gradients and spatial interpolation scheme are used. To prevent numerical instabilities arising from the discretization schemes, for all cases investigated the time step is dynamically adjusted to retain the convective CFL number below 0.1 [103]. The pressure-implicit split-operator (PISO) algorithm has been used for the pressure correction [104]. The computational domains use rectangular structured meshes with at least 20 cells to resolve the flame thickness. Inlet conditions were prescribed while at the sides of the domain, periodic/symmetric boundary conditions were imposed. To avoid possible reflections of pressure waves at the in- and outlet, partially non-reflective boundary conditions (PNRBC) are used. Even in cases of relatively low flow velocities, PNRBC are required in combustion problems with compressible formulation, as in the present situation where the pressure and the density of the mixture are related through the ideal gas law [105].

3.3 RESULTS AND DISCUSSIONS

3.3.1 Flame-flow interaction in a slot-burner

Figure 3.5a presents the computational domain. The simulation was carried out in a rectangular domain with a height of 20 mm in the stream-wise direction and 10 mm of width. The slot outlet has a width of 10 mm. A Poiseuille velocity profile is imposed in the slot outlet and zero velocity is enforced in the remaining of the bottom face. The unburned gas temperature T_u is prescribed at the burner rim. At the sides of the domain, a zero gradient condition was enforced [106].

Methane/air and dimethyl-ether/air premixed flames are solved at two equivalence ratios, $\phi = 0.7$ and $\phi = 1$, at $T_u = 300$ K and atmospheric pressure. In the following analysis, two definitions of the flame surface position are used according to the laminar, planar, adiabatic flame solved by Cantera. The first places the flame surface in the preheating zone by setting $Y_{F,o} = 0.9\ Y^0_{F,u}$. The second choice places the flame within the reaction zone by defining the flame as the mass fraction iso-line where the maximum heat release rate occurs, represented as $Y_{F,o} = Y^0_F(\dot{Q}'''_{max})$ [107].

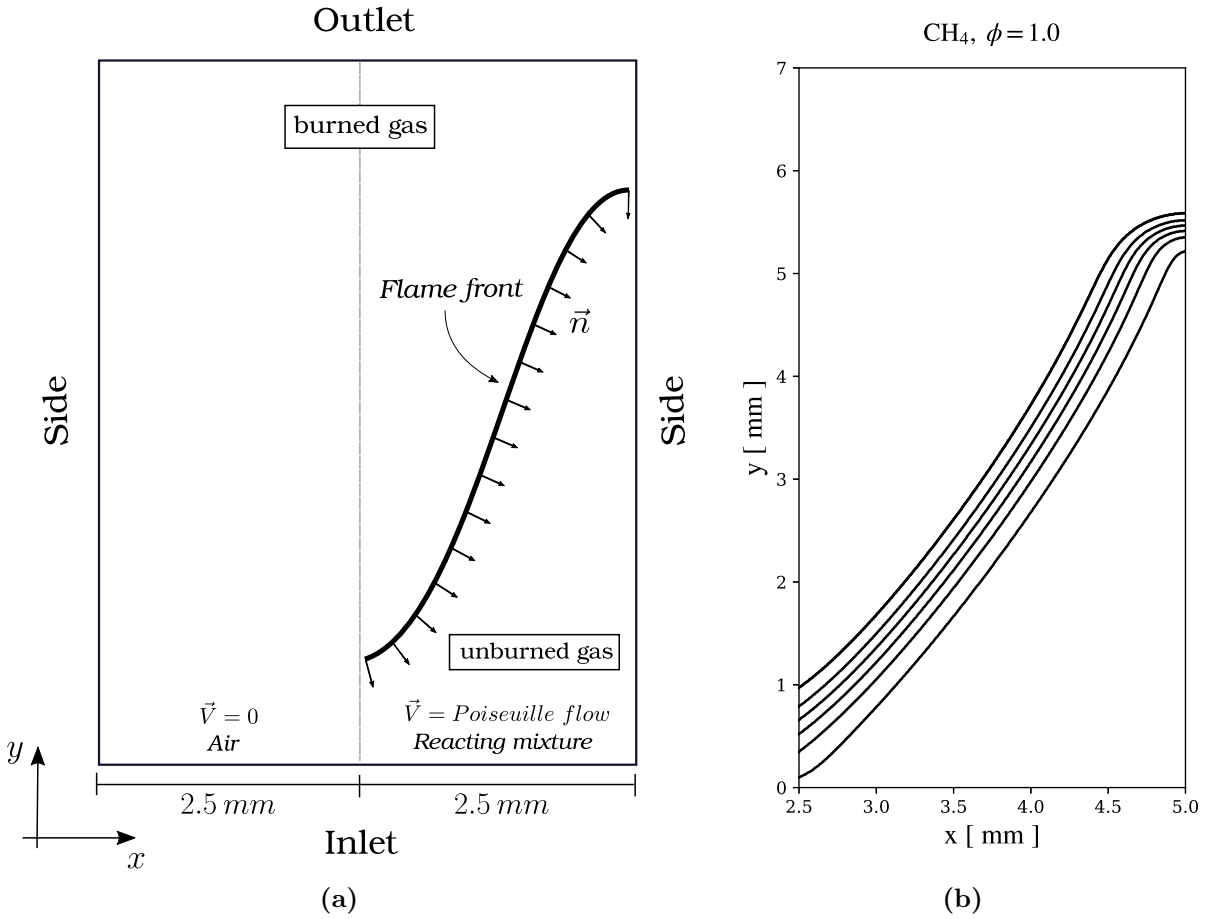

Figure 3.5: (a) Computational domain of slot burner and (b) isothermal lines from 400 K to 1900 K, at 300 K temperature steps, for the methane/air flame at $\phi = 1$.

Table 3.2 presents the laminar, planar, adiabatic flame parameters for the methane/air and dimethyl-ether/air flames. In Tab. 3.2, $Y_{F,o}(0.9\ Y^0_{F,u})$ and $Y_{F,o}(\dot{Q}'''_{max})$ are the values of the iso-lines of mass fraction for the two definitions of flame surface positions, $\langle u \rangle_{inlet}$ is the reactant mixture mean axial velocity at the inlet boundary condition and Le_{eff} is the effective Lewis number. This represents the average value of the fuel and oxidizer Lewis numbers weighted more heavily with respect to the deficient component in the mixture [83].

Table 3.1: Flame parameters for the methane/air and dimethyl-ether/air mixtures at atmospheric conditions.

Fuel	ϕ	S^0_l, cm/s	δ^0_l, mm	Le_{eff}	$\langle u \rangle_{inlet}$, cm/s	$Y_{F,o}(0.9\ Y^0_{F,u})$	$Y_{F,o}(\dot{Q}'''_{max})$
CH_4	1.0	37.0	0.46	1.00	80.0	0.0495	0.0033
CH_4	0.7	19.0	0.66	0.95	35.0	0.0351	0.0024
DME	1.0	47.0	0.26	1.23	80.0	0.0900	0.0019
DME	0.7	26.0	0.44	1.43	45.0	0.0648	0.0009

Figure 3.5b presents the isotherm lines from 400 K to 1900 K for the methane/air flame at $\phi = 1$. The flame is anchored at the burner rim and the liftoff distance is under 1 mm. The deformation caused by the flow field on the flame surface is visible. At the flame tip, the temperature iso-lines are closer, while near to the burner rim, the opposite occurs. The flame has a more flat profile in the intermediate region between the base and the tip.

Figure 3.6 shows the field of fuel consumption for the 4 cases run. DME at $\phi = 1$, Fig. 3.6b, presents the higher laminar flame speed (see Tab. 3.2), resulting in a thinner flame, shorter cone and smaller liftoff distance. As the equivalence ratio is reduced to $\phi = 0.7$, the flame thickness and liftoff distance increase, more significantly for methane, than for DME. The flame tail is also displaced to a position farther from the slot half width, resulting in fuel leakage and air entertainment.

The fuel heat release increases towards the tip for both fuels, mainly as a response to the Poiseuille flow profile at the slot exit. DME/air mixtures have a Lewis number above unity (see Tab. 3.2), meaning that heat transfer penetrates further than fuel mass transfer. Therefore, there is a focusing effect of heat in the tip of the burner, leading to preheating of the unburned mixture, increasing the reaction rate further. Methane/air mixtures have a Lewis number equal or slightly under unity, meaning that the mass and heat transfer stay in balance.

The results calculated from the application of Eq. (3.10) are presented in Fig. 3.7, plotted as Karlovitz number as a function of the dimensionless flame length. The dimensionless flame length is taken along the selected iso-line. Figure 3.7a presents the strain $\mathrm{Ka_s}$ and curvature $\mathrm{Ka_c}$ contributions for the stretch rate, as defined in Eq. (3.12), for the iso-line at $Y_{F,o}(\dot{Q}'''_{max})$. The strain and curvature effects are both positive and equivalent up to $s/s_{max} = 0.75$. Near the tip, the strain effect becomes positive and the curvature negative, as anticipated.

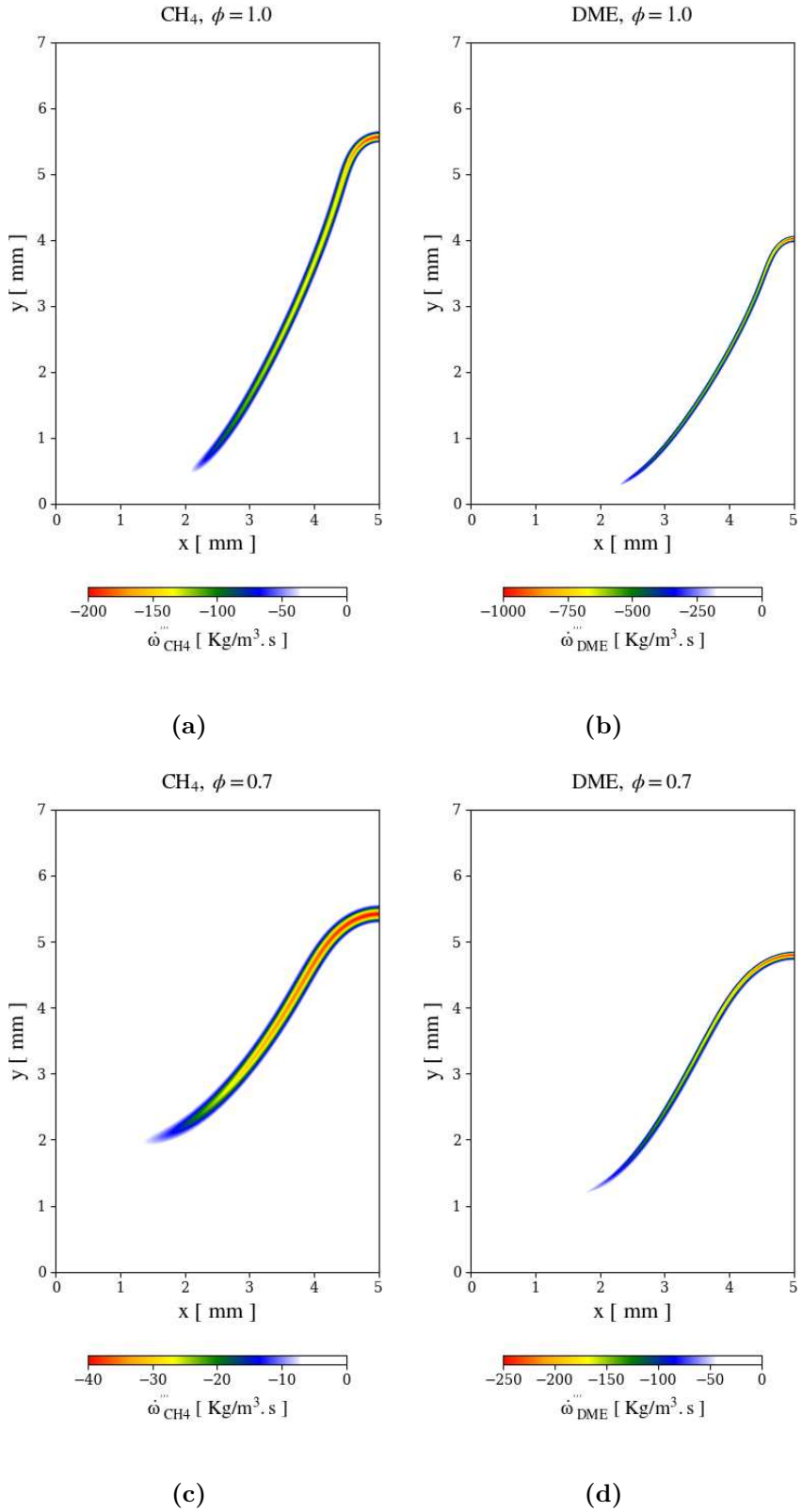

Figure 3.6: Fuel reaction rate, (a) methane, $\phi = 1.0$, (b) DME, $\phi = 1.0$, (c) methane, $\phi = 0.7$ and (d) DME, $\phi = 0.7$.

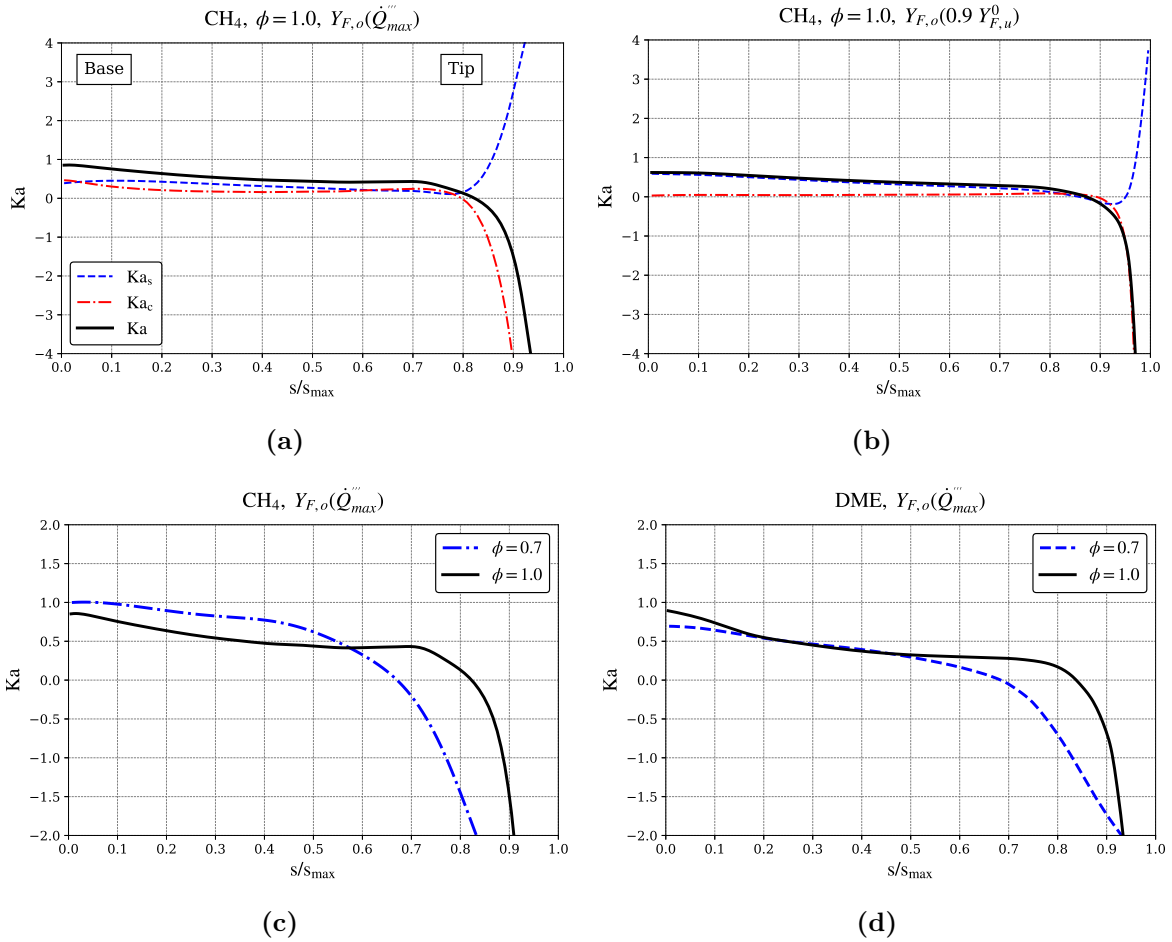

Figure 3.7: Karlovitz number as function of non-dimensional flame length, (a) Strain Ka_s and curvature Ka_c effects and overall Karlovitz number Ka for CH_4, $\phi = 1$, and $Y_{F,o}(\dot{Q}'''_{max})$, (b) Strain Ka_s and curvature Ka_c effects and overall Karlovitz number Ka for CH_4, $\phi = 1$, and $Y_{F,o}(0.9\ Y^0_{F,u})$, (c) Overall Karlovitz number Ka for CH_4, $\phi = 1$ and $\phi = 0.7$, (d) Overall Karlovitz number Ka for DME, $\phi = 1$ and $\phi = 0.7$.

The sum of both effects is a negative stretch rate. The $Y_{F,o}(0.9\ Y^0_{F,u})$ presents a similar behavior except that the curvature effect is near zero for $s/s_{max} < 0.9$. Since the strain rate effect is positive, the overall stretch rate is positive up to $s/s_{max} = 0.9$ and then becomes negative, as anticipated, but with a sharper slope. From Fig. 3.7a and 3.7b, we note that the $Y_{F,o}(\dot{Q}'''_{max})$ definition is more sensitive to variations in flame curvature, and, therefore, will be used for the remaining analysis.

Figures 3.7c and 3.7d compare the overall Karlovitz number of methane and DME flames for $Y_{F,o}(\dot{Q}'''_{max})$, for both equivalence ratios. The flames for $\phi = 0.7$ present a more non-uniform Karlovitz number profile, indicating that this condition is more affected by curvature, since the fuel reaction rate is weaker, as anticipated in Eq. (3.8). The nondimensional stretch rate is positive up to s/s_{max} between 0.65 and 0.7.

Figure 3.8 shows the nondimensional normalized displacement speed $\tilde{S}_d/S_l^o$ for the $Y_{F,o}(\dot{Q}'''_{max})$ for both fuels, at both equivalence ratios. Both fuels present the same general trends, indicating that the curvature term prevails in Eq. (3.19). The stoichiometric flames

present steeper gradients and a larger variation than the lean flames. The flames for both fuels change from $\tilde{S}_d/S_l^o$ lower to one to higher to one at the same nondimensional flame surface coordinate. Near the tip, the methane flame presents a larger positive deviation from the laminar planar flame speed, as a result of the larger curvature.

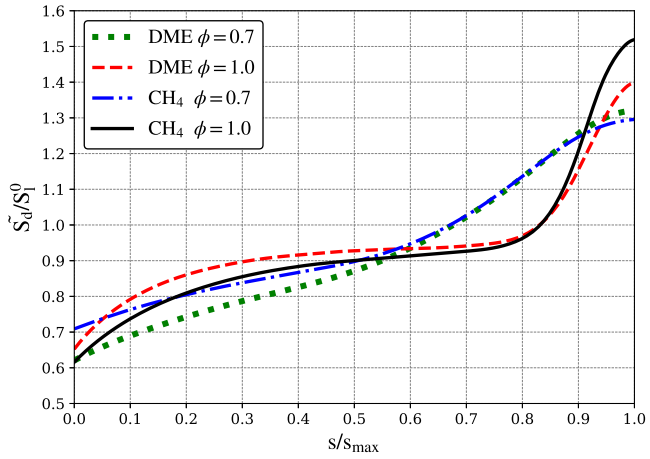

Figure 3.8: Nondimensional normalized displacement speed as a function of the nondimensional flame arc-length.

In Fig. 3.9 is shown the correlation of nondimensional normalized displacement speed to Karlovitz number. The general trends are: Near the base, the Karlovitz number tends to one and the displacement speed is smaller than the laminar flame speed as a result of positive curvature and heat loss to the burner rim. Towards the tip, the Karlovitz number becomes negative due to negative curvature and the displacement flame speed increases in respect to the laminar flame speed. The stoichiometric flames present sharper tip and therefore reach larger values of Karlovitz number.

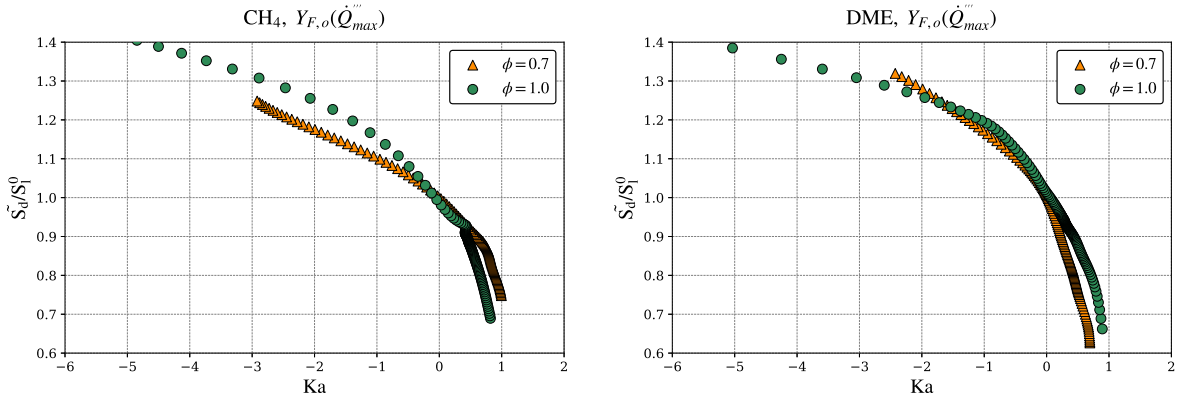

(a) **(b)**

Figure 3.9: Correlation between $\tilde{S}_d/S_l^0$ and Karlovitz number.

The structure of the two-dimensional flame is affected by tangent components of convection and diffusion fluxes, disturbing the local mass fraction distributions. Figure

3.10 presents the relative, two-dimensional, species i mass fraction along the flame surface, $\hat{Y}_i = Y_i/Y_i^0$, where Y_i^0 is the value calculated for the planar, adiabatic flame. It presents the curves for hydrogen and oxygen for the two choices of flame surface position. For methane at $\phi = 1$, the concentration of oxygen has a negligible variation ($D_{m,\mathrm{H_2}} > D_{m,\mathrm{CH_4}} > D_{m,\mathrm{O_2}}$).

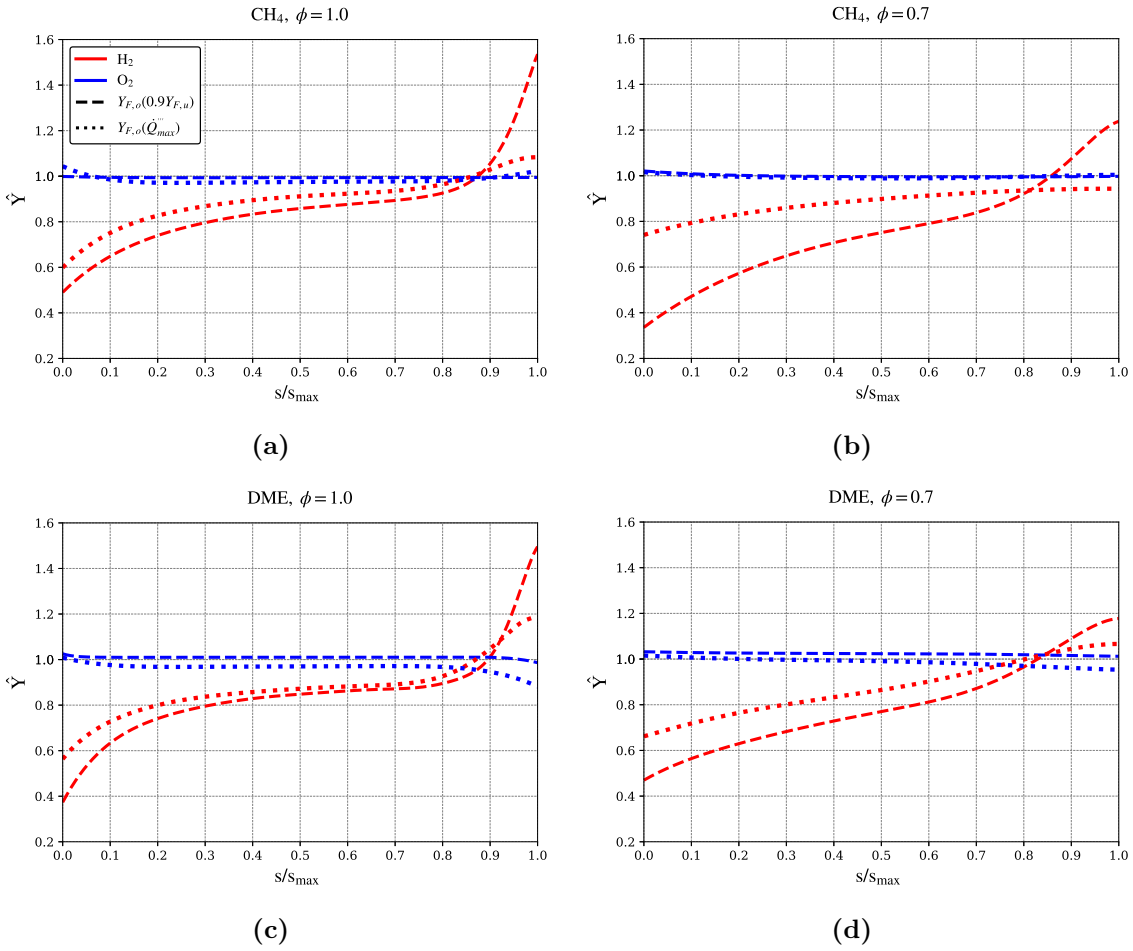

Figure 3.10: Relative, mass fractions of hydrogen and oxygen along the flame surface, $\hat{Y}_i = Y_i/Y_i^0$, where Y_i^0 is the value calculated for the planar, adiabatic flame.

Due to its higher difffusivity, hydrogen, on the other hand, presents a larger variation. Hydrogen is formed at the reaction region and diffuses to the unburned mixture. Therefore, the regions with positive curvature (near the base) present deficiency and regions with negative curvature (near the tip) present excess hydrogen. The stoichiometric flame presents higher curvature near the tip (Fig. 3.10a), therefore, higher excess when compared to the lean flame (Fig. 3.10b). The lean flame, however, presents a higher positive curvature near the base and therefore, the deficiency of hydrogen is larger. When the flame surface is chosen within the reaction region, the hydrogen profile is deficient in most of the flame surface, as a result of the diffusion to the unburned region. DME has the lower diffusion coefficient ($D_{m,\mathrm{H_2}} > D_{m,\mathrm{O_2}} > D_{m,\mathrm{DME}}$). Oxygen diffuses from the unburned mixture to the reaction region. Therefore, oxygen becomes deficient along the flame and

the effect increases as curvature increases (Fig. 3.10c and 3.10d).

Figures 3.11 and 3.12, in the first row, present the normal distributions of temperature, hydrogen and oxygen mass fractions for the methane flame at $\phi = 1$. Figures 3.11 and 3.12, in the second row, show the normal distributions of the hydrogen and oxygen reaction rates (d and e) and the heat release and volumetric energy diffusion (f). Figure 3.12 present the same results for the methane flame at $\phi = 0.7$. The curves correspond to two positions along the flame surface, one around half the flame height, where $\tilde{S}_d/S_l^0 = 0.83$, and the other near the tip, where $\tilde{S}_d/S_l^0 = 1.45$. The dotted line is the result for the planar, adiabatic flame for the same positions. The triangular markers identify the position of the flame surface for $Y_{F,o}(0.9\ Y_{F,u}^0)$.

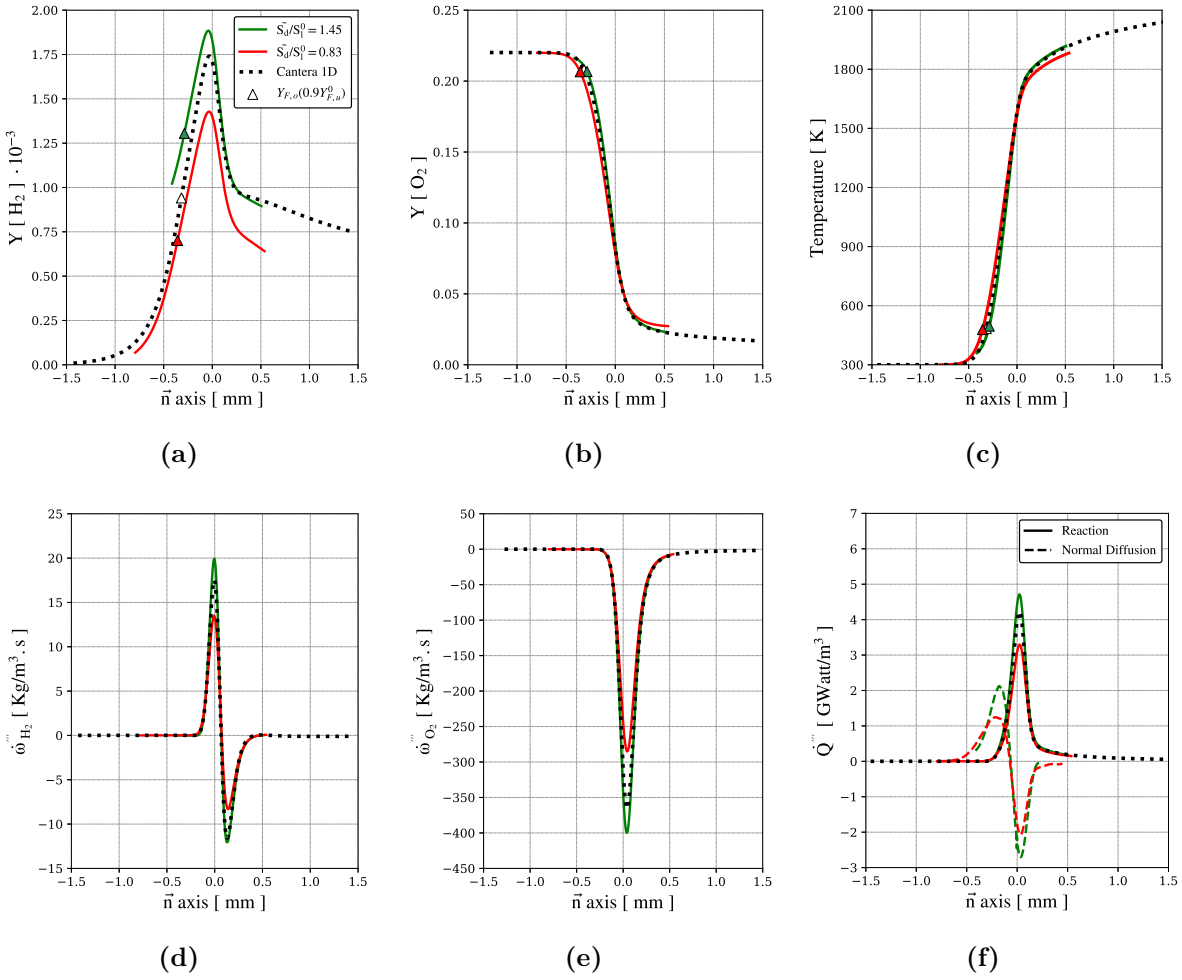

Figure 3.11: Normal flame distributions for the methane flame, at $\phi = 1$, for two positions along the flame surface, one around half the flame height, where $\tilde{S}_d/S_l^0 < 1$, and the other near the tip, where $\tilde{S}_d/S_l^0 > 1$. The dotted line is the result for the planar, adiabatic flame for the same positions. The triangular markers identify the position of the flame surface for $Y_{F,o}(0.9\ Y_{F,u}^0)$. (a) hydrogen mass fraction, (b) oxygen mass fraction, (c) temperature, (d) hydrogen reaction rate, (e) oxygen reaction rate and (f) heat release rate and volumetric energy diffusion.

The hydrogen distribution for the positively curved region (in red, Fig. 3.11a) presents a deficiency in the preheating and post-reaction region. Both the production and destruction rates in Fig. 3.11d are reduced. The oxygen mass fraction is not strongly affected (Fig. 3.11b), but the hydrogen deficiency has an effect in the oxygen destruction rate (Fig. 3.11e). As a result, both the energy diffusion flux and heat release are reduced (Fig. 3.11f). The distributions for the region with negative curvature (in green) follow the opposite trend. The temperature distribution (Fig. 3.11c) shows that in the region with positive curvature (in red) the equilibrium temperature is smaller than the temperature of the planar, adiabatic flame. The region with negative curvature (in green) shows the opposite trend, in which the temperature gradient is greater than the planar, adiabatic flame. The results for the lean flame in Fig. 3.12 present the same trends, but with smaller intensity.

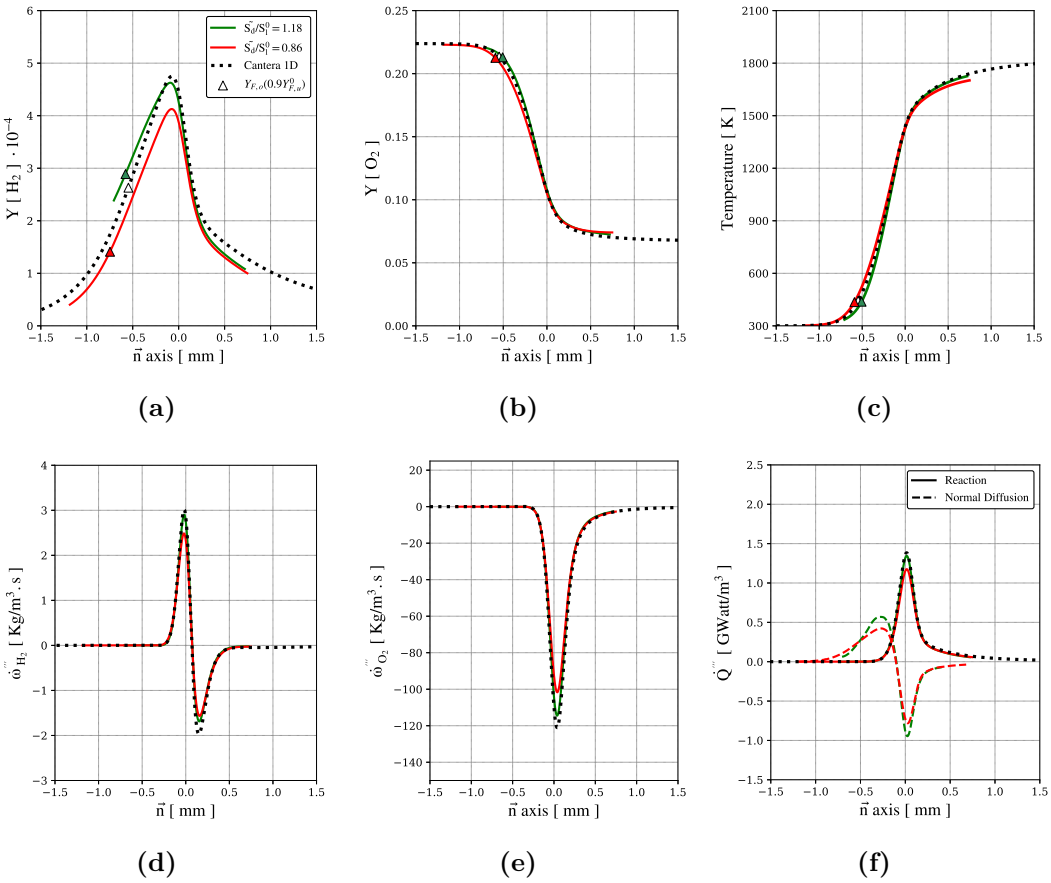

Figure 3.12: Normal flame distributions for the methane flame, at $\phi = 0.7$, for two positions along the flame surface, one around half the flame height, where $\tilde{S}_d/S_l^0 < 1$, and the other near the tip, where $\tilde{S}_d/S_l^0 > 1$. The dotted line is the result for the planar, adiabatic flame for the same positions. The triangular markers identify the position of the flame surface for $Y_{F,o}(0.9\ Y_{F,u}^0)$. (a) hydrogen mass fraction, (b) oxygen mass fraction, (c) temperature, (d) hydrogen reaction rate, (e) oxygen reaction rate and (f) heat release rate and volumetric energy diffusion.

3.3.2 Hydrogen flame instabilities

Bunsen flames are highly stretched due to the effects of the embedded flow field. These effects in turn tend to establish regions dominated by strain and curvature deformation. The geometrical shape is largely responsible for the spatial changes of the transport gradients inside the flame structure, and they also provide direct evidence of the deformation effects of the surface in the flame dynamics. The Bunsen flame was analyzed in steady-state condition with $\phi = 0.5$. The domain has a height of 20 mm in the stream-wise direction and 5 mm in width. A Poiseuille jet velocity profile is imposed in the inlet boundary with $\langle u \rangle = 3S_l^0$.

For planar flames, a set of simulations were carried out with the aim to study the behavior of linear and non-linear time evolution of initial perturbations imposed to initial planar flame. In all cases, the inlet velocity has a planar profile with $u = S_l^0$. For the linear analysis, the domain dimensions presents a constant length in streamwise direction of $L = 35\delta_l^0$, and different cases for crosswise direction were set up as $H = \lambda = 2\delta_l^0, 3\delta_l^0,\ 4\delta_l^0,\ 5\delta_l^0,\ 6\delta_l^0, 7\delta_l^0,\ 10\delta_l^0$ and $20\delta_l^0$ wich corresponds to normalized wavenumbers of $\hat{k} = 3.14, 2.094, 1.571, 1.256, 1.047, 0.898,\ 0.628$ and 0.314, respectively. A harmonic perturbation was introduced in temperature field, $T^{'} = T_0 \sin(ky)$ where $k = 2\pi/\lambda$. In this case, each domain has one wavelength and were studied flames with $\phi = 0.5$ and 0.7. To solve the non-linear problem, it was used a domain with 43 and 129 mm ($100\delta_l^0$ and $300\delta_l^0$) in streamwise and crosswise direction, respectively, yielding a mesh of 2150 x 6450 cells. Here, 60 wavelengths were initially imposed with $\lambda = 5\delta_l^0$ and $\phi = 0.5$.

Table 3.2 presents the laminar, planar, adiabatic flame parameters for the hydrogen/air flame solved with Cantera [70]. In Tab. 3.2, $Y_{F,o}(\dot{Q}^{'''}_{max})$ is the value of the isoline of mass fraction for the definition of flame surface position. The τ_f is the the characteristic flame time defined as $\tau_f = \delta_l^0/S_l^0$ and T_{ad} is the adiabatic flame temperature. For all simulations, the inlet boundary temperature is $T_u = 300$ K.

Table 3.2: Laminar, planar, adiabatic flame parameters for the hydrogen/air mixtures at atmospheric conditions.

ϕ	S_l^0, cm/s	δ_l^0, mm	τ_f, ms	T_{ad}, K	Le_{eff}	$Y_{F,o}(\dot{Q}^{'''}_{max})$
0.5	52.0	0.43	0.827	1646	0.51	0.00286
0.7	132.0	0.36	0.272	2021	0.69	0.00908

3.3.2.1 Highly stretched flames

Figure 3.13 presents the results for the Bunsen flame wherein Fig. 3.13a shows the normalized fuel reaction rate, and Figs. 3.13b and 3.13c depict the normalized flame consumption speed and Karlovitz number along the front, respectively. A visual inspection of Fig. 3.13a shows that the flame burns faster at the domain base reaching values of $4.5\hat{Q}$.

Since hydrogen has the highest burning rate at the base, it provides an almost zero lift-off effect. Towards the top, the burning rate slows down until the flame extinction in the front.

The previous description is quantified in Fig. 3.13b. At the base, the flame S_c is almost 2.5 times than the flat flame speed. Up to $s/s_{max} = 0.3$, the S_c drops reaching a linear decay region between $0.3 > s/s_{max} > 0.8$. Near the tip, the S_c decreases exponentially. Graph 3.13c shows that the flame presents three distinct regions. In the first one, at the base, the Ka is positive at the base where the front is positively curvate summed the flame-flow interaction that causes a tangential stretching. The second region is defined by a constant and weaker stretch rate. Near the tip, the negative curvature takes over the process resulting in a negative Ka.

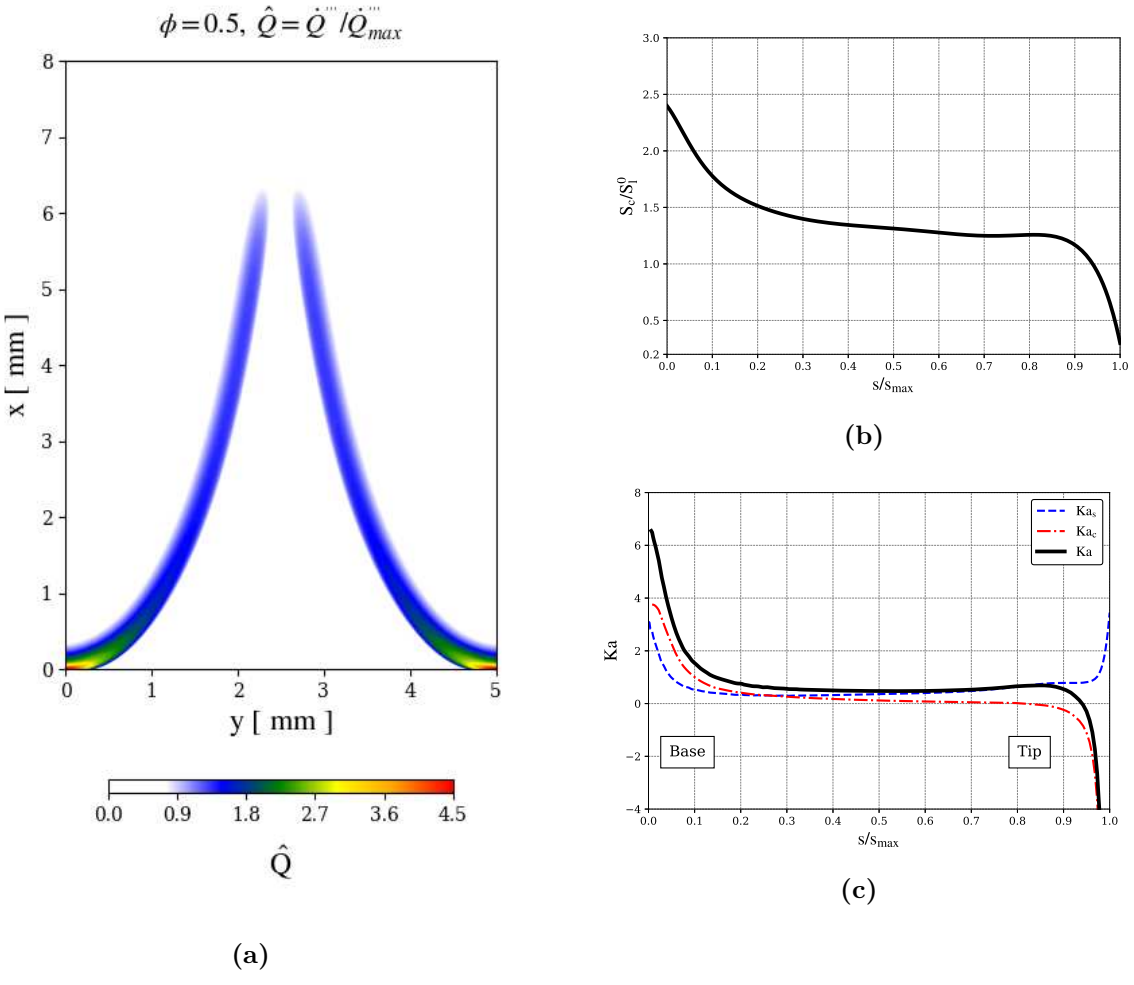

Figure 3.13: Simulation results for the Bunsen flame for hydrogen/air at $\phi = 0.5$, (a) normalized heat release rate, (b) normalized consumption speed as a function of the nondimensional flame arc-length and (c) Karlovitz number as a function of the nondimensional flame arc-length.

Figure 3.14 shows the correlation of flame speed with the front deformation caused by the flow interaction. Figures 3.14a, 3.14b, and 3.14c depict the relation of flame speed, respectively, with the total Karlovitz number, the Ka due to the curvature, and

related with the dimensionless curvature by the flame thickness. Unlike hydrocarbons, the hydrogen Ma is negative which means that the flame tends to increase the burning rate as the stretch rate also grows.

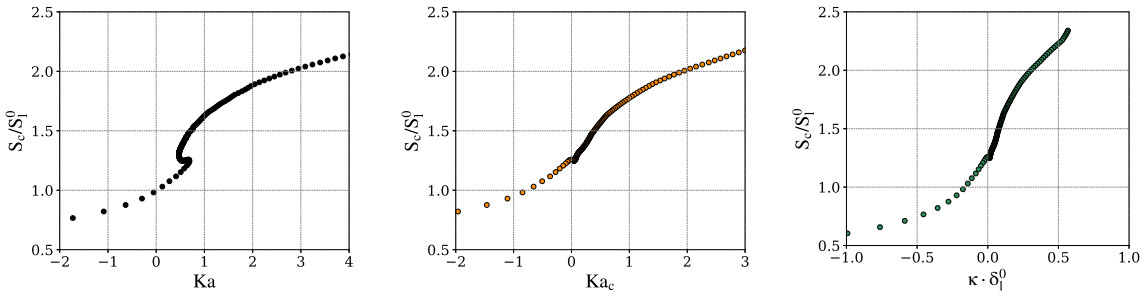

Figure 3.14: Bunsen flame correlation between flame consumption speed for $\phi = 0.5$ and, (a) Karlovitz number, (b) Karlovitz number due to curvature and (d) dimensionless curvature.

Figures 3.14a and 3.14b reproduce the theoretical behavior. Near zero, flame behaves as is predicted for weak deformation theory where the flame speed varies linearly with the stretch as shown in the asymptotic correlation in Eq. (3.4). In the Figs. 3.14b and 3.14c is observed that a significant points quantity are located at $\mathrm{Ka_c} = 0$ ($\kappa = 0$), and out of this region, the flame speed is substantially affected by positive and negative stretch.

The flame quenching caused by the negative stretch can be explained by the effect of thermo-diffusive instabilities. The Le < 1 makes the thermo-diffusive mechanism unbalanced, where the fuel comes out from the front faster than heat diffusion. The negatively curved flame surface leads to a defocused diffusion of hydrogen and a decreased local equivalence ratio. This effect cannot be compensated by the counteracting thermal diffusion [107, 108]. Figure 3.14a shows this effect in the deviation from the linear relation (3.4) for consumption speed far from unity. The reason for that is associate with the higher-order terms added by the curvature and Le < 1 interaction, Fig. 3.14c.

The stretch-diffusion relation is dominant in a Bunsen flame; however, the apparent hydrodynamic stability lies in its strong velocity tangential component in the flame surface. All structures on the flame surface are convected toward the flame tip at the tangential velocity, and thus have a finite residence time, $\tau = l/\vec{V}_t$, where l is the length of the slanted flame. This residence time must be compared with the growth time of instabilities $\tau = 1/\omega$. If the residence time is not large when compared with the growth time, then the small perturbations at the base will not have time to grow to an appreciable amplitude before they are convected out of the flame [109].

3.3.2.2 Planar flames: Linear growth of instabilities

During the firsts propagation stages, the flame front perturbation grows linearly. The following results present the behavior of fuel isoline coming from DNS. Figure 3.15 shows

the amplification of initial perturbation for the case $\hat{k} = 0.628$ ($H = 10\delta_l^0$).

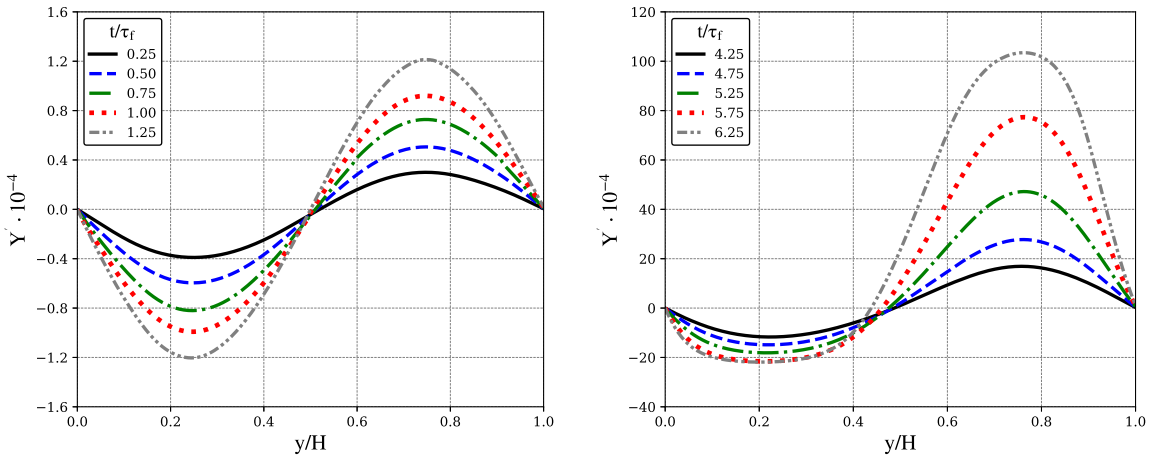

(a) **(b)**

Figure 3.15: Perturbation profiles for $\hat{k} = 0.628$ ($H = 10\delta_l^0$), (a) initial flame proagation, (b) thermo-diffusive effects.

In the beginning, in Fig. 3.15a, the perturbation profiles keep the sine form. Further, Fig. 3.15b, it can be observed that the diffusive effects take place and the profiles do not evolve homogeneously. For the convex region, $Y^{'} < 0$, the flame burns faster getting an extended low-curvature crest. On the other hand, in the concave region, $Y^{'} > 0$, the local flame speed is lower, which yields a trough-shaped flame structure with a depth increasing with temporal evolution.

Figure 3.16a reports the dimensionless dispersion relation, $\hat{\omega} = \omega \cdot \tau_f$, for the cases enumerated in section 3. Figure 3.16b complements the analysis illustrating the temporal evolution of the imposed initial amplification for three cases with $\phi = 0.5$. In the right graph is depicted the linear Darrieus-Landau coefficient and those computed by the simulations. The results are in line with those observed in the works of [30, 110]. The graph shows that for small wavenumbers, the growth rate tends to values predicted by hydrodynamic theory. However, the superimposed effect of diffusion (Le < 1) increases the $\hat{\omega}$. As the wavenumber gets larger, it reaches a maximum value, below ω_{DL}, and then, the growth rate becomes weaker towards negative values. In the last case, for $\hat{k} = 3.14$ ($H = 2\delta_l^0$) resulting in $\hat{\omega} = -1.78$, it is seen that for small wavelengths, the diffusion is able to damp the initial amplification rather than increase, seen in circle markers in Fig. 3.16b.

Figure 3.16a also compares the growth rate of $\phi = 0.5$ and $\phi = 0.7$. The curves present the same qualitative characteristics described previously, although for all wavenumbers, $\phi = 0.5$ shows higher $\hat{\omega}$ even for the damping effect. According to the Darrieus-Landau assumption, the amplification rate grows due to expansion factor and flame speed. However, such assumption is not sufficient since preferential diffusion effects associated with the

condition Le < 1 will have a large prominence in the dynamics of the flame front. In fact, the accuracy of other modelling approaches, as proposed by [97–99], which includes these additional diffusive effects, was considered in [110]. The main conclusion is that despite the fact that these models include this second-order term, and therefore the contribution related with low Le, in reality the growth rate is essentially a physical process of higher-order.

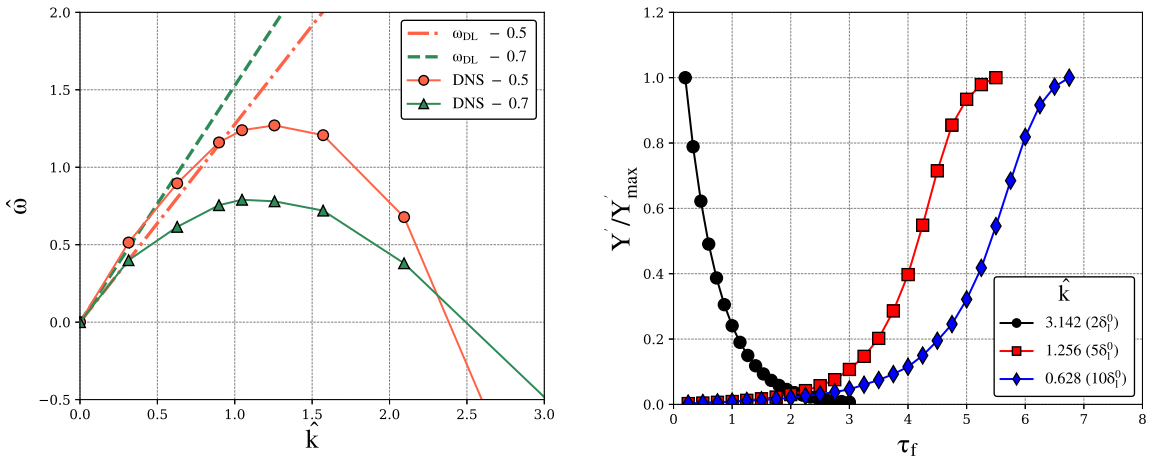

(a) **(b)**

Figure 3.16: Linear perturbations dynamic computed from the DNS for $\phi = 0.5$, (a) dispersion relation comparison between hydrodynamic theory and simulations, (b) Time evolution of the initial perturbations for $\hat{k} = 1.257,\ 2.094$ and 3.14.

In the results of the dispersion relation, a fourth order polynomial fit was used with the aim to map important features observed in the plot. For $\phi = 0.5$, the growth rate is null for $\hat{k} = 2.46$, $\hat{\omega}(2.46) = 0$. The hydrodynamic and the thermo-diffusive instabilities have the same rate in $\hat{k} = 1.04$, $\hat{\omega}(1.04) = \hat{\omega}_{DL} = \hat{\omega}_{TD}$, and the growth rate has the a maximum value in $\hat{k} = 1.28$, $\hat{\omega}(1.28) = \hat{\omega}_{max}$. For $\phi = 0.7$, the $\hat{\omega}(2.52) = 0$, $\hat{\omega}(\hat{k} \to 0) = \hat{\omega}_{DL} = \hat{\omega}_{TD}$ and $\hat{\omega}(1.17) = \hat{\omega}_{max}$.

Figure 3.17 shows the instantaneous flame absolute speed, $S_a = \vec{V}_f \cdot \vec{n} = \vec{V} \cdot \vec{n} - S_d$, and the density-weighted flame displacement speed, taking two points of Fig. 3.15b, $t/\tau_f = 4.25$ (left column) and $t/\tau_f = 6.25$ (right column). In general, the absolute speed mirrors the displacement speed for both plots since the apparent front speed also decays as the displacement speed decreases, and the opposite is valid for regions where the burning rate increases. At $t/\tau_f = 4.25$, the harmonic profile remains. However, even with the low curvature, the local burning rate is affected. As time elapsed to $t/\tau_f = 6.25$, the scenario changes drastically. The fuel consumption response to negative curvature, Fig. 3.17d, makes the flow push the front backward while the positively curved remains propagation towards the inlet boundary. This dynamic is responsible for leading the flame front to chaotic behavior, causing the flame wrinkling analyzed in the following section.

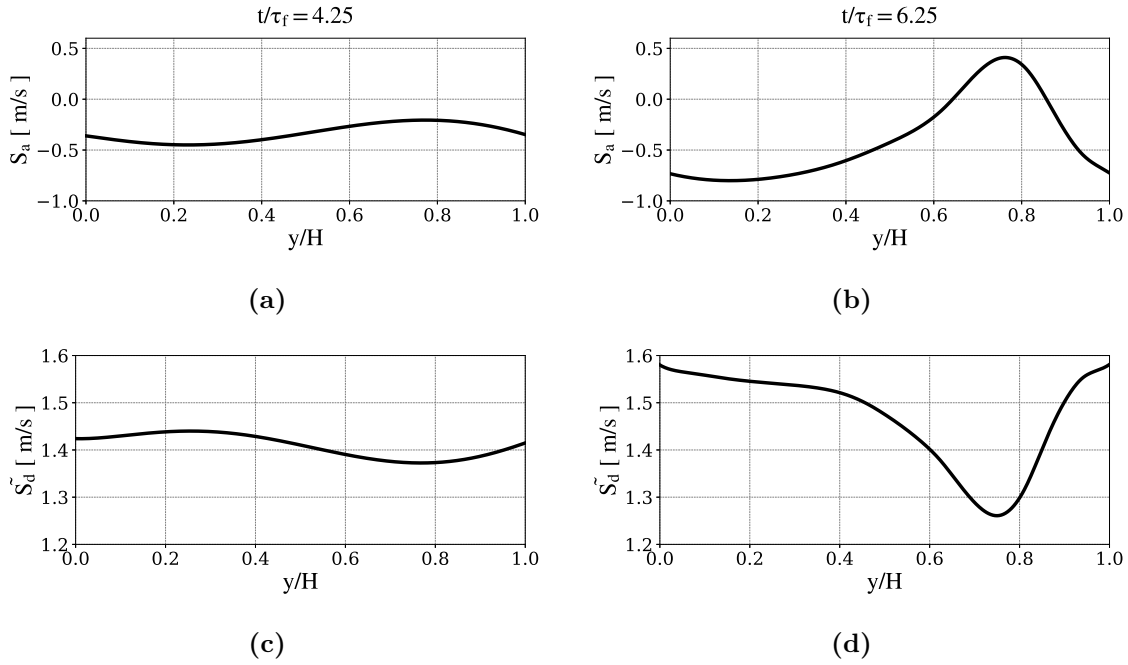

Figure 3.17: Flame speed profiles for the linear growth of initial perturbations with domain of $\hat{k} = 0.628$ ($H = 10\delta_l^0$), (a) absolute speed S_a at $t/\tau_f = 4.25$, (b) absolute speed S_a at $t/\tau_f = 6.25$, (c) displacement speed $\tilde{S}_d$ at $t/t_f = 4.25$ and (d) displacement speed $\tilde{S}_d$ at $t/\tau_f = 6.25$.

3.3.2.3 Planar flames: Non-linear growth of instabilities

Figure 3.18 shows three time steps that present the flame front evolution in the broad domain for $\phi = 0.5$; during the linear growth, $t = 5\tau_f$, the development of wrinking front at $t = 25\tau_f$ and the wrinkling front spreading $t = 60\tau_f$. Figures show the normalized temperature field $\hat{T} = (T - T_u)/(T_{ad} - T_u)$, and in Fig. 3.18d is seen, in a local magnification, the normalized heat release rate regarding the adiabatic flame, $\hat{Q} = \dot{Q}'''/\dot{Q}'''_{max}$. As was described in section 3.2, 60 wavelengths were imposed with $\lambda = 5\delta_l^0$, which were the fastest values found in the linear analysis.

At $t = 5\tau_f$, the harmonic waves keep the initial profile as reported in the former section. During the first stages, the flame front is dominated by the positive stretch and the temperature in the burnt side overshoots beyond the adiabatic temperature since the enthalpy is not conserved for sub-unity Lewis number flames [69, 111]. As the initial symmetry is broken, a wrinkled front is formed, composed of a broad range of small crests and trough-shapes geometries. In $t = 25\tau_f$, greatter wavelengths consumed the smaller ones, however, the front is still made up of smaller wavelengths that move forward and transversely, increasing the front area. It is observed in temperature field, regions with temperatures below the T_{ad}, and regions in superadiabatic conditions. Figure 3.18d shows a similar frame for the heat release rate. There are two highly curved regions, at right and left, that HRR has the order of $\hat{Q} = 0.5$, which decreases the flame propagation speed.

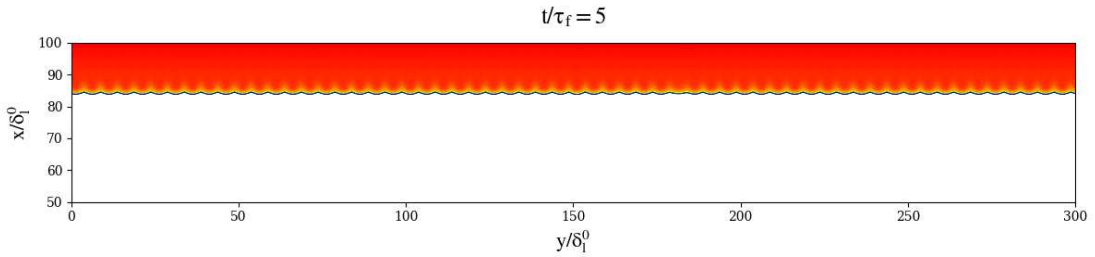

(a)

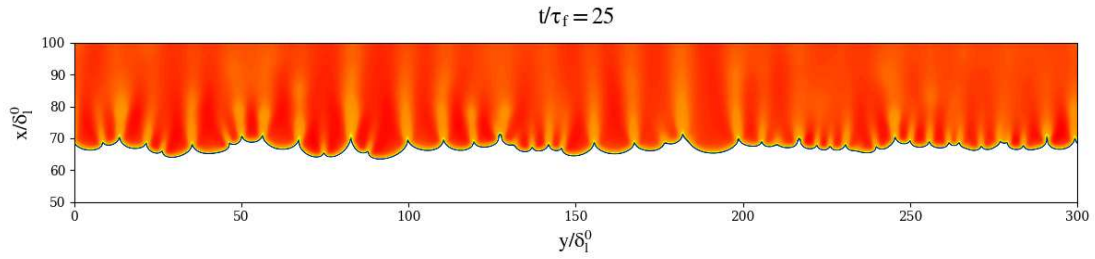

(b)

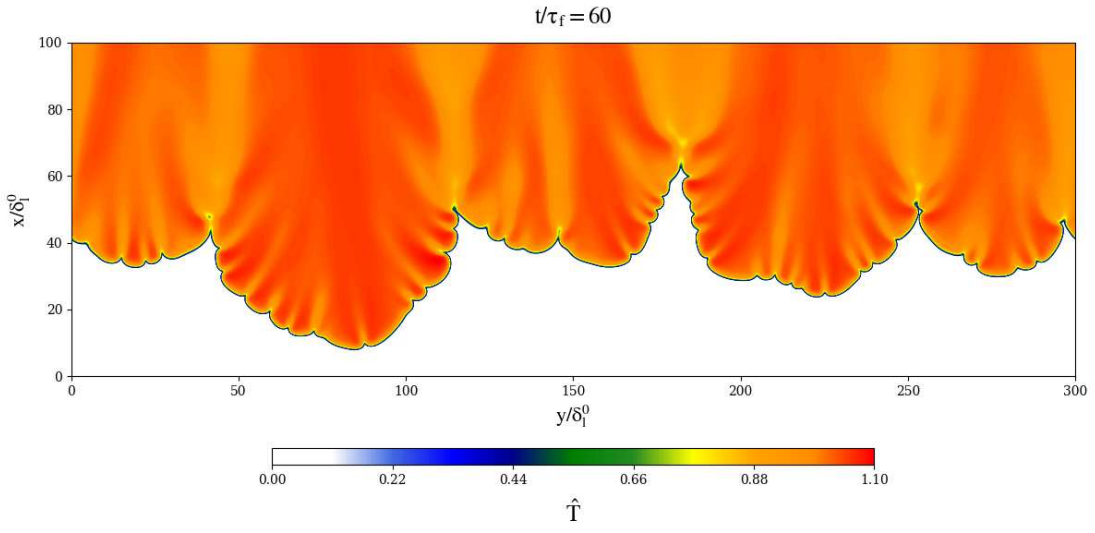

(c)

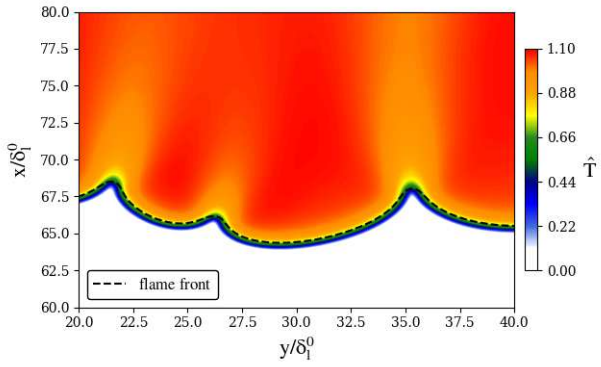

(d)

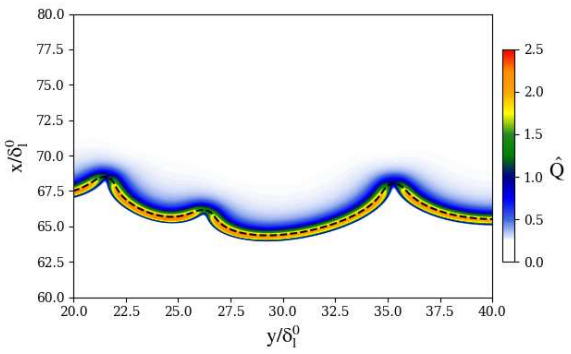

(e)

Figure 3.18: Time evolution of initial perturbations during the non-linear growth process, (a) temperature field at $t = 5\tau_f$, (b) temperature field at $t = 25\tau_f$, (c) temperature field at $t = 60\tau_f$, (d) temperature field magnified at $t = 25\tau_f$ and (e) heat release rate magnified at $t = 25\tau_f$.

On the other hand, it may be observed convex regions where the HRR can reach more than twice the value of the flat adiabatic flame. In $t = 60\tau_f$, Fig. 3.18c shows that the flame has five great structures, fingers, composed of small wrinkled fronts. The flame is subject to a spread propagation of self-sustained instabilities where positively stretched regions show the superadiabatic temperature. Nevertheless, the regions negatively stretched affects the entire temperature field. It can be seen that where $\kappa < 0$, the lower temperatures can penetrate the burned side. In addition, the five fingers are formed in regions where κ is strongly negative, presenting a trail of low temperaure that goes from the flame front to the domain outlet.

Figure 3.19 presents the normalized curvature and burning properties highlighted in the black dashed line in Fig. 3.18d and 3.18e. In Fig. 3.19a is seen the flame curvature along the front arc-length, s, until $s/\delta_l^0 = 100$.

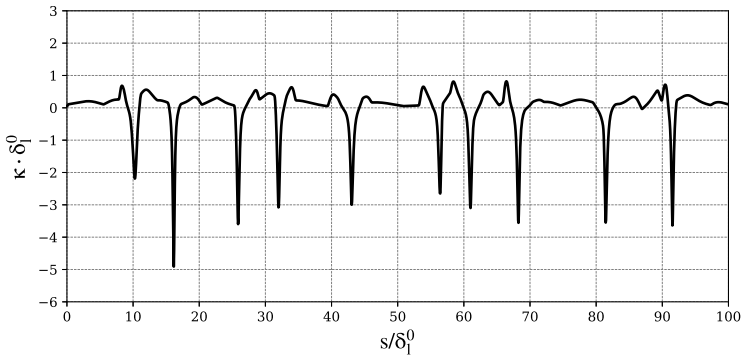

(a)

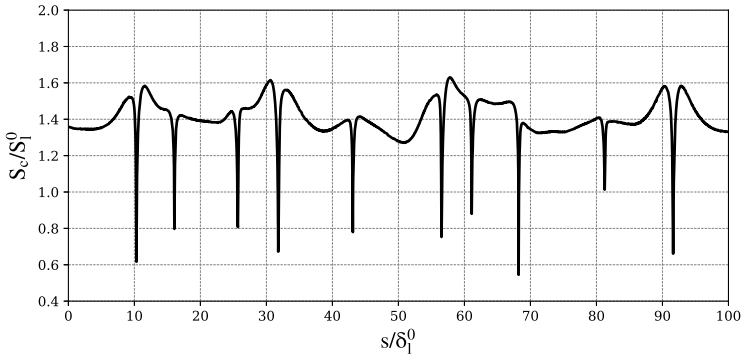

(b)

Figure 3.19: Flame front structural properties, (a) flame curvature and (b) flame consumption speed.

It can be observed that the current front area surpasses the initial value of the flat flame since the geometry is highly curved, reaching 1.25 times the y-coordinate. Yet, it shows that there is a broad spectrum of curvatures at the front. It has ten deeper troughs resulting in stronger values of negative curvature. Positive curvature values are smoother and more extended as may be checked in graph 3.18b. Figure 3.19b shows the normalized consumption speed regarding the flat flame speed. The Figure depicts the effects of local

curvature over the S_c. In regions where the negative κ is stronger, the normalized flame speed is much lower than unity. On the other hand, for posivity κ, the S_c/S_l^0 may reach values of $1.6S_l^0$.

The same correlation presented for the Bunsen flame curvature is shown for the current work frame in Fig. 3.20. The outcome forms a cloud of clustering points highly concentrated in regions above $\kappa = 0$, becoming less dense towards lower curvature values. The linear regression highlights that the Le effect over the Markstein number remains even with the chaotic flame behavior. Incidentally, a relation between Fig. 3.20 and Fig. 3.14c an be determined. For example, near $\kappa = 0$, the correlation for the Bunsen flame is linear (as predicted by Eq. (3.4)), and for the planar flame, the difference from the linear behavior tends to decrease at such values. For higher negative values, the deviation increases, and it is attributed to higher-order terms that the relation curvature-thermo-diffusive effects add to flame propagation dynamics.

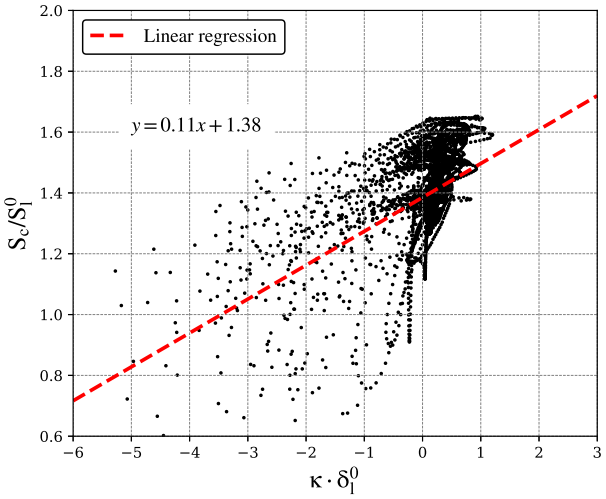

Figure 3.20: Correlation between dimensionless curvature and flame consumption speed for $\phi = 0.5$ at $t = 25\tau_f$ for the planar flame.

3.4 CONCLUSION

The effects of flame instabilities, curvature, normal and tangential strains in the flame stretch rate and flame displacement speed were studied using DNS for canonical flames; slot burners, Bunsen and planar flames, for three different lean fuels/air mixtures, methane, DME and hydrogen. Methane flame presents the Lewis number near one, while DME has Le > 1 resulting in stable flames. On the other hand, lean hydrogen flames offer Le < 1, which yields drastically different propagating properties than traditional hydrocarbons.

For methane and DME flames in the slot burner configuration, the strain and curvature contributions to the Karlovitz number have the same intensity in the region of positive curvature, but the curvature contribution becomes strongly negative and dominant in

the concave curvature region. The stoichiometric flames present stronger variations of Karlovitz number when compared to the lean flames. The dimensionless displacement speed normalized by the laminar flame speed (planar flame) is smaller than one in the region of positive curvature and grows above one in the region of negative curvature. The correlation with Karlovitz number is similar for both fuels and stoichiometries. The mass fraction of hydrogen along the flame surface presents strong deficiency in the positive curvature region and strong excess in the negative curvature region when compared to the planar, adiabatic flame. The trend is observed not only on the position of the flame surface, but also in the entire distribution along the normal direction as well.

For hydrogen, the Bunsen flame shows that stretch-chemistry and diffusion interaction substantially modify the local burning rate for sufficient lean mixtures. Positively curved regions may burn more than twice the flat flame speed, while negative curvature may cause the flame front extinction. At weaker stretched areas, the correlation of flame speed and Ka are in line with the linear theoretical model. However, far from these points, it was observed that the strain and curvature provide higher-order effects that cause significant deviation from linear theory. In the planar flame configuration, the outcomes show that the local flame speed depends on the growth rate, ω. The instabilities grow faster at a specific value of flame curvature related to the front wavelength. The dispersion relation presented for $\phi = 0.5$ shows that the $\lambda = 5\delta_l^0$ has the maximum growth rate value. For $\lambda = 2\delta_l^0$, the diffusive effects damp the initial perturbations. For a richer condition, $\phi = 0.7$, the lower Le tends to decrease the dimensionless $\hat{\omega}$. For the broad domain, the DNS shows that the initial perturbations lead to a chaotic flame behavior where the wrinkled front is composed of a range of small crests and trough-shapes geometries, formed transversally by great wavelengths made up of smaller ones. A linear regression fit, made with the correlation between flame curvature and flame consumption speed, shows that the deviation from the linear theory is lower for smaller curved regions, while for relatively high negative values the deviation from the linear theory increases significantly.

Chapter 4

Low-temperature chemistry in SI engines

Knocking limits the operation of highly compressed, downsized SI engines. It starts with a thermal ignition of the end-gas caused by the pressure increase resulting from the propagation of the turbulent deflagration wave and engine dynamics. Typically T, p and ϕ conditions at end-gas may lay in a cool flame regime. The cool flame has two main effects: (1) it precedes the main autoignition event and (2) it affects the propagation of the deflagration flame. Aside from autoignition, preignition of the mixture can lead to knocking as well [112–116]. As the preignition is strongly related to engine operation rather than chemistry, it will not be analyzed in this study. Here, we focus on two-stage autoignition.

4.1 BACKGROUND

Knocking refers to the occurrence of spontaneous combustion of the air-fuel mixture leading to high frequency pressure oscillation within the combustion chamber. The three main steps during abnormal combustion are illustrated in Fig. 4.1. They are the onset regime, that leads to autoignition of the end-gas, the pressure discontinuity, due to strong instantaneous heat release, and the pressure oscillations, caused by reverberation of sound waves [117]. These concepts are approached in the literature by (1) identifying the mechanism of autoignition, (2) defining which physical features lead to the formation of pressure waves, and (3) determining which effects cause the pressure waves to reach high intensities.

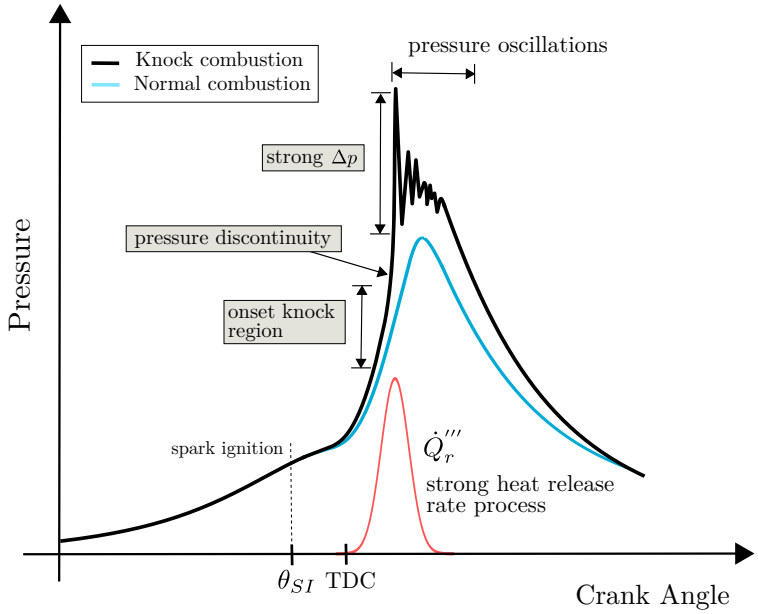

Figure 4.1: Schematic in-cylinder pressure behavior, for normal and abnormal combustion.

The propensity to engine knocking has been modeled using either semi-empirical algebraic or differential equations. One of the first algebric models was proposed by Douaud-Eyzat [118],

$$\tau = \mathrm{C}_1 \left(\frac{\mathrm{ON}}{100}\right)^{\mathrm{C}_2} p^{-\mathrm{C}_3} e^{\frac{\mathrm{C}_4}{T}}. \tag{4.1}$$

where τ is the ignition delay time, $\mathrm{C_i}$ are engine fitted constants and ON is the fuel octane number.

Later work added other parameters to the original model, such as residual gas fraction [119], equivalence ratio [120], and characteristics of the NTC region in the IDT curve [121].

Most engine simulation models adopt the Linvengood-Wu, Eq. 4.1. In this model, the integral from the crankshaft angle corresponding to the inlet valve closing θ_{IVC} to the onset of knocking $\theta_{\mathrm{KO,model}}$, is given by

$$\int_{\theta_{\mathrm{IVC}}}^{\theta_{\mathrm{KO,model}}} \frac{d\theta}{\Omega\tau} = 1, \tag{4.2}$$

must be equal to unity. In the integrand, Ω is the engine speed in rad/s and τ comes from an expression such as Eq. 4.1.

Using chemical kinetics mechanisms, Foong *et al.* [122] investigated the autoignition in a CFR engine employing mixtures of ethanol with several primary reference fuel (PRF) and toluene primary reference fuel (TRF), using the same standard conditions of the research octane number (RON). Among the results, they concluded that the incorporation of the NO chemical mechanism improved the level of agreement between numerical predictions and experimental results for fuels with low ethanol content.

Although many works follow the direction of increasing the number of parameters in the Linvengood-Wu model, the presence of the cool flame precludes obtaining a general simple algebraic or differential model, since it is strongly affected by the air-fuel combustion chemistry.

Although the mechanisms of low-temperature chemistry are reasonably known, their development under variable temperature and pressure, typical of engine conditions, has not been analyzed from the point of view of precursors of the end-gas autoignition. The low-temperature chemistry leads to the first-stage ignition and both, the first and second-stage ignitions, can be detected in ignition delay time curves. However, it is not clear how much the first-stage delay is affected by the transient temperature and pressure conditions in the end-gas, at different engine compression ratio and speeds, and how much the variation of the timing of the first-stage ignition affects the timing for the second-stage ignition. If the timing for the second-stage ignition is sufficiently delayed, knocking may be prevented.

In order to analyze these trends, an engine model which includes the modeling of the main combustion and the end-gas is required. The model needs to be tuned to measurements, to check its predictive capabilities, and then used to analyze the effects of engine speed and compression ratio on the development of the first-stage ignition and its role in the end-gas autoignition.

4.2 MATERIALS AND METHODS

A two-zone model is used here to study the effect of the first-stage ignition on the onset of knocking. The zones are separated by the turbulent flame brush. The Standard Coherent Flame Model is used to calculate the turbulent flame speed and to track the flame position as the combustion proceeds after the spark ignition. The burned gas behind the flame is assumed to remain under chemical equilibrium. The unburned gas ahead of the flame experiences physical effects, from the heating caused by the pressure variation and cooling by heat transfer to the cylinder walls, as well as, chemical effects, from the slow development of a low-temperature combustion chemistry. The chemistry of the unburned gas (the end-gas) is modeled assuming a uniform pressure, temperature, and composition fuel-air mixture and using a detailed chemical kinetics mechanism.

Figure 4.2 presents a rendering of the model. In Fig. 4.2, $\dot{Q}_f$ is the heat release rate of the main flame, $\dot{Q}_{wall}$ is the heat transferred to the cylinder walls, $\dot{Q}_r$ is the energy released by chemical reactions ahead of the main flame (in the end-gas), $\dot{Q}_{mech}$ is the engine indicated work. Furthermore, A_b, A_u and A_f are the surface areas of the burned gas, unburned gas, and flame front, respectively, and S_l is the local laminar flame speed.

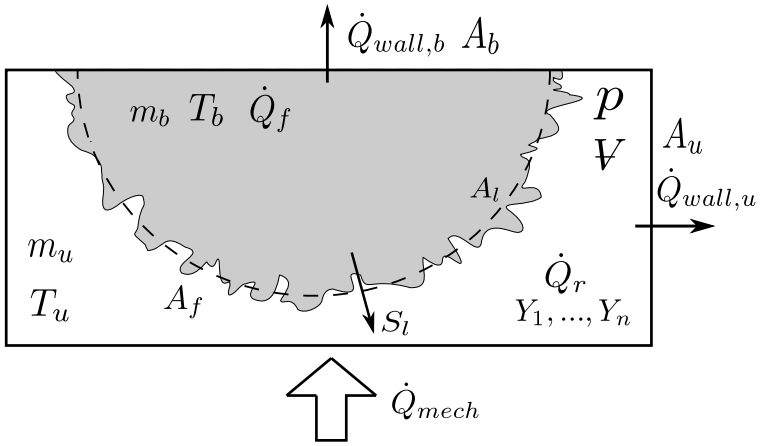

Figure 4.2: Rendering of the engine combustion model.

4.2.1 Engine modeling

The engine two-zone model represents the knocking process as a pure autoignition event that occurs in the bulk of the unburned zone. Thereby, no wall effect, other than heat transfer, is taken into account. In this way, the effects of the chemical kinetics mechanism in the end-gas can be analyzed independently of any physical effects resulting from mixture non-homogeneity. The modeling assumptions are summarized as follows: (1) The main combustion is spark ignited and occurs in a turbulent flamelet regime; (2) the states of the burned and unburned mixtures are spatially homogeneous; (3) the combustion products in the burned zone are at chemical equilibrium; (4) the chemical reactions in the unburned mixture are modeled using a detailed chemical kinetics mechanism; (5) the flame sheet dividing the burned and unburned zones has zero volume; (6) the flame heat release is calculated by the difference in thermal energy between the burned and unburned states; (7) no heat transfer occurs between the zones (i.e., across the flame brush); (8) the turbulence scales are based on the mean piston speed; and (9) the gas mixtures behave as ideal gases.

The simulations start from bottom dead center (BDC) after intake. The system of equations are based on those found in Ferguson [123], appendix A. The equation for the conservation of energy in the burned zone is

$$\frac{dT_b}{d\theta} = -\frac{\dot{Q}_{wall,b}}{\Omega m Y_b c_{p,b}} + \frac{T_b}{c_{p,b}}\frac{\partial v_b}{\partial T_b}\frac{dp}{d\theta} + \frac{h_u - h_b}{Y_b c_{p,b}}\frac{dY_b}{d\theta}, \tag{4.3}$$

where the first term on the right-hand side is the heat transfer to the walls, the second term computes the mechanical work, and the last term is the rate of heat release of the flame front associated with the energy difference between the two zones and the rate of consumption of the unburned mixture.

Analogously, the equation for the conservation of energy in the unburned zone becomes

$$\frac{dT_u}{d\theta} = -\frac{\dot{Q}_{wall,u}}{\Omega m(1-Y_b)c_{p,u}} + \frac{T_u}{c_{p,u}}\frac{\partial v_u}{\partial T_u}\frac{dp}{d\theta} + \frac{v_u}{c_{p,u}\Omega}\sum_{i=1}^{n}\dot{\omega}_i'''\tilde{h}_i, \tag{4.4}$$

where the first two terms have the same interpretation as in Eq. (4.3) and the last term calculates the net thermal energy released by chemical reactions.

The turbulent flame front separates the unburned and burned regions. The standard coherent flame model (CFM) is used [124]. The burning rate of the turbulent flame front is defined as

$$\frac{dm_b}{dt} = \rho_u S_l A_l \Xi f_{wall}, \tag{4.5}$$

where m_b is the mass of the burned region, ρ_u is density of the unburn mixture, S_l is the laminar flame speed, A_l is the laminar flame area, Ξ is the wrinkling factor, and f_{wall} is a factor that accounts for the flame-wall interaction.

The flame wrinkling factor is described by a physical equation which computes the progressive transition from the laminar kernel to the fully turbulent flame as

$$\frac{1}{\Xi}\frac{d\Xi}{dt} = \Gamma \frac{v'_{rms}}{l_0}\left(\frac{\Xi_{equ} - \Xi}{\Xi_{equ} - 1}\right) - \frac{2}{R_f}\frac{\rho_u}{\rho_b}(\Xi - 1)S_l. \tag{4.6}$$

This equation was derived from the flame surface density model of Zhou *et al.* [125], Demesoukas [126], and Richard *et al.* [127].

The first term in the right-hand side of Eq. (4.6) represents the wrinkling of the flame caused by all turbulent scales, while the second term represents the mean stretch due to thermal expansion of the spherical flame which destroys the turbulent wrinkling [128]. The turbulent term contains the efficiency function of the turbulent flow Γ,

$$log_{10}\Gamma = -\frac{1}{(s+0.4)}e^{-(s+0.4)} + \left(1 - e^{-(s+0.4)}\right)\left(\sigma_1\left(\frac{v'_{rms}}{S_l^0} - 0.11\right)\right), \tag{4.7}$$

$$s = log_{10}\left(\frac{l_0}{\delta_l^0}\right) \quad \text{and} \quad \sigma_1 = \frac{2}{3}\left(1 - \frac{1}{2}exp\left[-\left(\frac{v'_{rms}}{S_l^0}\right)^{1/3}\right]\right)\left(\frac{v'_{rms}}{S_l^0}\right)^{-1}.$$

The efficiency function, presented in Eq. (4.7), takes into account the laminar flame speed (S_l^0) and the laminar flame thickness (δ_l^0), as well as the effects of all turbulent scales. The strain rate of the flame front, caused by a pair of counter-rotating vortices, is integrated for all turbulent scales assuming that each scale wrinkles the flame front independently [108, 129].

The equilibrium factor,

$$\Xi_{equ} = 1 + 2\frac{v'_{rms}}{S_l}\sqrt{\frac{\mathrm{C}\ \Gamma}{\mathrm{Sc}}}, \tag{4.8}$$

is the result of the analytic solution of the steady one-dimensional flame density equation [130]. It contains the calibrating coefficient (C) of the combustion model and it is fuel dependent through the Schmidt number (Sc). The calibrating coefficient is adjusted to ensure that the simulated cylinder pressure matches the measurements for a given engine.

In this work, the laminar burning velocity in Eq. (4.5) is computed using the Metghalchi and Keck correlation for gasoline [131]. The laminar flame surface, A_l in Fig. 4.2, is based on the models by Medina and co-authors models [132].

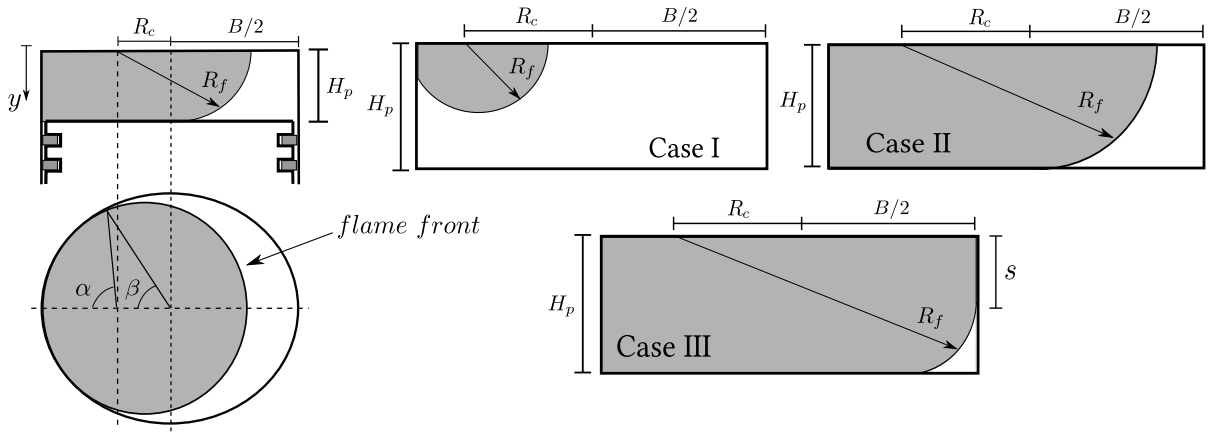

Figure 4.3: Area of the turbulent flame front. The letter B is the cylinder bore, H_p is the distance from the cylinder head to the piston, R_f defines the flame front radius, R_c is the center of the flame radius and s outlines the contact of flame with the opposite wall.

The area of the turbulent flame front is calculated geometrically as represented in Fig. 4.3. During the end of the combustion, the combustion rate decreases as the flame front interacts with the chamber walls. This is caused by the effects of friction and heat transfer in the flow and thermal boundary layers along the wall. The model developed by Aghdam *et al.* [133] and Lipatnikov and Chomiak [134] is used. The Woschni equation [135] is used to model the convection heat transfer to the walls.

The composition of the reactant mixture in the unburned zone is solved using the conservation of mass for the chemical species and a detailed chemical reaction mechanism. This reactant mixture is then consumed in the turbulent flame front and reemerges on the other side as a burned mixture. The composition of the burned mixture always follows chemical equilibrium at p and T_b. Since the species transfer across the turbulent flame front, by diffusion or as detached pockets, is neglected, the atomic population is uniform throughout the combustion chamber.

In order to follow the combustion chemistry at the end-gas, the most important reactions were sorted out in order to evaluate the main reaction paths and species in the low- and high-temperature regimes. For the selection of the important reactions, the relative sensitivity of the concentration of species i in respect to the rate constant $\dot{k}_j$ is defined as

$$S_{i,j}^{Rel} = c_i \frac{\partial \ln c_i}{\partial \ln \dot{k}_j}. \tag{4.9}$$

Then, the importance of each reaction was calculated by

$$I = \int_{t_0}^{t} S_{i,j}^{Rel}(t) dt. \tag{4.10}$$

An in-house code was built to simulate compression, combustion, and expansion in spark-ignition engines, Fig. 4.4. The simulations start at -146 CAD, at the intake valve closing, which corresponds to the BDC. In all Figures, 0 CAD corresponds to top dead center (TDC). The simulations run up to exhaust valve opening (EVO).

The code uses the Cantera library [70] for the calculation of thermodynamic properties and for the computation of reaction rates. The system of ordinary differential equations are solved by the algorithm LSODA, written by Petzold [136], Hindmarsh [137], and Brown and Hindmarsh [138]. The program was written in Python language.

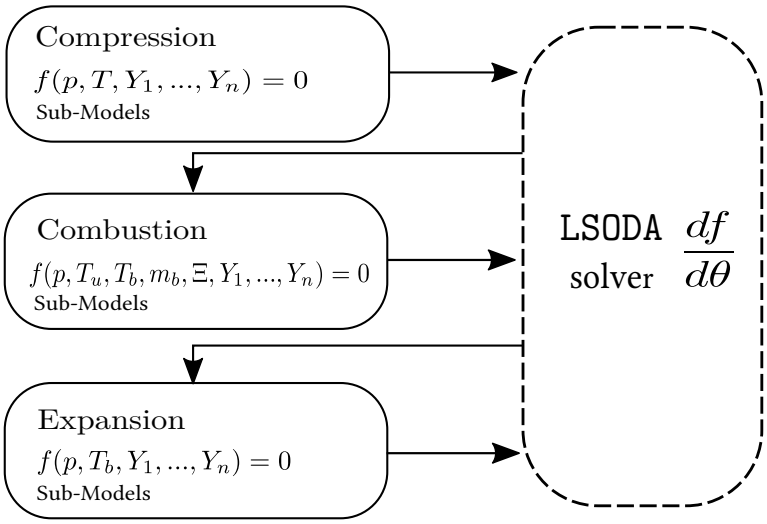

Figure 4.4: Engine solver workflow. The solver uses the LSODA capabilities for solving systems of ODEs coupled with Cantera's abilities to compute detailed thermochemical properties.

4.2.2 Measurements

A CFR engine (CFR Engines Inc.) was used for testing the engine simulation model and generating the knocking conditions. The tests were performed at Center of Applied Research at Technische Hochschule Ingolstadt, following the methodology described in [139]. The CFR engine is a stationary, constant speed, single cylinder, 4-stroke engine with a variable compression ratio. The in-cylinder pressure was measured during tests performed under standard RON conditions for spark-ignited engines (ASTM D2699), i.e., engine speed of 600 RPM, intake air temperature of 52 ^{o}C, spark timing at -13^o CAD, and a variable compression ratio. All experiments and simulations are done at stoichiometric conditions.

Figure 4.5 presents the measured pressure traces for both, normal (at compression ratio of 6.07 and 6.05) and abnormal (at compression ratio of 7.28) combustion, for PRF92 (92 % isooctane by volume) and PRF94 (94 % isooctane by volume), respectively. The pressure traces are averages over 200 cycles. The conditions for normal combustion, e.g., those shown in Fig. 4.5, were defined as the limiting conditions for the onset of knocking.

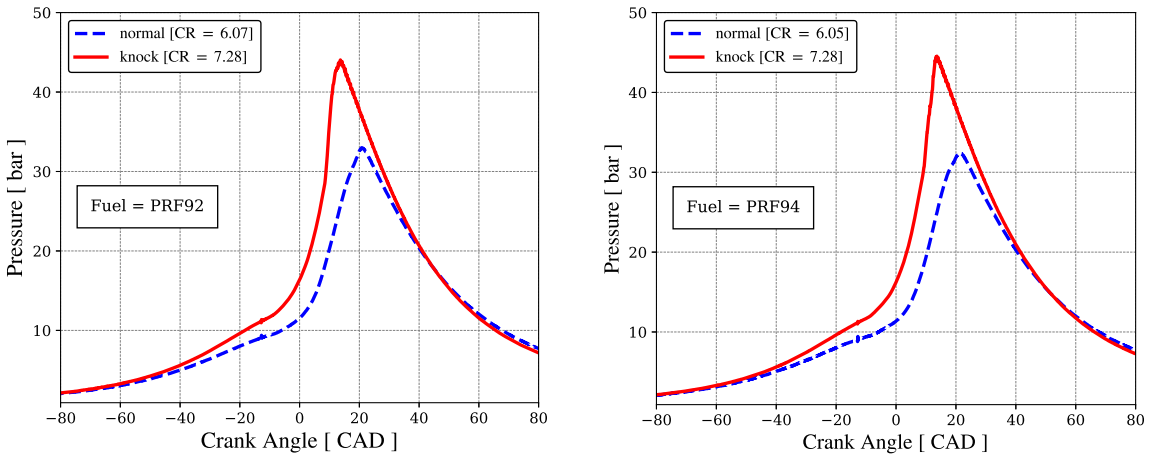

(a) **(b)**

Figure 4.5: In-cylinder mean pressure traces measured in CFR engine for normal and abnormal combustion, (a) for PRF92 and (b) for PRF94.

4.3 RESULTS AND DISCUSSIONS

First, the selection of a suitable chemical kinetics mechanism is presented. Then, the results of the engine model are compared to the measurements to ascertain its validity for this analysis. The chemical kinetics mechanisms are further analyzed in respect to the results they provide for the end-gas. The role of the first-stage ignition is analyzed and finally, a sensitivity analysis provides the main reactions and species leading to the first-stage ignition.

4.3.1 Chemical kinetics mechanisms

Table 4.1 presents the five reduced chemical kinetics mechanisms used in this study to model the combustion of iso-octane/n-heptane mixtures PRF with air. They were tested by comparing their capabilities of detecting the onset of knocking in the standard CFR engine. Reduced mechanisms were used manly due to the need to reduce the computational time, while still allowing for the inclusion of the most important chemical kinetics paths.

Figure 4.6 presents the ignition delay time curves calculated for PRF95, at $\phi = 1$, and pressures typical of engine combustion, using the mechanisms described in Table 4.1. The predictions are compared to the shock tube measurements performed by AlAbbad *et al.* [53]. Here, a simple homogeneous, adiabatic, and isochoric reactor was used to compute the IDT, as described in [140]. AlAbbad *et al.* performed a gradual pressure rise correction for the reflected shock wave, using a correction for dp_5/dt, which was converted to volume history and imposed on the homogeneous reactor calculations. Therefore, the predictions reported by [53] are slightly faster than the results predicted here. Overall, the measurements present a very weak NTC at the conditions presented.

Table 4.1: Chemical kinetics mechanisms used to model the end-gas thermal ignition.

Reference	Model	No species/reactions
Cai and Pitsch [59]	Reduced chemical mechanism of PRF mixtures	335/1613
Mehl *et al.* [141]	Reduced surrogate for gasoline	323/2469
Ranzi *et al.* [142]	Reduced surrogates for transportation fuels	156/3465
Andrae *et al.* [143]	Reduced chemical mechanism of TRF mixtures	137/640
Wang *et al.* [144]	Reduced chemical mechanism of PRF mixtures	73/448

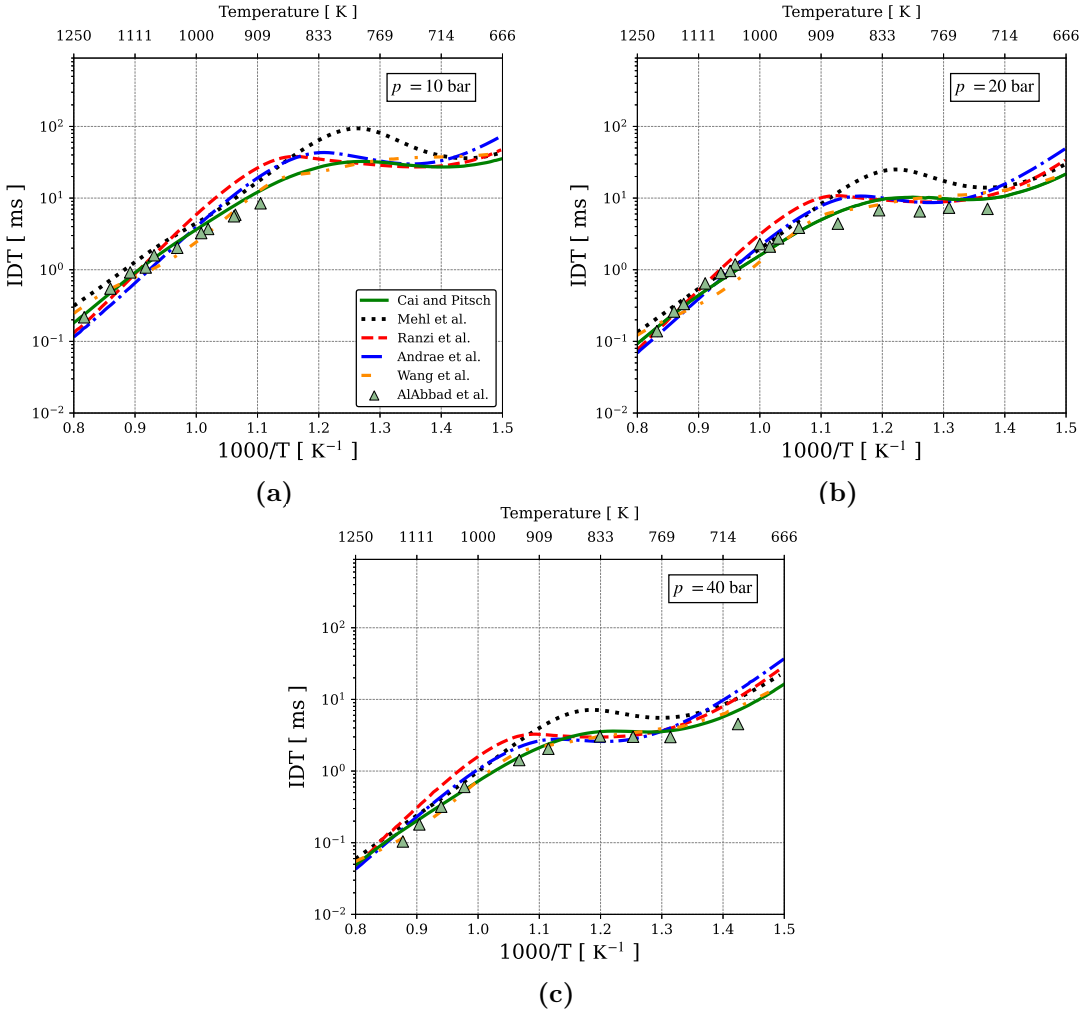

Figure 4.6: Ignition delay times for PRF95/air mixtures for $\phi = 1$ and pressures of (a) 10 bar, (b) 20 bar, and (c) 40 bar. Symbols denote the shock-tube measurements of AlAbbad *et al.* [53]. Solid lines show the predictions of the reduced chemical mechanisms.

At temperatures above 900 K, all reduced mechanisms predict the general trend of the measurements, within typical uncertainties. As the NTC region is approached, the predictions begin to diverge from the measurements and among themselves. However, most mechanisms, except Mehl *et al.*, that overshoots the IDT in the NTC region, are able to predict the temperature range of NTC and the peak IDT. We note that, while Wang *et al.* presents a reasonable prediction of the measurements, it does not produce an NTC region. At temperatures below 700 K, there are fewer measurements and the measurement uncertainty increases, preventing a fair comparison with the predictions. Overall, all mechanisms result in acceptable predictions in the high temperature range, while Cai and Pitsch and Wang *et al.* produce slightly better predictions in the intermediate and low-temperature ranges for the conditions presented.

In the sense of the Linvengood-Wu equation, the capability of predicting IDT curves enables a mechanism to become a good predictor of the onset of knocking. This aspect is explored next. First, Andrae *et al.* mechanism is used to explore the engine combustion model characteristics and results.

4.3.2 Test of the engine model

The following results present the comparison between the measured mean in-cylinder pressure and the pressure calculated by the engine model using Andrae *et al.* mechanism, at engine speed of 600 RPM and stoichiometric mixture. The model was initially tuned to reproduce the pressure trace for PRF92, at compression ratio of 6.07, and, then applied to the prediction of the results for PRF94, at compression ratio of 6.05. Figure 4.7 shows that the numerical results are in good agreement with the measurements in the CFR engine.

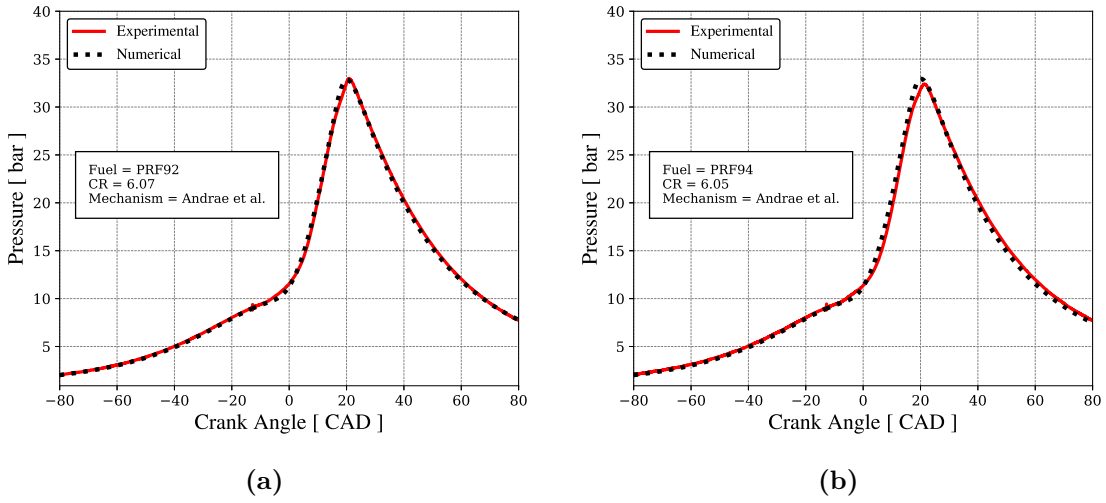

Figure 4.7: Comparison between the cylinder pressure measured in the CFR engine and the pressure predicted by the numerical model using Andrae *et al.* mechanism for normal combustion: (a) for PRF92 and (b) for PRF94.

Figure 4.8a presents the behavior of the equilibrium wrinkling factor (Ξ_{eq}) and the wrinkling factor, as affected by the wall (Ξ). The wrinkling factor starts at unit, increases as turbulence develops, and then decreases to zero as the flame reaches the cylinder wall. Fig. 4.8b presents the mass fraction of the burned mixture. The burned mass fraction undergoes three phases: the first, when reactants are consumed at a slower rate, the second, when the flame enters into a steady propagation regime and, the third, when the flame reaches the wall and extinguishes.

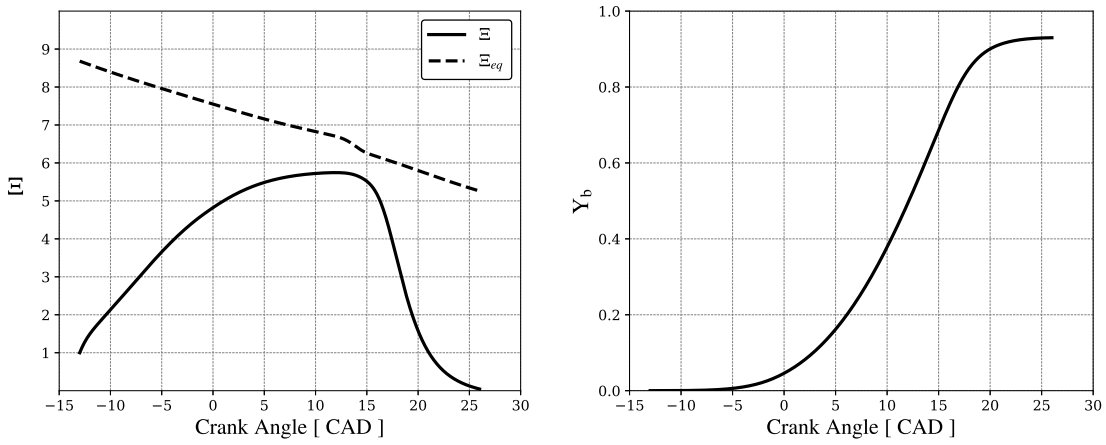

Figure 4.8: Submodels behavior with PRF92, Andrae *et al.* chemical mechanism and CR=6.07, (a) wrinkling factor and (b) mass fraction burned.

It is concluded that the model provides a reasonable reproduction of the flame propagation and the combined effects of the states of the burned and unburned fractions on the transient pressure and temperature. While several error compensation trade-offs may be present in the results of the model, it is possible to assume that the spatial average state of the end-gas is reasonably well predicted. Therefore, the predictive capability of the engine model is considered adequate for the purposes of this work.

4.3.3 Analysis of the onset of knocking

Using the model tuned to the measurements for PRF92 and tested against the measurements for PRF94 under normal combustion, the models of Andrae *et al.* and Wang *et al.* were applied to the simulations for PRF92 and PRF94 at the compression ratios considered to be at the edge of knocking in the CFR measurements (CR = 7.28). The air-fuel mixture is stoichiometric and the engine speed is kept at 600 RPM.

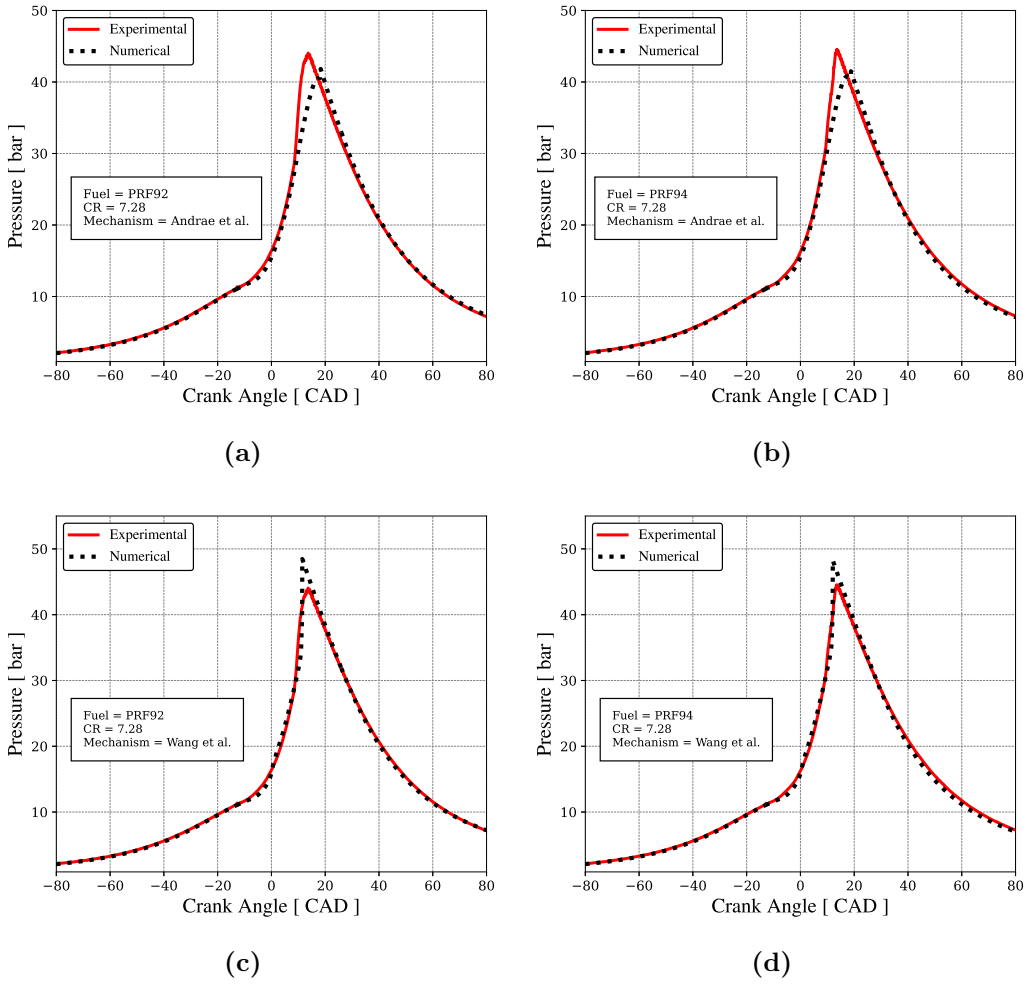

Figure 4.9: Comparison between the cylinder pressure measured in the CFR engine and the pressure predicted by the numerical model using Andrae *et al.* and Wang *et al.* mechanisms at conditions on the onset of knocking: (a) PRF92 with Andrae *et al.*, (b) PRF94 with Andrae *et al.*, (c) PRF92 with Wang *et al.*, and (d) PRF94 with Wang *et al.* mechanisms.

Figures 4.9a and 4.9b present the comparison of the measured pressure traces with the predictions using Andrae *et al.* mechanism. The model identified the occurrence of autoignition for both fuels, but with a smaller pressure increase and maximum pressure than the measurements. It also captured the crank angle where the inflection in the measured pressure trace occurs (at about -8 CAD). Figures 4.9c and 4.9d present the results calculated using Wang *et al.* mechanism. This mechanism captures both, the crank angle where the autoignition events start, and the rate of pressure increase. There is a maximum pressure overshoot of 9.3 % for PRF92 and 8.0 % for PRF94.

Since all simulations have the same thermodynamic condition at the spark ($\theta_{SI} = -13$ CAD), the temperature evolution of the unburned mixture depends on the combined effects of the piston expansion work, the compression work caused by the flame propagation, the heat release rate from the chemical reactions, and the heat loss to the walls. The end-gas temperature is presented on Figure 4.10, for all mechanisms listed on Table 4.1, for PRF94,

at compression ratios of 6.05 and 7.28, and engine speed of 600 RPM.

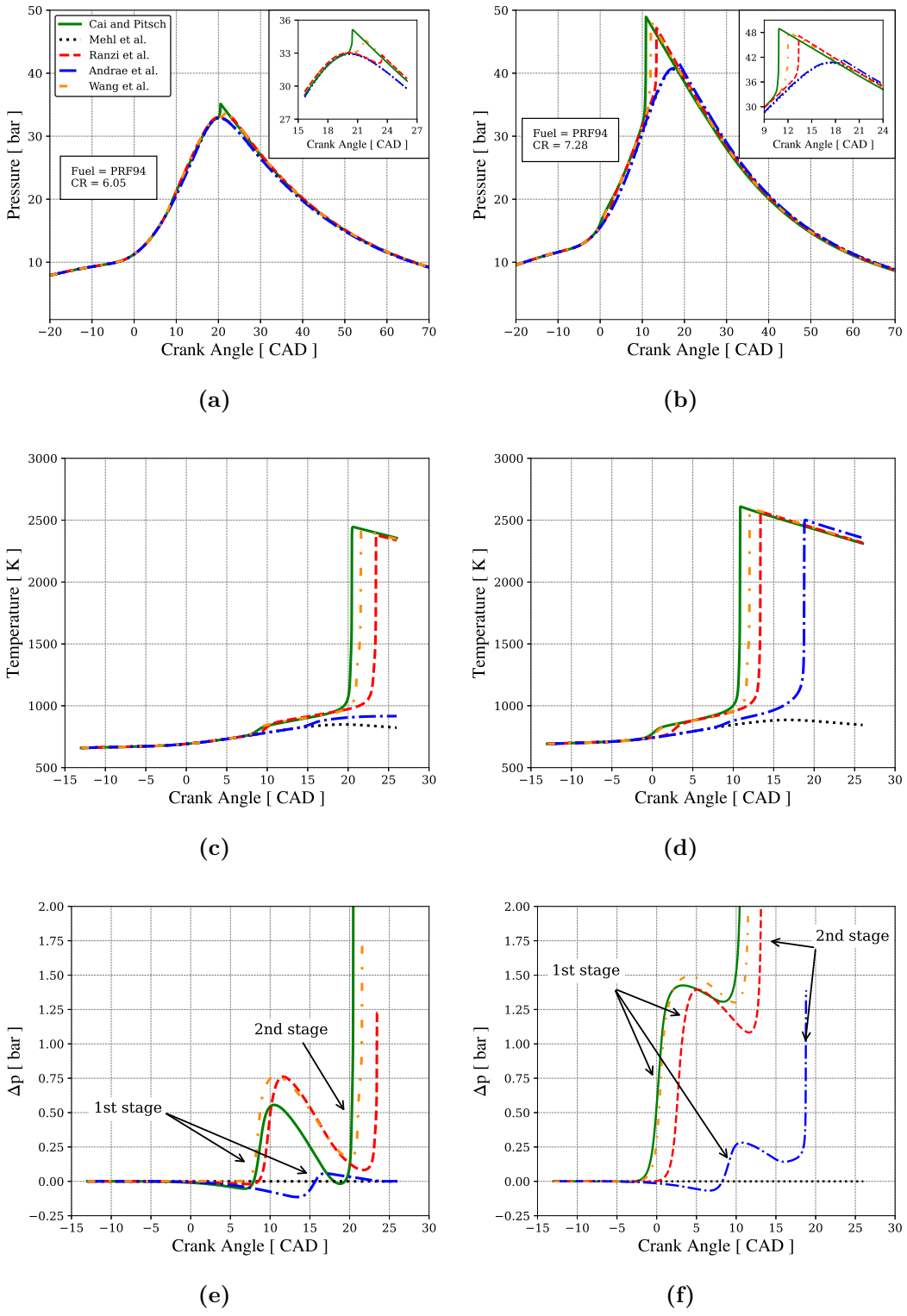

Figure 4.10: Comparison of the results of the numerical model, at two compression ratios and engine speed of 600 rpm, using different chemical kinetics mechanisms: In-cylinder pressure for (a) CR = 6.05 and (b) CR = 7.28, End-gas temperature for (c) CR = 6.05, and (d) CR = 7.28, and Difference of the pressure traces predicted for conditions that lead to knocking and the pressure traces at the same conditions, but with the end-gas chemical kinetics turned off, at (e) CR = 6.05 and (f) CR = 7.28.

Table 4.2: Summary of the timing and properties at the first and second-stage ignition at CR = 6.05 and CR = 7.28, calculated by the chemical kinetics mechanism by Wang *et al.*, at engine speed 600 RPM ($\vartheta = \vartheta_{1st} + \vartheta_{2nd}$).

	at $\theta_{SI} = -13$ CAD		first-stage ignition				second-stage ignition				
CR	p,	T,	θ_{1st},	T_u,	p,	ϑ_{1st},	θ_{2nd},	T_u,	p,	ϑ_{2nd},	ϑ,
–	bar	K	CAD	K	bar	CAD	CAD	K	bar	CAD	CAD
6.05	8.4	663	8.6	750	~ 19	21.6	21.8	~ 1000	~ 33	13.4	35.0
7.28	10.8	708	0.6	750	~ 16	13.6	11.5	~ 1000	~ 34	11.5	25.1

Figure 4.10a presents the pressure traces for the limiting condition when knocking is not detected in the measurements. Figure 4.10c presents the evolution of the unburned mixture temperature as predicted by the mechanisms from Table 4.1. In the range of crank angle between 5 CAD and 20 CAD, all mechanisms, except Mehl *et al.*, show first-stage ignition. However, only the mechanisms by Wang *et al.*, Ranzi *et al.*, and Cai and Pitsch resulted in second-stage ignition (autoignition of the end-gas). This ranking is not obvious when observing solely the IDT curves predicted by the mechanisms, as in Fig. 4.6. One might argue that the mechanism by Mehl *et al.* present the largest ignition delay time in the NTC region, which would be the reason why it does lead to ignition in the present situation. However, a similar analysis is not as well easily applied for the remaining mechanisms. In fact, the autoignition in Fig. 4.10 comes from the dynamic coupling of the characteristic engine and reaction times. This behavior becomes more pronounced when the compression ratio is increased to 7.28, as shown in Figs. 4.10c and 4.10d. In this situation, the mechanism by Andrae *et al.* also undergoes autoigniton of the end-gas. Reactivity increases in the order Cai and Pitsch, Wang *et al.*, Ranzi *et al.*, and Andrae *et al.* and the reason for this ranking is still not clear. If these different mechanisms would represent different fuels, the reason for their ranking would also be not clear as well.

In Fig. 4.10c and 4.10d we also observe that, although the first-stage ignition occurs earlier for the higher compression ratio, the second-stage ignition occurs approximately at 1000 K, 33 bar. If we go back to Fig. 4.6, we notice that at 1000 K, 30 bar, the ignition delay time increases in the order Wang *et al.*, Cai and Pitsch, Mehl *et al.*, Andrae *et al.*, and Ranzi *et al.*, a classification that underestimates the fact that Ranzi *et al.* mechanism results in autoignition on Fig. 4.10b, while Mehl *et al.* does not. This reactivity order is more closely followed by the order of IDT in the low temperature range of Fig. 4.6. Therefore, it seems that the end-gas ignition is more closely dictated by the occurrence of the first-stage ignition, while the second-stage ignition occurs at a fixed crank-angle interval, or at a fixed temperature from the first.

A closer look at the pressure increase also evidences the different reactivity exhibited by the different mechanisms. Figures 4.10e and 4.10f present the difference of the pressure traces predicted for conditions that lead to knocking and the pressure trace at the same base conditions, but with the end-gas chemical kinetics turned off (a frozen condition), $\Delta p = p - p_{\mathrm{CKoff}}$. We will first analyze the physical and chemical effects leading to the

first and second-stage ignitions. Table 4.2 summarizes the important characteristics of the first-stage and second-stage ignitions, as explored below. In this table, ϑ is the ignition delay expressed in crank angle degrees. It is related to the ignition delay expressed in seconds, τ, by

$$\tau = \left(\frac{\pi}{180\ \Omega}\right)\vartheta. \tag{4.11}$$

In both compression ratios shown in Figs. 4.10e and 4.10f, the spark occurs at -13 CAD. Following Table 4.2, the pressure and temperature at CR = 7.28 (Figs. 4.10c and 4.10d), at the moment of spark (θ_{SI}), are about 28 % and 7 % higher, respectively, than the pressure and temperature at CR = 6.05 (4.10a and 4.10b). Therefore, at the lower compression ratio, since p and T are smaller, the reactions leading to first-stage ignition take longer, resulting in larger ϑ_{1st}, which ends up pushing the first-stage ignition to about 10 CAD. Conversely, at CR = 7.28 the initial p and T are higher, leading to a shorter ϑ_{1st}, resulting in the first-stage ignition at about 0.6 CAD. Therefore, the initial pressure and temperature mostly determine the timing to reach the conditions for first-stage ignition. In both conditions, first-stage ignition occurs when the end gas reaches about 750 K. However, at the lower compression ratio (CR = 6.05), the first-stage ignition occurs at 19 bar, while for CR = 7.28, it occurs at 16 bar. Therefore, the higher initial values of T and p at CR = 7.28 lead to a shorter first-stage ignition delay and to first-stage ignition at a lower pressure. Therefore, the kinetics at these higher T and p develops faster, pulling the first-stage ignition closer to TDC.

The second-stage ignition (the end-gas autoignition event) occurs approximately 13.4 CAD after the first-stage ignition for CR = 6.05 and 11.5 CAD after first-stage ignition for CR = 7.28. In both cases, however, it occurs approximately at 1000 K and 33 bar (see the insets in Figs. 4.10a and 4.10c). The shorter second-stage ignition delay (ϑ_{2nd}) for higher CR is also a consequence of the initial higher T and p at θ_{SI}. During the second-stage delay, the end-gas temperature for both compression ratios is about the same, going from 800 K to 1000 K. The fact that the first-stage ignition for the higher CR occurs at a lower pressure (16 bar) does not produce a larger second-stage ignition delay for CR = 7.28 as compared to CR = 6.05. Therefore, the conditions for the second-stage ignition delay are strongly set by those during the first-stage ignition delay. Even with different initial conditions at the beginning of the second-stage delay, the ignition kinetics for both compression ratios catch up at 1000 K, 33 bar.

At figure 4.10e, we also notice a small pressure difference decrease after TDC, but before first-stage ignition at CR = 6.05, for the mechanisms of Cai and Pitsch, Ranzi *et al.*, and Andrae *et al.*. For these mechanisms, the pressure developed when the end-gas chemical kinetics is on is smaller than the pressure developed when the end-gas chemical kinetics is off during the expansion period. To explore this aspect, the trade-off between flame speed and heat release rate is explored.

The characteristic times for compression and expansion are determined by the engine

speed, which, thus, controls the charge compression and expansion. Besides the piston work, the temperature of the end-gas increases due to the compression work produced by the heat release from the propagation of the turbulent flame and also due to the heat release rate from the chemical reactions. The increase in end-gas temperature decreases the ignition delay time of the unburned mixture ahead of the flame front. Concurrently, the higher temperature increases the laminar flame speed in the turbulent flame, thus reducing the characteristic time to burn the end-gas. Therefore, the instant when end-gas autoignition occurs, at a given engine speed, is a consequence of the flame front propagation and the heat release in the end-gas, controlled by low-temperature kinetics.

Figure 4.11 presents the laminar flame speed at the unburned gas conditions S_l and the heat release rate HRR in the end-gas calculated for the two compression ratios using the mechanism by Andrae *et al.*.

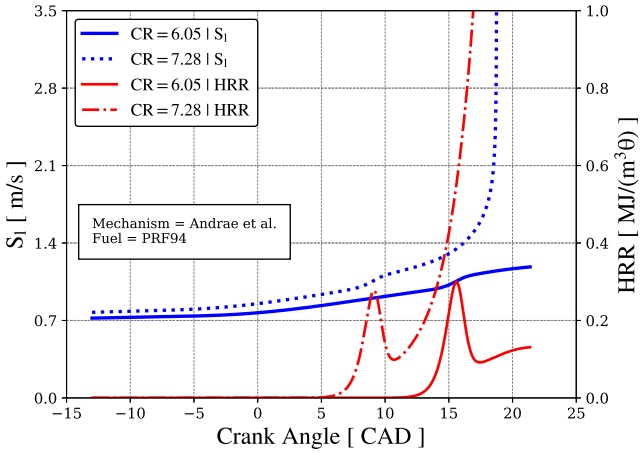

Figure 4.11: Flame front speed (blue lines) and heat release rate (red lines) using Andrae *et al.* mechanism. The solid lines are the results for CR = 6.05 and dotted lines are the results for CR = 7.28. The engine speed is 600 RPM.

At the higher compression ratio (CR = 7.28), the flame front finds a hotter end-gas. Then the flame speed is higher, leading to a smaller time for consumption of the end-gas ($\vartheta = 26.4$ CAD). However, the ignition delay, $\vartheta_{2nd} = 11.5$ CAD, is shorter, leading to autoignition. For the lower compression ratio (CR = 6.05), the flame front consumes the end-gas and reaches the wall ($\vartheta = 26.4$ CAD) before the thermal ignition occurs ($\vartheta_{2nd} = 21.8$ CAD). The heat release is negligible even at the first-stage ignition. It peaks up about 4 CAD to 8 CAD after the first-stage ignition. We also observe that the peak heat release following the first-stage ignition is approximately the same for both cases.

We observe in Fig. 4.10e a pressure difference drop from 0 to 7 CAD. From Fig. 4.11, the heat release rate during this period is negligible. From Fig. 4.10c, the end-gas temperature deviation from the result with no chemical kinetics is negligible. As a consequence, the laminar flame speed shown in Fig. 4.11 is basically the same as that for the result with no chemical kinetics. Therefore, the pressure difference reduction observed

in Fig. 4.10e is due to a change in properties of the end-gas mixture leading to an effect equivalent to a small increase of the specific heat ratio γ.

We also notice the decrease in the pressure difference in Fig. 4.10e after the first-stage ignition, which is more pronounced for CR = 6.05. When the end-gas chemical kinetics is turned off, the cylinder pressure is a result from the competition of the expansion work caused by the piston, the compression work on the end-gas caused by the flame propagation, and the heat loss to the walls (we recall that the CFR engine is motored to operate at 600 RPM). When the end-gas chemical kinetics is turned on, as shown in Fig. 4.11, a positive (exothermic) heat release rate increases after 10 CAD as a result of the chemical reactions occurring during the second-stage ignition delay. In Fig. 4.10c, we observe an increasing departure of the end-gas temperature in respect to the temperature when chemical kinetics is off. However, the heat generated by the intermediate-temperature kinetics is not enough to compensate the effects of property change, and the pressure difference drops. At CR = 7.28, the faster flame propagation increases the rate of compression work on the end-gas and the heat release rate from the end-gas chemical reactions is also larger. As a consequence, the end-gas temperature departures progressively from the baseline and,even in the presence of a larger heat loss to the wall, the pressure difference remains approximately constant.

4.3.3.1 Effect of compression ratio

Figure 4.12 presents the in-cylinder pressure calculated for CR from 5.0 to 9.0 (with 0.4 increments), at 600 RPM, using Wang *et al.* mechanism. The first-stage ignition is visible as a small pressure increase before the main end-gas autoignition. This pressure increase is clearly visible in the pressure trace for CR > 7.0.

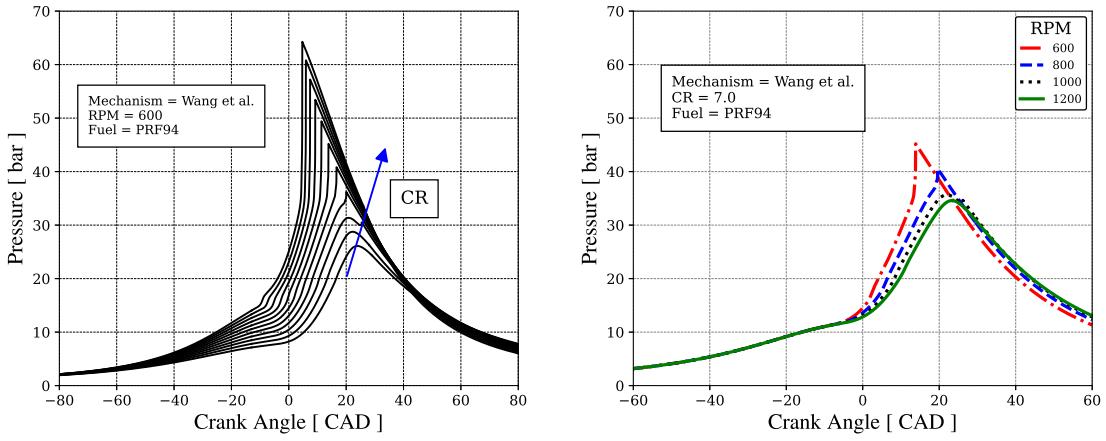

Figure 4.12: In-cylinder pressure for different compression ratios for Wang *et al.* mechanism.

As CR increases, the first-stage ignition occurs earlier, without a substantial increase in the heat release rate, as presented in Fig. 4.11. As a result of the higher CR and earlier

first-stage ignition, the second stage ignition (or main ignition event) also occurs earlier, but, increases in intensity as CR increases, as expected.

The timing for the first-stage ignition is mapped in Fig. 4.13, as a function of the compression ratio, calculated using the four different chemical kinetics mechanisms. The conditions where second-stage ignition also occurs are indicated as a plus sign. As discussed above, Fig. 4.13 shows that the 1st stage ignition occurs earlier as CR is increased, in a approximately linear dependence. The second-stage ignition occurs only for higher CR. The mechanisms by Wang *et al.*, Ranzi *et al.*, and Cai and Pitsch result in approximately the same predictions for the 1st stage ignition delay time, as noticed in Fig. 4.10.

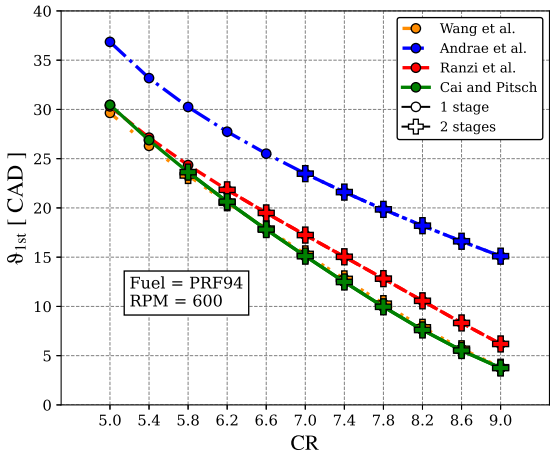

Figure 4.13: First-stage ignition delay angle ϑ_{1st} for different compression ratios, at 600 RPM. The circles indicate compression ratios when only first-stage ignition occurs, while the plus symbols indicate the compression ratios when the second stage ignition also occurs.

4.3.3.2 Effect of engine speed

Figure 4.14 presents the end-gas (a) temperature and (b) pressure as a function of time, for different speeds, at the same compression ratio of 7.0, calculated using the mechanism by Wang *et al.*. The vertical dashed lines connecting the curves to the time axis identify the spark timing at each speed. Since compression is basically isentropic, all curves present essentially the same temperature and pressure at the instant of the spark, slightly above 10 bar. The insets present the same curves, but plotted as a function of crank angle. The curve at 600 RPM is similar to the curves presented in Fig. 4.10.

Autoignition of the end-gas occurs at engine speeds below 1200 RPM. Figure 4.14a shows that the first-stage ignition occurs at about 750 K and second-stage ignition occurs when the end-gas reaches about 950 K to 1000 K. The peak end-gas temperature after autoignition is higher for the lower speed, since autoigition occurs still in the compression stroke. As the engine speed is increased, the second-stage ignition occurs earlier, but the timing in CAD is pushed forward, to conditions after TDC (see the inset in Fig. 4.14b).

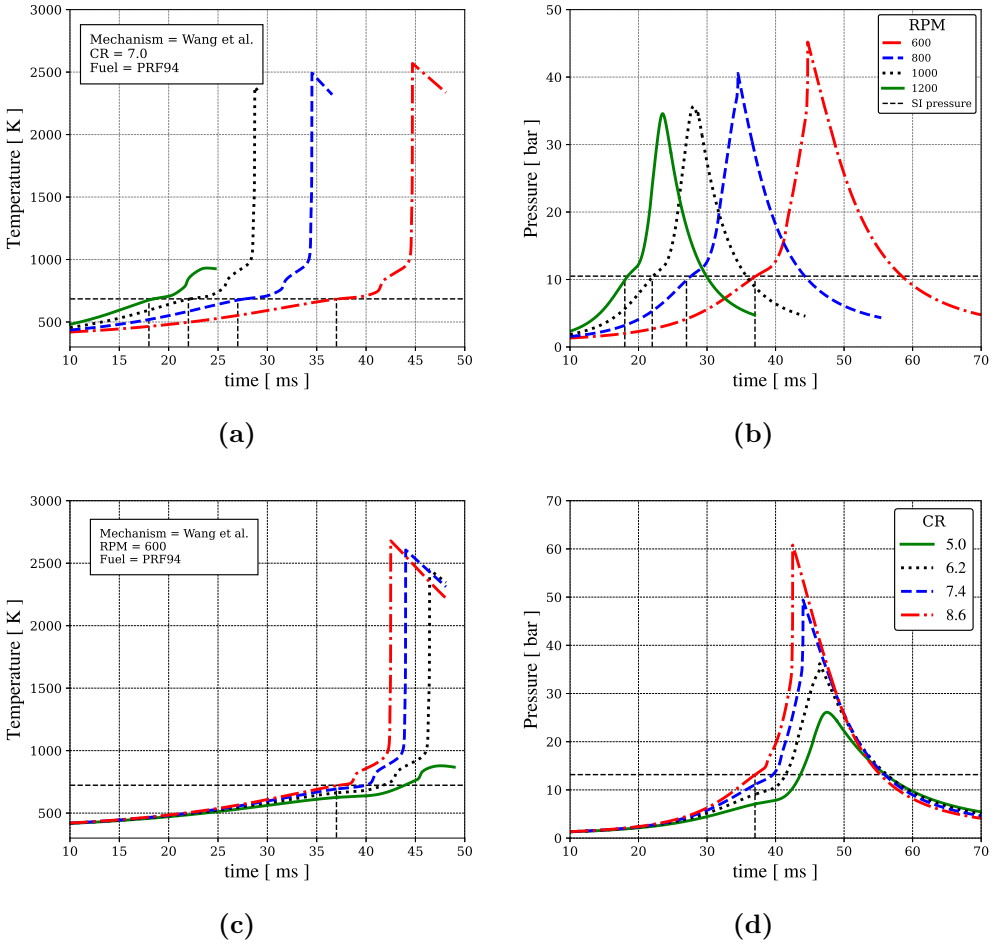

Figure 4.14: End-gas (a) Temperature and (b) Pressure as a function of time, for different engine speeds, at CR = 7.0, calculated using the mechanism by Wang *et al.* The vertical dashed lines identify the instant of the spark at each speed.

The maximum pressure and temperature at higher engine speeds reduce, until, at 1200 RPM, autoignition ceases to occur. From Fig. 4.14a, we also notice that the volume of end-gas when autoignition occurs reduce when engine speed increase. Therefore, although end-gas temperature and pressure is higher for lower speeds, it takes longer to consume the end-gas. However, the development of the combustion after autoigntiton is not the focus here and several effects are not modeled.

Figures 4.15 presents the first-stage ignition delay time, temperature and pressure as a function of the compression ratio for different engine speeds, using Wang *et al.* mechanism. The plus symbols identify those conditions leading to second-stage ignition (end-gas autoignition).

As the compression ratio increases, the temperature and pressure at the spark ignition increase. This leads to a reduction of the ignition delay time of the first-stage ignition as compression ratio increases. As the engine speed increases, the smaller elapsed time for heat transfer also increases the temperature and pressure of the end-gas at the spark ignition. Therefore, the ignition delay time for the first-stage ignition decreases as engine speed

increases. Also, as the engine speed increases, the time available for combustion decreases. Therefore, for higher speeds, the second-stage ignition only occurs at progressively higher compression ratios.

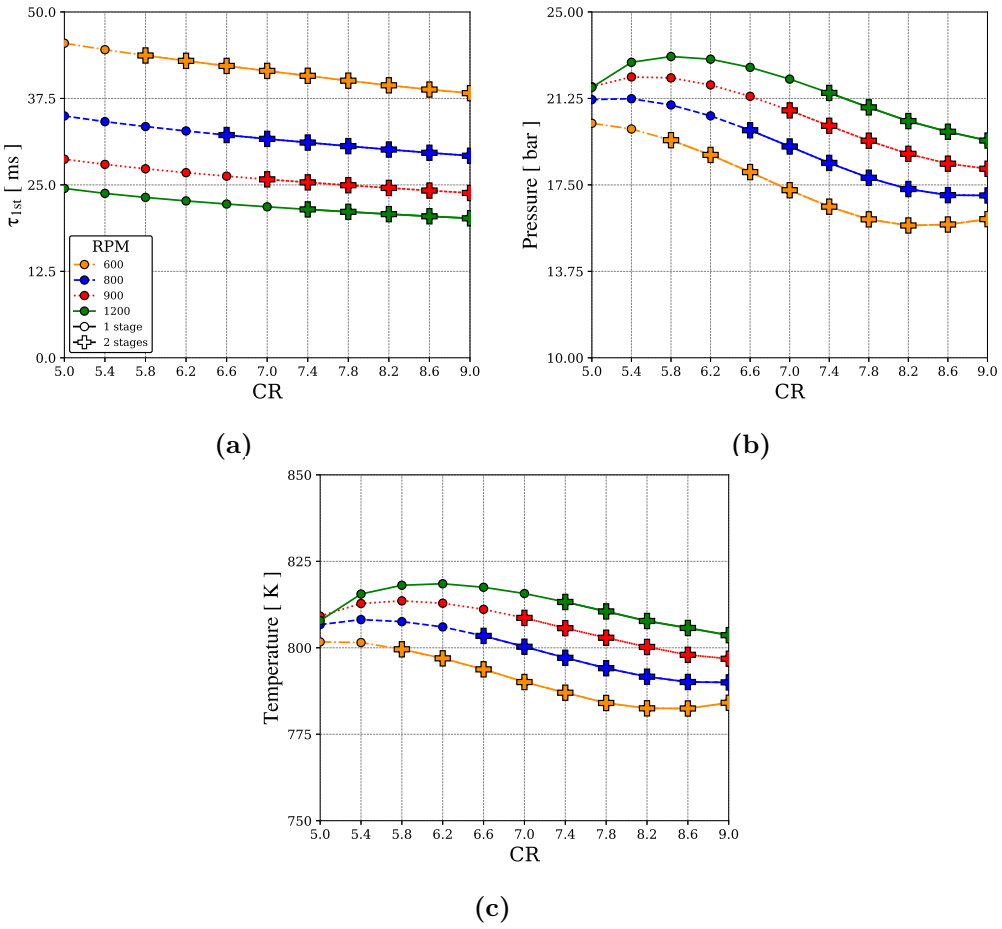

Figure 4.15: Behavior of first-stage ignition delay, pressure and temperature using Wang *et al.* chemical mechanism: (a) first-stage ignition delay, (b) pressure, and (c) temperature, for different engine speeds.

Figure 4.16 shows the ignition delay, expressed in crank angle, for the first-stage ignition (ϑ_{1st}) and end-gas autoignition ($\vartheta = \vartheta_{1st} + \vartheta_{2nd}$) as a function of compression ratio, for different engine speeds. We observe in Figure 4.16a that ϑ_{1st} decreases as the CR increases, as a result of the increased initial T and p at the moment of spark. We also realize that all conditions shown undergo first-stage ignition, however, only those conditions within the region shaded in blue present the second-stage ignition, leading to thermal ignition of the end-gas. What is interesting in this figure is the fact that the boundary of the shaded region is a horizontal line corresponding to $\vartheta_{1st} \sim 20$ CAD. Figure 4.16b presents the total ignition delay time expressed in crank angle (ϑ). As engine speed increases, the reduction in heat loss increases the overall thermal energy within the combustion chamber, leading to auto-ignition even at small compression ratios. The upper boundary at about $\vartheta \sim 40$ CAD is limited by the end of combustion for the engine model. Therefore, the results show that, for this engine, autoignition occurs when the first-stage ignition delay ϑ_{1st} is

at most 20 CAD and the time from the first-stage ignition to the second-stage ignition $\vartheta_{2nd} = \vartheta - \vartheta_{1st}$ is, at most, 20 CAD (approximately).

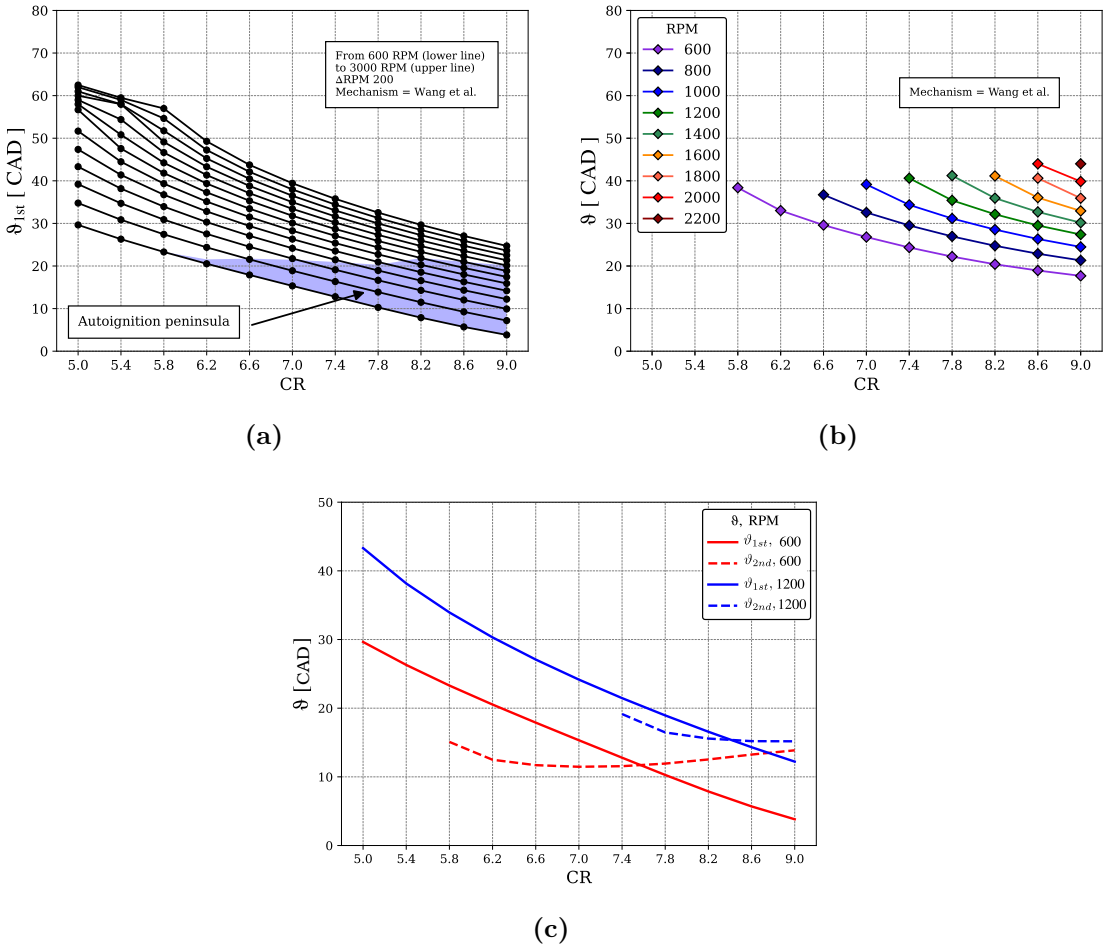

Figure 4.16: (a) 1st-stage, ϑ_{1st}, (b) eng-gas ignition delay, ϑ, and (c) comparison of first and second-stage ignition delays, ϑ_{1st} and ϑ_{2nd}, as a function of compression ratio, for different engine speeds.

This condition is easily seen by comparing the upper limit of the shaded blue area in Fig. 4.16a and the upper limit in 4.16b. Figure 4.16c compares ϑ_{1st} and ϑ_{2nd} at 600 and 1200 RPM. We notice that ϑ_{2nd} at 600 RPM varies from about 10 to 15 CAD, with a minimum in between. The existence of a local minimum is explained as follows. At low CR, the increase in CR increases the mixture energy at spark, which tends to decrease τ in the low temperature branch of the ignition delay curve. At high CR, the initial temperature moves to the NTC region of the ignition delay curve. Therefore, as CR is increased, the increase of the mixture energy at spark leads to an increase in τ. The value of CR where the ϑ_{1st} and ϑ_{2nd} curves cross each other is visible in the ignition delay time diagram in Fig. 2.1a. At higher engine speed Ω, both ϑ_{1st} and ϑ_{2nd} increase. This occurs because, although the increased internal energy decreases the ignition delay time, the increase in engine speed supersedes this effect causing an increase in the ignition delay angle. Also, the value of CR where ϑ_{1st} crosses ϑ_{2nd} moves to higher CR because the NTC region in

the ignition delay curve is moved to higher temperature at higher pressure (see Fig. 4.6).

From the analysis above, we might ask when the kinetics for the ignition delay becomes important during the engine cycle. During the engine simulation, it is relatively easy to start the kinetics calculation at any time. Defining θ_{sc} as the crank angle when the chemical kinetics is turned on, Fig. 4.17a presents the first-stage ignition delay angle calculated for different θ_{sc}, at different engine speeds. Spark ignition occurs at -13 CAD (in respect to TDC), which is the limit for the calculations. Since, at these high speeds, compression in this engine model is approximately isentropic, the vertical lines identify the end-gas temperature and pressure at -30, -70 and -110 CAD. Taking the curve for 1800 RPM, the calculated ϑ_{1st} is insensitive to the start of the end-gas chemical kinetics as long as it is turned on before -30 CAD. In this engine, the temperature and pressure at this crank angle are 653 K and 8.57 bar, respectively. These initial temperature and pressure at -30 CAD comes purely from the engine compression. Therefore, low-temperature kinetics is important even -17 CAD before the spark ignition. When the kinetics is turned after -30 CAD, the calculated ignition delay time increases in an approximate parabolic shape, in respect to the value that one would assume as correct. This behavior is reproduced by all the other engine speeds, with the same limiting crank angle of - 30 CAD. The development of the second-stage ignition is affected in the same way, as shown in Fig. 4.17b. At 2200 RPM, when the kinetics is turned on after -20 CAD, autoignition does not occur.

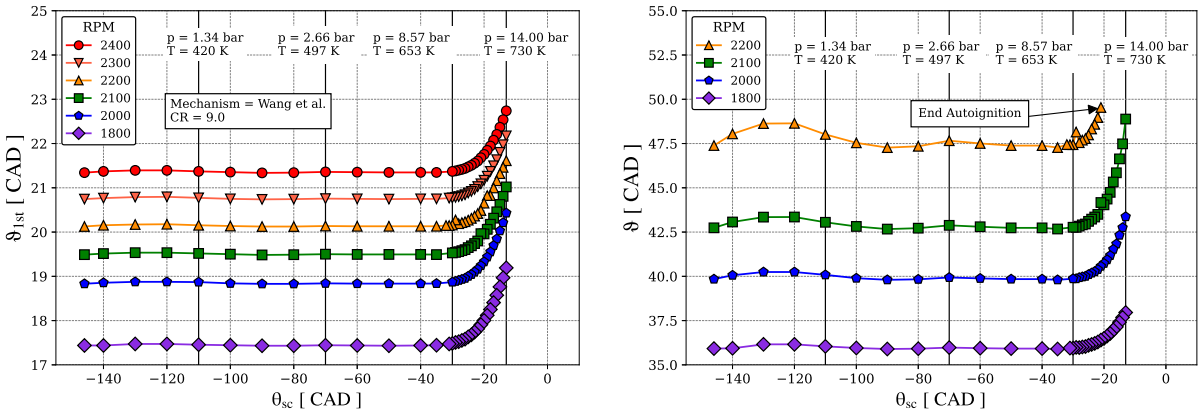

(a) **(b)**

Figure 4.17: Analysis of the autoigntion for different resident time of the unburn mixture using the Wang *et al.* mechanism with PRF94: (a) 1st stage and (b) 2nd stage.

From the results in Fig. 4.17, it appears that chemical suppression of the first-stage ignition at temperatures above 650 K contributes strongly to delaying end-gas autoignition. In terms of an IDT curve, as that shown in Fig. 2.1a, this corresponds to a measure that would increase the τ_{1st} branch without, necessarily, affecting the τ_{2nd} branch, since the latter becomes accessible only later in the cycle, when the charge no longer has elapsed time available to undergo autoignition. In Fig. 2.1a, the results predicted by Mehl *et al.* mechanism could well represent this hypothetical fuel with first-stage supression.

Figure 4.18 summarizes this conclusion. In this Figure, θ_{sc} denotes the crank angle where the chemical kinetics is turned on. θ^* is the critical crank angle where the delaying of chemical kinetics, $\theta_{sc} > \theta^*$, increases ϑ_{1st}, denoted ϑ^*_{1st} when the kinetics is delayed. The delay expressed by ϑ^*_{1st} pushes the second-stage ignition further to lower pressures in the engine expansion process. Then, the intensity of autoignition is reduced and, eventually, eliminated when ϑ^*_{1st} is sufficiently high.

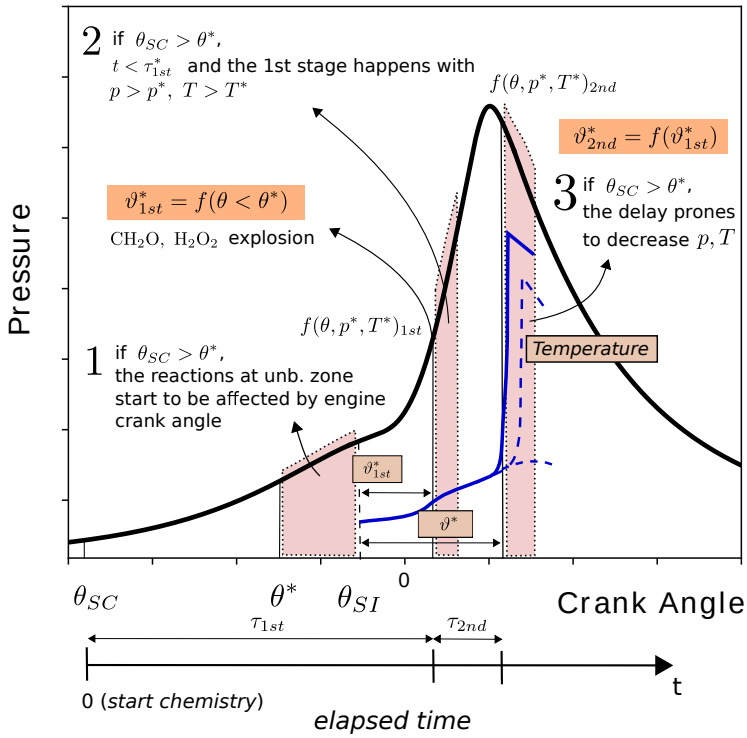

Figure 4.18: Scheme of key autoignition events during engine combustion. The θ_{sc} indicates when the chemistry is turned on, θ_{SI} is the angle of spark ignition and the marked areas present the regions where the main events occur.

4.3.4 Sensitivity analysis

The prediction of the mechanisms can be further explored by analyzing the sensitivity of the production of given species to the rate of chemical reactions. The analysis will be limited to the engine operating at CR = 7.28 and 8.3 for PRF94 fuel, since the general conclusions apply to the other mixtures. The analysis will focus the production of formaldehyde CH_2O and hydrogen peroxide H_2O_2 which are produced during first-stage ignition and are species prone to be detected by fluorescence methods.

Behavior of CH_2O and H_2O_2 as main ignition tracers: Formaldehyde and hydrogen peroxide are used as tracers for the autoignition. Figure 4.19 compares, qualitatively, the evolution of the mass fractions of CH_2O and H_2O_2 and the temperature.

The rate of formation of CH_2O and H_2O_2, using Wang *et al.*, Cai and Pitsh and Ranzi *et al.* mechanisms, Fig. 4.19b, 4.19c and 4.19d respectively, is higher around the top dead center associated with a stronger increase of heat rate release.

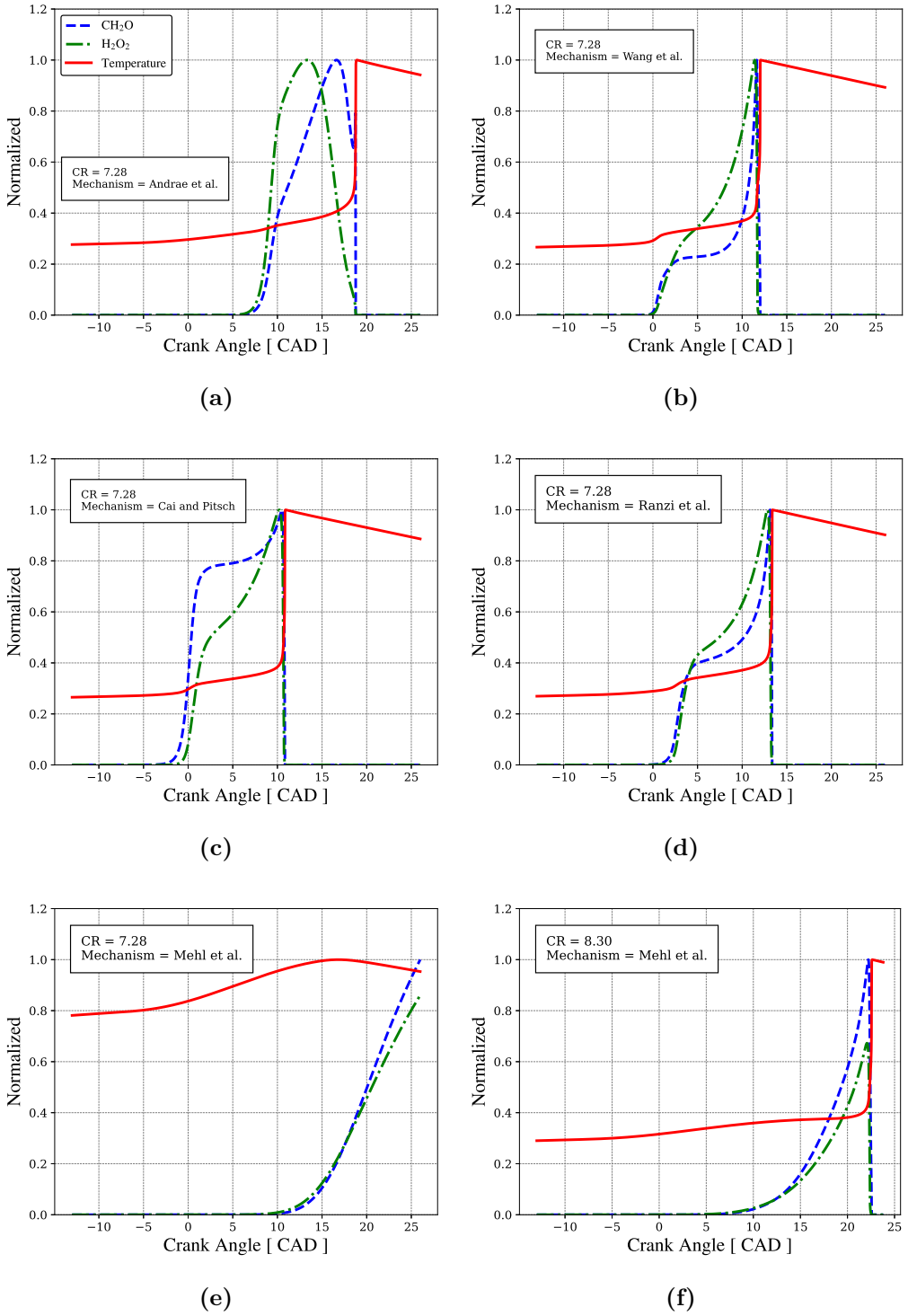

Figure 4.19: Behavior of CH_2O and H_2O_2 for the chemical mechanisms compared and their impact on temperature for PRF94: (a) Andrae *et al.*, (b) Wang *et al.*, (c) Cai and Pitsch, (d) Ranzi *et al.*, (e) Mehl *et al.* and (f) Mehl *et al.* (with different compression ratio).

The mechanism by Andrae *et al.* (Fig. 4.19a) results in a more progressive variation of CH_2O and H_2O_2 and, therefore, a lower heat release rate. Using Mehl *et al.* mechanism results in lower rates of formation of CH_2O and H_2O_2 (Fig. 4.19e). However, as CR is increased to 8.3 (Fig. 4.19f), the results approach those of the other mechanisms.

Relative sensitivity analysis: Here, the sensitivity calculated with the mechanisms of Wang *et al.* and Andrae *et al.* are presented, since they have a similar number of species and were built with similar elementary reactions (Fig. 4.20 present the results for the sensitivity for CH_2O and H_2O_2). Additional results, for other chemical mechanisms, can be seen in appendix B.

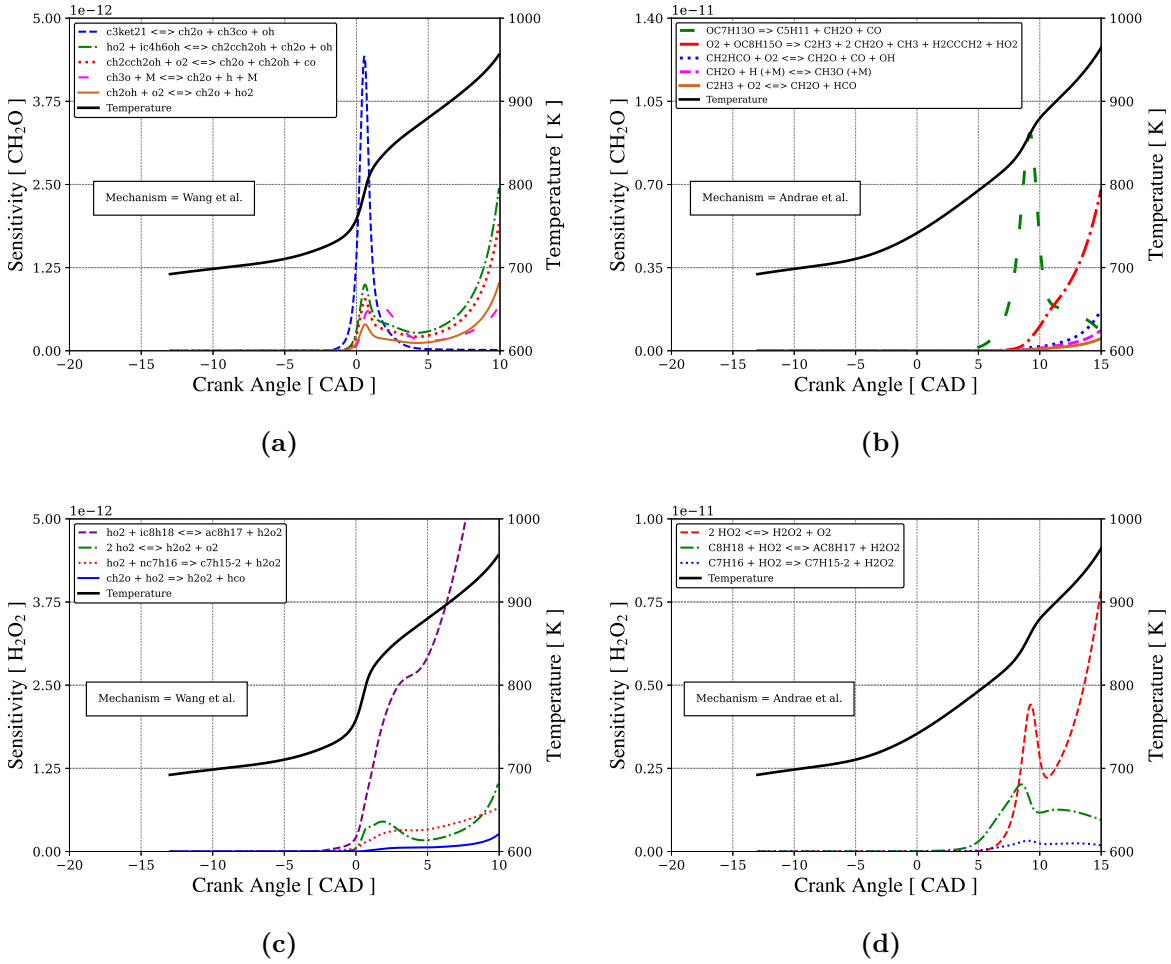

Figure 4.20: Relative sensitivity analysis for the formation of CH_2O and H_2O_2 for Wang *et al.* and Andrae *et al.* mechanisms with PRF94 and CR=7.28: (a) Wang *et al.* for CH_2O, (b) Andrae *et al.* for CH_2O, (c) Wang *et al.* for H_2O_2 (d) Andrae *et al.* for H_2O_2.

Figure 4.20a and 4.20b presents the relative sensitivity of the important reactions to the formation of CH_2O, using Wang *et al.* and Andrae *et al.* mechanisms. The most important reactions are the decomposition of propionic acid ($CH_3COCH_2OHO \rightharpoonup CH_2O + CH_3CO + OH$) in Wang *et al.* and the radical formation from the fuel in Andrae *et al.*. The third body reaction $CH_3O + M \rightleftharpoons CH_2O + H + M$ appears in both mechanisms.

Figures 4.20c and 4.20d present basicaly the same result for both mechanisms, where the formation of the hydrogen peroxide is ruled by reactions involving the fuel species. Moreover, the reaction $2HO_2 \rightleftharpoons H_2O_2 + O_2$ appear for both mechanisms.

4.4 CONCLUSIONS

In this work, the onset of knocking in a CFR engine is analyzed using a two-zone model. The Standard Coherent Flame Model is used to track the flame position and to calculate the turbulent flame speed as the combustion proceeds after the spark ignition. The speed of the turbulent flame in the flamelet regime depends on the laminar flame speed at the unburned gas temperature and pressure. The burned gas behind the flame is assumed to remain under chemical equilibrium. The unburned gas ahead of the flame is considered spatially uniform and the chemistry is modeled using a detailed chemical kinetics mechanism. The unburned gas start to change its state as soon as it is heated by the engine compression. Heat transfer to the cylinder walls is estimated using a surface-averaged convection coefficient. The transient pressure traces obtained from the simulations are compared to measurements performed on a CFR engine, fueled by PRF92 and PRF94 mixtures, under normal and knocking conditions.

The chemical kinetics mechanisms by Cai and Pitsch (335 species/1613 reactions), Mehl *et al.* (323/2469), Ranzi *et al.* (156/3465), *et al.* (137/640), and Wang *et al.* (73/448) were used. When compared to available measurements in high-pressure shock tube, all mechanisms, except Mehl *et al.*, provide adequate predictions of the ignition delay curves in the temperature and pressure range of interest. Mehl *et al.* mechanism overpredicts the IDT in the NTC region. When the mechanisms are applied to the prediction of the onset of knocking in the CFR engine, all mechanisms, except Mehl *et al.*, exhibit end-gas autoignition, however, at different crank angles than the measurements suggest.

The simulations indicate that reactivity increases in the order of Cai and Pitsch, Wang *et al.*, Ranzi *et al.*, and Andrae *et al.*, an this ordering is not clearly visible in the IDT curves. The way the mechanisms respond to the end-gas conditions depend from a dynamic coupling of the characteristic engine, flame and reaction times. The engine characteristic time is determined by the engine speed. The turbulent flame propagation speed determines the characteristic time for burning the end-gas layer. In an engine producing active power, this time is coupled to the engine characteristic time. The CFR engine, on the other hand, operates in motored mode and, therefore, both flame and engine times are decoupled. Finally, the end-gas reaction characteristic time is determined by the autoignition delay, from the chemical kinetics mechanism, under the variable temperature and pressure conditions.

The results suggest that the interaction of the chemical kinetics mechanism with the engine operation depends strongly on the timing of the first-stage ignition. The results for PRF94 indicate that the first-stage ignition occurs when the end gas reaches approximately 750 K, regardless of engine speed. The time it takes to reach that temperature changes according to the engine speed and during that time several reactions take place. However, the main chemical path leading to the first-stage ignition does not depend on the details of the composition of the mixture, but only on the overall air/fuel composition, and is

simply thermally activated. The pressure at the moment of first-stage ignition becomes just a function of the compression ratio and heat loss to the cylinder walls.

The second-stage ignition follows a similar trend and occurs when the end-gas mixture reaches 1000 K. However, the temperature evolution in the end gas departures from that of the motored engine and is affected by the reactions taking place during the second-stage ignition delay. Therefore, the second-stage ignition delay, although connected to a high-temperature ignition chemistry, depends on the nature and amount of species created during the first-stage ignition delay.

Since the first-stage ignition is key to control the onset of knocking, species that delay the NTC region to lower temperatures tend to reduce the propensity for knocking. This has been illustrated by the results obtained using the mechanism by Mehl *et al.*. This mechanism does not lead to second-stage ignition for compression ratios smaller than seven because of the over prediction of ignition delay in the NTC region. Therefore, for fuel design with the aim of increasing efficiency and energy density, it is key to develop an understanding of which species formed during the NTC region tend to delay the first-stage thermal ignition. This understanding may help to identify species to be added to fuel blends to delay the occurrence of knocking beyond the combustion duration.

Chapter 5

Flame assisted by low-temperature chemistry

The reactant mixture's thermochemical state before a deflagrative flame defines the flame speed. The cold boundary is a numerical approach to model the free propagation flame in an infinite domain at steady-state adiabatically [145] where the location of diffusivity and reactive flame structure are sufficiently far downstream of the domain inlet [29] in the sense that it does not affect the solution. It is assumed that the solution is an "observation window" moving with the flame at a speed corresponding to the inlet velocity. This implies that, between the cold boundary and the flame location, the reactant mixture has a much longer ignition delay than the fluid flow residence time. In many enginnering applications, this approximation is valid and produces accurate results. However, in others, such as internal combustion engines and gas turbines, the temperature and pressure conditions make the IDT $\sim \tau_{res}$. It may lead to premixed flames being assisted by reactions ahead of the main front affecting the burning properties. In the current literature, this phenomenon corresponds to flame propagation assisted by low-temperature chemistry [19, 41]. In practice, the physical results lead to the coupling between the autoignition process and flame propagation. Nowadays, it is a recognized concept, and many studies [22, 37, 40, 42, 56, 58, 146–164] are getting into performing simulations that can bridge the transient chemistry of ignition delay time with flame front propagation.

5.1 BACKGROUND

Traditionally, simulations involving flame speed under autoignitive conditions are performed at transient and steady states. Since the cool flames have a very limited time span, numerical simulations are a suitable tool for studying processes that occur transiently. For instance, Martz *et al.* [146] found that, in conditions above the NTC region, the reaction front is controlled by chemistry rather than transport. The temperature and pressure conditions influence the chemical time scale and heat rate release of the autoignition process. For this purpose, Pan *et al.* [37] and Faghih *et al.* [147] show that likewise to the NTC in

temperature-IDT diagrams, the burning speed also shows a non-monotonic behavior. Such property gives rise to the double flame structure, when cool and hot flames coexist [148]. In this condition, the hot flame after the cool flame has a much larger propagation speed than the single hot flame. Yiqing *et al.* [149] investigated the cool flame front formation from a hot particle ignition in quiescent and flowing stoichiometric DME/air mixtures. In addition to conclusions of former works, they found that an isolated single cool flame might be stabilized by a hot particle under certain inlet flow velocity despite its intrinsic transient behavior. The majority of works have been performed in premixed flames. However, in many devices, non-premixed or partially premixed combustion is used for reactive controlling. Yiqing *et al.* [150] explored this configuration, performing simulations focused on how the LTC affects non-premixed flames in forced ignition, taking the mixing layer as a parameter. They found that such configuration is able to form a penta-brachial flame structure consisting of a trailing warm flame and a trailing cool flame attached to the hot triple flame, in which the process is attributed to the low- and intermediate-temperature chemical reaction.

The steady-state simulations have allowed a better understanding of the double and cool flame as well as brought the possibility of comparing theoretical and experimental results with flames in LTC conditions [56,151–160]. Sankaran [161] presented a study using lean mixtures of H_2/air focused on the domain-size ahead of main front. The distance from the inflow to the main flame, called induction length, L_f, was parametrically stretched in order to result in a variable residence time for the reactant mixture. The methodology was able to provide propagation speeds ranging from diffusion-controlled flame to an increasingly spontaneous propagation front. The results highlighted that the eigenvalue solution, at autoignitive conditions, depends not only on the thermochemical state, but also the domain size. Furthermore, the study showed that even hydrogen, which is a single-stage ignition fuel, is able to be affected by domain size. Ju *et al.* [22,58] conducted simulations of one dimensional freely-propagation in near-limit steady-state cool flames. A flammability limit diagram was presented, showing that cool flames give a new set of limits for fuel with low-temperature chemistry. The existence of lean and rich cool flames extends the lean and rich flammability limits of conventional hot flames. Krisman *et al.* [40] brought the definition of reference flame speed, S_R, being the flame speed that takes into account the upstream residence time limit, in which no reaction can happen ahead of the main flame. In addition, subsequent propagation regimes have been identified (in two-stage ignition fuel) that define transitions under autoignitive conditions. Recently, Zhang and Ju [162] focused on the autoignition process for the cool and warm flames. They found that the flame speed increase with the increase of the ignition Damköhler number (Da = τ_{res}/IDT) however, differently when compared to cool and warm flames. In addition, Savard *et al.* [163] showed that in stabilized double flames at deflagration limit, the reactivity of the cool flame products is reduced, which delays the hot-temperature chemistry ignition in the cool-hot structure. This effect is responsible for pushing further

downstream the hot flame regarding the residence time-space.

5.2 MATERIALS AND METHODS

As presented in the background, some engineering devices work with high temperatures and pressures where the residence time of the reactant mixture, τ_{res}, has the same order of magnitude as the IDT. Since low-temperature chemistry can give rise to a cool front and at the same time modifies the stoichiometry and temperature of the reacting mixture ahead of the main front, this work is divided into two parts. First, analyze the effects of the low-temperature chemistry over the species, temperature, diffusivity and reactive terms of transport equations and, consequently, compute its impact on the main front flame speed. The second part turns to study the dependence on the size of hot spots where the pressure and an intermediate temperature give rise to a chemically active region. Therefore, the effects of hot spot size on the autoignition process, flame speed propagation, and structural variation according to pressure cases are investigated.

5.2.1 Configuration

In this study, an one-dimensional, isobaric, transient and steady state, propagating premixed flame is considered for the simulations of both the main flame and the cool flame front, Fig. 5.1. In order to observe the transient behavior of the HFF and the CFF from the first ignition stage to the second one, the domains were set up to have an upstream length that provides a sufficient residence time until the unburnt mixture reaches the IDT.

Steady-state simulations were performed in conditions where the low-temperature chemistry assists the main front. In the transient cases, the simulations were carried out in order to promote the flame propagation in an environment where chemical reactions of LTC are taking place at the same time as the hot front propagates. The inlet temperature, T_u, is chosen to be high enough to reach the IDT and and T_{ad} is equal to the adiabatic flame temperature as part of of the initialization procedure of the main front, Fig. 5.1a.

The cool flame front propagation was also studied. A LTC kernel is initiated as a hot spot, as it is illustrated in Fig. 5.1b. In that cases, the inlet temperature is set up to $T_{inlet} = 300$ K and the T_{hot} is at an intermediate temperature, $T_{hot} = 722$ K, which can give rise to a chemically active region.

DME/air premixed flames were solved at $\phi = 1.0$ using the reduced chemical mechanism [101] consisting of 30 species and 175 reactions, with 9 species assumed to exist under quasi-steady state. Table 5.1 and Fig. 5.2 report five cases shown in Tab. 5.1 and being marked in the IDT diagram in Fig. 5.2a. At the pressure of 8 bar, simulations were performed for different inlet temperatures that resulted in different chemical behavior, Fig. 5.2b. According to the respective pressure, $T = 722$ K is in the NTC lower base where the first and second ignition stages have equivalent duration. For P8T675 (Tab. 5.1), the first stage happens close to IDT and the low-temperature chemistry has a brief life, unlike

what occurs with P8T800 which the cold boundary has a very short duration, and the difference between IDT and the first stage is longer.

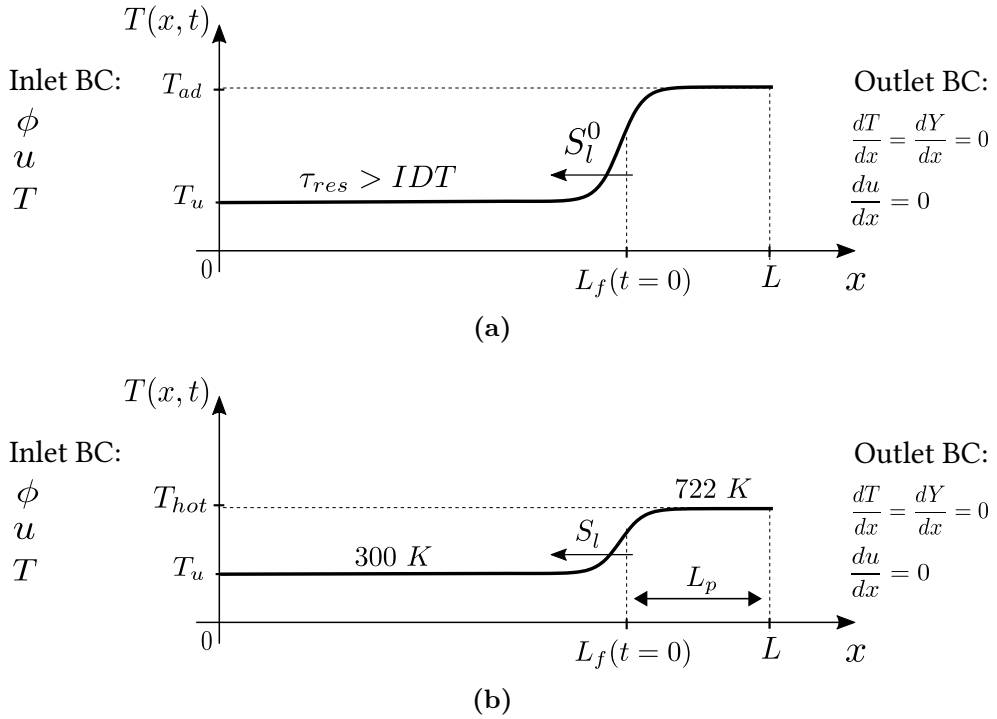

Figure 5.1: Schematic of the 1D domain for laminar flame front propagation at initial condition for (a) hot flame front for five cases in Tab. 5.1 and (b) cool flame front at P8T722, P20T722 and P40T722.

Figure 5.2c shows that beyond the ignition delay influence, the LTC duration is substantially decreased as pressure increases. In addition, the HRR is also fairly affected during the 1st and the 2nd autoignition process where the reactions become faster, increasing the HRR. In the appendix C is provided a more detailed analysis of the pressure effect over the LTC in the chemical mechanism.

In the transient analysis, the length of the domains for the pressures of 8, 20 and 40 bar extend to $L = 15, 6$ and 6 mm, respectively, and in the same way $L_f = 10, 4$ and 4 mm. Particularly in section 5.3.3.2, an investigation was conducted regarding the effect of the hot spots size, $L_p = L - L_f$, and its impact on cool flame propagation and ignition delay time. Therefore, L_p is parametrically varied in these cases.

Table 5.1: Cases for analysis and their physical parameters.

Case	p [bar]	T_{inlet} [K]	IDT [ms]	τ_{1st} [ms]	S_l^0 [m/s]
P8T675	8	675	7.95	6.38	1.13
P8T722	8	722	4.25	2.12	1.33
P8T800	8	800	5.12	0.74	1.69
P20T722	20	722	2.04	1.69	0.98
P40T722	40	722	1.64	1.52	0.77

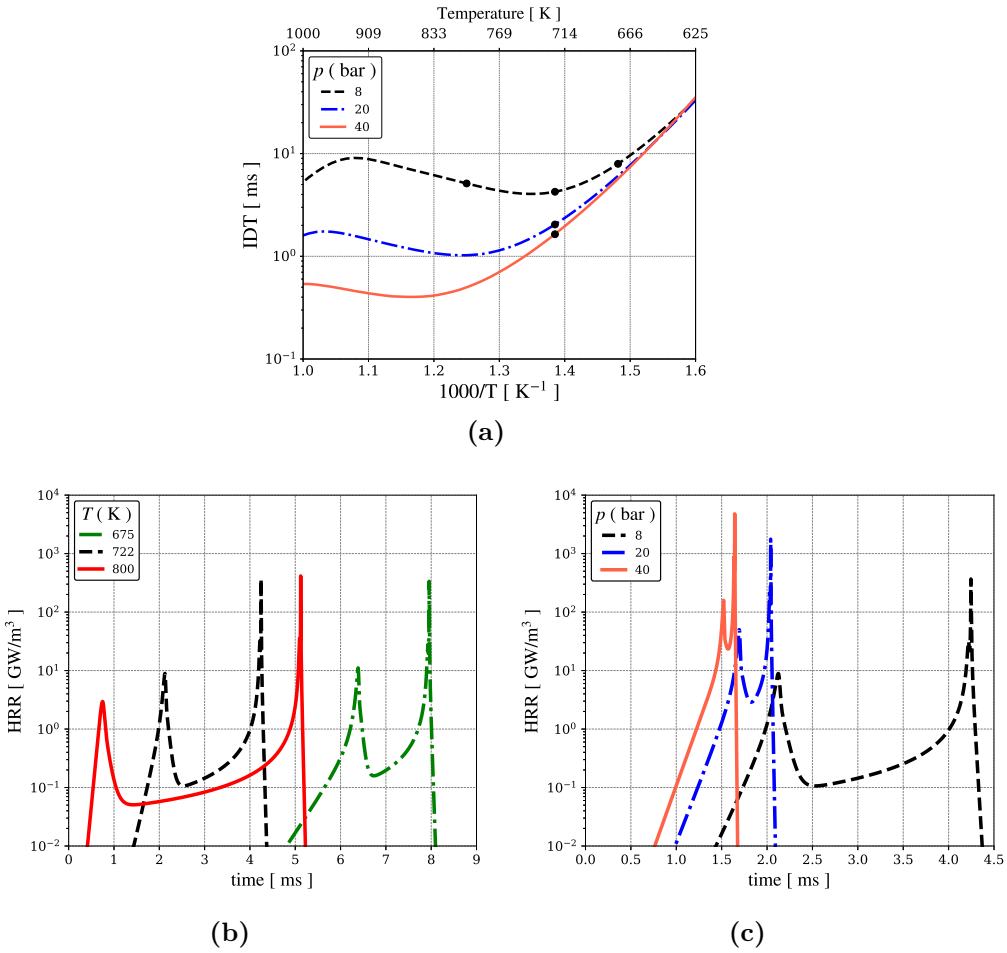

Figure 5.2: Constant pressure, 0D ignition delay time for DME/air mixture at stoichiometric condition, (a) IDT diagram with the five cases marked, (b) HRR history for ignition process at P8T675, P8T722, P8T800 and (c) at P8T722, P20T722 and P40T722.

5.2.2 Computational methods and analysis

For the steady-state solutions, Cantera was used to define the boundaries of the autoignitive process and provide the flame speed eigenvalue to compare with transient simulations. The LTC effect was assessed through two parameters, the domain induction length, L_f, and the flow residence time, τ_{res}. L_f is defined as the point of maximum heat release rate. The reacting mixture time scale or the flow residence time is represented by $\tau_{\text{res}} = \int_0^{L_f} dx/u(x)$, where $u(x)$ is the axial velocity profile in the domain [40, 163].

For the transient analysis, the simulations were performed using the direct numerical simulation code EBI-DNS (Engler-Bunte-Institute), which solves the governing equations employing the finite volume method [71, 107] and has been validated for ignition applications before [165]. The fully compressible Navier-Stokes, species, and energy equations for a reacting gas mixture are solved coupled to the chemical kinetics library Cantera [70]. Cantera's treatment of chemical reactions was implemented utilizing OpenFOAM's [73] standard capabilities of modeling non-reactive flows. A validation test case between Cantera and EBI-DNS for a steady-state flame assisted by LTC is presented in appendix

D.

The boundary conditions at the domain inlet are prescribed, and zero-gradients at the outlet for mass fractions, temperature, and velocity are set, Fig. 5.1. The partially non-reflecting boundary condition has been applied to the inlet and outlet boundaries for pressure to bypass sound waves at those boundaries. At $t = 0$, a hyperbolic tangent function to initialize the gradients that compose the flame front is utilized. The grid provides at least 20 cells inside the main flame sheet.

Two different approaches were used for the computations of the main flame front speed and the cool flame front. For the HFF, the definition of the density-weighted flame displacement speed $\tilde{S}_d = \rho S_d/\rho_u$ is used since it is not sensitive to reactions that happen ahead of the front. The CFF speed is defined, here, based on fuel consumption speed, S_c, as

$$S_c = \frac{1}{\rho_u(Y_{F,u} - Y_{F,b})} \int_0^L \dot{\omega}_F^{'''} dx.$$

Under transient conditions, the LTC may happen in an entire domain if the medium does not present transport gradients. So, in order to integrate the Eq. (2.3) only in the CFF region, it is addressed a definition that delimitates the integration boundaries. Taking the transport equation for the fuel,

$$\frac{\partial \rho Y_i}{\partial t} = -\rho u \frac{\partial Y_i}{\partial x} + \frac{\partial}{\partial x}\left(\rho D_{m,i} \frac{\partial Y_i}{\partial x}\right) + \dot{\omega}_i^{'''}, \tag{5.1}$$

the cool flame front was defined in the region where

$$\dot{m}_{diff}^{''} = \int_{-\infty}^{+\infty} \frac{\partial}{\partial x}\left(\rho D_{m,i} \frac{dY_i}{dx}\right) dx \to 0, \tag{5.2}$$

which is the same condition that delimits the regular flame region.

When the combustion process is led under autoignition conditions, the time scales may differ significantly depending on pressure and temperature, Fig. 5.2. Thereby, a comparative analysis between different thermophysical conditions becomes difficult. It is suitable to define a progress time variable, $\hat{\Delta\tau}$,

$$\hat{\Delta\tau} = \frac{(t - \tau_{1st})}{(\mathrm{IDT} - \tau_{1\mathrm{st}})}, \tag{5.3}$$

wherein is taken as reference the 1st autoignition stage, τ_{1st}, as 0 point and IDT as 1. This expression is taken to parametrically compare the cases in Table 5.1.

Any combustion process that starts from an autoignitive condition, under premixed or non-premixed mixture, is prone to ignite giving rise to a deflagrative wave in regions where the transport-reaction process is facilitated, such as local gradients and/or the temperature-stoichiometry relation. The reaction zone of a premixed flame is characterized by a balance between diffusion and reaction, wherein gradients are sufficient such that the upstream diffusive transport radicals and heat assist the unburned mixture ignition,

leading to a propagating flame. In the reaction zone of a premixed flame, convection plays a secondary role. This is in contrast to a autoingtion front, which propagates purely due to gradients of IDT and where gradients of species and temperature are insufficient for diffusion to contribute to flame propagation [40]. Therefore, the transport profiles for a premixed flame correspond to a diffusion-reaction balance, whereas an autoignition front corresponds to a convection-reaction balance. With the aim in distinguishing between flame deflagration and autoignition fronts, a volumetric transport analysis was carried out to identify the balance between diffusion-reaction and infer the effects of the LTC over the flame fronts. Here, a characteristic Damköhler number, $\mathrm{Da_E}$, was used to provide insights into the structural variation of the HFF and the CFF for the cases evaluated. It is represented by the ratio of positive and negative peaks of reaction and diffusion of energy equation, respectivetly, within the front yielding

$$\mathrm{Da_E} = \frac{max(\dot{Q}''')}{max\left(-\frac{\partial}{\partial x}\left(\lambda\frac{\partial T}{\partial x}\right)\right)}. \tag{5.4}$$

5.3 RESULTS AND DISCUSSIONS

5.3.1 Steady flame propagation assisted by LTC

The steady-state simulations address the unique solution to the flame propagation problem. In this framework, the outcomes are able to show the LTC feedback regarding the flame speed and the respective induction time for the mixture ahead of the flame front.

Figure 5.3 depicts the behavior of flame speed in a range of high inlet temperatures, Fig. 5.3a, and the temperature profiles that outcomes from four points of the curves, Fig. 5.3b.

Figure 5.3a shows the Cantera's simulation results for the unstretched laminar flame speed as a function of inlet temperature and domain length at $p = 8$ bar. The dashed line represents the S_l^0 when the cold boundary problem is not taken into account, or in other words, when the inlet mixture residence time is close to zero, referenced as $L_f = 0$. The solid and dotted lines compare the flame speed for two different main flame locations, $L_f = 1$ and 1.5 cm, respectively. From the results, it is clear that the traditionally monotonic increasing seen in dashed line is not observed for the other lines since the condition $S_l^0 \sim T^\gamma$ is not more valid under autoignitive conditions.

For the pressure of 8 bar, it is seen in Fig. 5.3a that the cold boundary is close to $T \approx 650$ K. Right after, the S_l solution results in a flow induction time, τ_{res}, that overlaps the time for the 1st autoignition stage and the curves $L_f = 1$ and 1.5 decouple from the dashed one. As the inlet temperature increases, the flame speed grows up to reach a peak, around $T \approx 730$ K, then decreases. The decay process goes by $T \approx 900$ K, followed by an exponential growth.

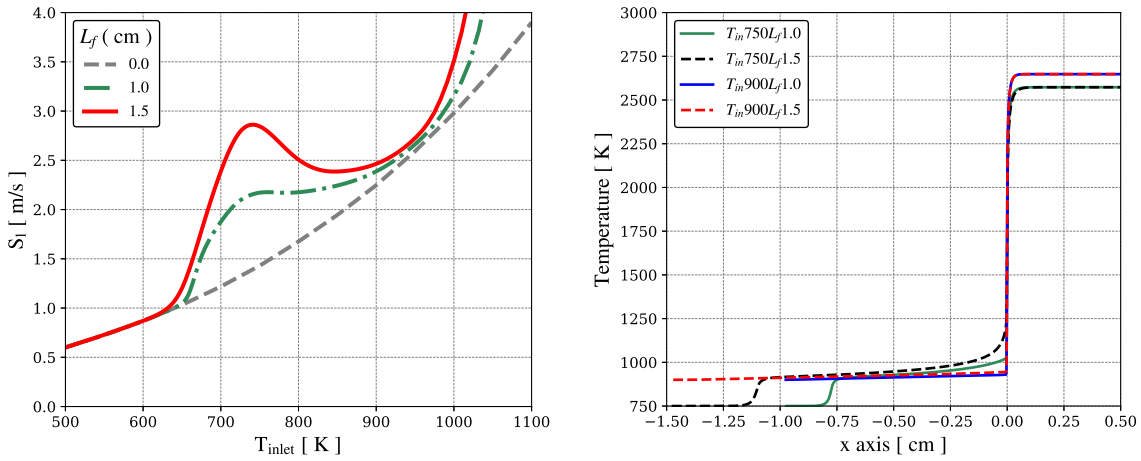

(a) **(b)**

Figure 5.3: Flame speed as function of inlet temperature and domain length at $p = 8$ bar, (a) S_l^0 regardless the domain length (gray dashed line), the S_l dependence for the flame position at $L_f = 1$ cm (green dashed-dot line) and $L_f = 1.5$ cm (red solid line) and (b) temperature profiles.

The previous narrative demonstrates the similar behavior of the S_l results with the ignition delay time diagram for fuels with NTC [37, 147]. The S_l^0 is not an unique solution as function of temperature, but also depends on flame position regard to domain entrance, $S_l = f(\phi, T_u, p, \tau_{res})$. The S_l peaks are marked by the temperature where the 1st and 2nd ignition stages have the same duration. After, when the S_l decreases, the 2nd stage is dominated over the 1st stage during the IDT. For high temperatures, $T > 900$ K, an exponential behavior occurs because the fuel does not present two autoignition stages. The reacting mixture behaves as if it had only one stage from that temperature, as seen [161]. These behaviors are illustrated by Fig. 5.3b. For the results for both flame positions $L_f = 1.0$ and 1.5 at $T_{inlet} = 750$ K, the double flame structure is made up of the CFF followed by the HFF. For $L_f = 1.5$, it is seen that the entrance temperature in the HFF is higher than the $L_f = 1.0$. It is the consequence of the greater residence time resulting in a higher S_l. For the $T_{inlet} = 900$ K, there's no formation of double flame, then the temperature profiles are flat until the main flame. The effect of the flow residence time outcomes with a small difference for S_l between $L_f = 1.0$ and 1.5.

The following two sections focus on conditions where the 1st autoignition stage acts over the main flame. An analysis is performed on the effects of the induction length and thermophysical conditions over the double flame structure, chemical kinetics, and flame speed.

5.3.1.1 Induction length and temperature effects

Figure 5.4 reports the flame solution response to the domain size for inlet temperatures of $T_{inlet} = 675$, 722 and 800 K at $p = 8$ bar, as enumerated in Table 5.1. Figure 5.4a plots the induction length, L_f, against the resulting inlet velocity, S_l, for the aforementioned

temperatures. The eigenvalue converges to $S_l = S_l^0$ with decreasing domain size [166] for the three cases. Each line becomes independent of L_f according to its autoginitive properties as is reflected in Fig. 5.4b. For $T_{inlet} = 675$ K, the autoignition effect takes longer to start acting. Taking a constant L_f, it results in a lower burning rate. For $T_{inlet} = 800$ K, the transition from a regular flame to a flame assisted by LTC happens with the flame located a few millimeters from the domain entrance since, at this temperature, the 1st stage is shorter. Traditionally, for the solutions limited by the non reactive inlet gas, the flame speed is always larger as the inlet temperature increases. However, it is observed that from $L_f = 11.5$ mm, the flame speed for $T_{inlet} = 722$ K assumes higher values than $T_{inlet} = 800$ K. Such conditions cannot be predicted with present-day combustion models.

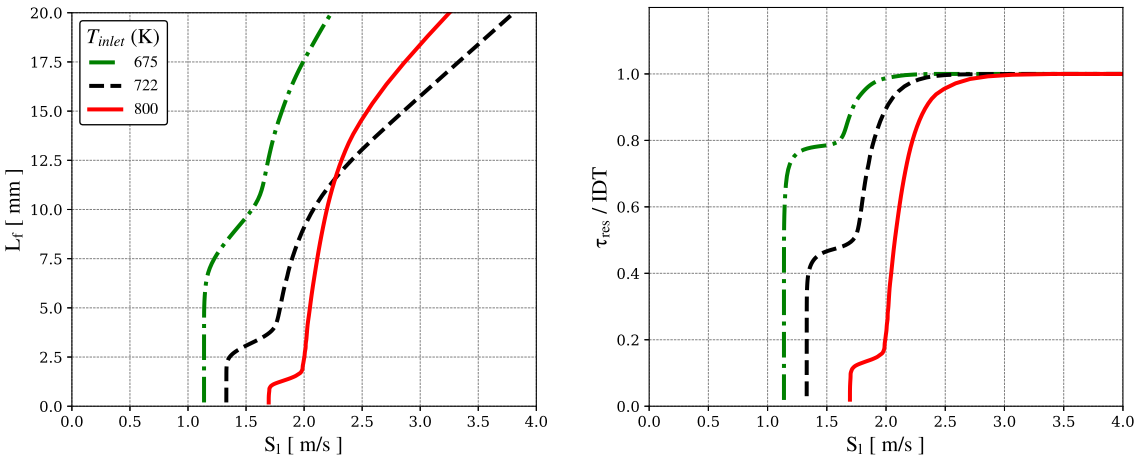

(a) **(b)**

Figure 5.4: Residence time influence on flame speed at $p = 8$ bar, (a) induction length against the flame speed and (b) normalized flow residence time against the flame speed.

Comparing the Figs. 5.4, it can be seen that there are three propagation regimes; the normal flame deflagration, the flame assisted by LTC, and an autoignitive front assisted by LTC. When the lift effect makes the flow residence time close to τ_{1st}, the LTC affects the main flame speed and the L_f. This process reflects the changing of the slopes in Figs. 5.4 which becomes more intense as the inlet temperature increases from 675 to 800 K. It is seen in Fig. 5.4a that the S_l increases during the period marked by the 1st autoignition stage. Later, when the $\tau_{res} > \tau_{1st}$, the CFF decouples from the main front giving rise to the double flame structure. In such way, the slopes in 5.4a change again. From this condition, the lift effect grows more rapidly increasing the residence time which results in an autoignitive propagation, Fig. 5.4b.

Figure 5.5 shows the temperature and fuel mass fraction profiles for a range of fluid residence times at $T_{inlet} = 722$ K centered on the maximum heat release rate. The dotted line represents the profiles where the S_l is independent of L_f, S_l^0. In Fig. 5.5a is seen that as S_l becomes greater than S_l^0, the cool flame moves away from the hot front. Furthermore,

the cool flame does not have a constant position since its induction time is fixed and the inlet speed is not, the CFF also is pushed away from the inlet boundary.

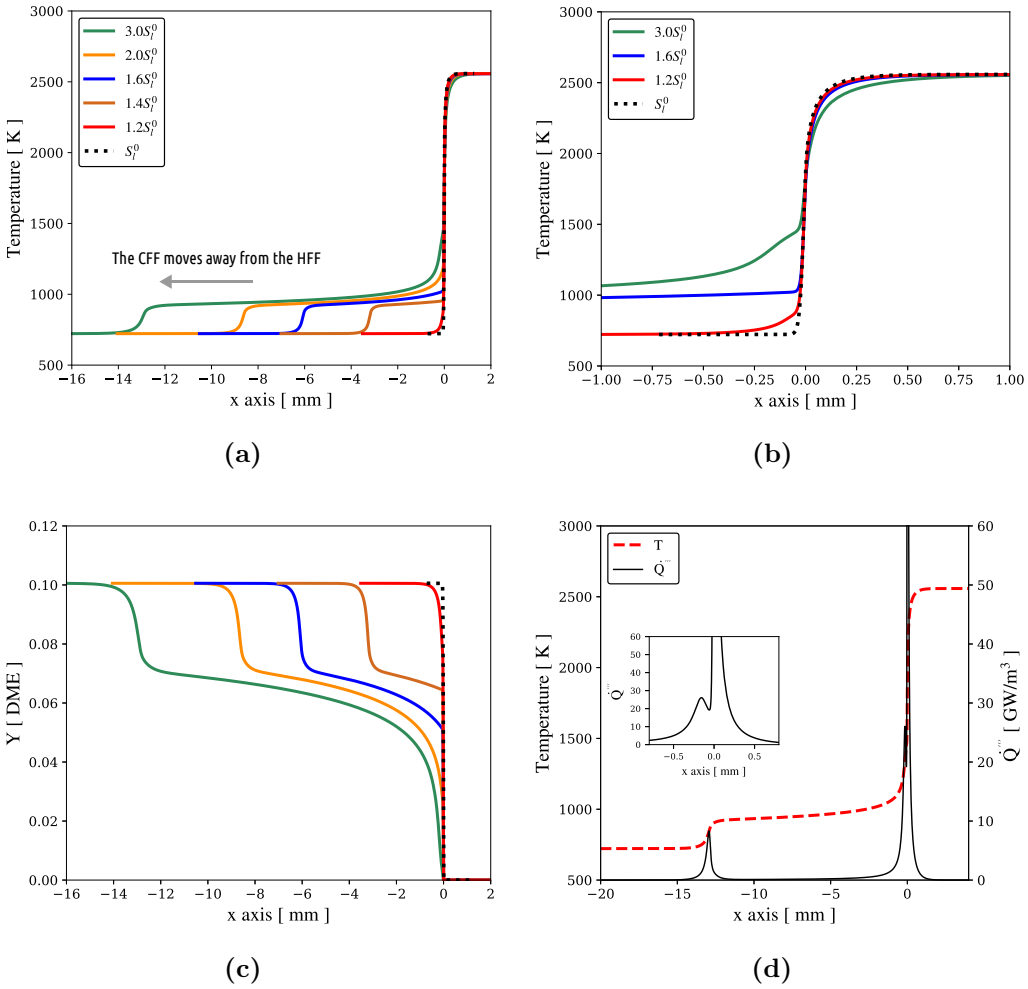

Figure 5.5: Flame profiles under a range of fluid residence times at $p = 8$ bar and $T = 722$ K, (a) double flame temperature, (b) main front temperature, (c) fuel mass fraction in the double flame and (d) temperature and HRR profile for $S_l = 3S_l^0 = 4.0$ m/s.

During this process, the intermediate temperature between the cool and hot front rises which affects the temperature profile in the main flame, Fig. 5.5b. For instance, for $S_l = 2S_l^0$ and $3S_l^0$ is observed that instead of a infinitely fast chemical kinetics adjacent to $x = 0$, the temperature profiles have a smooth gradient until the maximum HRR. It is also seen in the comparison of Fig. 5.5b where the hot fronts are magnified. Figure 5.5d shows that such effect is caused by an intermediate peack of HRR that occurs just before the maximum peak of HRR. The local fuel consumption rate is modified according to position of the CFF, Fig. 5.5c. The initial DME consumption in the cool front is quite similiar for all cases, but as the S_l increases, more fuel is consumed in the range between the CFF and HFF. In the limit case, $S_l = 3S_l^0$, it is observed that there is no fuel entering in the main front.

Figure 5.6 addresses the behavior of other species to the analysis of double flame

structure. In Fig. 5.6a, it is seen that species like CO and H_2O already turn up as sub-products of CFF. Highly oxygenated species like $CH_3OCH_2O_2$ show a peak of production and destruction in the cool front. As consequence, H_2O_2 and CH_2O have a formation jump in CFF and keep increasing in concentration up to the hot front.

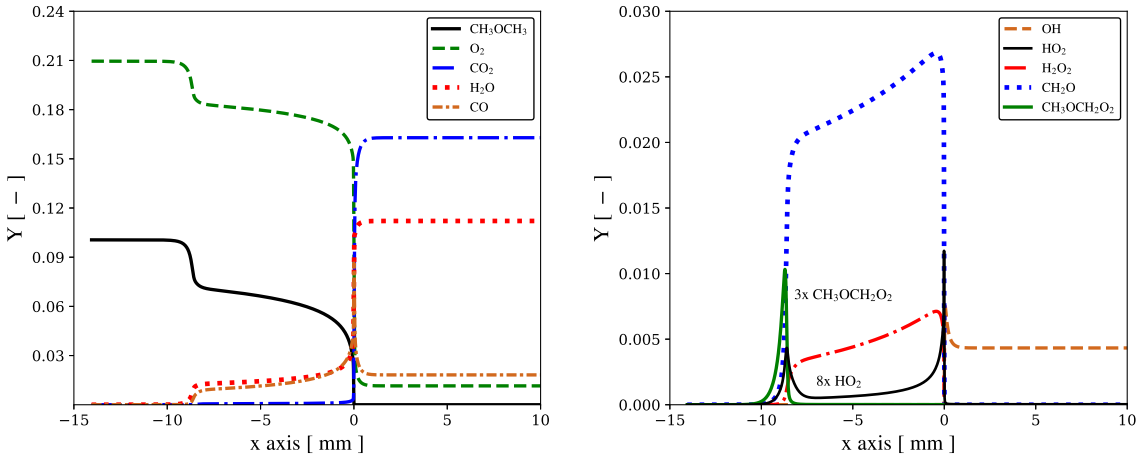

Figure 5.6: Species mass fraction profiles for P8T722 with $S_l = 2S_l^0$, (a) main species and (b) intermediate species.

A volumetric transport comparison between a regular flame and a flame in the autoignitive regime is presented in Fig. 5.7. The inlet temperature in Fig. 5.7b is substantially above 722 K, and the temperature profile is much smoother than Fig. 5.7a. It is seen that part of the energy is consumed along the double flame structure. It turns out in a thicker flame with the reaction and diffusion term weaker but with a more significant imbalance between them in which the reaction term dominates the transport process.

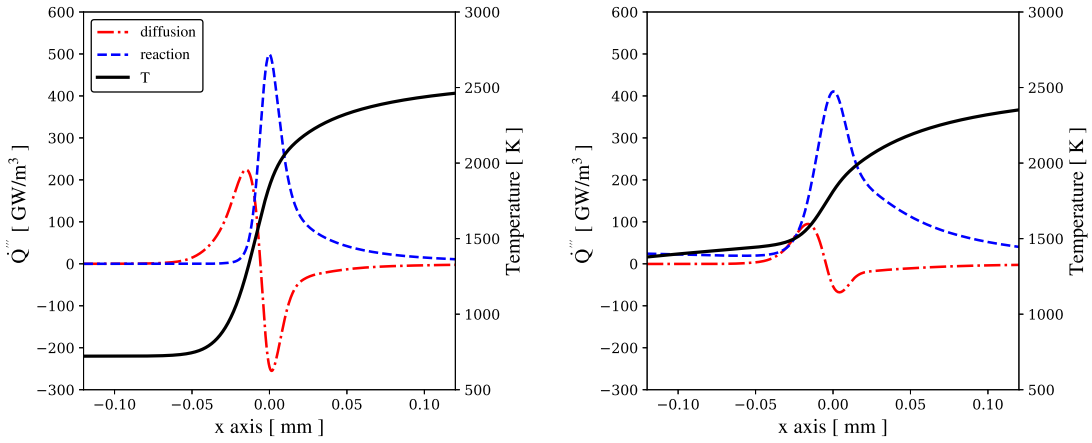

Figure 5.7: Transport budget in terms of energy for P8T722, (a) $S_l = S_l^0$ and (b) $S_l = 3S_l^0$.

The changes caused in the fuel burning rate and consequently in the entire flame dynamic occur mainly because the chemical kinetics fit into the fluid flow residence time. Figure 5.8 compares the result of a sensitivity analysis carried out in a regular flame in $S_l = S_l^0$ and a flame at $S_l = 3S_l^0$ ($L_f = 21.3$ mm).

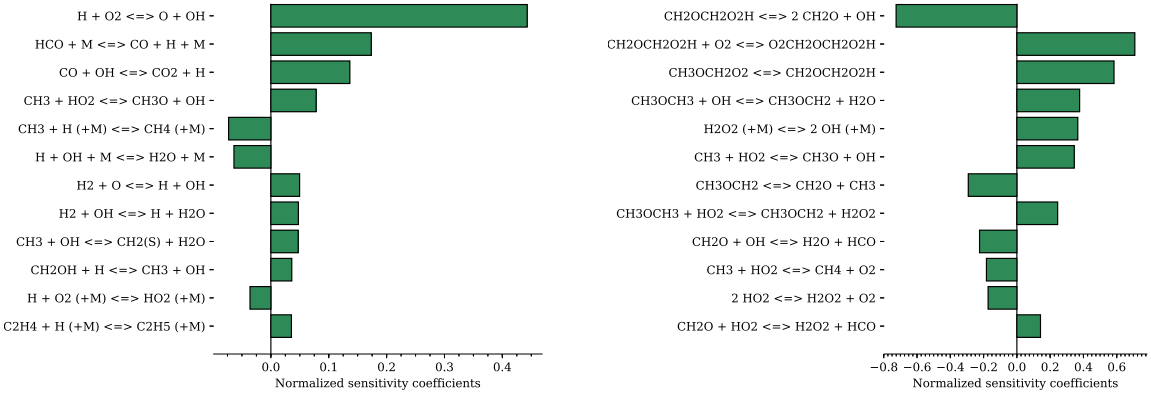

Figure 5.8: Comparison of normalized sensitivity coefficients for flames P8T722, (a) at regular flame, $S_l = S_l^0$ and (b) double flame $S_l = 3S_l^0$.

Figure 5.8a shows that as all hydrocarbons, the DME burning rate depends mainly on high temperature reactions such as the chain branching $H + O_2 \rightleftharpoons O + OH$ reaction and the termination steps like $HCO + M \rightleftharpoons CO + H + M$ and $CO + OH \rightleftharpoons CO_2 + H$. The scenario is different for the double flames in autoignitive condition. Figure 5.8b shows that the production of heavier species through reactions $CH_2OCH_2O_2H \rightleftharpoons 2CH_2O + OH$, $CH_2OCH_2O_2H2 + O_2 \rightleftharpoons O_2CH_2OCH_2O_2H$ and the isomerization $CH_3OCH_2O_2 \rightleftharpoons CH_2OCH_2O_2H$ sets a rate-limiting reaction cycle. Furthermore, it is seen unlike Fig. 5.8a, the double flame shows a dependence on the initiation reactions like $CH_3OCH_3 + OH \rightleftharpoons CH_3OCH_2 + H_2O$ and $CH_3OCH_3 + HO_2 \rightleftharpoons CH_3OCH_2 + H_2O_2$.

5.3.1.2 Pressure effect

In a regular flame, the increase in pressure negatively affects the flame speed since the diffusion coefficients decrease with pressure rises, $S_l^0 \sim p^{-\beta}$. Figure 5.9 shows that yet this effect is still present in non-regular flames, Fig. 5.9b, it addresses an additional imbalance factor between the reaction and diffusion since the pressure rising increases the HRR. Figure 5.9a reports this behavior when the flame speed is independent and dependent on L_f for pressures of $p = 8$, 20 and 40 bar at $T_{inlet} = 722$ K.

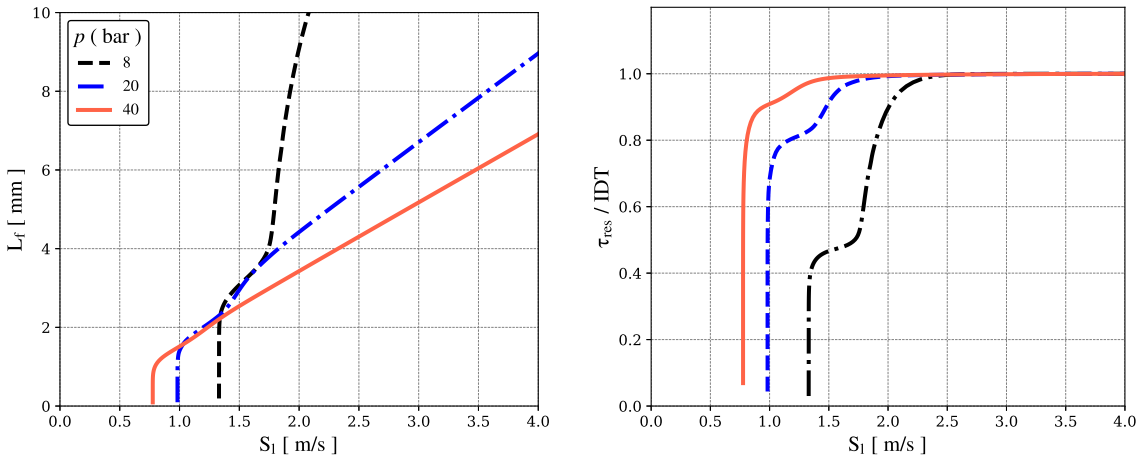

(a) **(b)**

Figure 5.9: Residence time influence on flame speed for $p = 8$, 20 and 40 bar at $T_{inlet} = 722$ K. (a) Induction length against the flame speed and (b) normalized flow residence time against the flame speed.

The increase in pressure reduces the ignition delay, so in Fig. 5.9a, the S_l transition at $p = 40$ bar starts closer to the domain entrance, followed by the case of $p = 20$ bar. On $L_f = 2.2$ mm, the flame P40T722 assumes the highest burning rate due to the advanced LTC effects. Figure 5.9b shows that at $p = 8$ bar, the 1st stage turns up close to the half of IDT, while for $p = 20$ and 40 bar, it becomes relatively longer, affecting how L_f varies with S_l. This results in different slopes from that observed in Fig. 5.4. For instance, taking P40T722, the first transition does not promote a substantial variation in S_l when the CFF is decoupling from the main front. In addition, the transition from the first to the second regime becomes smoother as pressure grows from P8T722 to P40T722.

Figures 5.10a and 5.10b compare the results for $p = 40$ bar with those of Fig. 5.5 taking into account the absolute values of S_l where they are close for both pressures ($5.4S_l^0(\text{P40}) = 3S_l^0(\text{P8}) = 4.0$ m/s, $2.6S_l^0(\text{P40}) = 1.6S_l^0(\text{P8}) = 2.6$ m/s and $2.1S_l^0(\text{P40}) = 1.2S_l^0(\text{P8}) = 1.65$ m/s). Figure 5.10a shows that the distance between the CFF and HFF decreases more than one order of magnitude from $p = 8$ to $p = 40$ bar, e.g. the curve of $5.4S_l^0$. It is attributed to the difference IDT $- \tau_{1st}$, which is much longer for P8T722. Moreover, the HRR history presented in Fig. 5.2c shows that between the two autoignition stages, the LTC is more active for P40T722 releasing heat, at least, more than two orders of magnitude than the P8T722.

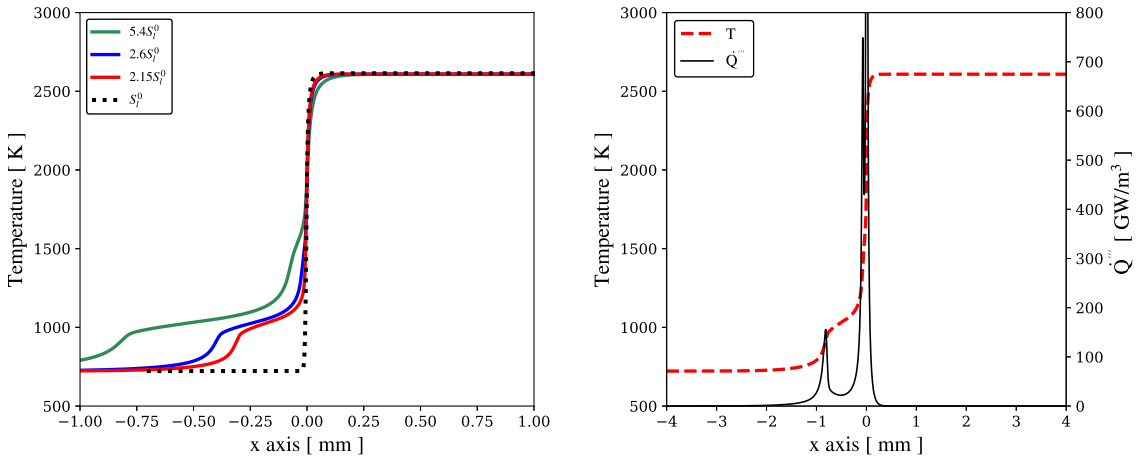

Figure 5.10: Flame profiles under a range of fluid residence time at P40T722, (a) double flame temperature and (b) main front temperature at $S_l = 5.4S_l^0$

This effect is also seen in Fig. 5.10b, the CFF's peak as well the LTC HRR have an order of magnitude greater than $p = 8$ bar, Fig. 5.5d. The kernel of these changes is found in the chemical kinetics shown Fig. 5.11. In such condition, the isomerization process $CH_3OCH_2O_2 \rightleftharpoons CH_2OCH_2O_2H$ is the dominant rate-limiting reaction. Furthermore, more reactions involving heavy and oxygenated species appear in the sensitivity analysis like $HO_2CH_2OCH \rightleftharpoons OCH_2OCHO + OH$, $O_2CH_2OCH_2O2H \rightleftharpoons HO_2CH_2OCHO + OH$ gather those seen previously as $CH_2OCH_2O_2H \rightleftharpoons 2CH_2O + OH$ and $CH_2OCH_2O_2H2 + O_2 \rightleftharpoons O_2CH_2OCH_2O_2H$.

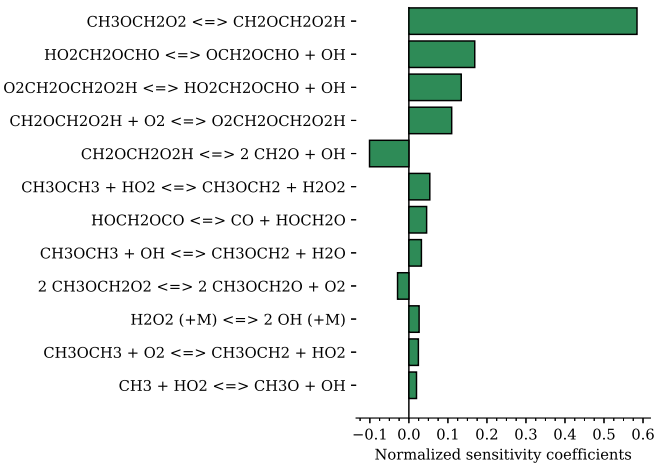

Figure 5.11: Normalized sensitivity coefficients for P40T722 at $S_l = 5.4S_l^0$.

5.3.2 Unsteady flame propagation assisted by LTC

5.3.2.1 Flow-chemistry interaction

In combustion devices, the flame interacts with the fluid flow, producing different burn regimes. Therefore, whether the double flame may exist, it is necessary to study how the flow can affect the burning rate. Figure 5.12 shows the behavior of flame speed for the HFF and CFF in a range of inlet velocities for P8T722, from the normal flame propagation to the IDT.

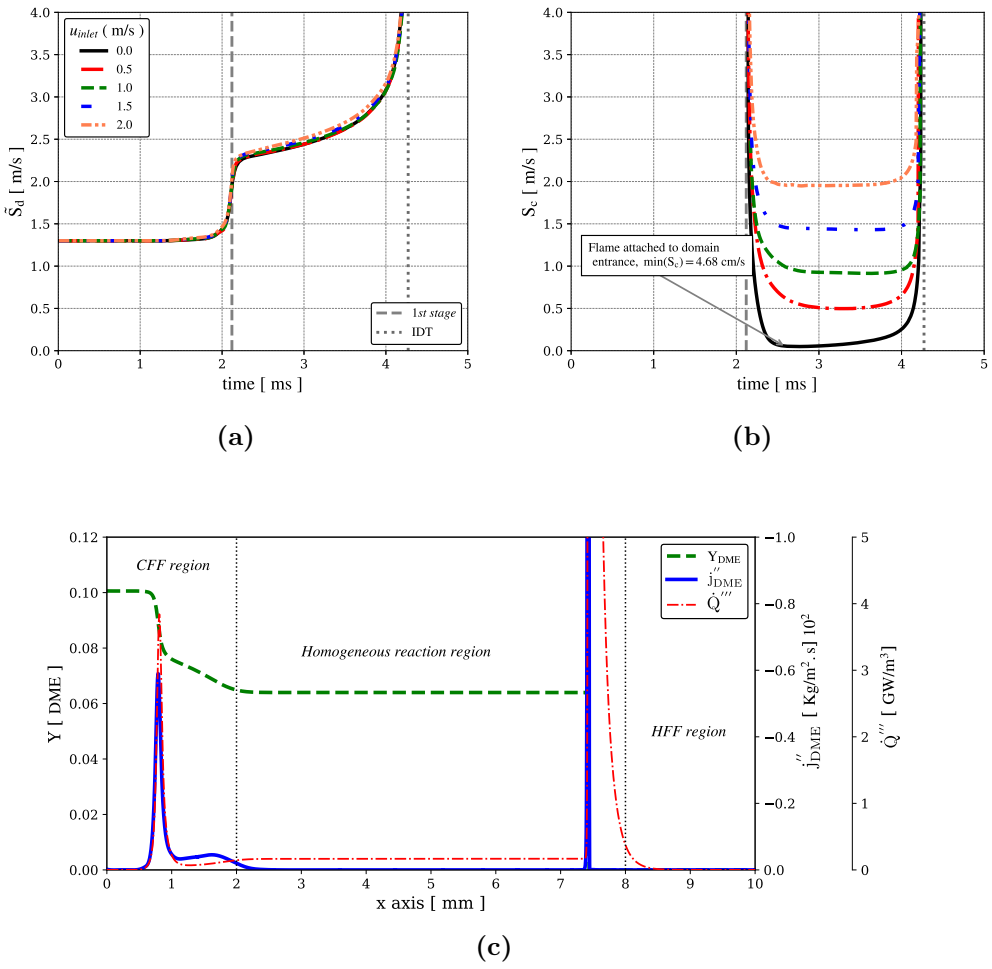

Figure 5.12: Inlet velocity effect over the burning rate for P8T722, (a) hot flame front, (b) cool flame front and (c) double flame structure at LTC half-life.

It is seen in Fig. 5.12a, the normal flame propagation followed by the 1st autoignition stage, which is the trigger to form the double flame structure. Regardless of inlet velocity, the transition process occurs similarly for all cases. From this point on, all cases follow an exponential increase in the displacement speed until the IDT. This frame is entirely different for the cool front which changes S_c as inlet velocity increases, Fig. 5.12b. Figure 5.12c shows the double flame structure in which is plotted the DME mass fraction, the HRR and the DME mass diffusion flux at the LTC half-life for $u_{inlet} = 0.50$ m/s. Three

regions can be seen: the hot flame front, the cool flame front where close the domain entrance occurs the partial DME oxidation. Between the two fronts, a homogeneous region behaves as a constant pressure reactor with no spatial gradients but heat is released as a function of time.

For the case of $u_{inlet} = 0.00$ m/s in Fig. 5.12b, the S_c curve shows a minimum value of $S_c = 4.68$ cm/s right after the τ_{1st} and then a slow growth in the oxidation rate followed by the thermal explosion when the elapsed time is on the IDT boundary. For $u_{inlet} = 0.50$ m/s, the CFF speed takes a value closer to inlet velocity at the minimum point and then the process goes on like the previous case. This characteristic in the process occurs for all cases, except that the minimum flame speed value is reached more quickly as u_{inlet} becomes higher.

Figure 5.13 presents the flame profiles regarding the different inlet velocities at the LTC half-life. In Fig. 5.13a is seen the temperature profiles, which may be observed that the hot front temperature does not suffer any effect of inlet flux except for the front position being lifted off as u_{inlet} becomes higher. However, the cool front temperature does not keep the same shape according to u_{inlet}.

For the case of $u_{inlet} = 0.00$ m/s, the cool front is anchored at $x = 0$ and temperature gradient decreases progressively until the homogeneous zone. On the other hand, for velocities different from zero, the fronts take a position proportional to the mass flux and the temperature profiles are stretched. Figure 5.13b shows the DME mass fraction and it is observed that the fuel oxidation corroborates with the behavior in temperature. However, it is seen that indeed the fuel mass fraction does not decrease downstream as the inlet velocity increases which would reflect a net gain in consumption speed. Instead, the integral $\int \dot{\omega}_F''' \, dx$ is stretched by the advection flux. The flow effect is magnified in Fig. 5.13c and 5.13d where the CFFs are centered in the maximum HRR for the cool front. The heat release rate is substantially affected by the flow which outcomes with distinct temperature and species profiles. For instance, comparing the three temperature profiles in Fig. 5.13c, it can be seen that the flame front is thicker as u_{inlet} increases and the temperature in $x = 0$ becomes higher with lift-off effect. Figure 5.13d depicts the behavior of formaldehyde and $CH_3OCH_2O_2$ which show up in different LTC stages. Even CH_2O mass fraction presents a small difference at the cool front, the $CH_3OCH_2O_2$ exhibits a notably increase in magnitude and its thickness of action, as seen for HRR. It can diffuses until 1 mm ahead the CFF. Evidently, for the case of $u_{inlet} = 0.00$, the HRR and the species profiles are affected by the heat losses that happen due to limited temperature at inlet boundary condition.

More generally, the nature of CFF is attributed to the transient behavior of LTC and the flow that adds a longer residence time as u_{inlet} increases. In this way, the CFF S_c increases limited to $\tau_{res} <$ IDT. Eventually, if $\tau_{res} \geq$ IDT the CFF will become an autoignitive front. Therefore, the CFF displays as an active hot pocket that can increase the heat release intensity as a function of the advection term.

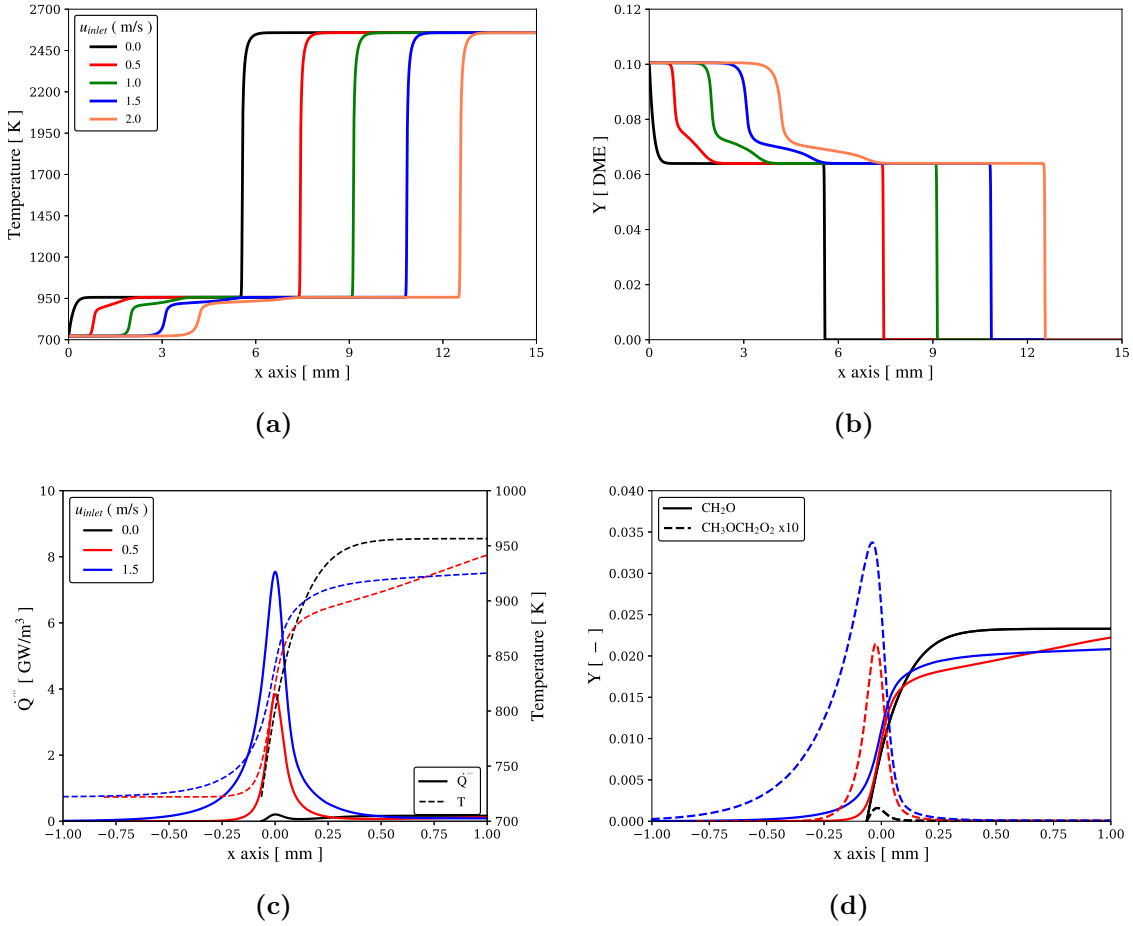

Figure 5.13: Double flame profiles in a range of inlet velocities for P8T722 at LTC half-life, (a) double flame temperature and (b) fuel mass fraction, (c) cool flame front temperature, HRR and (d) CH_2O, $CH_3OCH_2O_2$ mass fraction for $u_{inlet} = 0.0,\ 0.5$ and 1.5 m/s.

5.3.2.2 Thermophysical effects

In the former section, the analysis was focused on the effect of inlet velocity over the double flame. Now the study turns to the effects of temperature and pressure. Figure 5.14 shows the HFF speed as a function of time for the cases P8T675, P8T722 and P8T800 as well the temperature and fuel mass fraction ahead of the main front. From now on, all analyses were performed with $u_{inlet} = 0$. As the autoignition time scale has a strong dependence on initial temperature, the graphs show in abscissa axis the relation $\hat{\Delta\tau}$ according Eq. (5.3).

During the flame propagation, when the inlet flow's reaction rate is still in the cold boundary, the inlet temperature has the main role in the burning rate. However, after the 1st stage, the curves for the HFF speed are close for both temperatures, as can be observed in Fig. 5.14a when the normalized time, $\hat{\Delta\tau}$, is compared. Nevertheless, the temperature and fuel mass fraction are different in homogeneous region, being the HFF temperature higher for the lower inlet temperatures, Figure 5.14b, and the fuel mass fraction greater when the inlet temperature is higher, Fig. 5.14c. These behaviors are consequences of

the LTC ahead of main front and they are summarize in Fig. 5.14d which compares a normalized progress variables Y and T given by $\hat{Y}_{u\to h} = \frac{Y_F - Y_{F,u}}{Y_{F,b} - Y_{F,u}}$ and $\hat{T}_{u\to h} = \frac{T - T_u}{T_b - T_u}$, respectively[1]. Despite the differences in Figs. 5.14b and 5.14c, Fig. 5.14d shows that for both inlet temperatures, the thermochemical relation $\hat{Y}_{u\to h}$ and $\hat{T}_{u\to h}$ follow the same temporal correlation. This is one point that explains the results of Fig. 5.14a.

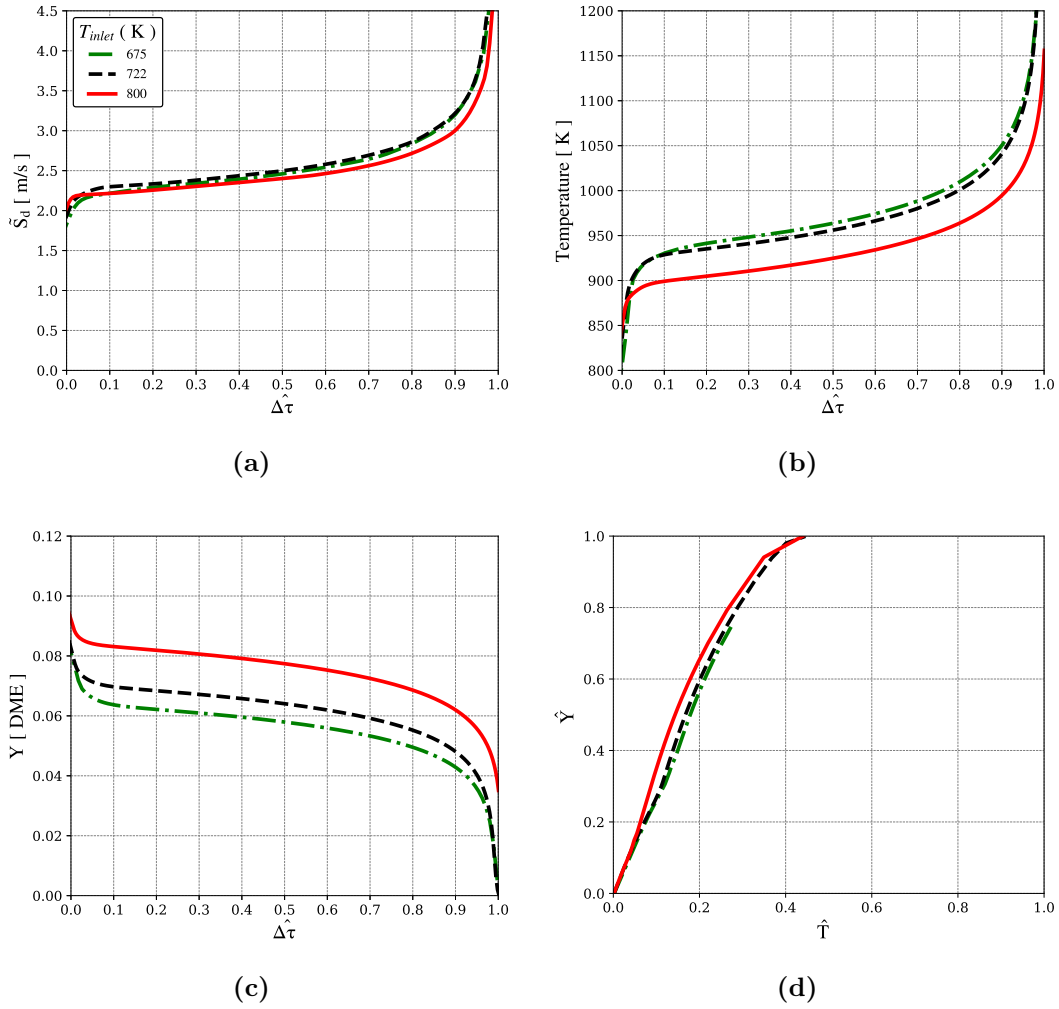

Figure 5.14: HFF properties for different inlet temperatures, 675 (green line), 722 (red line) and 800 K (blue line), as function of normalized time, $\hat{\Delta}\tau$, at pressure of 8 bar, (a) displacement speed, (b) inlet temperature and (c) fuel mass fraction ahead the HFF and (d) thermochemical relation of LTC.

From the classical thermal theory of flames, the maximum temperature derivative is given by

$$\left.\frac{dT}{dx}\right|_{max} = \frac{\rho_u S_l^0 c_p}{\lambda_{ig}}(T_{ig} - T_u),$$

then,

[1]The subindex, $u \to h$, indicates from the unburnt to the homogeneous region. In the same way, $h \to b$ indicates from the homogeneous region to the equilibrium condition behind the HFF.

$$S_l^0 = \frac{\alpha}{\frac{(T_b - T_{min})}{\frac{dT}{dx}|_{max}}} = \frac{\alpha}{\delta_l^0},$$

where D_{th} is the thermal diffusivity term. According to later equations, an ambiguous interpretation can arise from what happen inside the flame boundary layer, since the fuel was partially consumed in the cool flame. The analysis is complete adding a reaction time scale, t_{ch}, during the burn process. This was done trough

$$\overline{\dot{\omega}_F'''} = \frac{1}{\hat{Y}_{h\to b,h} - \hat{Y}_{h\to b,b}} \int_0^1 \dot{\omega}_F''' d\hat{Y}_{h\to b}, \qquad \hat{Y}_{h\to b} = \frac{Y_{F,h} - Y_f}{Y_{F,h} - Y_{F,b}},$$

$$\tau_{ch} = \frac{\rho_h Y_{F,h}}{\overline{\dot{\omega}_F'''}}.$$

The term $\overline{\dot{\omega}_F'''}$ represents the mean fuel reaction rate, $\hat{Y}_{h\to b}$ is a progress variable for fuel mass fraction taken from homogeneous reaction region to complete burn gas, and $\rho_h Y_{F,h}$ is the fuel mass at homogeneous region.

The state of the homogeneous region rules the HFF behavior. For the P8T675, the 1st stage is stronger than the others and the difference between $(T_{ad} - T_{min})$ becomes the lowest, Fig. 5.15a. The gradient of T also decreases, for both inlet temperatures, meaning that the reaction rate is slowing down, Fig. 5.15b. On the other hand, the effect of high temperatures ahead the front causes an increase in thermal diffusion, Fig. 5.15c. Figure 5.15d shows that the combined effects result in a time scale decreasing for the fuel reaction rate, and also it presents curves quite close for the t_{ch} which corroborates with results in Fig. 5.14a. The tendency observed in Fig. 5.15d highlights the strong impact that the high temperatures can cause on the burning rate.

The effect of pressure on the flame speed is shown in Fig. 5.16, where transient and steady-state results are compared in Fig. 5.16a and the absolute values are evaluated in Fig. 5.16b. Figure 5.16a shows that the transient effect of LTC promotes a greater variation in the S_d during the 1st ignition state. From that point, the transient process results in a significant difference when compared with steady-state regime.

Unlike the temperature analysis, Fig. 5.16b shows that pressure acts decreasing the flame speed as the relation $S_l \sim p^{-\beta}$, at least during part of LTC life. However, by the end of the process, the autoignitive condition takes place, decreasing the effect of diffusion. Further, the reactive term dominates the flame propagation, which outcomes with similar values for S_d for both cases. The small graph in Fig. 5.16b brings out the relation of S_d/S_l^0. It is seen that despite the pressure raising causes the S_d to decrease, high pressures present a more significant net gain in the burning rate.

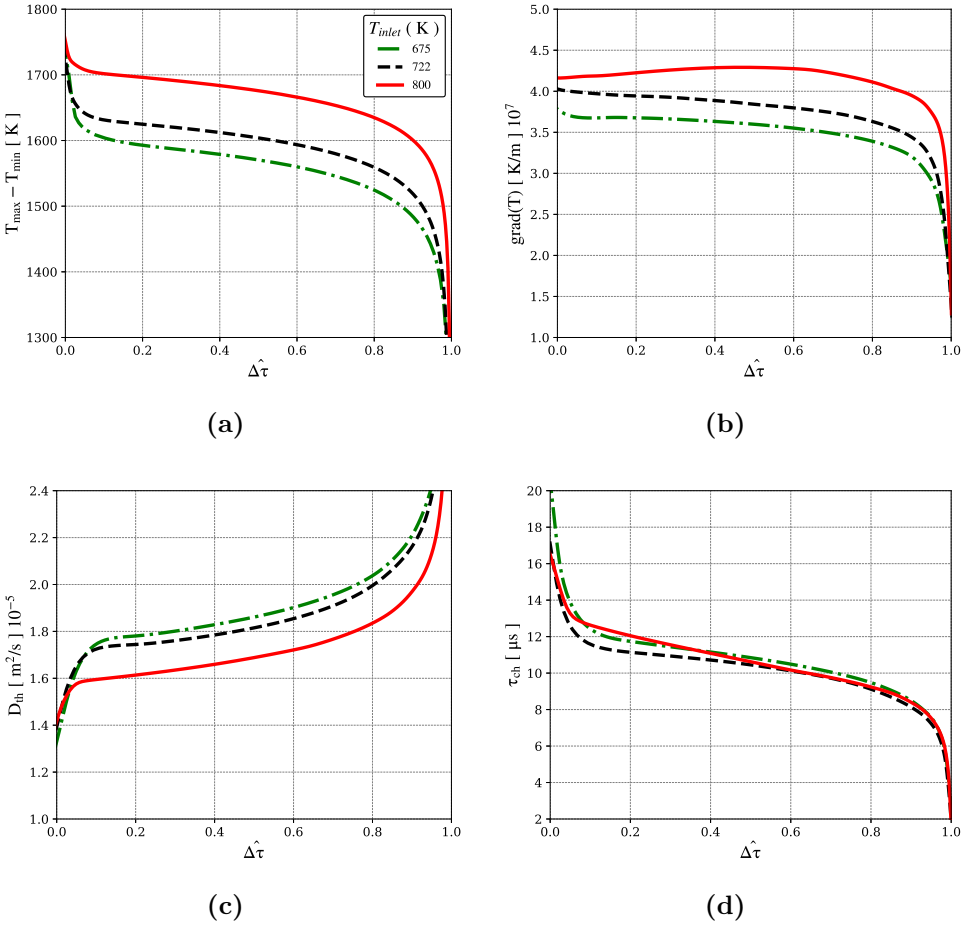

Figure 5.15: Thermal features of HFF transition process for different inlet temperatures, P8T675 (green line), P8T722 (red line) and P8T800 (blue line), as function of normalized time, $\hat{\Delta}\tau$. (a) difference between temperature of homogeneous burn region and the adiabatic flame temperature, (b) maximum temperature gradient, (c) thermal diffusion coefficient and (d) fuel reaction time scale.

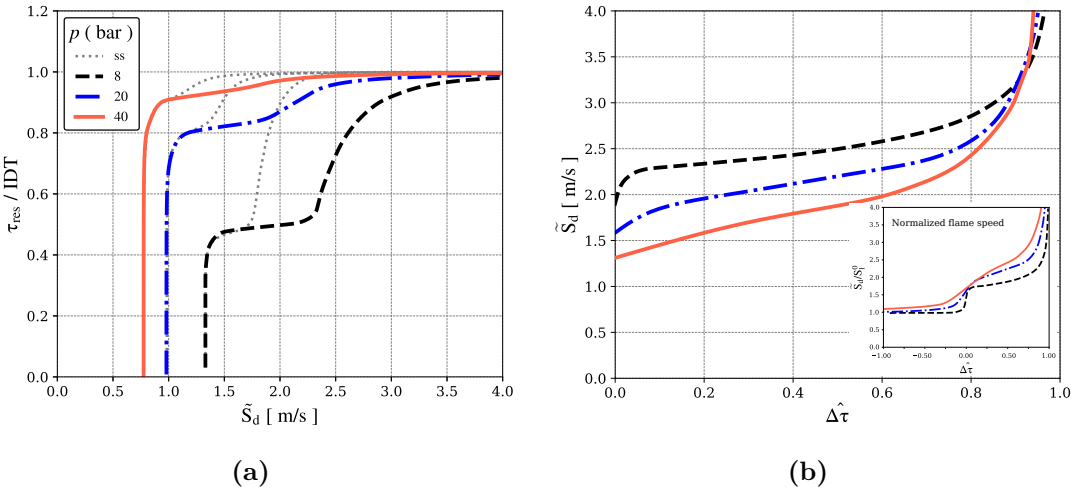

Figure 5.16: Residence time influence on flame speed at transient conditions for P8T722, P20T722 and P40T722, (a) residence time for transient and steady-state, ss (dotted lines), as function of displacement flame speed and (b) S_d comparison.

The following results show a more detailed frame in which the reaction-diffusion transport terms for species and energy equation are observed regarding the structural change in the HFF. Figure 5.17 presents a transport budget analysis for the energy equation from normal flame propagation to flame assisted by LTC for the cases P8T722 (left column) and P40T722 (right column). In the first row, it is seen that the pressure raises results in an increase in HRR of one order magnitude. Nevertheless, the transport coefficients are negatively influenced which decreases the effect of the flame pre-heating zone. Comparing the two following rows, the reaction term in Eq. (5.4) becomes dominant as the low-temperature chemistry evolves from $\hat{\Delta\tau} = 0.15$ to 0.90. Although less fuel is available for the main front, the HRR is slightly higher for both cases. The LTC increases the temperature ahead of the HFF which decreases the diffusion term, and yet, this effect is more intense as pressure increases from $p = 8$ to 40 bar. At $\hat{\Delta\tau} = 0.90$, Fig. 5.17f, the reaction term is 6 times the diffusion term, resulting in a thicker flame dominate by the high temperature.

Figure 5.18 complements the energy equation analysis where is evaluated the profile change of a progress variable c regarding the HRR. In a normal flame, the reaction rates are determined by the burnt side of the flame where the thermal explosion occurs. With the evolution of LTC towards the autoignition, the diffusion term becomes weaker and the peak of HRR moves forward in the flame front structure, away from the burn side. The reaction layer is not thin in progress variable space and it is even thicker for P40T722. The asymptotics theory is not applicable for these cases where the HRR is stretched towards $\hat{T} = 0$.

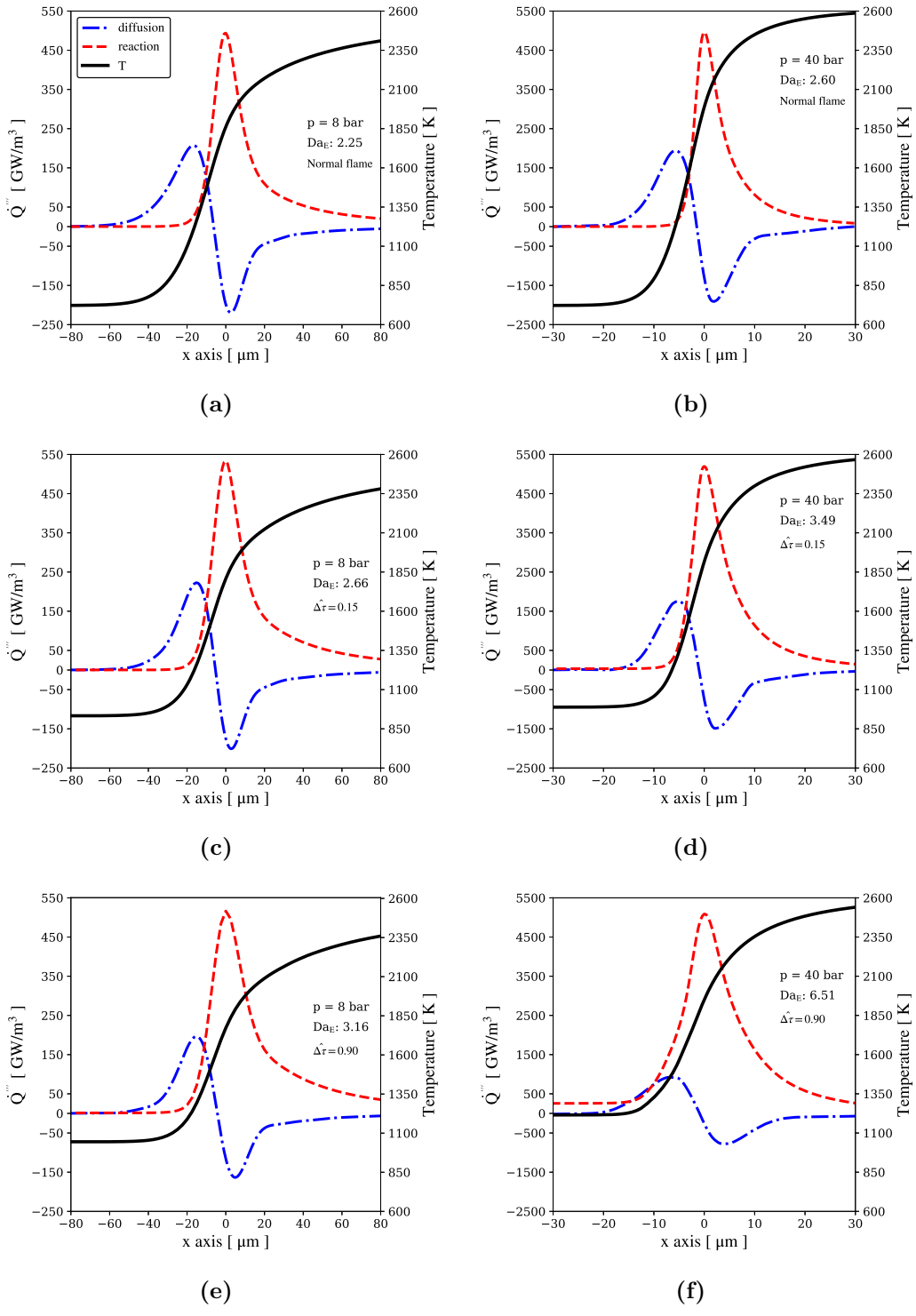

Figure 5.17: Transport budget in terms of energy for P8T722 and P40T722, (a) normal flame for P8T722, (b) normal flame for P40T722, (c) $\hat{\Delta}\tau = 0.15$ for P8T722 (d) $\hat{\Delta}\tau = 0.15$ for P40T722 (e) $\hat{\Delta}\tau = 0.90$ for P8T722 (f) $\hat{\Delta}\tau = 0.90$ for P40T722.

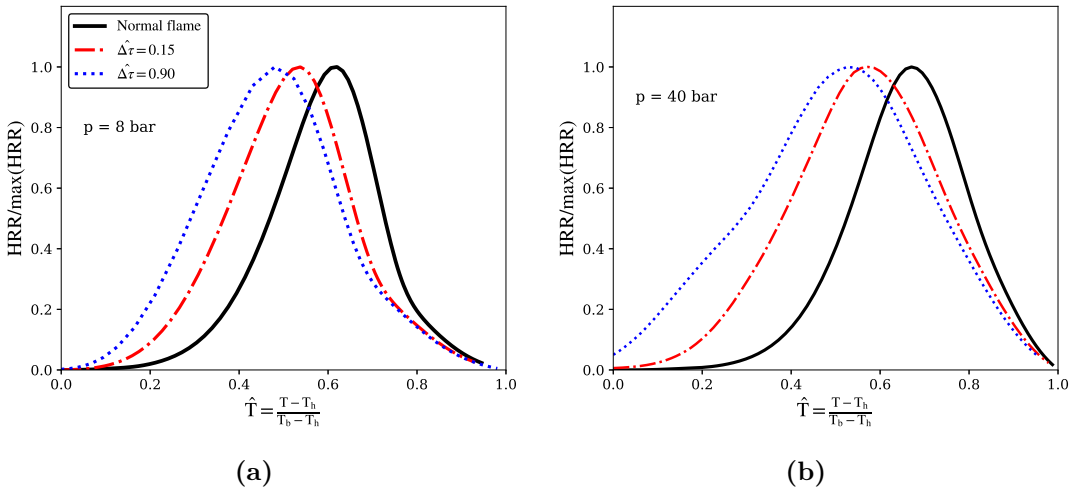

Figure 5.18: HRR regarding the progress variable c space for the cases, (a) P8T722 and (b) P40T722.

Figure 5.19 reports the transport budget for the fuel and formaldehyde mass fraction. In the first row, it is seen that the pressure effect is prone to narrow the diffusion zone for both species. The formaldehyde is formed in preheat zone and then consumed in the reaction layer. After the 1st stage, the second row shows that the fuel consumption rate becomes slightly slower and the CH_2O makes up the reacting mixture that enters the main flame. Moreover, less formaldehyde is formed in the pre-heating zone since part of the reactions occurs in the homogeneous region. At $\hat{\Delta}\tau = 0.90$, the flame composition and structure are quite different than $\hat{\Delta}\tau = 0.15$ and the pressure effect turns up more evident. From P8T722 to P40T722 is seen a substantial reduction of fuel consumption rate. At P8T722 the reduction is 1.32 times, while at P40T722, the reduction is 1.97. For $p = 40$ bar, it can be observed more clearly that part of the fuel is being burnt in the homogeneous region, resulting in less remaining fuel in the HFF. Figures 5.19k and 5.19l show that formaldehyde concentration increases upstream to HFF from $\hat{\Delta}\tau = 0.15$ to $\hat{\Delta}\tau = 0.90$ which does not outmes with consumption rate-raising but a reduction in the diffusion upstream.

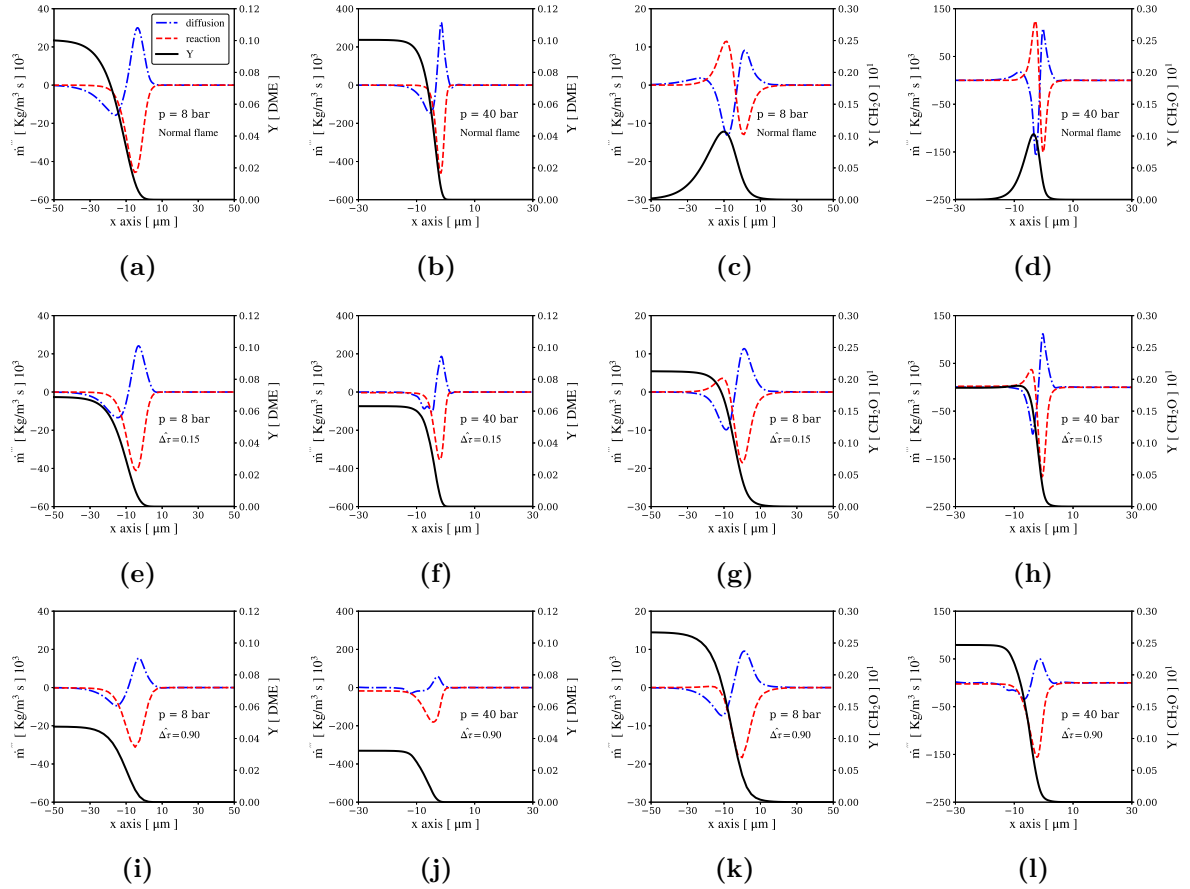

Figure 5.19: Transport budget in terms of DME and formaldehyde for the HFF, (a) normal flame for DME at P8T722, (b) normal flame for DME at P40T722, (c) normal flame for CH_2O at P8T722, (d) normal flame for CH_2O at P40T722, (e) $\hat{\Delta}\tau = 0.15$ for DME at P8T722, (f) $\hat{\Delta}\tau = 0.15$ for DME at P40T722, (g) $\hat{\Delta}\tau = 0.15$ for CH_2O at P8T722, (h) $\hat{\Delta}\tau = 0.15$ for CH_2O at P40T722, (i) $\hat{\Delta}\tau = 0.90$ for DME at P8T722, (j) $\hat{\Delta}\tau = 0.90$ for DME at P40T722, (k) $\hat{\Delta}\tau = 0.90$ for CH_2O at P8T722 and (l) $\hat{\Delta}\tau = 0.90$ for CH_2O at P40T722.

In order to identify the changes in the flame reaction structure for the main front assisted by LTC, the dimensionless sensitivity coefficients were calculated for cases of normal flame propagation and $\hat{\Delta}\tau = 0.90$ at P8T722, Fig. 5.20. As depicted in [19], the hot flame is ruled by chain-branching reaction pathway $H + O_2 \rightleftharpoons OH + O$ seen in Fig 5.20a and 5.20b. However, it is noteworthy that when the autoignition process assists the main flame, the reactions $H_2O_2 + M \rightleftharpoons 2OH + M$ and $CH_2O + OH \rightleftharpoons H2O + HCO$ show up in sensitivity analysis, affecting the outcomes of rate-limiting steps. In the transient regime, unlike of steady-state, the main front is not attached to the reactions of the CFF. The HFF propagates in the reactive medium and it is not sensitive to LTC rate-limiting.

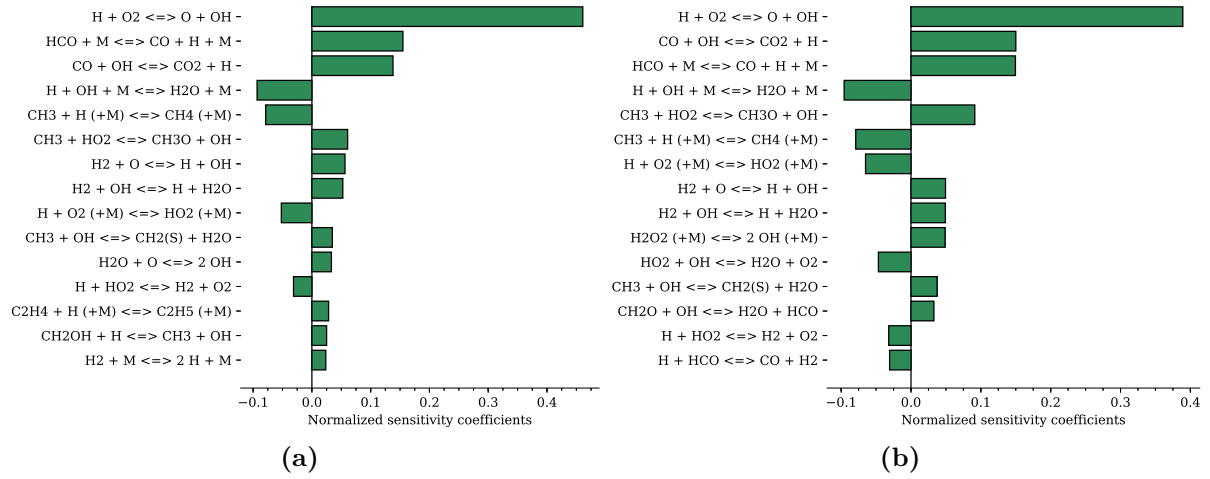

Figure 5.20: Normalized sensitivity coefficients for the HFF assisted by LTC at P8T722, (a) normal flame propagation and (b) HFF at $\hat{\Delta}\tau = 0.90$.

5.3.3 Cool flame front

In the above discussions, the main flame displacement speed still represents the eigenvalue of the system of equations, despite the transient regime ahead of HFF. The low-temperature chemistry rules the consumption speed in HFF, therefore the inlet properties of the flame may be taken as the partial products of the CFF (as stoichiometric and temperature). However, it is also needed to investigate the thermophysical and transport properties of the cool flame front in order to understand how its interface interacts with the flow, heat loss, and the burning process between the homogeneous and an unburnt region.

In this section, two approaches were used to investigate the cool flame front features. First, a hot spot configuration is used with the same setup as the previous simulations except for the temperature profile. The second approach is focused on the dynamics of the hot kernel size.

5.3.3.1 The hot kernel as a deflagration wave

The results presented previously, in section 5.3.2.1, were carried out considering that the cool flame originates due to the homogeneous intermediate inlet temperature and the front stabilizes at the domain boundary unless a non-zero mass flow is imposed. Here, to identify some specific characteristics of the CFF, hot pockets are established with an intermediate temperature of 722 K followed by an upstream region with 300 K in which no reaction can occur ahead of the front, Fig. 5.1b.

Figure 5.21 shows the results for the consumption speed and Damköhler number along the dimensionless time for P8T722, P20T722 and P40T722. Figure 5.21a presents the evolution of S_c from the 1st stage to the ignition delay time. Afterward the 1st peak of HRR, the cool flame front propagates towards the unburnt gas and the S_c goes towards

a quasi-equilibrium condition. It is seen that close to $\hat{\Delta\tau} = 0$, the consumption speed is higher for both pressures which undergo a sharp drop in the burning rate. The quasi-equilibrium condition is described as a process that along a slowing down mechanism, the S_c reaches a minimum and then starts a reversing evolution that accelerates as the elapsed time approaches the IDT.

According to Eq. 5.4, the $\mathrm{Da_E}$ is plotted along the $\hat{\Delta\tau}$ in Fig. 5.21b. After the 1st stage, the flame structure is dominated by reaction term that is much faster than diffusion setting up an autoignition front. Subsequently, the diffusion term appears decreasing the Damköhler number, and it remains decaying for both pressures. Figure 5.21c depicts HRR decay at the cool front through a parameter called $\mathrm{Ta_{CFF}}$ that represents the temperature at the maximum heat release rate. It is observed that the CFF comes out from the homogeneous region, from higher temperatures, and propagates towards lower temperatures.

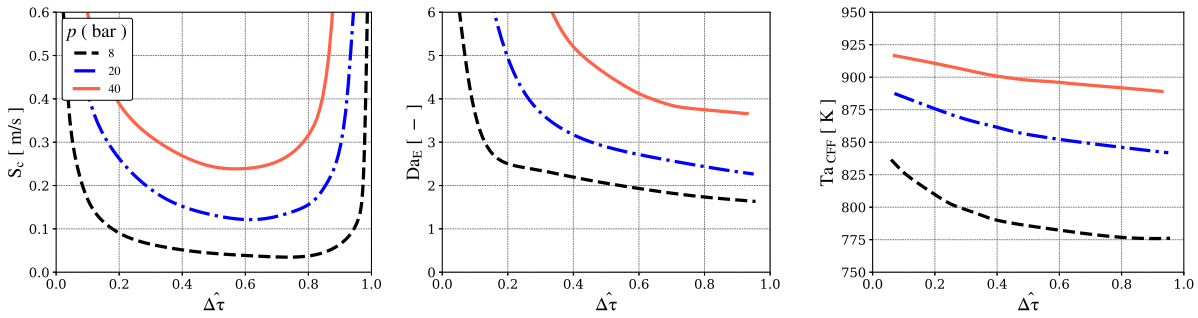

Figure 5.21: Characteristics of cool flame propagation for P8T722 (black dashed line), P20T722 (blue dot-dashed lines) and P40T722 (red solid lines), (a) cool front consumption speed, (b) reaction-diffusion Damköhler number history and (c) temperature at the peak of HRR.

The different pressures showed a standard qualitative behavior. However, this parameter has a substantial impact on increasing the consumption speed. As pressure is raised, the heat release rate increases and the gap between the 2nd and the 1st stage is narrowed, Fig. 5.2. Comparing case P8T722 with P40T722 in Fig. 5.21c, the pressure raises results in the heat losses decreasing, making the cool front propagate at higher temperatures.

Figure 5.22 addresses the flame profiles for the cases P8T722 and P40T722 where the first and third columns are relate to $p = 8$ bar and the second and fourth to $p = 40$ bar. For both plots, the profiles represent the times $\hat{\Delta\tau} = 0.15, 0.50$ and 0.90. A self-sustainable structure for both pressures can be observed, which shows a well-defined pre-heat/diffusion and reaction zone.

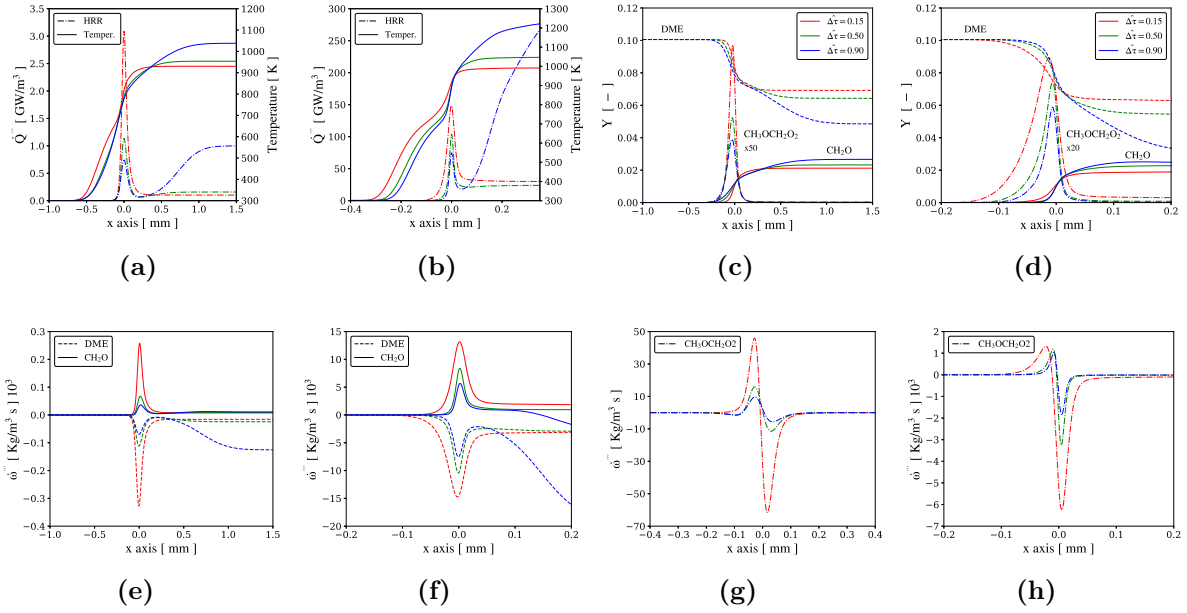

Figure 5.22: Cool flame front profiles for the cases P8T722 and P40T722, (a) HRR and temperature for P8T722 and (b) P40T722, (c) species mass fraction of DME, CH_2O and $CH_3OCH_2O_2$ for P8T722 and (d) P40T722, (e) reactions rate of DME, CH_2O for P8T722 and (f) P40T722, (g) reaction rate of $CH_3OCH_2O_2$ for P8T722 and (h) P40T722.

Figures 5.22a and 5.22b show the HRR and temperature profiles. At $\hat{\Delta\tau} = 0.15$, the heat release reaches the higher rate in the front which is also shown in Fig. 5.21a. However, the temperature behind the front is lower since it depends on the reactions in the homogeneous region. In the course of time, the HRR decreases balancing the volumetric transport, Fig. 5.21b, and the temperature in the homogeneous region is raised. At $\hat{\Delta\tau} = 0.90$ for P40T722, the LTC behind the front dominates the burning rate process. When pressures are compared, it is observed that the P40T722's HRR reaches almost two orders of magnitude than P8T722 resulting in a significant difference in Fig. 5.21a. Figures 5.22c and 5.22d present the mass fraction profiles for the DME, formaldehyde and $CH_3OCH_2O_2$ and Figs. 5.22e, 5.22f, 5.22g and 5.22h complement them. DME is consumed in the front and in the homogeneous region. The process of HRR is mirrored for DME in Figs. 5.22e and 5.22f. Furthermore, formaldehyde is formed more at the front than in the homogeneous region because it presents a more active process. Nevertheless, close to IDT, CH_2O is consumed in homogeneous region resulting in the strong variation in the S_c. In a homogeneous reactor, $CH_3OCH_2O_2$ exists just during the 1st autoignition stage. However, in the CFF, it is produced and consumed during all process. Comparing the pressures, for P8T722, the $CH_3OCH_2O_2$'s rate of production and destruction is lower than P40T722, and the $CH_3OCH_2O_2$ concentration becomes higher for $p = 40$ bar.

5.3.3.2 Hot spot size effect

To evaluate the hot kernel size role, L_p, simulations were performed for the cases P8T722, P20T722 and P40T722, Fig. 5.23. For P8T722, the results for $L_p \geq 1.0$ mm outcomes with the solid line which were shown in previous graphs. From $L_p < 1.0$, the 2nd ignition stage becomes delayed and the S_c tends to decrease from the point where the minimum value was reached. For the cases of $L_p = 0.9$ and 0.8 mm, the 2nd stage is not so much delayed. For $L_p = 0.7$ mm, the consumption speed decreases substantially during the process and the simulation was carried out until 5 times the IDT without ignition.

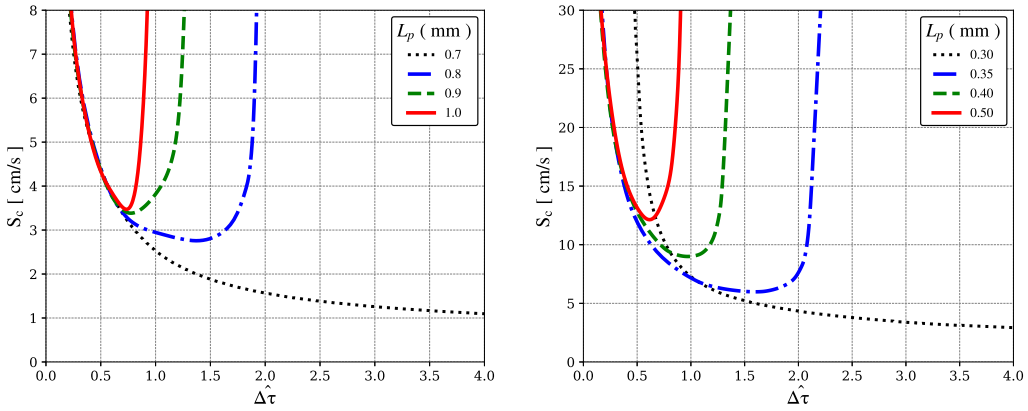

(a) **(b)**

Figure 5.23: Cool flame consumption speed regarding the hot kernels size, L_p, (a) P8T722 and (b) P20T722.

For P20T722, the cool flame kernel starts to be impacted from $L_p < 0.5$ mm. The curves show that the delay begins before the flame reaches the minimum S_c. For $L_p \leq 0.3$ mm, the 1st stage also becomes delayed and the 2nd stage happens twice after IDT. It is worth noting that the temperature kernel at $L_p = 0.3$ mm remained constant before the 1st stage. For the P40T722, the kernels with $L_p < 0.3$ mm are more affected by the length. The small sizes delay the 1st stage and the temperature kernel is not able to remain the profile with a maximum temperature of 722 K during the process.

The S_c decreasing observed in Figs. 5.23 is attributed to the homogeneous region. From the critical lengths, it was seen that the cool front propagates towards lower temperatures in the kernel profile and the chemical kinetics behind the CFF are affected by the transport gradients. The results show that even the LTC can give rise to a hot kernel in certain conditions, its size also affects the burning rate and can push the IDT away from the results that match with homogeneous reactor. Such observations evidence the difficulties of create models to predict the autoignition process in engines.

5.3.4 Regime diagram

To summarize the results found in this investigation, Fig. 5.24 shows a diagram that correlates the flame speed and its structural transition regime, $\mathrm{Da_E}(t)$, caused by LTC. Figure 5.24a shows the LTC influence over the HFF (open circles) and the CFF (solid circles). The rectangle identifies the region between the 1st stage and the 2nd stage[2] entitled LTC life. The time arrows identify the directions of time increasing for the cool and hot fronts. In addition, the τ_{1st} markers place the $\mathrm{Da_E}$ position where the first peak of HRR occurred, and the IDT markers locate the transition for the homogeneous region thermal explosion.

For the HFFs, the $\mathrm{Da_E}(t)$ keep increasing from the regular flame structure (e.g., $t = 0$ ms, $\mathrm{Da_E}(t) = 2.25$, $S_c(t) = 1.33$ m/s in P8T722) to the autoignitive condition (e.g., $t = 4.18$ ms, $\mathrm{Da_E}(t) = 3.70$, $S_c(t) = 3.85$ m/s in P8T722). It is noticed that the variations of $\mathrm{Da_E}(t)$ are weaker inside the LTC life and stronger during the τ_{1st} and IDT processes for both cases. As the pressure becomes higher, the HFF decreases the flame speed. The flames at low pressures have less dominance of the reactive term in the autoignitive process ahead of them. This effect is attributed to the increase in the heat release rate and the smaller time scale in the LTC as the pressure becomes higher.

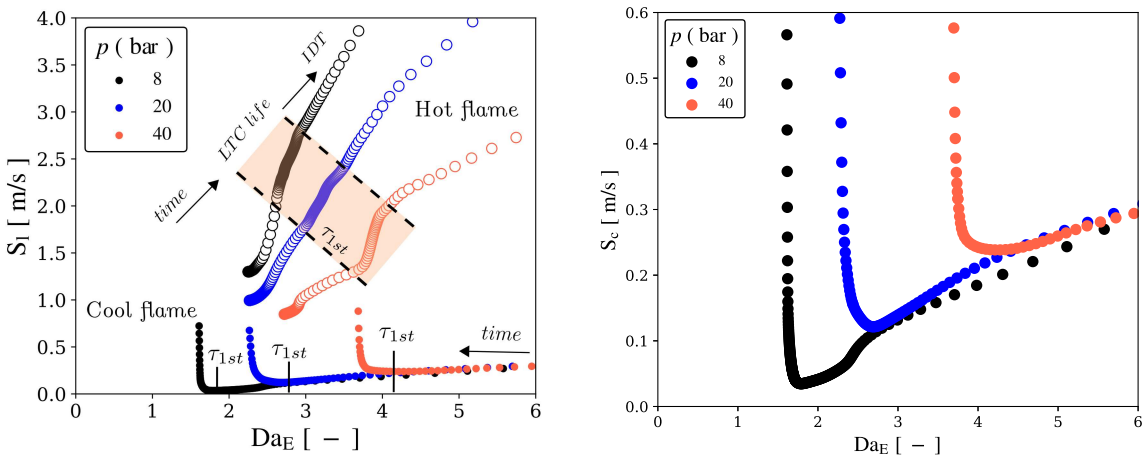

(a) (b)

Figure 5.24: Flame speed and Damköhler number correlation, (a) general diagram for the HFF and CFF regarding the cases analyzed and (b) zoom in at CFF structure variation.

Figures 5.24a and 5.24b show the CFF behavior. Three regimes can be identified; 1. the transition from 1st stage to the minimum S_c and $\mathrm{Da_E}$ in which the cool front undergoes a high $\mathrm{Da_E}$ variation during the 1st stage caused by its strong HRR and the gradients adjusting; 2. a region where the S_c and $\mathrm{Da_E}$ values tend to reach a minimum value together. In addition, it can be extended to lower S_c if the CFF kernel length reaches a critical size; and 3. a second transition process close to IDT where the S_c grows sharply.

[2]The begining of 2nd stage is identified when CH_2O is consumed in the homogeneous region.

In the third regime, the HRR in the front is decreasing in value, Fig. 5.21c. However, in the homogeneous region, CH_2O is consumed and the HRR grows towards the IDT, seen in Figs. 5.22b and 5.22d. Thereby, an autoignitive front coming out from the homogeneous region takes place in the CFF increasing the consumption speed exponentially.

5.4 CONCLUSIONS

In the present study, DNS were carried out for DME/air unstretched premixed flames in order to investigate how the low-temperature chemistry gives rise to a double flame structure and modifies the main front propagation. In addition, analyses were performed to understand the initialization and propagation of cool flame fronts. The results are focused on the impact of thermophysical properties under the flame speed and the structure of flames during the LTC.

The transient results showed that the double flame structure presents three regions; the hot flame region, the homogeneous region and the cool flame front region. The solution for a hot flame still represents the eigenvalue solution for the flame speed according to the temperature and stoichiometric condition of the homogeneos region. The observation showed that the cool front is stretched according to the flow velocity resulting in an apparent consumption rate increase.

The thermophysical effect was parametrically evaluated and the results show that, at transient condition, the temperature has a less significant effect than the pressure on laminar flame speed. For cases simulated, the double flame structure is substantially affected by the pressure in which the reactive term becomes dominant as pressure is raised. The low-temperature chemistry increases the temperature ahead of the HFF, which decreases the diffusion term, and yet, this effect is more intense as pressure was increased from $p = 8$ to 40 bar. By the end of the autoigition process, the results showed that the reaction term is 6 times greater than the diffusion term, resulting in a thicker flame dominated by the high temperature ahead of the main front. In addition, even with the predominance of the reaction term over the diffusion term, the fuel consumption in the HFF inner reaction layer is reduced regarding a regular flame structure, where the results showed a reduction of the fuel reaction rate of 1.3 for $p = 8$ bar and 1.9 for $p = 40$ bar.

Unlike the hot flame, the cool front showed that with the pressure raises, its burning rate also increases since it is structurally more dependent on the reactive term than the diffusive term. The hot spot size investigation shows that the cool flame initialization depends on a critical size to give rise to a cool front. However, once a cool flame is initiated is not a mandatory condition that the LTC will promote an autoignition process (according to the IDT of a 0D reactor) since the active chemistry behind the front also showed a dependence on the hot spot size.

In order to explore the results found in this work, future research will consider the potential effects of the low-temperature chemistry in more realist frameworks, e.g., in

Bunsen flames and boundary layer flows, where the flames are subject to stretch rate or wrinkled by turbulence motions, or in addition, where the double and cool flames fronts are exposed to heat losses.

Chapter 6

Summary and Recommendations

6.1 SUMMARY

In this dissertation, the challenge aspects of autoignition and propagation of low-temperature flames were investigated using thermodynamic models and detailed numerical simulations at piston engines condtions.

In Chapter 3, an analysis of classical flame propagating theory and direct numerical simulations results were performed in order to observe the interplay between flow and flame position and structure when premixed flames undergo hydrodynamic and thermo-diffusive effects in two canonical configurations, Bunsen flames and planar flames. Generally, the results presented in this chapter show that at weaker stretched regions, the correlation of flame speed and Karlovitz number lines up with the linear theoretical model for methane, DME, and hydrogen. Nevertheless, far from these points, it was observed that the strain and curvature provide higher-order effects that cause significant deviation from linear theory. Specifically, the flame tracking showed that, for methane and DME flames in the slot burner configuration, the strain and curvature contributions to the Karlovitz number have the same intensity in the region of positive curvature, but the curvature contribution becomes strongly negative and dominant in the concave curvature region. The stoichiometric flames present stronger variations of Karlovitz number when compared to the lean flames. The dimensionless displacement speed is smaller than one in the region of positive curvature and grows above one in the region of negative curvature since, for the methane and DME, the Lewis number is above the unity. For hydrogen, the Bunsen flame shows that stretch-chemistry and diffusion interaction substantially modify the local burning rate for sufficient lean mixtures. Positively curved regions may burn more than twice the flat flame speed, while negative curvature may cause flame front extinction. In the planar flame configuration, the outcomes show that the local flame speed depends on the growth rate. The instabilities grow faster at a specific value of flame curvature related to the front wavelength. Below certain wavelengths, the initial perturbations are damped due to the thermo-diffusive effect. In addition, the simulations show that initial perturbations can lead to a chaotic flame behavior where an initial planar flame becomes

a wrinkled front composed of a range of small crests and trough-shapes geometries formed transversally by great wavelengths made up of smaller ones. A linear regression, made with the correlation of curvature and consumption speed, showed that the deviation from the linear theory is lower for the smaller curved points, while for higher negative values, the deviation increases.

In Chapter 4, the onset of knocking in a CFR engine is analyzed using a quasi-dimensional model. The knocking phenomena was represented by the two autoignition stages of a PRF for gasoline. Reduced chemical kinetics mechanisms were used and compared with the aim to study the main reactions and reaction paths responsible for leading the autoignition process during the end-gas. The way the mechanisms respond to the end-gas conditions depends on a dynamic coupling of the characteristic engine, flame, and reaction times. The engine characteristic time is determined by the engine speed. The turbulent flame propagation speed determines the characteristic time for burning the end-gas layer, and the end-gas reaction characteristic time is determined by the autoignition delay, from the chemical kinetics mechanism, under the variable temperature and pressure conditions. The results suggest that the interaction of the chemical kinetics mechanism with the engine operation depends strongly on the timing of the first-stage ignition. The results indicate that the first-stage ignition occurs when the end-gas reaches approximately a certain critical temperature value regardless of engine speed. The second-stage ignition follows a similar trend and occurs when the end-gas mixture reaches 1000 K, however, with a dependency on the nature and amount of species created during the first-stage ignition delay. In addition, it was noticed that the NTC region in the ignition delay diagrams plays an essential role in decreasing the knocking propensity in the studied engine. Therefore, for fuel design with the aim of increasing efficiency and energy density, it is key to develop an understanding of which species formed during the NTC region tends to delay the first-stage thermal ignition. This understanding may help to identify species to be added to fuel blends to delay the occurrence of knocking beyond the combustion duration.

Chapter 5 approached the initialization and propagation of cool flames and propagation of doubles flames (hot flames assisted by the low-temperature chemistry) in relevant conditions for internal combustion engines. The investigation provided physical and chemical insights about flames' structural transitions and their impact on the flame speed when the system is under the autoignition regime. For the simulated cases, the double flame structure is substantially affected by the pressure in which the reactive term becomes dominant as the pressure is raised. Unlike normal flames, the cool flame burning rate increases with pressure since it is structurally more dependent on the reactive source than the diffusive term. A hot spot size investigation shows that the cool flame initialization depends on a critical size to give rise to a cool front. However, once a cool flame is initiated is not a mandatory condition that the LTC will promote an autoignition process (according to the IDT of a 0D reactor) since the active chemistry behind the front also showed a dependence on the hot spot size.

6.2 RECOMMENDATIONS FOR FUTURES WORKS

Based on the results of the present thesis, the following are some recommendations for potential improvements in our analysis, understanding, and extensions for the studies of flame propagation of hydrogen flames, the thermodynamic of autoignition phenomena in IC engines, and flames initialization and propagation under the autoignition process.

The thermo-diffusivity instabilities of hydrogen coupled with turbulence can be a source of additional wrinkling during flame propagation. In order to raise the burning rate of lean H_2, an increase in the Karlovitz number can play an important role in this aim for premixed and partially premixed combustion. In addition, the transient flame deformation responds promptly to flow perturbations in frequencies of order to the thermo-diffusive time scale, τ_f [107], which suggests that controlling flow frequency increases the flame area. Modulated turbulence for combustion applications can be a source of control of this effect in systems such as the low swirl cases [167]. Moreover, using combustion chambers that allow greater turbulent velocity fluctuation and the integral scale length of turbulence may induce a sharp increase in the Karlovitz number resulting in Ka $>>$ 1. Such a combination makes the flame regime goes from flamelet to the thickened reaction zone regime (TRZ), in which the flame structure is disturbed by the more minor turbulent scales [168]. Therefore, the global burning rate of combustion devices can be enhanced by extending the combustion regime for the TRZ. In present-day literature for hydrogen flames, there are just a few studies about this theme, and the combustion modelling does not cover conditions of turbulent combustion for fuels in the TRZ regime and Le $<$ 1.

In many studies found in literature about engine knocking, the research focuses on seeking fuels and fuel blends that raise the global IDT. Chapter 4 showed that due to the combination of temperature, pressure, and low-temperature chemistry, the first ignition stage is almost inevitable for the PRF tested in the CFR engine. Future studies could fruitfully explore this issue further by analyzing the existence of important reactions and additives that are able to extend the second ignition stage, once the LTC is activated.

Flames under the effects of curvature, normal and tangential strains modify the local burning rate. Two-dimensional simulation of double flames in Bunsen flames brings the dependency on stretch rate coupled to the residence time and its results in the global flame speed. In addition, turbulence flow analysis is essential to understand the existence and the role of low-temperature chemistry in the combustion process of the main flame front. As the flame front becomes thicker with the LTC ahead, the interaction of turbulent flow can cause a thicker front. Recently, Wang *et al.* [42] performed a direct numerical simulation of a turbulent boundary layer under autoignitive conditions. They emulated a fuel with a short ignition delay time using a mixture with hydrogen at high temperature. However, the effects of autoignition process found in fuels with complex LTC like DME were not studied.

Appendix A

Thermodynamic model for the engine

The mathematical model used in this work is based on Ferguson [123]. The description uses intensive thermodynamic properties, which become dependent on a thermodynamic library able to retrieve them as the solution is resolved according to the time steps.

The first law of thermodynamics yields

$$dU = \delta Q - \delta W, \tag{A.1}$$

where for a time-dependent closed system or, according to here, for a system dependent on θ, the Eq. (A.1) is rewritten as

$$mc_v \frac{dT}{d\theta} = \frac{dQ}{d\theta} - p\frac{dV}{d\theta}. \tag{A.2}$$

Mass exchanges may also be included in this model, which gives

$$mc_v \frac{dT}{d\theta} + c_v T\frac{dm}{d\theta} = \frac{dQ}{d\theta} - p\frac{dV}{d\theta}. \tag{A.3}$$

In Eq. (A.3), the thermal variations may be written as a function of intensive internal energy, u. The Eq. (A.3) yields

$$m\frac{du}{d\theta} + u\frac{dm}{d\theta} = \frac{dQ}{d\theta} - p\frac{dV}{d\theta}. \tag{A.4}$$

Equation (A.4) is a generalized thermodynamic model for a piston engine system. For the purpose of this work, the l.h.s. mass exchanges term is eliminated because the blowby effects are neglected.

The internal energy for the two-zone model is defined as

$$u = \frac{U}{m} = Y_b u_b + (1 - Y_b)u_u, \tag{A.5}$$

where u_b is the internal of the burnt zone defined by the temperature T_b, and u_u is the internal energy of the unburned zone as a function of T_u. The specific volume for each zone is given by

$$v = \frac{V}{m} = Y_b v_b + (1 - Y_b) v_u. \tag{A.6}$$

Each zone is a function of its respective thermodynamic state. Thereby, v_b is defined as

$$v_b = v_b(T_b, p), \tag{A.7}$$

where according to the chain rule

$$\frac{dv_b}{d\theta} = \frac{\partial v_b}{\partial T_b}\frac{dT_b}{d\theta} + \frac{\partial v_b}{\partial p}\frac{dp}{d\theta}, \tag{A.8}$$

in which is the same for the unbuned zone

$$\frac{dv_u}{d\theta} = \frac{\partial v_u}{\partial T_u}\frac{dT_u}{d\theta} + \frac{\partial v_u}{\partial p}\frac{dp}{d\theta}. \tag{A.9}$$

The relation for u_b, T_b and p are similar, in which

$$u_b = u_b(T_b, p), \tag{A.10}$$

and yet

$$\frac{du_b}{d\theta} = \frac{\partial u_b}{\partial T_b}\frac{dT_b}{d\theta} + \frac{\partial u_b}{\partial p}\frac{dp}{d\theta}. \tag{A.11}$$

In Bridgman's work [169], several state functions are defined where the first-order partial derivatives can all be written in terms c_p, $\partial v/\partial p$ and $\partial v/\partial T$. Thus, the terms of partial differentials are rewritten as a function of these properties. The burned zone becomes

$$\frac{du_b}{d\theta} = \left(c_{p,b} - p\frac{\partial v_b}{\partial T_b}\right)\frac{dT_b}{d\theta} - \left(T_b\frac{\partial v_b}{\partial T_b} + p\frac{\partial v_b}{\partial p}\right)\frac{dp}{d\theta}, \tag{A.12}$$

and for unburned zone

$$\frac{du_u}{d\theta} = \left(c_{p,u} - p\frac{\partial v_u}{\partial T_u}\right)\frac{dT_u}{d\theta} - \left(T_u\frac{\partial v_u}{\partial T_u} + p\frac{\partial v_u}{\partial p}\right)\frac{dp}{d\theta}. \tag{A.13}$$

According to (A.4), the total internal energy variation is written as

$$m\frac{du}{d\theta} = \left(Y_b\frac{du_b}{d\theta} + (1 - Y_b)\frac{du_u}{d\theta} + (u_b - u_u)\frac{dY_b}{d\theta}\right)m. \tag{A.14}$$

Equations (A.12) and (A.13) are inserted in Eq. (A.14) yielding

$$\begin{aligned} m\frac{du}{d\theta} = {} & mY_b\left(c_{p,b} - \frac{pv_b}{T_b}\frac{\partial v_b}{\partial T_b}\right)\frac{dT_b}{d\theta} + m(1 - Y_b)\left(c_{p,u} - \frac{pv_u}{T_u}\frac{\partial v_u}{\partial T_u}\right)\frac{dT_u}{d\theta} \\ & - \left[mY_b v_b\left(\frac{\partial v_b}{\partial T_b} + \frac{\partial v_b}{\partial p}\right) + m(1 - Y_b)v_u\left(\frac{\partial v_u}{\partial T_u} + \frac{\partial v_u}{\partial p}\right)\right]\frac{dp}{d\theta} \\ & + m(u_b - u_u)\frac{dY_b}{d\theta}. \end{aligned} \tag{A.15}$$

The combustion heat release is defined through the difference between the unburned and burned zone enthalpy.

The heat losses through the walls, Eq. (A.4), are given by

$$\frac{dQ_{wall}}{d\theta} = \frac{-\dot{Q}_{wall,b} - \dot{Q}_{wall,u}}{\Omega}, \tag{A.16}$$

where Ω is the engine speed.

The energy equation is writte in terms of the temperature variation in each zone

$$\frac{dT_b}{d\theta} = -\frac{\dot{Q}_{wall,b}}{\overline{\omega} m Y_b c_{pb}} + \frac{T_b}{c_{pb}} \frac{\partial v_b}{\partial T_b} \frac{dp}{d\theta} + \frac{h_u - h_b}{Y_b c_{pb}} \frac{dY_b}{d\theta}, \tag{A.17}$$

$$\frac{dT_u}{d\theta} = -\frac{\dot{Q}_{wall,u}}{\overline{\omega} m (1 - Y_b) c_{pu}} + \frac{T_u}{c_{pu}} \frac{\partial v_u}{\partial T_u} \frac{dp}{d\theta}. \tag{A.18}$$

The pressure variation is given from Eq. (A.6) for the specific volume. The v variation results in

$$\frac{dv}{d\theta} = \frac{1}{m}\frac{dV}{d\theta} = Y_b \frac{dv_b}{d\theta} + (1 - Y_b)\frac{dv_u}{d\theta} + (v_b - v_u)\frac{dY_b}{d\theta}, \tag{A.19}$$

where Eqs. (A.8) and (A.9) can be inserted in Eq. (A.19) yielding

$$\begin{aligned} \frac{1}{m}\frac{dV}{d\theta} = {} & Y_b \frac{\partial v_b}{\partial T_b}\frac{dT_b}{d\theta} + (1 - Y_b)\frac{\partial v_u}{\partial T_u}\frac{dT_u}{d\theta} \\ & + \left[Y_b \frac{\partial v_b}{\partial p} + (1 - Y_b)\frac{\partial v_u}{\partial p} \right] \frac{dp}{d\theta} + (v_b - v_u)\frac{dY_b}{d\theta}. \end{aligned} \tag{A.20}$$

Finally, replacing Eqs. (A.17) and (A.18) in Eq. (A.20), we have

$$\frac{dp}{d\theta} = \frac{A + B + C}{D + E}, \tag{A.21}$$

where the letters yield

$$A = \frac{1}{m}\frac{dV}{d\theta},$$

$$B = \frac{\partial v_b}{\partial T_b}\frac{\dot{Q}_{wall,b}}{m Y_b \overline{\omega} c_{pb}} + \frac{\partial v_u}{\partial T_u}\frac{\dot{Q}_{wall,u}}{m(1 - Y_b)\overline{\omega} c_{pu}},$$

$$C = -(v_b - v_u)\frac{dY_b}{d\theta} - \frac{\partial v_b}{\partial T_b}\frac{h_u - h_b}{c_{pb}}\frac{dY_b}{d\theta},$$

$$D = Y_b \left(\frac{T_b}{c_{pb}} \left(\frac{\partial v_b}{\partial T_b} \right)^2 + \frac{\partial v_b}{\partial p} \right),$$

$$E = (1 - Y_b) \left(\frac{T_u}{c_{pu}} \left(\frac{\partial v_u}{\partial T_u} \right)^2 + \frac{\partial v_u}{\partial p} \right).$$

Ferguson used the polynomials created by Olikara and Borman [170] to determine the chemical equilibrium of 10 species. The equilibrium constants are used in the algorithm developed by Gordon and McBride [171], in which the mass fractions of each of the 10 species are defined as a function of temperature and pressure and, then, the enthalpy, entropy, volume and specific internal energy and specific heat of the system are computed.

Appendix B

Sensitivity analysis

The following Figures show the sensitivity results for Ranzi *et al.* [142], Cai and Pitsch [59] and Mehl *et al.* [141].

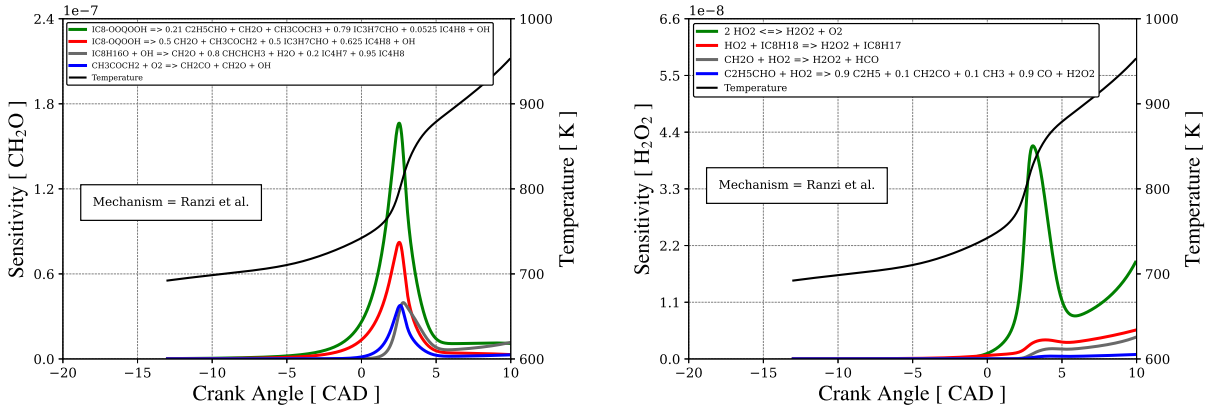

(a) **(b)**

Figure B.1: Relative sensitivity analysis for the formation of (a) CH_2O and (b) H_2O_2 for Ranzi *et al.* mechanism with PRF94 and CR=7.28.

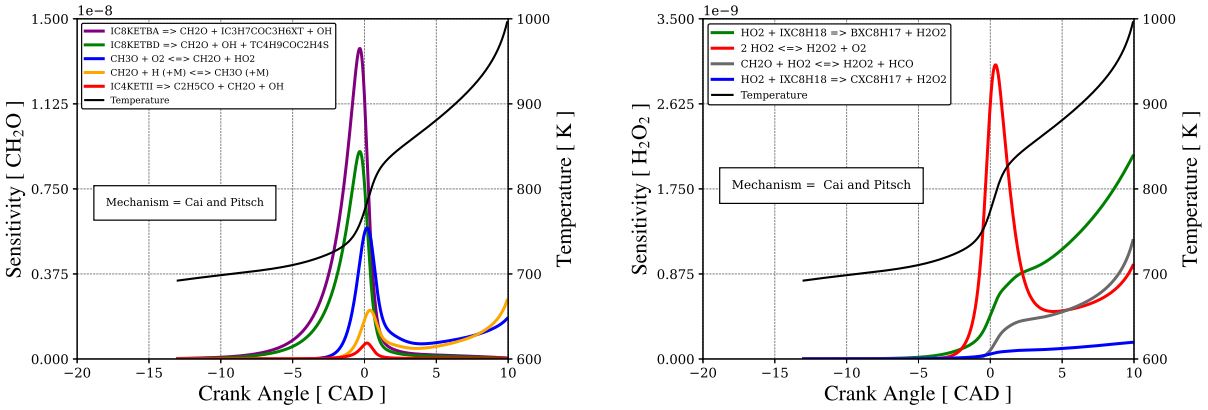

(a) **(b)**

Figure B.2: Relative sensitivity analysis for the formation of (a) CH_2O and (b) H_2O_2 for Cai and Pitsch mechanism with PRF94 and CR=7.28.

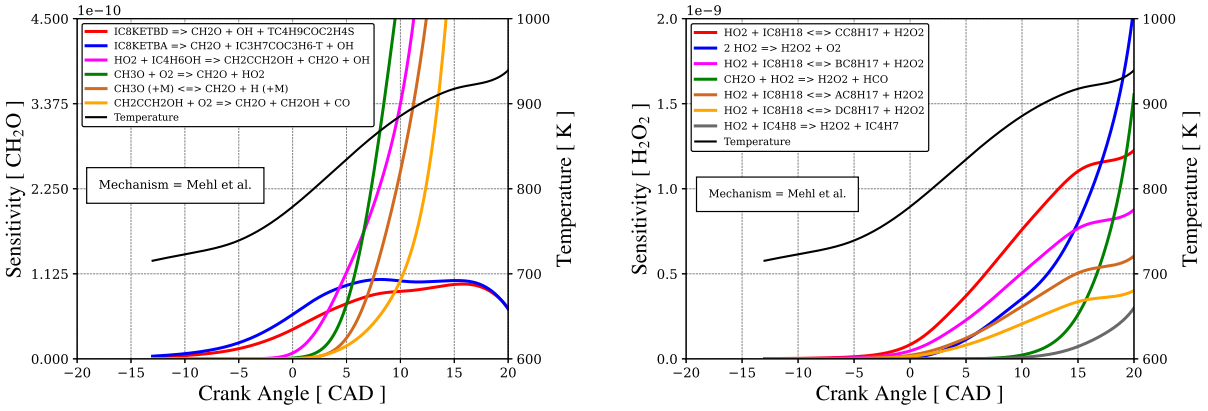

(a) **(b)**

Figure B.3: Relative sensitivity analysis for the formation of (a) CH_2O and (b) H_2O_2 for Mehl *et al.* mechanism with PRF94 and CR=8.30.

Appendix C

DME chemical mechanism

In this section, it is identified some chemical characteristics of low-temperature chemistry of the DME mechanism [101] and the effect of pressure in terms of reaction pathways. Figure C.1 shows the reaction pathway analysis where are pointed out four important branches responsible for forming formaldehyde for the cases P8T722 and P40T722.

In the literature, the main LTC chain branching pathway governing fuel oxidation in cool flames is defined as fuel $\rightharpoonup$ R $\rightharpoonup$ RO_2 $\rightharpoonup$ QOOH $\rightharpoonup$ OH + aldehyde, which produces multiple radicals during the autoignition process [19, 38]. Formaldehyde emerges as a good tracer for intermediate- and high-temperature ignition since it is formed in the first-stage ignition and consumed at later stages of the thermal explosion. Hydroperoxides (QOOH) are also important during the cool flame process as they are intermediate species that control the dynamics of low- and intermediate-temperature.

According to DME mechanism [101], CH_3OCH_3 $\rightharpoonup$ CH_3OCH_2 $\rightharpoonup$ $CH_3OCH_2O_2$ $\rightharpoonup$ $CH_2OCH_2O_2H$ $\rightharpoonup$ OH + 2 CH_2O represents the main LTC pathway where the last reaction controls the evolution of the cool flame for both pressures in the cases P8T722 and P40T722, shown in Fig. C.1. The formation of QOOH depends mainly on reactions $O_2CH_2OCH_2O_2H \rightleftharpoons CH_2OCH_2O_2H + O_2$ and $CH_3OCH_2O_2 \rightleftharpoons CH_2OCH_2O_2H$.

From P8T722 to P40T722 is seen in Fig. 5.2a that the NTC is dislocated from $T = 722$ to 840 K, and also, the IDT increasing is reduced for the higher pressure. For $p = 8$ bar, four main reaction paths identified in Fig. C.1 lead to CH_2O formation. First, in P1, the formation of formaldehyde results from the abstraction of H from the fuel forming the methoxymethyl radical, CH_3OCH_3 $\rightharpoonup$ CH_3OCH_2 $\rightharpoonup$ CH_2O. In the pathway P2, CH_3OCH_3 $\rightharpoonup$ CH_3OCH_2 $\rightharpoonup$ CH_3 $\rightharpoonup$ CH_3O $\rightharpoonup$ CH_2O finishes in the pressure dependent reation $CH_3O + M \rightleftharpoons CH_2O + H + M$. The branching P3 was already mentioned, and normally, it is referenced as the main LTC pathway. The fourth branching P4, is the longest, CH_3OCH_3 $\rightharpoonup$ CH_3OCH_2 $\rightharpoonup$ $CH_3OCH_2O_2$ $\rightharpoonup$ $CH_2OCH_2O_2H$ $\rightharpoonup$ $O_2CH_2OCH_2O_2H$ $\rightharpoonup$ HO_2CH_2OCHO $\rightharpoonup$ OCH_2OCHO $\rightharpoonup$ $HOCH_2OCO$ $\rightharpoonup$ CH_2OH $\rightharpoonup$ CH_2O, and it is characterized by unimolecular and isomerization reactions. When pressure is raised to $p = 40$ bar, the reactive increases since it increases the flux through reaction QOOH $\rightleftharpoons$ $_2CH_2O$ + OH than QOOH + O_2 $\rightleftharpoons$ O_2QOOH. It ends up suppressing P4, which forms CO at the end

of the reaction pathway. Therefore, when the pressure has increased, the competition between P3 and P4 results in a suppression of P4, resulting in a dominance of the faster path to form formaldehyde.

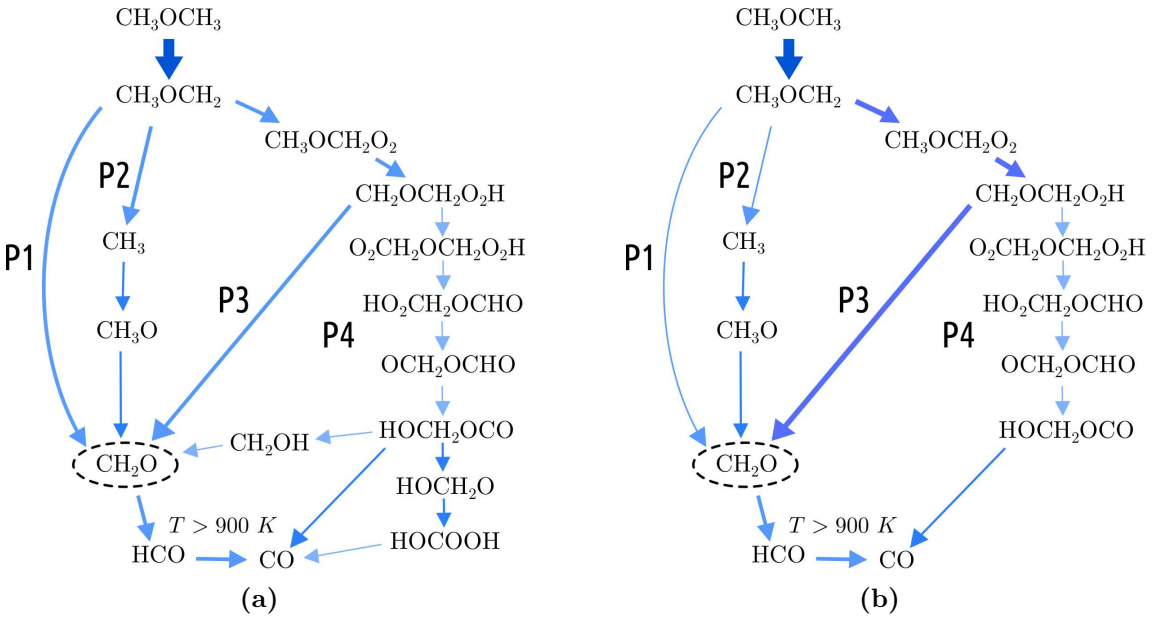

Figure C.1: Reaction pathways for DME at 722 K and for different pressures. The thickness of arrows here represents the relative importance of different reaction pathways based on carbon flux. (a) P8T722 and (b) P40T722.

Appendix D

Flame structure validation

Figure D.1 shows the validation case P40T722 for the double flame profiles comparing the results for the steady-state solution with $u_{inlet} = S_l = 2.3$ m/s. Figures D.1a and D.1b present the temperature and the heat release rate results, respectively, while Figs. D.1c and D.1d show the profiles of selected species. The profiles depict the flames centralized in the maximum heat release rate. Both solutions anchor the hot flame front at $x = 4$ mm.

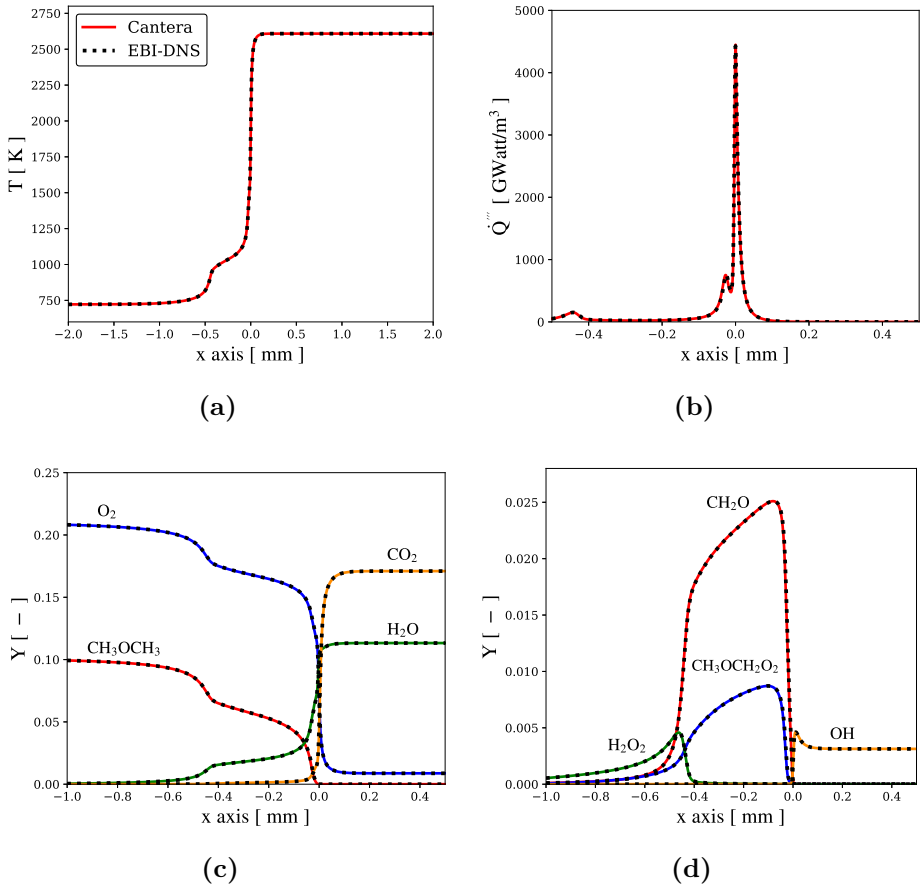

Figure D.1: Double flame results comparing the solution computed with Cantera and EBI-DNS at steady-state regime for P40T722 and $u_{inlet} = S_l = 2.3$ m/s. (a) temperature, (b) heat release rate, (c) DME, oxygen, carbon dioxide and water and (d) formaldehyde, OH, H_2O_2, $CH_3OCH_2O_2$.

Appendix E

List of Publications

R. Meier, T. C. Cardoso, A. M. Oliveira, "Numerical Study of Triple Flames in Partially Premixed Methane and Hydrogen-Air Mixtures", *In: Proceedings of 19th Brazilian Congress of Thermal Sciences and Engineering*, Bento Gonçalves, Brazil, 2022.

R. Meier, A. M. Oliveira, "Effects of hydrodynamic and thermo-diffusive instabilities in the local burning rate of lean premixed hydrogen/air laminar flames", *In: Proceedings of 26th ABCM International Congress of Mechanical Engineering*, Florianópolis, Brazil, 2021.

R. Meier, A. M. Oliveira, "Linear Growth rate of instabilities caused by initial perturbations in lean hydrogen premixed flames", *In: 8th Brazilian Combustion Institute Summer School of Combustion*, virtual edition, Fortaleza, Brazil, 2021, *Poster*.

R. Meier, A. M. Oliveira, "Transient pressure effects in the propagation of the premixed cool flames", *In: The 38th International Symposium on Combustion*, Adelaide, Australia, 2021, *Poster*.

R. Meier, A. M. Oliveira, "Detailed Numerical Simulation of the Flame-flow Interaction in a Slot-burner Laminar Premixed Flame", *In: Proceedings of 18th Brazilian Congress of Thermal Sciences and Engineering*, virtual edition, Brazil, 2020.

R. Meier, A. M. Oliveira, "Zero-dimensional analysis of the end gas processes in SI engines using detailed chemical kinetics", In: 17th International Conference on Numerical Combustion, Aachen, Germany, 2019, *Presentation*.

Bibliography

[1] Ministry of the Ecological Transition, "Données et études statistiques, pour le changement climatique, l'énergie, l'environnement, le logement, et les transports," 2021, accessed 2021-11-04. [Online]. Available: https://www.statistiques.developpement-durable.gouv.fr/tous-les-chiffres?theme=5

[2] I. Tiseo, "Carbon footprint of select modes of transport per kilometer of travel in 2018," 2021, accessed 2021-11-04. [Online]. Available: https://www.statista.com/statistics/1185559/carbon-footprint-of-travel-per-kilometer-by-mode-of-transport/

[3] International Energy Agency, IEA, "World energy balances: Overview," 2021, accessed 2022-03-04. [Online]. Available: https://www.iea.org/reports/world-energy-balances-overview

[4] G. Kalghatgi, "Is it really the end of internal combustion engines and petroleum in transport?" *Applied Energy*, vol. 225, pp. 965–974, 2018.

[5] R. Mével, K. Chatelain, G. Blanquart, and J. Shepherd, "An updated reaction model for the high-temperature pyrolysis and oxidation of acetaldehyde," *Fuel*, vol. 217, pp. 226–239, 2018.

[6] M. Carlier, "Electrified and battery electric vehicles - global sales 2020-2025," 2021, accessed 2022-04-04. [Online]. Available: https://www.statista.com/statistics/960920/global-electric-vehicle-market-share-by-segment/

[7] A. Masri, "Challenges for turbulent combustion," *Proceedings of the Combustion Institute*, vol. 38, no. 1, pp. 121–155, 2021.

[8] F. Williams, *Theoretical and Numerical Combustion*. Menlo Park, California: The Benjamin Cummings Publishing Company, 1985.

[9] X. Gu, D. Emerson, and D. Bradley, "Modes of reaction front propagation from hot spots," *Combustion and Flame*, vol. 133, no. 1, pp. 63–74, 2003.

[10] I. Glassman, *Combustion*, 4th ed. San Diego: Academic Press, 2008.

[11] Z. Chen, "Studies on the initiation, propagation, and extinction of premixed flames," Ph.D. dissertation, Princeton University, Princeton, 2009.

[12] M. P. Musculus, P. C. Miles, and L. M. Pickett, "Conceptual models for partially premixed low-temperature diesel combustion," *Progress in Energy and Combustion Science*, vol. 39, no. 2, pp. 246–283, 2013.

[13] A. Krisman, E. R. Hawkes, M. Talei, A. Bhagatwala, and J. H. Chen, "A direct numerical simulation of cool-flame affected autoignition in diesel engine-relevant conditions," *Proceedings of the Combustion Institute*, vol. 36, no. 3, pp. 3567–3575, 2017.

[14] Z. Wang, H. Liu, and R. D. Reitz, "Knocking combustion in spark-ignition engines," *Progress in Energy and Combustion Science*, vol. 61, pp. 78–112, 2017.

[15] M. Yao, Z. Zheng, and H. Liu, "Progress and recent trends in homogeneous charge compression ignition (hcci) engines," *Progress in Energy and Combustion Science*, vol. 35, no. 5, pp. 398–437, 2009.

[16] W. Sun, S. H. Won, X. Gou, and Y. Ju, "Multi-scale modeling of dynamics and ignition to flame transitions of high pressure stratified n-heptane/toluene mixtures," *Proceedings of the Combustion Institute*, vol. 35, no. 1, pp. 1049–1056, 2015.

[17] J. Warnatz, U. Maas, and R. W. Dibble, *Combustion: Physical and Chemical Fundamentals, Modeling and Simulation, Experiments, Pollutant Formation*, 4th ed. Heidelberg: Springer, 2006.

[18] S. Deng, P. Zhao, D. Zhu, and C. K. Law, "Ntc-affected ignition and low-temperature flames in nonpremixed dme/air counterflow," *Combustion and Flame*, vol. 161, no. 8, pp. 1993–1997, 2014.

[19] Y. Ju, C. B. Reuter, O. R. Yehia, T. I. Farouk, and S. H. Won, "Dynamics of cool flames," *Progress in Energy and Combustion Science*, vol. 75, p. 100787, 2019.

[20] P. Lignola and E. Reverchon, "Cool flames," *Progress in Energy and Combustion Science*, vol. 13, no. 1, pp. 75–96, 1987.

[21] J. E. Dec, "Advanced compression-ignition engines-understanding the in-cylinder processes," *Proceedings of the Combustion Institute*, vol. 32, no. 2, pp. 2727–2742, 2009.

[22] Y. Ju, C. B. Reuter, and S. H. Won, "Numerical simulations of premixed cool flames of dimethyl ether/oxygen mixtures," *Combustion and Flame*, vol. 162, no. 10, pp. 3580–3588, 2015.

[23] S. E. Hosseini and B. Butler, "An overview of development and challenges in hydrogen powered vehicles," *International Journal of Green Energy*, vol. 17, no. 1, pp. 13–37, 2020.

[24] E. T. Network, "The etn hydrogen gas turbines report: the path towards a zero-carbon gas turbine," 2020, accessed 2021-12-01. [Online]. Available: https://etn.global/news-and-events/news/hydrogen-gas-turbines-report/

[25] A. Goldmann, W. Sauter, M. Oettinger, T. Kluge, U. Schröder, J. R. Seume, J. Friedrichs, and F. Dinkelacker, "A study on electrofuels in aviation," *Energies*, vol. 11, no. 2, 2018.

[26] A. Omari, B. Heuser, S. Pischinger, and C. Rüdinger, "Potential of long-chain oxymethylene ether and oxymethylene ether-diesel blends for ultra-low emission engines," *Applied Energy*, vol. 239, pp. 1242–1249, 2019.

[27] C. Lhuillier, P. Brequigny, F. Contino, and C. Mounaïm-Rousselle, "Experimental study on ammonia/hydrogen/air combustion in spark ignition engine conditions," *Fuel*, vol. 269, p. 117448, 2020.

[28] T. Poinsot and D. Veynante, *Combustion Theory: The Fundamental Theory of Chemically Reacting Flow Systems*. Philadelphia, USA: Edwards, 2005.

[29] C. Law, *Combustion Physics*. Germany: Princeton University, 2006.

[30] L. Berger, K. Kleinheinz, A. Attili, and H. Pitsch, "Characteristic patterns of thermodiffusively unstable premixed lean hydrogen flames," *Proceedings of the Combustion Institute*, vol. 37, no. 2, pp. 1879–1886, 2019.

[31] M. Matalon, "Intrinsic flame instabilities in premixed and nonpremixed combustion," *Annual Review of Fluid Mechanics*, vol. 39, pp. 163–191, 2007.

[32] O. Kwon, G. Rozenchan, and C. Law, "Cellular instabilities and self-acceleration of outwardly propagating spherical flames," *Proceedings of the Combustion Institute*, vol. 29, no. 2, pp. 1775–1783, 2002.

[33] G. Jomaas, C. K. Law, and J. K. Bechtold, "On transition to cellularity in expanding spherical flames," *Journal of Fluid Mechanics*, vol. 583, pp. 1–26, 2007.

[34] J. Heywood, *Internal Combustion Engines Fundamentals*. New York: McGraw-Hill, 1988.

[35] X. Zhao, Z. Zhu, Z. Zheng, Z. Yue, H. Wang, and M. Yao, "Effects of flame propagation speed on knocking and knock-limited combustion in a downsized spark ignition engine," *Fuel*, vol. 293, p. 120407, 2021.

[36] H. Vafamehr, A. Cairns, O. Sampson, and M. M. Koupaie, "The competing chemical and physical effects of transient fuel enrichment on heavy knock in an optical spark ignition engine," *Applied Energy*, vol. 179, pp. 687–697, 2016.

[37] J. Pan, H. Wei, G. Shu, Z. Chen, and P. Zhao, "The role of low temperature chemistry in combustion mode development under elevated pressures," *Combustion and Flame*, vol. 174, pp. 179–193, 2016.

[38] F. Battin-Leclerc, "Detailed chemical kinetic models for the low-temperature combustion of hydrocarbons with application to gasoline and diesel fuel surrogates," *Progress in Energy and Combustion Science*, vol. 34, no. 4, pp. 440–498, 2008.

[39] K. Kohse-Höinghaus, "Combustion in the future: The importance of chemistry," *Proceedings of the Combustion Institute*, vol. 38, no. 1, pp. 1–56, 2021.

[40] A. Krisman, E. R. Hawkes, and J. H. Chen, "The structure and propagation of laminar flames under autoignitive conditions," *Combustion and Flame*, vol. 188, pp. 399–411, 2018.

[41] Y. Ju, "Understanding cool flames and warm flames," *Proceedings of the Combustion Institute*, vol. 38, no. 1, pp. 83–119, 2021.

[42] H. Wang, Z. Wang, K. Luo, E. R. Hawkes, J. H. Chen, and J. Fan, "Direct numerical simulation of turbulent boundary layer premixed combustion under auto-ignitive conditions," *Combustion and Flame*, vol. 228, pp. 292–301, 2021.

[43] K. Aditya, A. Gruber, C. Xu, T. Lu, A. Krisman, M. R. Bothien, and J. H. Chen, "Direct numerical simulation of flame stabilization assisted by autoignition in a reheat gas turbine combustor," *Proceedings of the Combustion Institute*, vol. 37, no. 2, pp. 2635–2642, 2019.

[44] D. K. Srivastava, *Advances in Internal Combustion Engine Research*, 1st ed. Singapore: Springer Nature Singapore Pte Ltd, 2018.

[45] H. Curran, P. Gaffuri, W. Pitz, and C. Westbrook, "A comprehensive modeling study of iso-octane oxidation," *Combustion and Flame*, vol. 129, no. 3, pp. 253–280, 2002.

[46] S. Tanaka, F. Ayala, J. C. Keck, and J. B. Heywood, "Two-stage ignition in hcci combustion and hcci control by fuels and additives," *Combustion and Flame*, vol. 132, no. 1, pp. 219–239, 2003.

[47] D. Davidson, B. Gauthier, and R. Hanson, "Shock tube ignition measurements of iso-octane/air and toluene/air at high pressures," *Proceedings of the Combustion Institute*, vol. 30, no. 1, pp. 1175–1182, 2005.

[48] X. He, M. Donovan, B. Zigler, T. Palmer, S. Walton, M. Wooldridge, and A. Atreya, "An experimental and modeling study of iso-octane ignition delay times under homogeneous charge compression ignition conditions." *Combustion and Flame*, 2005.

[49] S. Walton, X. He, B. Zigler, M. Wooldridge, and A. Atreya, "An experimental investigation of iso-octane ignition phenomena," *Combustion and Flame*, vol. 150, no. 3, pp. 246–262, 2007.

[50] L. Cancino, M. Fikri, A. Oliveira, and C. Schulz, "Autoignition of gasoline surrogate mixtures at intermediate temperatures and high pressures: Experimental and numerical approaches," *Proceedings of the Combustion Institute*, vol. 32, no. 1, pp. 501–508, 2009.

[51] ——, "Ignition delay times of ethanol-containing multi-component gasoline surrogates: Shock-tube experiments and detailed modeling," *Fuel*, vol. 90, no. 3, pp. 1238–1244, 2011.

[52] M. Mehl, W. J. Pitz, C. K. Westbrook, and H. J. Curran, "Kinetic modeling of gasoline surrogate components and mixtures under engine conditions," *Proceedings of the Combustion Institute*, vol. 33, no. 1, pp. 193–200, 2011.

[53] M. AlAbbad, T. Javed, F. Khaled, J. Badra, and A. Farooq, "Ignition delay time measurements of primary reference fuel blends," *Combustion and Flame*, vol. 178, pp. 205–216, 2017.

[54] J. F. Griffiths and C. B. Mohamed, "Chapter 6 experimental and numerical studies of oxidation chemistry and spontaneous ignition phenomena," *Comprehensive Chemical Kinetics*, vol. 35, pp. 545–660, 1997.

[55] J. Griffiths and B. Whitaker, "Thermokinetic interactions leading to knock during homogeneous charge compression ignition," *Combustion and Flame*, vol. 131, no. 4, pp. 386–399, 2002.

[56] P. Zhao, W. Liang, S. Deng, and C. K. Law, "Initiation and propagation of laminar premixed cool flames," *Fuel*, vol. 166, pp. 477–487, 2016.

[57] S. Desai, R. Sankaran, and H. G. Im, "Unsteady deflagration speed of an autoignitive dimethyl-ether (dme)/air mixture at stratified conditions," *Proceedings of the Combustion Institute*, vol. 37, no. 4, pp. 4717–4727, 2019.

[58] Y. Ju, "On the propagation limits and speeds of premixed cool flames at elevated pressures," *Combustion and Flame*, vol. 178, pp. 61–69, 2017.

[59] L. Cai and H. Pitsch, "Optimized chemical mechanism for combustion of gasoline surrogate fuels," *Combustion and Flame*, vol. 162, no. 5, pp. 1623–1637, 2015.

[60] J. H. Knox, *Photochemistry and reaction kinetics: The interpretation of cool flame and low-temperature combustion phenomena.* Cambridge University Press, 1967.

[61] R. F. Gould, *Oxidation of organic compounds.* Advances in Chemistry Series, 1968.

[62] R. Pollard, "Chapter 2 hydrocarbons," in *Gas-Phase Combustion*, ser. Comprehensive Chemical Kinetics, C. Bamford and C. Tipper, Eds. Elsevier, 1977, vol. 17, pp. 249–367.

[63] R. Cox and J. Cole, "Chemical aspects of the autoignition of hydrocarbon-air mixtures," *Combustion and Flame*, vol. 60, no. 2, pp. 109–123, 1985.

[64] R. Walker and C. Morley, "Chapter 1 basic chemistry of combustion," in *Low-Temperature Combustion and Autoignition*, ser. Comprehensive Chemical Kinetics, M. Pilling, Ed. Elsevier, 1997, vol. 35, pp. 1–124.

[65] B. Bäuerle, F. Hoffmann, F. Behrendt, and J. Warnatz, "Detection of hot spots in the end gas of an internal combustion engine using two-dimensional lif of formaldehyde," *Symposium (International) on Combustion*, vol. 25, no. 1, pp. 135–141, 1994.

[66] Z. Wang, O. Herbinet, N. Hansen, and F. Battin-Leclerc, "Exploring hydroperoxides in combustion: History, recent advances and perspectives," *Progress in Energy and Combustion Science*, vol. 73, pp. 132 – 181, 2019.

[67] N. Peters, *Turbulent Combustion*. United Kingdom: Cambridge University Press, 2000.

[68] A. Lipatnikov, *Fundamentals of Premixed Turbulent Combustion*. London: CRC Press, 2013.

[69] G. K. Giannakopoulos, A. Gatzoulis, C. E. Frouzakis, M. Matalon, and A. G. Tomboulides, "Consistent definitions of "flame displacement speed" and "markstein length" for premixed flame propagation," *Combustion and Flame*, vol. 162, no. 4, pp. 1249–1264, 2015.

[70] D. G. Goodwin, H. K. Moffat, I. Schoegl, R. L. Speth, and B. W. Weber, "Cantera: An object-oriented software toolkit for chemical kinetics, thermodynamics, and transport processes," https://www.cantera.org, 2022, version 2.6.0.

[71] T. Zirwes, F. Zhang, P. Habisreuther, M. Hansinger, H. Bockhorn, M. Pfitzner, and D. Trimisn, "Quasi-dns dataset of a piloted flame with inhomogeneous inlet conditions," *Flow, Turbulence and Combustion*, vol. 104, pp. 997–1027, 2020.

[72] R. Kee, M. Coltrin, and P. Glarborg., *Chemically Reacting Flow: Theory and Practice*, 2005.

[73] OpenCFD, "Openfoam user guide," version 2.0.1, 2011.

[74] Sundials: Suite of nonlinear and differential/algebraic equation solvers. [Online]. Available: http://computation.llnl.gov/casc/sundials/main.html

[75] T. T. Zirwes, "Memory effects in premixed flames: Unraveling transient flame dynamics with the flame particle tracking method," Ph.D. dissertation, Karlsruher Institut für Technologie (KIT), 2021.

[76] B. J. McBride, S. Gordon, and M. A. Reno, "Coefficients for calculating thermodynamic and transport properties of individual species," *National Aeronautics and Space Administration, NASA*, vol. 4513, 1993.

[77] J. O. Hirschfelder, C. F. Curtiss, and R. B. Bird, *Molecular Theory Of Gases And Liquids*. New York: Wiley-Interscience, 1954.

[78] B. E. Poling, J. M. Prausnitz, and J. P. O'Connell, "The properties of gases and liquids," *Journal of the American Chemical Society*, vol. 123, no. 27, pp. 6745–6745, 2001.

[79] G. Dixon-Lewis, "Flame structure and flame reaction kinetics. ii. transport phenomena in multicomponent systems," *Proceedings of the Royal Society of London. Series A, Mathematical and Physical Sciences*, vol. 307, no. 1488, pp. 111–135, 1968.

[80] V. Giovangigli, "Multicomponent flow modeling," *Science China Mathematics*, vol. 55, pp. 285–308, 1999.

[81] R. Bird, W. Stewart, and E. Lightfoot, *Transport Phenomena*. Wiley, 2006, no. v. 1.

[82] L. Monchick and E. A. Mason, "Transport properties of polar gases," *Journal of Chemical Physics (U.S.)*, vol. 35, 1961.

[83] M. Matalon, C. Cui, and J. Bechtold, "Hydrodynamic theory of premixed flames: Effects of stoichiometry, variable transport coefficients and arbitrary reaction orders," *Journal of Fluid Mechanics*, vol. 487, pp. 179 – 210, 06 2003.

[84] H. Markstein, "Non-steady flame propagation," *The Journal of the Royal Aeronautical Society*, vol. 68, no. 647, 1964.

[85] N. Peters, P. Terhoeven, J. H. Chen, and T. Echekki, "Statistics of flame displacement speeds from computations of 2-d unsteady methane-air flames," *Symposium (International) on Combustion*, vol. 27, no. 1, pp. 833–839, 1998.

[86] J. H. Chen and H. G. Im, "Correlation of flame speed with stretch in turbulent premixed methane/air flames," *Symposium (International) on Combustion*, vol. 27, no. 1, pp. 819–826, 1998.

[87] G. Barenblatt, Y. Zeldovich, and A. Istratov, "Diffusive-thermal stability of a laminar flame," *J. Appl. Mech. Tech. Phys.*, vol. 4, pp. 21–26, 01 1962.

[88] P. Clavin and G. Joulin, "Premixed flames in large scale and high intensity turbulent flow," *Journal De Physique Lettres*, vol. 44, pp. 1–12, 1983.

[89] P. Clavin and P. Garcia-Ybarra, "The influence of the temperature dependence of diffusivities on the dynamics of flame fronts," *Journal de Physique Théorique et Appliquée*, vol. 2, pp. 245–263, 01 1983.

[90] P. García-Ybarra, C. Nicoli, and P. Clavin, "Soret and dilution effects on premixed flames," *Combustion Science and Technology*, vol. 42, no. 1-2, pp. 87–109, 1984.

[91] P. Clavin and C. Nicoli, "Effect of heat losses on the limits of stability of premixed flames propagating downwards," *Combustion and Flame*, vol. 60, no. 1, pp. 1–14, 1985.

[92] P. Clavin and J. C. Graña-Otero, "Curved and stretched flames: the two markstein numbers," *Journal of Fluid Mechanics*, vol. 686, p. 187–217, 2011.

[93] F. Egolfopoulos, N. Hansen, Y. Ju, K. Kohse-Höinghaus, C. Law, and F. Qi, "Advances and challenges in laminar flame experiments and implications for combustion chemistry," *Progress in Energy and Combustion Science*, vol. 43, pp. 36 – 67, 2014.

[94] S. S. Goldsborough, S. Hochgreb, G. Vanhove, M. S. Wooldridge, H. J. Curran, and C.-J. Sung, "Advances in rapid compression machine studies of low- and intermediate-temperature autoignition phenomena," *Progress in Energy and Combustion Science*, vol. 63, pp. 1 – 78, 2017.

[95] G. Darrieus, "Propagation d'un front de flamme," *La Technique Moderne, unpublished*, 1938.

[96] L. Landau, "On the theory of slow combustion," in *Dynamics of Curved Fronts*, P. Pelcé, Ed. San Diego: Academic Press, 1944, pp. 403–411.

[97] P. Pelce and P. Clavin, "Influence of hydrodynamics and diffusion upon the stability limits of laminar premixed flames," in *Dynamics of Curved Fronts*, P. Pelcé, Ed. San Diego: Academic Press, 1988, pp. 425–443.

[98] M. Matalon and B. Matkowsky, "On the stability of plane and curved flames." *SIAM Journal on Applied Mathematics*, vol. 44, no. 2, pp. 327–343, Jan. 1984.

[99] M. Frankel and G. Sivashinsky, "The effect of viscosity on hydrodynamic stability of a plane flame front," *Combustion Science and Technology*, vol. 29, pp. 207–224, 1982.

[100] R. Kee, J. Grcar, M. Smooke, J. Miller, and E. Meeks, "Premix: A fortran program for modeling steady laminar one-dimensional premixed flames," *Sandia National Laboratories*, 1985.

[101] A. Bhagatwala, Z. Luo, H. Shen, J. Sutton, T. Lu, and J. Chen, "Numerical and experimental investigation of turbulent dme jet flames," *Proceedings of the Combustion Institute*, vol. 35, no. 2, pp. 1157–1166, 2015.

[102] J. Li, Z. Zhao, A. Kazakov, and F. Dryer, "An updated comprehensive kinetic model of hydrogen combustion," *International Journal of Chemical Kinetics*, vol. 36, pp. 566 – 575, 10 2004.

[103] T. Zirwes, F. Zhang, and H. Bockhorn, "Memory effects of local flame dynamics in turbulent premixed flames," *Proceedings of the Combustion Institute*, 2022.

[104] J. H. Ferziger and M. Peric, *Computational Methods for Fluid Dynamics*. Berlin: Springer, 2002.

[105] T. Poinsot and S. Lelef, "Boundary conditions for direct simulations of compressible viscous flows," *Journal of Computational Physics*, vol. 101, no. 1, pp. 104–129, 1992.

[106] Y. Rastigejev and M. Matalon, "Numerical simulation of flames as gas-dynamic discontinuities," *Combustion Theory and Modelling*, vol. 10, no. 3, pp. 459–481, 2006.

[107] F. Zhang, T. Zirwes, P. Habisreuther, and H. Bockhorn, "Effect of unsteady stretching on the flame local dynamics," *Combustion and Flame*, vol. 175, pp. 170–179, 2017.

[108] T. Poinsot and D. Veynante, *Theorical and Numerical Combustion*. USA: Edwards, 2005.

[109] G. Searby, S. Candel, D. Durox, T. Schuller, and D. Dunn-Rankin, *Instability Phenomena during Flame Propagation*, 02 2009.

[110] C. Altantzis, C. E. Frouzakis, A. G. Tomboulides, M. Matalon, and K. Boulouchos, "Hydrodynamic and thermodiffusive instability effects on the evolution of laminar planar lean premixed hydrogen flames," *Journal of Fluid Mechanics*, vol. 700, p. 329–361, 2012.

[111] L. Berger, A. Attili, and H. Pitsch, "Intrinsic instabilities in premixed hydrogen flames: parametric variation of pressure, equivalence ratio, and temperature. part 2 – non-linear regime and flame speed enhancement," *Combustion and Flame*, vol. 240, p. 111936, 2022.

[112] K. Takeuchi, K. Fujimoto, S. Hirano, and M. Yamashita, "Investigation of engine oil effect on abnormal combustion in turbocharged direct injection - spark ignition engines." *SAE 2012-05-1017*, 2012.

[113] X. Luo, H. Teng, T. Hu, R. Miao, and L. Cao, "Mitigating intensities of super knocks encountered in highly boosted gasoline direct injection engines." *SAE 2015-01-0015*, 2015.

[114] J. Willand, M. Daniel, E. Montefrancesco, B. Geringer, and P. H. M. Kieberger., "Limits on downsizing in spark ignition engines due to pre-ignition," *MTZ worldwide*, vol. 70, no. 5, pp. 56–61, 2009.

[115] Y. Moriyoshi, T. Yamada, D. Tsunoda, M. Xie, T. Kuboyama, and K. Morikawa., "Numerical simulation to understand the cause and sequence of lspi phenomena and suggestion of cao mechanism in highly boosted si combustion in low speed range." *SAE Technical Paper 2015-01-0755.*, 2015.

[116] M. Mayer, P. Hofmann, J. Williams, and D.Tong., "Influence of the engine oil on pre-ignitions at highly supercharged direct-injection gasoline engines," *MTZ worldwide*, vol. 77, no. 6, pp. 36–41, Jun 2016.

[117] Z. Wang, H. Liu, T. Song, Y. Qi, X. He, S. Shuai, and J. Wang, "Relationship between super-knock and pre-ignition," *International Journal of Engine Research*, vol. 16, no. 2, pp. 166–180, 2015.

[118] A. Douaud and P. Eyzat., "Four-octane-number method for predicting the anti-knock behavior of fuels and engines." *SAE 780080*, 1978.

[119] B. Hoepke, S. Jannsen, E. Kasseris, and W. Cheng., "Egr effects on boosted si engine operation and knock integral correlation." *SAE International Journal Engines 2012-01-0707.*, vol. 5, pp. 547–559, 2012.

[120] L. Chen, T. Li, T. Yin, and B. Zheng., "A predictive model for knock onset in spark-ignition engines with cooled egr." *Energy Conversion and Management*, vol. 87, pp. 946–955, November 2014.

[121] E. Pipitone, S. Beccari, and G. Genchi., "A refined model for knock onset prediction in spark ignition engines fueled with mixtures of gasoline and propane." *Journal of Engineering for Gas Turbines and Power*, November 2015.

[122] T. M. Foong, M. J. Brear, K. Morganti, G. da Silva, Y. Yang, and F. L. Dryer, "Modeling end-gas autoignition of ethanol/gasoline surrogate blends in the cooperativefuel research engine," *Energy & Fuels*, vol. 31, pp. 2378–2389, 2017.

[123] C. Ferguson, *Internal Combustion Engines: Applied Thermosciences.* New York: Wiley & Sons, 1986.

[124] S. Richard, S. Bougrine, G. Font, L. Francois, and F. Berr, "On the reduction of a 3d cfd combustion model to build a physical 0d model for simulating heat release, knock and pollutants in si engines," *Oil Gas Science and Technology - Revue de l'IFP*, vol. 64, pp. 223–242, 2009.

[125] J. X. Zhou, B. Moreau, C. Mounaïm-Rousselle, and F. Foucher, "Combustion, performance and emission analysis of an oxygen-controlling downsized si engine," *Oil & Gas Science and Technology - Revue d'IFP Energies nouvelles*, vol. 71, p. 49, 2016.

[126] S. Demesoukas, P. Brequigny, C. Caillol, F. Halter, and C. Mounaïm-Rousselle, "0d modeling aspects of flame stretch in spark ignition engines and comparison with experimental results," *Applied Energy*, vol. 179, pp. 401–412, 2016.

[127] S. Richard, S. Bougrine, G. Font, F. Lafossas, and F. L. Berr, "On the reduction of a 3d cfd combustion model to build a physical 0d model for simulation heat release, knock and polluants in si engines," *Oil and Gas Science and Technology*, vol. 64, pp. 223–242, 2009.

[128] S. Bougrine, S. Richard, O. Colin, and D. Veynante, "Fuel composition effects on flame stretch in turbulent premixed combustion: Numerical analysis of flame-vortex interaction and formulation of a new efficiency function," *Flow, Turbulence and Combustion*, vol. 93, no. 2, pp. 259–281, 2014.

[129] C. Meneveau and T. Poinsot, "Stretching and quenching of flamelets in premixed turbulent combustion," *Combustion and Flame*, vol. 86, no. 4, pp. 311–332, 1991.

[130] J. Duclos, D. Veynante, and T. Poinsot, "A comparison of flamelet models for premixed turbulent combustion," *Combustion and Flame*, vol. 95, no. 1, pp. 101–117, 1993.

[131] M. Metghalchi and J. C. Keck, "Burning velocity of mixtures of air with methanol, isooctane, and indolene at high pressure and temperature," *Combustion Flame*, vol. 48, 1982.

[132] A. Medina, P. Curto-Risso, A. Hernández, L. Vargas, F. Brown, and A. Sen, *Quasi-dimensional simulation of spark ignition engines: from thermodynamic optimization to cyclic variability.* London, UK: Springer, 2014.

[133] E. Aghdam, A. Burluka, T. Hattrell, K. Liu, C. Sheppard, J. Neumeister, and N. Crundwell, "Study of cyclic variation in an si engine using quasi-dimensional combustion model," *SAE Technical Papers - 2007-01-0939.*

[134] A. Lipatnikov and J. Chomiak, "Modeling of pressure and non-stationary effects in spark ignition engine combustion: A comparison of different approaches," *SAE Technical Papers - 2000-01-2034.*

[135] G. Woschni, "A universally applicable equation for the instantaneous heat transfer coefficient in the internal combustion engine," in *National Fuels and Lubricants, Powerplants, Transportation Meetings.* SAE International, 1967, p. 19.

[136] Lsoda: Ordinary differential equation solver for stiff or non-stiff system. [Online]. Available: http://www.oecd-nea.org/tools/abstract/detail/uscd1227

[137] A. C. Hindmarsh, "Odepack, a systematized collection of ode solvers," *IMACS Transactions on Scientific Computation*, vol. 1, pp. 55–64, 1983.

[138] P. N. Brown and A. C. Hindmarsh, "Reduced storage matrix methods in stiff ode systems," *Journal. Applied Mathematics*, pp. 40–91, 1989.

[139] A. da Silva Jr., J. Hauber, L. Cancino, and K. Huber, "The research octane numbers of ethanol-containing gasoline surrogates," *Fuel*, vol. 243, pp. 306–313, 2019.

[140] L. R. Cancino, A. K. da Silva, A. Toni, M. Fikri, A. A. M. Oliveira, C. Schulz, and H. J. Curran, "A six-compound, high performance gasoline surrogate for internal combustion engines: Experimental and numerical study of autoignition using high-pressure shock tubes," *Fuel*, vol. 261, p. 116439, 2020.

[141] M. Mehl, J. Y. Chen, W. J. Pitz, S. M. Sarathy, and C. Westbrook, "An approach for formulating surrogates for gasoline with application toward a reduced surrogate mechanism for cfd engine modeling," *Energy & Fuels*, vol. 25, pp. 5215–5223, 2011.

[142] E. Ranzi, A. Frassoldati, A. Stagni, M. Pelucchi, A. Cuoci, and T. Faravelli, "Reduced kinetic schemes of complex reaction systems: Fossil and biomass-derived transportation fuels," *International Journal of Chemical Kinetics*, vol. 46, no. 9, pp. 512–542, 2014.

[143] J. C. G. Andrae, T. Brinck, and G. Kalghatgi, "Hcci experiments with toluene reference fuels modeled by a semidetailed chemical kinetic model," *Combustion and Flame*, vol. 155, pp. 696–712, 2008.

[144] H. Wang, M. Yao, and R. D. Reitz, "Development of a reduced primary reference fuel mechanism for internal combustion engine combustion simulations," *Energy and Fuels*, vol. 27, no. 12, 11 2013.

[145] D. M. Smooke, J. A. Miller, and R. J. Kee, "Determination of adiabatic flame speeds by boundary value methods," *Combustion Science and Technology*, vol. 34, no. 1-6, pp. 79–90, 1983.

[146] J. B. Martz, G. A. Lavoie, H. G. Im, R. J. Middleton, A. Babajimopoulos, and D. N. Assanis, "The propagation of a laminar reaction front during end-gas auto-ignition," *Combustion and Flame*, vol. 159, no. 6, pp. 2077–2086, 2012.

[147] M. Faghih, H. Li, X. Gou, and Z. Chen, "On laminar premixed flame propagating into autoigniting mixtures under engine-relevant conditions," *Proceedings of the Combustion Institute*, vol. 37, no. 4, pp. 4673–4680, 2019.

[148] W. Zhang, M. Faqih, X. Gou, and Z. Chen, "Numerical study on the transient evolution of a premixed cool flame," *Combustion and Flame*, vol. 187, pp. 129–136, 2018.

[149] Y. Wang, H. Zhang, T. Zirwes, F. Zhang, H. Bockhorn, and Z. Chen, "Ignition of dimethyl ether/air mixtures by hot particles: Impact of low temperature chemical reactions," *Proceedings of the Combustion Institute*, vol. 38, no. 2, pp. 2459–2466, 2021.

[150] Y. Wang, W. Han, T. Zirwes, F. Zhang, H. Bockhorn, and Z. Chen, "Effects of low-temperature chemical reactions on ignition kernel development and flame propagation in a dme-air mixing layer," *Proceedings of the Combustion Institute*, 2022.

[151] H. J. Emeléus, "The spectra of the phosphorescent flames of carbon disulphide and ether," *J. Chem. Soc.*, vol. 129, pp. 2948–2951, 1926.

[152] J. F. Griffiths and T. Inomata, "Oscillatory cool flames in the combustion of diethyl ether," *J. Chem. Soc., Faraday Trans.*, vol. 88, pp. 3153–3158, 1992.

[153] H. Pearlman, "Low-temperature oxidation reactions and cool flames at earth and reduced gravity," *Combustion and Flame*, vol. 121, no. 1, pp. 390–393, 2000.

[154] C. B. Reuter, S. H. Won, and Y. Ju, "Experimental study of the dynamics and structure of self-sustaining premixed cool flames using a counterflow burner," *Combustion and Flame*, vol. 166, pp. 125–132, 2016.

[155] Y. Ju, E. Lin, and C. Reuter, "The effect of radiation on the dynamics of near limit cool flames and hot flames," *55th AIAA Aerospace Sciences Meeting*, 2017.

[156] T. Farouk, D. Dietrich, and F. Dryer, "Three stage cool flame droplet burning behavior of n-alkane droplets at elevated pressure conditions: Hot, warm and cool flame," *Proceedings of the Combustion Institute*, vol. 37, no. 3, pp. 3353–3361, 2019.

[157] V. Nayagam, D. L. Dietrich, P. V. Ferkul, M. C. Hicks, and F. A. Williams, "Can cool flames support quasi-steady alkane droplet burning?" *Combustion and Flame*, vol. 159, no. 12, pp. 3583–3588, 2012.

[158] T. Farouk, M. Hicks, and F. Dryer, "Multistage oscillatory "cool flame" behavior for isolated alkane droplet combustion in elevated pressure microgravity condition," *Proceedings of the Combustion Institute*, vol. 35, no. 2, pp. 1701–1708, 2015.

[159] W. Affleck and A. Fish, "Knock: Flame acceleration or spontaneous ignition?" *Combustion and Flame*, vol. 12, no. 3, pp. 243–252, 1968.

[160] C. B. Reuter, S. H. Won, and Y. Ju, "Experimental study of the dynamics and structure of self-sustaining premixed cool flames using a counterflow burner," *Combustion and Flame*, vol. 166, pp. 125–132, 2016.

[161] R. Sankaran, "Propagation velocity of a deflagration front in a preheated autoigniting mixture," *9th U.S. National Combustion Meeting*, 2015.

[162] T. Zhang and Y. Ju, "Structures and propagation speeds of autoignition-assisted premixed n-heptane/air cool and warm flames at elevated temperatures and pressures," *Combustion and Flame*, vol. 211, pp. 8–17, 2020.

[163] B. Savard, A. Wehrfritz, K. Lam, Q. Margerte, L. Ferney, and S. Farjam, "Decreased mixture reactivity and hot flame speed in the products of diffusion-affected autoignitive cool flames in the ntc regime," *Combustion and Flame*, vol. 222, pp. 434–445, 2020.

[164] Y. Zhang, X. Yang, W.Shen, H. Zhang, S. Wang, and J. Lyu, "Numerical study on the stabilization of a self-sustaining steady-state premixed cool flame," *Microgravity Science and Technology*, vol. 31, pp. 845–854, 2019.

[165] T. Zirwes, F. Zhang, T. Häber, and H. Bockhorn, "Ignition of combustible mixtures by hot particles at varying relative speeds," *Combustion Science and Technology*, vol. 191, no. 1, pp. 178–195, 2019.

[166] A. Krisman, C. Mounaïm-Rousselle, R. Sivaramakrishnan, J. A. Miller, and J. H. Chen, "Reference natural gas flames at nominally autoignitive engine-relevant conditions," *Proceedings of the Combustion Institute*, vol. 37, no. 2, pp. 1631–1638, 2019.

[167] T. C. de Souza, "Modulated turbulence for premixed flames," Ph.D. dissertation, Eindhoven University of Technology, Eindhoven, 2014.

[168] E. Suillaud, K. Truffin, O. Colin, and D. Veynante, "Direct numerical simulations of high karlovitz number premixed flames for the analysis and modeling of the displacement speed." *Combustion and Flame*, vol. 236, p. 111770, 2022.

[169] P. Bridgman, "A complete collection of thermodynamic formulas," *Physical Review*, vol. 3, pp. 273–281, 1914.

[170] C. Olikara and G. L. Borman, "A computer program for calculating properties of equilibrium combustion products with some applications to i.c. engines," in *1975 Automotive Engineering Congress and Exposition*. SAE International, 1975.

[171] S. Gordon and B. McBride, "Computer program for calculation of complex chemical equilibrium compositions, rocket performance, incident and reflected shocks, and chapman-jouquet detonations," *NASA SP-273*, 1971.